Cell-cell adhesion mediated by mobile receptor-ligand pairs: a biomimetic study

Dissertation

zur

Erlangung des Doktorgrades

der

Mathematisch-Naturwissenschaftlichen Fakultät

der

Rheinischen Friedrich-Wilhelms-Universität Bonn

vorgelegt von

Susanne Franziska Fenz

aus

Frankfurt am Main

Bonn Dezember 2008

Angefertigt mit Genehmigung der Mathematisch-Naturwissenschaftlichen Fakultät
der Rheinischen Friedrich-Wihelms-Universität Bonn
Erscheinungsjahr: 2009

1. Gutachter: Prof. Dr. Rudolf Merkel
2. Gutachter: Prof. Dr. Ulrich Kubitschek
Tag der Promotion: 20.03.09
Diese Dissertation ist auf dem Hochschulschriftenserver der ULB Bonn unter http://hss.ulb.uni-bonn.de/diss_online elektronisch publiziert.

meiner großartigen Familie

Acknowledgment - Vielen Dank ...

... meinem Doktorvater Herrn Prof. Rudolph Merkel für die Möglichkeit dieses spannende Thema unter optimalen Bedingungen bearbeiten zu können, für die immerwährende Diskussionsbereitschaft, die bereitwilligen Erklärungen und nicht zuletzt die vermittelte Begeisterung für die Forschung an der Grenze von Physik, Biologie und Chemie.

... my supervisor Kheya Sengupta for the introduction to the field of biomimetic systems, for the great support from near and far, for your encouragement, patience and hospitality!

... Ana Smith for your advice concerning the interpretation of the data from a theoretical point of view. Thank you very much for the last-minute reading of the thesis and numerous skype sessions.

... Prof. Ulrich Kubitschek für die Zweitbetreuung dieser Arbeit. Vielen Dank für die interessanten Gespräche und Diskussionen in Bonn.

... Bernd Hoffman und Simone Born für die unermüdlichen Versuche dem E. Coli ein leuchtendes E-cadherin abzuringen, für die kompetente und immer freundliche Beratung in allen biologischen Fragen.

... Norbert Kirchgessner und Sebastian Houben für die Unterweisung in matlab, die große Hilfsbereitschaft zu allen Zeiten und Unzeiten und die Not-Schokoladenrationen.

... Cornelia Monzel für die vielen aufschlussreichen Diskussionen und das unermüdliche Korrekturlesen! Ich danke Dir für Deine große Hilfsbereitschaft auch über das Fachliche hinaus.

... Sabine Dieluweit für die Versuche das E-cadherin mit dem AFM oder durch Tieffrieren dingfest zu machen, außerdem für die immer bereitwillige und geduldige chemische Beratung und nicht zuletzt für die Initative zu unseren schönen Kulturausflügen.

... Christoph Möhl für die Einweisung in das vertrackte Confocal und die FRAP-Technik.

... Agnes Csiszar für die Beratung in Lipid- und Vesikelfragen, für die nette 'Kellergesellschaft' und die lustigen - viel zu seltenen - Spieleabende.

... Dieter Waschbüsch für die biologische Beratung und die praktische Hilfe rund ums Auto.

... Claudia Cesa for you friendship, for the sleeping place in Jülich, for the nice girls-evenings and pancakes for breakfast.
... Wolfgang Rubner für die Beratung in allen technischen Fragen.
... dem Team der Werkstatt für die superschnelle Herstellung aller in dieser Arbeit verwendeten Bauteile.
... Claudia Klamandt für die immer freundliche und hilfsbereite Unterstützung bei verwaltungstechnischen Dingen.
... meiner Kochgruppe für das Durchfüttern in den letzten Wochen!
... der gesamten Arbeitsgruppe des IBN-4 für die ganz besondere, freundschaftliche Arbeitsatmosphäre.

... Stefan, weil Du jeden Augenblick meines Lebens bereicherst. Dafür, dass Du mich in letzten Wochen ertragen hast, für die gemeinsam durchgearbeiteten Nächte, fürs Haushalt schmeißen, fürs Da-sein in jeder Zeit...
... meiner Familie für die liebevolle Unterstützung, für die unzähligen Briefe, Carepakete, Besuche und Anrufe, für die unermüdliche Aufmunterung, Motivation und Liebe!

Abstract

Adhesion of cells to other cells is of vital importance for multicellular organisms. It is mediated by specific bonds between cell surface molecules. These molecules can be either attached to some rigid internal structure of the cell or freely diffusing within the membrane. The present work aims at a quantitative understanding of the physical processes in cell-cell adhesion caused by such mobile cell adhesion molecules.

To unequivocally separate physical processes from active biological cell response, a **biomimetic model system** was developed. It consisted of a giant unilamellar vesicle (GUV) adhering via specific ligand-receptor interactions to a solid supported lipid bilayer (SLB). Adhesion was mediated by either biotin-neutravidin (an avidin analogue) or the extracellular domains of the homophilic cell adhesion molecule E-cadherin (Ecad). While the biotin-neutravidin interaction is known to be extremely strong (Gibbs free energy of bonding ΔG_0 in solution $\sim$ 35 k_BT) the Ecad-Ecad bond represented the case of very weak binding ($\Delta G_0 \sim 2$ k_BT). In each case, receptors and ligands were bound to the SLB and the membrane of the GUV where they were able to freely diffuse laterally.

Microinterferometry (reflection interference contrast microscopy, RICM) was employed to dynamically quantify vesicle shapes with lateral resolution of $\sim$ 250 nm and axial resolution of a few nanometers. Fluorescence microscopy (FM) yielded lateral distributions and diffusivities of fluorescently labelled membrane molecules. A microscope was modified for simultaneous application of FM and RICM. In addition, the quantitative interpretation of RICM images was extended.

In membrane adhesion mediated by both binding pairs in high concentration the final **equilibrium** was characterized with respect to membrane distance, tension, and adhesion energy density with the help of RICM. The adhesion energy densities and tensions in the strong binding case were beyond the measurable range accessible with the applied technique ($>10^{-6}$J/m^2 and $>10^{-5}$N/m^2) while for weak binding considerably lower values were measured (10^{-7}J/m^2 and 10^{-6}N/m^2). The measured

inter-membrane distance of 7 nm for biotinylated vesicles adhered via neutravidin was in very good agreement with the expected height calculated from the molecular size of neutravidin plus the lengths of the biotin linkers. The corresponding measurement of 50 nm on the Ecad bound vesicle indicates that here Ecad was bound by only partial overlap of its extracellular domains.

The fluidity of the SLB and the **diffusion of the receptors** was studied during vesicle adhesion. Continuous photobleaching (CP) was used to measure the in-plane diffusion of tracer lipids and receptors in the SLB membrane. In the strong interaction (biotin-neutravidin) case, binding of soluble receptors to the SLB alone led to reduced diffusion of tracer lipids. From theoretical considerations, this could be attributed partially to introduction of obstacles and partially to viscous effects. Further specific binding of a GUV membrane caused additional slowing down of tracers (up to 15%) and immobilization of receptors, and led to accumulation of receptors in the adhesion zone till full coverage was achieved. It was shown that a crowding effect due to the accumulated receptors alone was not sufficient to account for the slowing down - an additional friction from the membrane also played a role. In the weak binding case (Ecad), no significant change in diffusion of tracer lipids was observed upon protein binding and subsequent vesicle binding. Here, the insensitivity of diffusion to membrane binding arose due to the large inter-membrane distance which reduced membrane induced friction. It was concluded that the effect of inter-membrane adhesion on diffusion depended strongly on the choice of the receptors.

In the strong binding case vesicle adhesion was achieved at low and high concentrations of receptors and ligands while the weak binding case required high concentrations. As a consequence, the **dynamics of vesicle adhesion** were studied for a broad range of receptor-ligand concentrations for strong binding and merely at high concentrations for weak binding. It was shown that low ligand concentrations in the vesicle retarded the establishment of the initial nucleation center while low concentrations of receptors on the bilayer mainly influenced the final adhered state. Complete adhesion and full receptor accumulation was reached only above a threshold concentration. Simultaneous observation of the adhered area in RICM and the corresponding receptor distribution in fluorescence revealed that adhesion and accumulation went hand in hand above the threshold but at lower concentrations a large

time lag between both processes was found. Receptors were accumulated mostly at the edges of the adhesion zone where they were effectively immobilized and acted as obstacles for newly arriving receptors.

In the case of strong (biotin-neutravidin) binding and high concentrations the adhesion process followed the classical pattern of nucleation, linear growth and saturation. It was shown that the reduced volume of the vesicle and the resulting fluctuation amplitude of the vesicle membrane influenced the adhesion process in all three stages. Vesicles exhibiting large fluctuations were found to establish multiple nucleation centers (NCs) and consequently their area vs. time curves were characterized by a steeper slope. While the high number of NCs accelerated the growth regime, saturation was retarded by the competing NCs and the resulting in high probability of trapping liquid in the form of bubbles. Variation of the receptor and ligand concentrations revealed the influence of mobile receptor-ligand pairs on the adhesion dynamics. Increasing the receptor concentration on the bilayer resulted in accelerated growth but also in retarded saturation. The relatively large receptors (lateral size $\sim$ 4-5 nm) were immobilized by jamming at very high concentrations. Due to the small size of the ligands (which in this case were biotinylated lipids with lateral size 8 Å), increasing the ligand concentration in the vesicle membrane was not accompanied by reduced mobility, and therefore the overall adhesion process was accelerated. In the case of weak binding (Ecad), the adhesion process was predominantly classical as described above, but two different types of adhesion dynamics, characterized by either only dilute bonds or an abundance of small NCs respectively, were observed in addition. This was interpreted as a sign for the sensitivity of the system to small environmental changes.

Finally, experiments on vesicle unbinding by competitive binding of free biotin molecules were performed. As expected, the bond between neutravidin and a biotinylated lipid from the bilayer was found to be extremely stable. However, the situation was different in the case of neutravidin mediated vesicle adhesion. Addition of free biotin to a completely adhered vesicle led to retraction of the contact zone and partial unbinding of the vesicle membrane. Weakening of the bond due to the thermally induced membrane fluctuations was proposed as an explanation for this observation.

Contents

Chapter 1

Introduction

The existence of higher organisms is based on the ability of single cells to organize into multicellular structures. If the survival of the organism no longer depends on one cell performing all functions necessary for life, but collectively on several cells, the individual cells can specialize. This way, for example, vertebrates developed the major tissue types: nervous, lymphoid, epithelial, and connective tissue as well as specialized blood cells [1]. Each of these tissue types consists of specialized cells embedded at least in parts in a macro-molecular scaffold, the extracellular matrix (ECM). The ECM is formed by a variety of macromolecules that are secreted by cells. Besides stabilizing the tissue, the ECM is also involved in several other cell functions like signalling and recognition. The contact of cells with the ECM is called cell-matrix adhesion, but cells also bind directly to each other in cell-cell adhesion. In case of mature adhesion sites, specialized cell adhesion molecules (CAMs) form supra-molecular structures, which are usually connected to the cytoskeleton inside the cell, thus forming a mechano-chemical link between cells or between a cell and the ECM. Focal adhesions mediated by integrins in case of cell to ECM adhesion, and adherens junctions mediated by cadherins in case of cell-cell adhesion are examples of such structures. In the nascent stages of cell adhesion, before fully mature focal adhesions or adherens junctions are formed, the cell membrane simply adheres to another surface without exhibiting any specific structures. Owing to the transient nature of the events that occur during early stages of cell adhesion, they were hard to visualize prior to the development of advanced imaging techniques and are only

beginning to be studied in detail. Important physical and biological events occur in between the very first recognition of an adhesive surface and the formation of mature contact structures. Since CAMs reside on the cell membrane, the membrane itself plays an important role in adhesion. Before discussing membrane adhesion we will briefly address cell membranes.

Membranes

Biological membranes form the outer layer of cells. They consist of an asymmetric lipid bilayer with phospholipids and cholesterol as the main components. Membrane proteins are either embedded in this bilayer as integral transmembrane proteins or attached to lipids or transmembrane proteins in the membrane (for a schematic view of a plasma membrane see Figure 1.1). Many of theses lipids and proteins are glycosilated and contribute to a layer of polysaccharides at the outer cell surface. This dense mesh is called glycocalix and protects the cell against mechanical and chemical damage. From the inside, the membrane is stabilized by the actin rich cell cortex. The membrane separates the contents and processes of the cell interior from the surrounding environment. At the same time it plays a role in cell-cell communication, cell-cell recognition and transport processes to supply the cell with all necessary nutrients (amino acids, saccharides, peptides, proteins, ...) [2–5]. In order to fulfill all these tasks, membranes need equipment (glycolipids, membrane proteins, etc.) and transport mechanisms. The basic means of short-range transport within the plane of the membrane is passive diffusion. Long-range transport in membranes requires active transport mechanisms. Transport of small molecules across the membrane is mediated by a variety of channels and pumps. Another transport mechanism, mostly for larger objects, is realized by endo-and exocytosis of small vesicles.

The view of the contribution of lipids and proteins to all these membrane related functions changed substantially over the last decades. In the 1970s the fluid mosaic model was introduced [7]. It described the lipid bilayer as a passive fluid medium in which the active molecules, the proteins, move. Some striking observations in epithelial cells proved this picture to be oversimplified. Lipids were found to form functional microdomains insoluble even in strong detergents [8, 9]. In the meantime, basic research on lipid bilayers and vesicles with three components, two

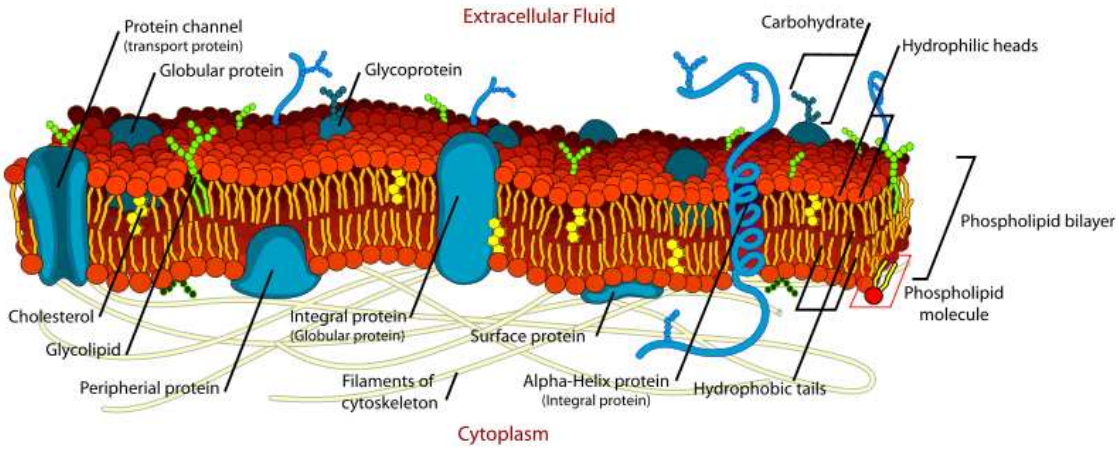

Figure 1.1: Schematic view of a cell membrane. [6]

kinds of lipids with different phase transition temperatures and cholesterol, revealed that even lipid mixtures exhibited complex phase separation behavior [10–13]. Although the observations on cells and biomimetic systems are still to be integrated into a global picture, it is accepted that lateral inhomogeneities are necessary for the function of biological membranes [14]. At present, the consensus is to describe a membrane as a highly complex, compartmentalized system with a broad range of dynamic processes [14–16].

Adhesion Proteins

The principal CAMs, also called receptors, for cell-matrix adhesion are the integrins. They bind to extracellular matrix proteins like collagens, fibronectin, and laminins. Occasionally, integrins are also found to promote cell-cell adhesion (e.g. neutrophils on endothelium). The major CAMs or receptors responsible for cell-cell adhesion in vertebrate tissue are cadherins of which one prominent representative is E-cadherin. It belongs to the superfamily of cadherins where it is a member of the subgroup 'classic cadherins'. Cadherins play a vital role in the development and maintenance of multicellular organisms. Tissue morphogenesis is controlled by spatial and temporal regulated cadherin expression [17, 18]. During development cadherins control histogenic cell separation and segregation [19]. Hence, they ensure the correct composition of tissue and organs. In adults, cadherins preserve the structural integrity of tissue and direct reorganization, for example wound healing after injury [20]. As a consequence, mutations in cadherin encoding genes lead to tissue disorder, increased

invasiveness of tumor cells and malignancy [21].

Besides the explicit adhesion molecule that forms the connection between one cell and another cell or one cell and the extracellular matrix, an abundance of additional proteins contribute to adhesion [22]. The development and maintenance of the adhesion site is regulated by a variety of mechanisms, some of which are actively controlled. Some examples include: competitive binding, phosphorylation, conformational changes. There is large interest to elucidate the underlying processes both from the biological and the physical side. Especially in the early stages of adhesion (up to ~ 1 min) physical laws are expected to dominate because the cell needs some time to initiate an active response.

Physical Forces in Cell Adhesion

The main attractive forces arise from the specific interaction of the cell adhesion molecules while several other effects hamper adhesion. One contribution comes from the fact that the CAMs that were initially freely diffusing in the cell membrane are immobilized and accumulated at the adhesion site. This state is entropically unfavorable. Moreover, the cell membrane has to be bend at the sites of bond formation. Polymers sticking out of the cell membrane (glycocalix) additionally hinder adhesion due to steric repulsion. Thus, molecular accumulation, shape deformations and steric repulsion contribute to the free energy of adhesion. Since CAMs are embedded in a relatively soft deformable surface, the undulation entropy of the membrane may also contribute to the free energy. Superimposed on all this is the stabilizing effect of the cytoskeleton which binds to the adhesion molecules from the cytosolic side.

Mimetic Systems

In a real cell, it is impossible to control all parameters involved in adhesion. Thus, physical contributions are studied with the help of biomimetic systems where the cell is mimicked by a giant unilamellar vesicle. Giant unilamellar vesicles (GUVs) consist of a spherical closed lipid bilayer serving as a simplified model for the cell membrane. The vesicles are functionalized with cell adhesion molecules which interact with a corresponding receptor that is either immobilized on a surface (to study cell-matrix adhesion), coupled to a fluid lipid bilayer on a solid support or in the membrane of another vesicle (to study cell-cell adhesion). Lipid-coupled polymers

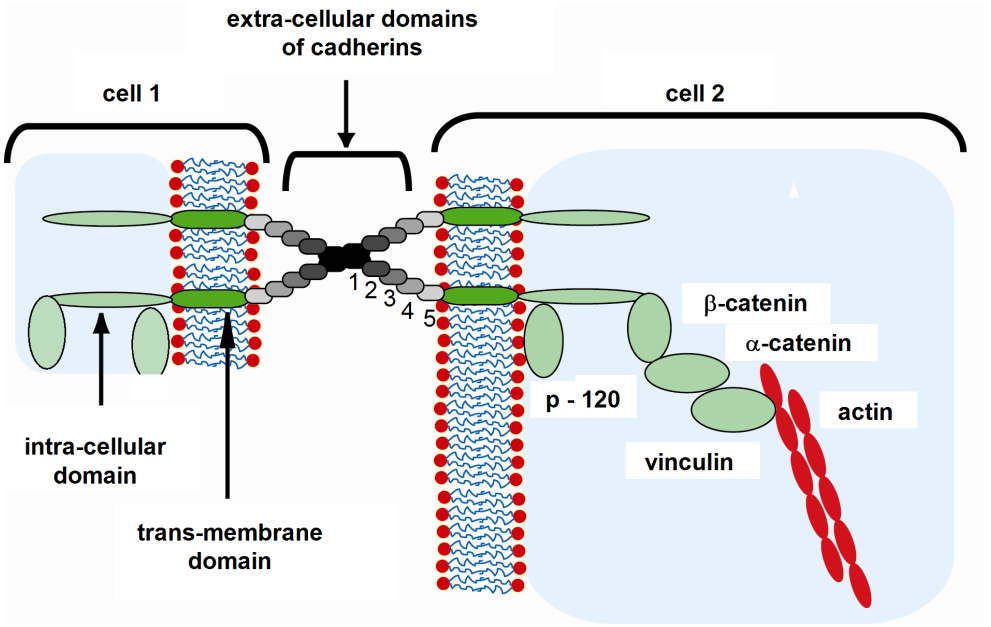

Figure 1.2: Simplified schematic diagram of cadherin mediated cell-cell adhesion. (not to scale, courtesy K. Sengupta, following [21]).

can be incorporated in the vesicle membrane to mimic the glycocalix. This simplified scheme allows us to study the key features of cell adhesion: cooperative binding, diffusion controlled receptor segregation, membrane deformation and the influence of the glycocalix. Biomimetic model systems like giant unilamellar vesicles allow not only to study the global event of cell adhesion characterized by shape deformations, but also to investigate processes within the model membrane.

In this thesis, a model system was developed to mimic cell-cell adhesion. It consisted of a giant unilamellar vesicle adhering via specific ligand-receptor interactions to a supported lipid bilayer. Two kinds of specific interactions were employed. An artificial version of E-cadherin was used as a model protein for weak homophilic binding while the heterophilic receptor-ligand pair biotin/avidin was employed to mimic strong specific binding.

E-cadherin/E-cadherin

'E' in E-cadherin (Ecad) stands for epithelium - the tissue, where Ecad is predominately found. There, for example at the interface of intestine and blood stream, its main function is to form a transport barrier [23].

Cadherins are transmembrane glycoproteins with a molecular weight of ~ 120 kDa. They consist of an extracellular domain for homophilic binding, a single hydropho-

bic domain located in the membrane and an intracellular domain responsible for signalling. The latter one can also be indirectly linked to the cell cytoskeleton [24]. Five repeated globular domains arranged in tandem ($\sim$ 110 amino acids each) form the extracellular domain responsible for specific adhesion. They are named EC01 to EC05 starting with the outmost domain.

It is generally believed that cadherins bind in a two step process. First, two cadherins of the same cell form a lateral or *cis* dimer before they bind to the *cis* dimer on the surface of another cell forming a *trans*-tetramer. However, it is still under discussion whether the *cis* dimerization is obligatory for cadherin function [23]. A prerequisite for proper cadherin binding is the presence of at least 500 μM Ca^{2+} [25–27]. Each of the four EC domain junctions is stabilized by three calcium ions [28, 29]. Hence, upon Ca^{2+} binding the extracellular domain behaves no longer like a flexible rod but is activated for binding. It is known that EC01 plays a major role in adhesion and selectivity [30, 31], but maximum bond strength (2 k_BT) is observed only when all five domains overlap [32]. Since cadherins fulfil a variety of tasks it is likely that more than one site is involved in the specific function of the protein.

There is an on-going debate about the binding geometry of Ecad-Ecad bonds. Based on experiments probing the binding strength of the full length extra cellular cadherin domains and several deletion mutants with the surface force apparatus or micropipette aspiration (see [23] and references within), the interdigitation model [23, 33] was proposed. In this, three different binding configurations are possible: overlap of only the outmost domains (EC01 EC01), of the three outmost domains (EC01-EC03 EC01-EC03) or all domains (EC01-EC05 EC01-EC05).

Besides the described homophilic binding, the cadherin ectodomain is also capable of heterophilic binding to several extracellular proteins [21]. Moreover, Prakasam *et al.* showed that N-, E- and C-cadherin may also form heterophilic bonds with each other [34]. The binding strength of these mixed cadherin bonds is overall comparable with homophilic cadherin bonds. This result questions the hitherto believed role of cadherin in cell segregation during morphogenesis. It implies that the cadherin expression level cannot be the only determining factor in cell sorting.

Biotin/Avidin

Biotin, also called vitamin H, was first described by F. Steinitz in 1898 [35]. He

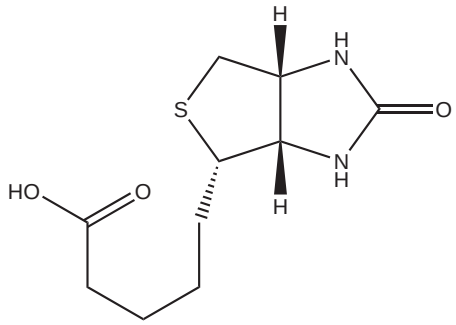

Figure 1.3: Structural formula of biotin (created with ChemDraw).

observed in animal tests that a heat stable factor from yeast or liver is an essential nutrition component. The factor was termed vitamin H (skin = German: Haut) because it cured dermatitis caused by feeding with excess of raw egg white. In 1942 the chemical structure of biotin was determined by V. de Vigneaud [36] (see Figure 1.3) and later confirmed by total synthesis [37] and X-ray crystallography [38]. Biotin is found in most plant and animal tissue in low concentrations [39]. It is an essential growth factor because it acts as a coenzyme for many vital processes, e.g. fatty acid biosynthesis [40, 41]. Due to its carboxyl group, biotin can be easily covalently bound to other molecules in order to functionalize or tag them. Since the carboxyl group is far away from the active ring system, biotin retains its binding specificity while being used as a tag [42]. In this thesis biotinylated lipids were used to functionalize model membranes.

Avidin was identified as the biotin antagonist from egg white [43, 44]. It was first isolated from chicken eggs by Esmond E. Snell [45] in 1941. Avidin is a glycoprotein with a molecular weight of 66 kDa found in egg white of birds, reptiles and amphibians [46]. It consists of eight β strands. Each pair of these forms one classical antiparallel β barrel resulting in four identical subunits. Each subunit binds one biotin molecule [47]. While the affinity of the tetramer for biotin is extremely high, $K_D = 10^{-15}$ M, the monomer binds biotin only with $K_D = 10^{-7}$ M [47]. The high biotin binding affinity suggests that avidin could function as an anti-biotic protein inhibiting bacterial growth [48]. Each bond exhibits a Gibbs free energy of binding of 35 k_BT that is one of the highest known in biology [49]. The biotin/avidin interaction is mainly promoted by two contributions. First, the ureido-ring of biotin is hydrogen bonded at multiple contact points within the binding pocket [50, 51].

Second, a change in the tertiary and quaternary structure takes place [52, 53]. The loop between β strand three and four forms a lid encasing biotin in the barrel via van der Waals and hydrophobic interactions [50, 51].

The binding pair biotin/avidin is frequently used in model systems to study the phenomenon of biomolecular recognition. Biomolecular recognition comprises all specific interactions that are based on the cooperation of a diversity of non-covalent forces (van der Waals, hydrophobic, ionic), e.g. protein-protein, protein-peptide, protein-ligand and protein-DNA interactions [54, 55]. Avidin is very popular as a model protein because it is very stable against heat [56], detergents [57] and extreme pH values [47]. One drawback is its isoelectric point of about 10.5 that can lead to unspecific interaction with negatively charged components of the cell at neutral pH. Due to its high stability the biotin/avidin binding pair is especially useful. In addition, its high association constant and binding strength guarantees for optimum reliability. That is why several applications in life science were developed on the basis of the biotin/avidin interaction: purification and labeling techniques, diagnostics, targeted drug delivery and nanotechnology [58].

Thesis Outline

A microscope set-up was developed that allows for investigation of vesicle adhesion on solid supported lipid bilayers by reflection interference contrast microscopy and simultaneous observation of the receptor fate in the bilayer with fluorescence microscopy. Dynamics of vesicle adhesion as well as equilibrium states were studied in a broad range of receptor and ligand concentrations. Full understanding of the observations was achieved by separate analysis of lipid and receptor mobility on the bilayer.

Chapter 2

Materials and Techniques

In this chapter the materials and standard techniques employed in this project are introduced. The model system is described in full detail together with the preparation techniques. The imaging section provides first an overview of the basic light microscopy techniques and the microscope set-up used to characterize the model system. Second, it focuses on specialized applications allowing for the determination of specific features like inter membrane distances or diffusion constants.

2.1 Materials

2.1.1 Buffers and Solutions

PBS (phosphate buffered saline) was used as standard buffer and prepared as follows: 140 mM NaCl, 3 mM KCl, 10 mM Na_2HPO_4, 2 mM KH_2PO_4, pH 7.2. The osmolarity was typically 300 mOsM/l.

The PIPES (piperazine-N,N'-bis(ethanesulfonic acid), Sigma, Saint Louis, MO) buffer contained 10 mM PIPES and 140 mM NaCl. The pH was adjusted to 7.2 by adding NaOH. The osmolarity (300 mOsM/l) was checked with an osmometer (Osmomat 030, Gonotec GmbH, Berlin, Germany).

The HEPES (4-(2-hydroxyethyl)piperazine-1-ethanesulfonic acid)), Sigma, Saint Louis, MO) buffer contained 10 mM HEPES and 140 mM NaCl. The pH was adjusted to 7.4 by adding NaOH. The osmolarity was typically 300 mOsM/l.

As ECad needs calcium to activate binding a PBS (PIPES, HEPES) based buffer was prepared with 750 μM $CaCl_2$ in addition (PBS-, PIPES-, HEPES-Ca).
For studies on competitive binding a PBS based buffer with 0.2 mg/ml biotin was used. For this purpose, 10 mg of biotin (Sigma, Saint Louis, MO) were dissolved in 50 ml PBS. The resulting buffer (PBS-biotin) was iso-osmolar and had a slightly lower pH 6.9 due to the carboxyl group of the biotin molecules.
For electroswelling of vesicles a 230 mOsM/l sucrose solution was employed. 0.7 g of sucrose (Sigma) was dissolved in 10 ml ultrapure water and the osmolarity was checked with an osmometer.

2.1.2 Lipids

All lipids: SOPC (1-stearoyl-2-oleoyl-sn-glycero-3-phosphocholine), DOPE-PEG 2000 (1,2-dioleoyl-sn-glycero-3-phosphoethanolamine-N- (methoxy(polyethyleneglycol)-2000)), chain-labeled NBD-PC (1-oleoyl-2-[12-[(7-nitro-2-1,3-benzoxadiazol-4-yl)amino]dodecanoyl]-sn-glycero-3-phosphocholine), head-labeled NBD-PE (1,2-dioleoyl-sn-glycero-3-phosphoethanolamine-N-(7-nitro-2-1,3-benzoxadiazol-4-yl) ammonium salt), DOPE-cap-biotin (1,2-dioleoyl-sn-glycero-3-phosphoethanolamine-N-(cap biotinyl)) and DOGS-NTA (1,2-dioleoyl-sn-glycero-3-[(N-(5-amino-1-carboxypentyl) iminodiacetic acid)succinyl]) were purchased from Avanti Polar Lipids (Alabaster, AL) and were used without further purification.

2.1.3 Proteins

Neutravidin (Invitrogen, Eugene, OR) was reconstituted in PBS and ultracentrifugated at 137000 g and 4°C for 2 hours to eliminate protein aggregates. Neutravidin covalently linked to the fluorescent label Oregon Green, henceforth called neutravidin-OG, was purchased at the same source and treated identically. In some experiments neutravidin-OG was replaced by tetramethylrhodamine labelled neutravidin (neutravidin-TMR).
The E-cadherin Fc chimera (R&D Systems, Minneapolis, MN), henceforth referred to as Ecad, was purchased as lyophilized powder containing 50 mM buffer salts(a

mixture of 2-amino-2-hydroxymethyl-propane-1,3-diol Tris and citrate), 0.2 M NaCl and 2 mM $CaCl_2$. It was reconstituted in sterile water for 24 hours at 4°C according to the instructions of the manufacturer. Its calcium dependent activity was checked by a bead assay each time before use (see below).
TRITC (tetramethylrhodamine isothiocyanat) labelled protein A was purchased from Sigma (Saint Louis, MO) and reconstituted in PBS.

2.1.4 General Materials

Thickness corrected glass coverslips (d = 170 ± 10 μm, Assistent, Karl Hecht KG, Sondheim, Germany) were cleaned by the following detergent treatment: Ultrasonication in 2% Hellmanex solution (Hellma, Müllheim, Germany) for 10 minutes, flushing thoroughly with ultrapure water produced by a water purification system (Millipore, San Francisco, CA) and again ultrasonication (2x15 minutes) in ultrapure water followed by flushing with ultrapure water.
A micrometer scale with 100 lines per mm (Carl Zeiss, Göttingen, Germany) served as a calibration object to determine the picture pixel size.
4.5 μm polystyrene beads (Polybead Microspheres 2.5% solids, slightly negatively charged due to sulfate ester groups on the surface, Polysciences Inc., Warrington, PA) were employed in self-designed bead assays.

2.2 Model Membranes

2.2.1 Preparation Techniques

This section explains the techniques applied to generate model membranes. Lipid molecules are the main components of biological membranes as well as model membranes. Each lipid consists of a polar head group and one or two apolar hyrodcarbon chains. This amphiphilic character governs the self-organization of single lipids to supramolecular structures in aqueous solutions [59, 60]. Above a critical concentration of lipids, the hydrophobic effect promotes formation of bilayers and closed configurations without water-exposed edges.

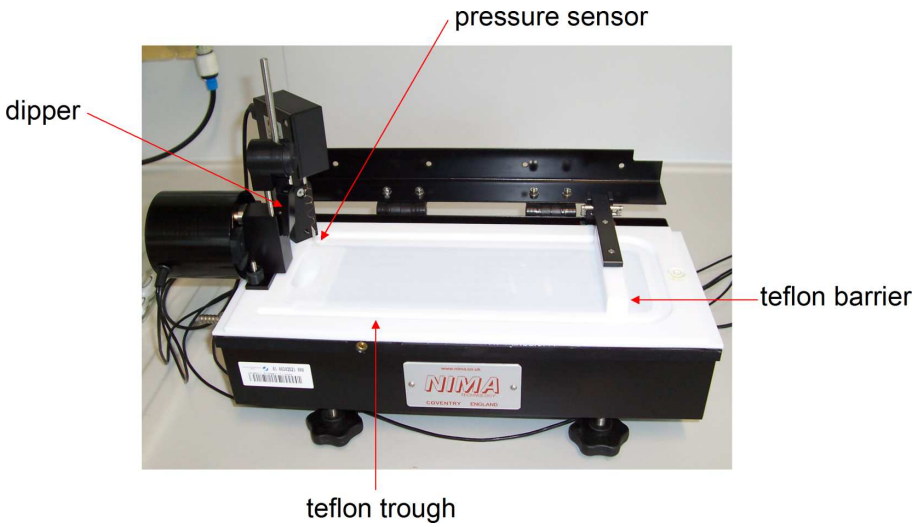

Figure 2.1: Film balance. The arrows point at the main components required to prepare SLBs according to Langmuir-Blodgett Langmuir-Schäfer. See text for detailed description.

2.2.1.1 Solid Supported Lipid Bilayers (SLBs): Langmuir- Blodgett Langmuir-Schäfer Technique

In this work SLBs were used to mimic a cell membrane. SLBs consist of a lipid bilayer formed on top of a solid, here a glass slide. A thin lubricating layer of water (∼1 nm [61–63]) ensured unhindered mobility of the lipids in the plane of the bilayer. SLBs are very important as model membranes because their defined planar geometry allows for optimum control of key parameters (e.g. phase state, receptor concentration) and easy accessibility for observation with light microscopy. In principle there are two techniques commonly applied to prepare SLBs: vesicle fusion [64, 65] and Langmuir-Blodgett [66]. For vesicle fusion tense small vesicles are produced by sonication and exposed to a hydrophilic glass slide under correct buffer conditions. The vesicles burst on contact with the glass forming a symmetric bilayer till the surface is covered. Excess lipid has to be removed by washing the sample.

Here, a variant of the Langmuir-Blodgett technique, called Langmuir-Blodgett Langmuir-Schäfer [67], was applied because it allows for the preparation of asymmetric SLBs (see capter 7). The SLB was prepared with the help of a film balance (Nima, Coventry, UK). A film balance consists mainly of four elements (see Figure 2.1, [68]): A teflon trough which contains ultra-pure water on which a monolayer of lipids is

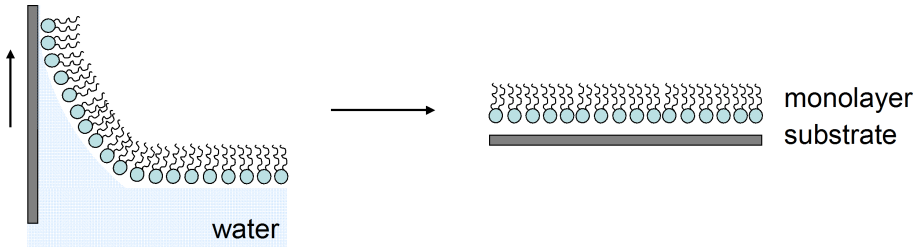

Figure 2.2: Langmuir-Blodgett technique: preparation of lipid monolayers on hydrophilic substrates.

spread, a pressure sensor, which measures the change in surface pressure[1] after addition of a surfactant, a mobile teflon barrier which compresses the film and a dipper which allows for controlled immersion and extraction of a solid substrate.

The lipid bilayer was prepared in a two step procedure: First, the hydrophilic glass substrate was driven under the water surface with the dipper and the lipid mixture, dissolved in chloroform (details see Chapter 2.2.2), was gently deposited onto the water surface. The chloroform spreads, evaporates, and leaves behind a monolayer of lipids which are oriented according to their amphiphilic character. The mobile teflon barrier compressed the monolayer till the desired surface-pressure was reached (here: 20 mN/m). Since Teflon is neither wetted by water nor by alkanes it forms an optimal barrier. The substrate was then drawn slowly up through the water surface (here: 10 mm/min), with the surface to be coated perpendicular to the water surface. The lipids adsorbed to the substrate, with their hydrophilic heads pointing towards the solid, and formed a monolayer: this was the first layer of the bilayer (Figure 2.2). At the same time, the surface pressure was maintained constant by a feed back mechanism that continued to advance the barrier as necessary. This ensured homogeneous lipid density over the glass substrate. Preparation of monolayers requires extremely clean equipment. Otherwise, dirt would accumulate at the air-water interface and contaminate the monolayer.

[1]Here, the term surface pressure is used to describe the interfacial tension due to the amphiphilic film with respect to pure water.

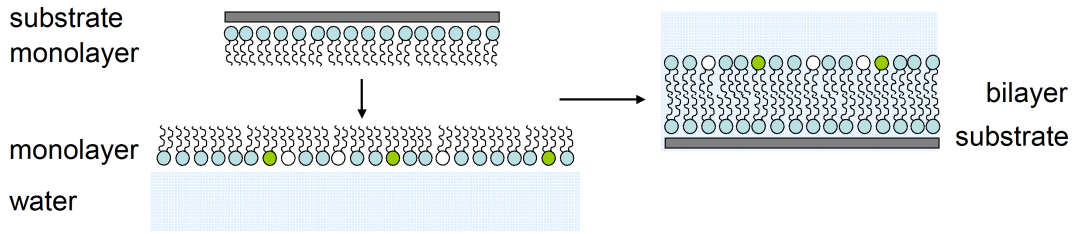

Figure 2.3: Langmuir-Schäfer technique.

In order to prepare the second lipid layer, the appropriate lipid mix, not necessary the same as before, (details see Chapter 2.2.2) was gently deposited onto the water surface and the surface pressure was adjusted as described above. The substrate, which was earlier coated with a monolayer was pressed horizontally through the water surface whereby the second lipid layer was transferred (Figure 2.3). The Langmuir-Blodgett Langmuir-Schäfer technique allows the preparation of SLBs with defined geometry, height homogeneity and a low number of defects at the same time. An exemplary image of a fluorescently labeled SLB can be seen in Figure 3.10. Care was taken to ensure that the substrate with the SLB was never exposed to air and was used directly after preparation.

To prevent contact of the deposited bilayer with air a small teflon tray was placed in the subphase, i.e. under water. It contained a frame onto which the glass slide was pressed (see Figure 2.4 for illustration). Like this the SLB could be brought to a larger vessel filled with water where the glass slide was transferred to the observation chamber with the coated side facing upwards (see Figure 2.5). The chamber was assembled under water. It consisted of a two metal rings, each with a thread so that they could be screwed together. One of the rings had an indentation fitting for the slide. The aqueous phase was shielded from the metal by a thin teflon insert that was put over a metal ring support. An o-ring from perbunan served as washer and sealed the chamber. All metal parts were made of stainless steel. The chamber filling was $\sim$ 1 ml (For technical details see Appendix A).

2.2.1.2 Giant Unilamellar Vesicles (GUVs): Electroswelling

One of the self assembled structures that lipids form in aqueous solution is the vesicle. It is made of one single closed lipid bilayer (see Figure 2.6). This configuration

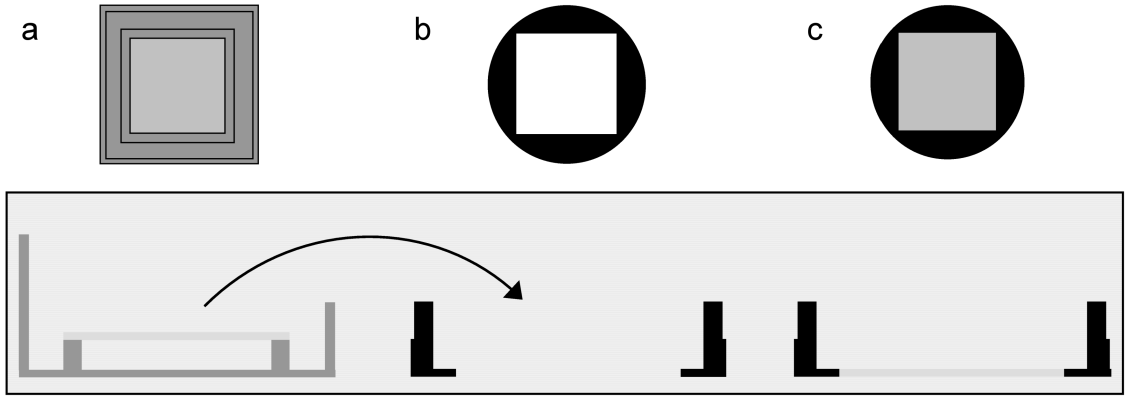

Figure 2.4: a: Teflon bassin with teflon frame and glass slide. b: Lower half of the chamber with indentation for the slide. c: Slide inside the chamber. The upper row shows the top view and the lower row the side view. Not to scale, for technical details see Appendix A.

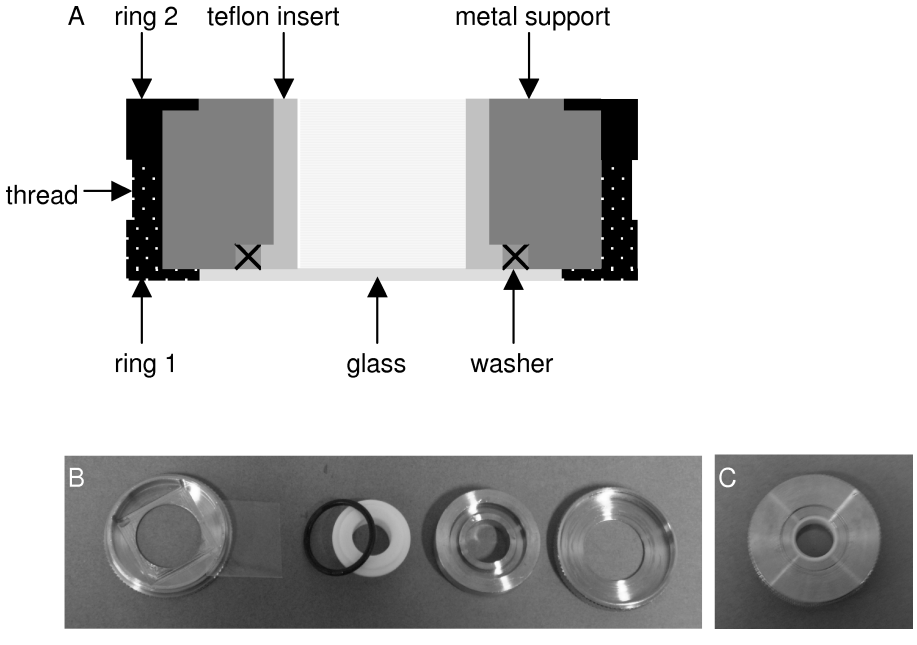

Figure 2.5: Observation chamber. A: Sketch showing a vertical cut through the chamber (Not to scale, for technical details see Appendix A). B: Components of the observation chamber. C: Assembled chamber from top. The outer diameter of the chamber is 4 cm.

Figure 2.6: Spontaneous self-assembly of amphiphilic lipid molecules to giant unilamellar vesicles. Sketch courtesy C. Monzel, IBN4, FZJ [76].

is energetically favourable because the apolar chains are buried within the bilayer and thus concealed from the water. Large (many microns in diameter) vesicles with a single outer membrane are called giant unilamellar vesicles (GUV) In this thesis GUVs were used as biomimetic models for cells.

Besides the spontaneous formation of vesicles from lipid crystals in water resulting in different numbers of layers and diameters [69], there are several techniques to produce vesicles of defined lamellarity and size: extrusion [70], electroswelling [71], electroinjection [72], reverse evaporation and emulsion [73] and microfluidic jetting [74]. The behavior of amphiphilic molecules in aqueous solution is an interesting field of research on its own [60, 75].

The GUVs used in this study had a diameter of 20-30 μm. Hence, they fitted to the typical size of a real cell (some tens of micrometers [1]) and were suitable objects to be investigated by light microscopy (see Chapter 2.3.2). In order to get large unilamellar vesicles at reasonable numbers the electroswelling technique [71] was chosen. For electroswelling, 20 μl of the required lipid dissolved in chloroform (for details see Chapter 2.2.2) were dispersed uniformly on indium tin oxide coated glass slides (4x4x0.5 cm, pgo, Iserlohn, Germany). The slides were put in vacuum (10 mbar) for 4 hours to ensure complete chloroform evaporation. After transferring the slides to a swelling chamber made of teflon, the chamber was filled with 230 mOsmol/l sucrose solution. Alternating current (10 Hz, 1.7 V, 2 hours) was applied to the slides separated by a teflon spacer (d = 1 mm). For the experiment, approximately 20 μl of the vesicle solution was transferred with a pipette to the observation chamber (see also Section 2.2.1.1) filled with 300 mOsmol/l PBS. Thus, the osmotic difference between inside and outside buffer was kept at 70 mOsmol/l. This osmotic difference ensures that the vesicles were floppy, and exhibited a large excess area. This property was necessary to enable vesicle adhesion (see Chapter 4). Moreover real cells also have a

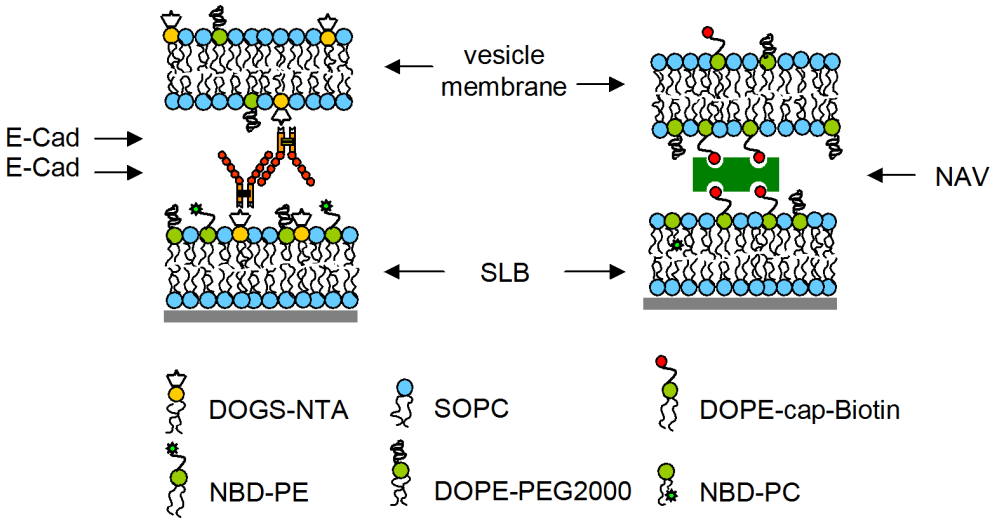

Figure 2.7: Sketches of the model systems illustrating the membranes and binding molecules involved. Left: Weak specific binding: E-cadherin-E-cadherin. Right: Strong specific binding: biotin-neutravidin. See text for details and abbreviations.

large excess area and exhibit fluctuations [77–80]. To mimic cell adhesion correctly it is necessary to establish similar conditions because adhesion is different depending on whether membrane tension or bending dominates [81]. The osmolarity of the solutions was measured with a freezing point osmometer (Osmomat 030, Gonotec GmbH, Berlin, Germany). For each experiment, the refractive indices of the vesicle solution and the outer buffer were determined for each experiment with an Abbé refractometer (AR4D, Krüss, Hamburg, Germany).

2.2.2 Design of the Model System

In this work, a SLB served as mimick of the membrane of one cell and a GUV modelled the membrane of a second cell (see Figure 2.7). Specific receptor ligand pairs were incorporated into the respective fluid membranes to mediate GUV adhesion to the SLB. Thus, both binding partners - receptors and ligands - were mobile. Mobile receptor-ligand pairs contribute to cell-cell adhesion. However, mobile pairs were much less studied up to now and are therefore an interesting model system. Two binding scenarios were studied: The case of strong specific binding was realized by biotin/avidin and the case of weak specific binding by the cell adhesion molecule E-cadherin.

2.2.2.1 Binding Pairs

Biotin/Avidin

Avidin has two functional analogues: streptavidin and neutravidin. Streptavidin shows a very similar crystal structure as avidin [48] but has a completely different origin: It is expressed in the bacterium *streptomyces avidinii* [82]. Moreover, streptavidin is nonglycosilated (molecular weight 53 kDa) and has an isoelectrical point in the neutral range. Thus, it is less prone to unspecific interaction. Streptavidin should not be used in combination with cell adhesion molecules because it contains a tripeptide that is very similar to the binding sequence of fibronectin. Fibronectin is one constituent of the extracellular matrix and involved in cell-surface adhesion [83]. Streptavidin has the additional characteristic to crystalize on membranes under defined conditions [84–87]. Hence, it is not suitable as a model receptor in mobility studies.

In this study the avidin analogue neutravidin was used. It is produced from avidin by chemical removal of the carbohydrate. The functional motifs are conserved [83] yet its isoelectric point is lowered to 6.3. As a consequence neutravidin has the advantage to be almost uncharged at neutral pH. Therefore, neutravidin shows less unspecific interaction than avidin or streptavidin.

In the scenario of strong binding, SLB bound neutravidin molecules served as the receptors and biotinylated lipids in the GUV served as ligands.

E-cadherin/E-cadherin

In this thesis, a commercially available E-cadherin chimera construct was employed. It consisted of all five Ecad ectodomains (Met 1 - Ile 707) genetically fused to an immunglobulin Fc-fragment (Pro 100 - Lys 330) via a short flexible linker (IEGRMD). The Fc-fragment exhibited a hexahistidin tag (his6). The final product is a dimer with two Fc-fragments covalently bound via a disulfide bond. Ecad was bound to chelating lipids in the GUV and the SLB, where it served as receptor and ligand to mimic weak homophilic binding.

2.2.2.2 Membrane Constitutents

The **matrix lipid** was SOPC in all SLBs and GUVs studied (structural formula of SOPC see Figure 2.9). SOPC belongs to the family of phospholipids. It exhibits two fatty acid chains with 18 carbon atoms each. One chain is formed by the saturated stearic acid and the other by the unsaturated oleic acid. Its double bond creates a kink in the chain obstructing efficient packing and leading to a low phase transition temperature of 6.5 °C [75]. This ensures membrane fluidity at the given experimental settings (surface-pressure at transfer: 20 mN/m, temperature: 21°C). E-cadherin was bound to a fluid SLB via **chelating lipids** following Schmitt *et al.* [88]. DOGS-NTA carries the highly efficient chelating group N-nitrilotriacetic acid (NTA) covalently linked to its headgroup. The metal ion Ni^{2+} is complexed by NTA via four coordination sites leaving two accessible to an electron donor. In this case the donors were two of the histidins from the hexahistidin tag of the chimera. For a sketch illustrating the NTA-Ni-his complex see Figure 2.8. The affinity of chelated Ni^{2+} to histidin is very high: $K_D = 10^{-13}$ M. Thus, the Ecad is strongly bound to the SLB. Due to the weakness of the Ecad-Ecad bond it was necessary to work at high DOGS-NTA concentrations (5%) in both the SLB and the vesicle to enable stable vesicle binding.

Biotinylated lipids (DOPE-cap-biotin) were used to functionalize membranes with neutravidin. Due to a short linker (HOOC-$(CH_2)_5$-NH_2) separating the lipid head group and the biotin moiety, the latter could bind at the deep binding pockets within neutravidin. The concentration of DOPE-cap-biotin varied from 0% to 5% depending on the addressed issue. All percentages refer to the number of matrix lipid molecules.

To ensure specific GUV binding to the SLB, 2% **PEG** (polyethylene glycol) phospholipids (DOPE-PEG) were employed in each of the membranes. Pure SOPC membranes tended to stick together unspecifically. PEG lipids exhibit a polymer chain at the headgroup that introduces repulsive forces (structural formula of DOPE-PEG see Figure 2.9). Here, a PEG chain with a molecular weight of 2000 g/mol corresponding to on avarage 45 ethylene oxide repeats was used. According to de Gennes [90], sparsely pinned polymers adopt a mushroom configuration in good

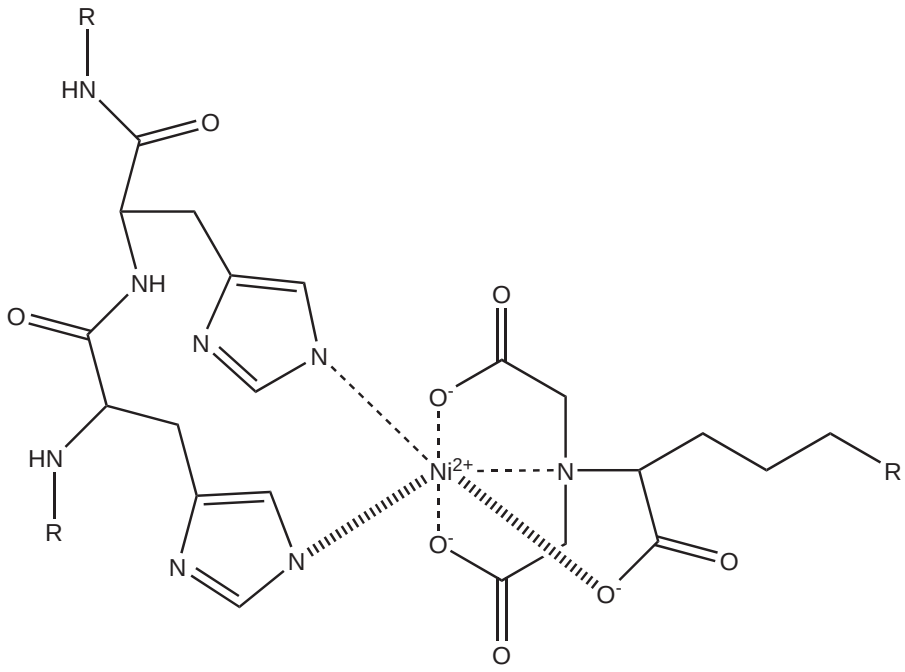

Figure 2.8: Structural formula of the NTA-Ni-his complex (created with ChemDraw).

solvents. Thus, the thickness of the polymer layer can be estimated as the Flory radius $R_F = \alpha\, N^{3/5}$ [59], where α is the length of the monomer and N the number of monomers. In the given case $\alpha = 3.5$ Åand $N = 45$ resulting in a thickness of 34.4 Å [91]. The PEG lipids also mimic the glycocalix of real cells. This glycocalix is a hydrated mesh of negatively charged polysaccharides linked to glycoproteins and glycolipids in the cell membrane [1].

In order to monitor SLB quality and fluidity, NBD labeled **fluorescent** lipids were induced at a maximum concentration of 2%. Higher concentrations lead to self-quenching [92]. The fluorescent label is located either at the hydrophobic chain (chain NBD-PC, biotin/neutravidin) or at the hydrophilic headgroup (head NBD-PE, Ecad/Ecad) according to necessity (see also Chapter 7).

2.2.2.3 Functionalization

SLBs prepared by the Langmuir-Blodgett Langmuir-Schäfer technique and GUVs prepared by electroswelling were subsequently functionalized. For the case of strong specific binding via neutravidin, SLBs were incubated with neutravidin or neutravidin-OG (TMR) in large excess at a final concentration of at least 60 μg/ml in PBS buffer for 30 minutes. Excess protein was removed by exchanging the buffer against pro-

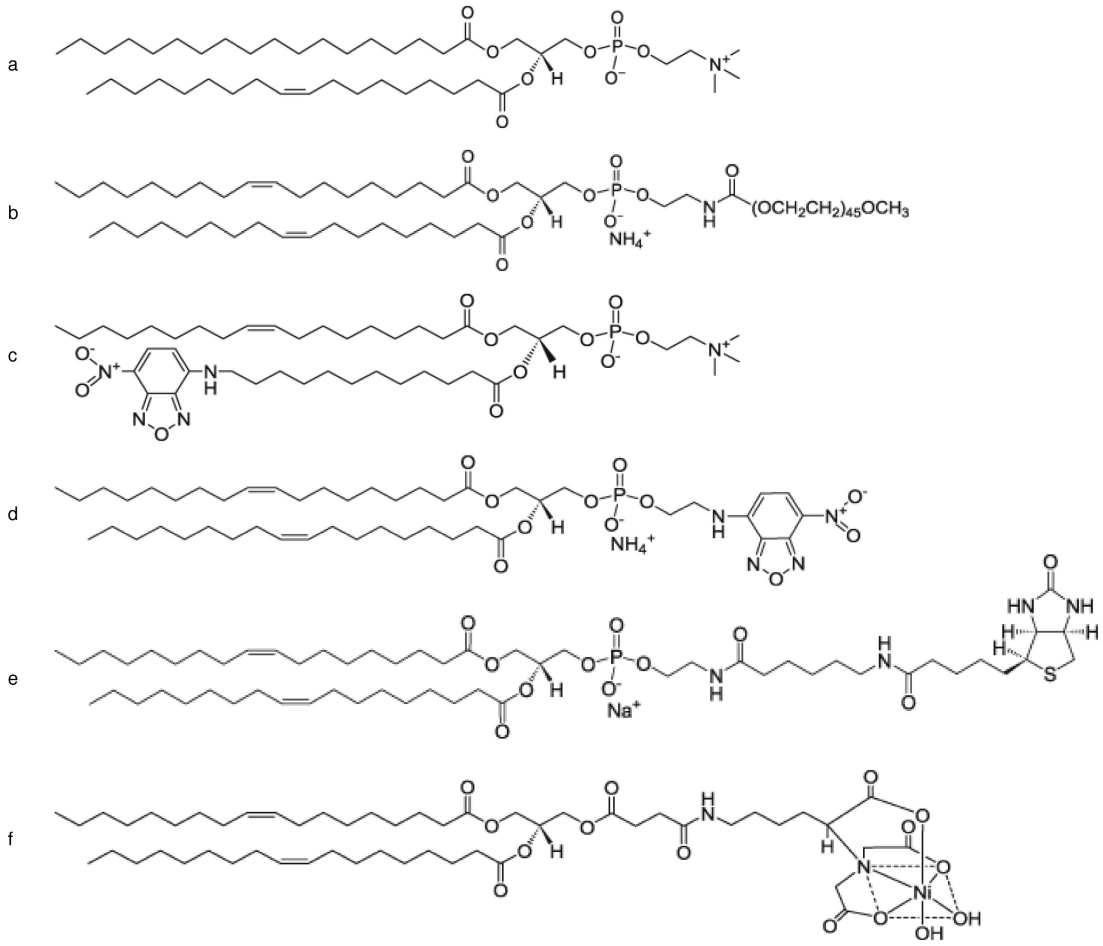

Figure 2.9: Structural formulas of the lipids forming the model membranes. a: SOPC, b: DOPE-PEG 2000, c: chain labeled NBD-PC, d: head labeled NBD-PE, e: DOPE-cap-biotin, f: DOGS-NTA [89].

objective	pixel size [nm]	STD [nm]	N
20x LD Achroplan	311	0.2	15
63x EC Plan-Neofluar Antiflex	100	0.1	35

Table 2.1: Results for the pixel sizes in the object as determined with a calibration object. N denotes the number of measurements.

tein free PBS in a series of typically ten washing steps. For the case of weak specific binding via Ecad, SLBs were first loaded with 2 μM nickel sulfate for 15 minutes and afterwards exposed to Ecad in a final concentration of 6 μg/ml for 3 hours to ensure saturation. The sample was washed five times with PBS in between each step and ten times in the end. For certain experiments, additional passivation steps with 5 mg/ml BSA (bovine serum albumin) were introduced before neutravidin incubation and directly before vesicle addition.

To functionalize vesicles nickel sulfate and Ecad were added in the same final concentrations as above to 500 μl of vesicle solution. Typically 10 μl of the vesicle solution were added to the functionalized SLB. Hence, the nickel sulfate concentration inside the measuring chamber was only $\sim$ 4 nM. In the case of Ecad mediated binding $CaCl_2$ was added together with the vesicles in a final concentration of 750 μM.

2.3 Imaging

2.3.1 Microscope Set-up

Fluorescence recovery after photobleaching (FRAP) measurements were carried out on a laser scanning confocal microscope (LSM-510, Carl Zeiss, Göttingen, Germany), equipped with a 1.40 NA 63x Plan Apochromat objective and an argon ion laser excitation (488 nm, 30 mW).

Except for the FRAP measurements all image acquisition was done with an inverted microscope (Axiovert200, Carl Zeiss, Göttingen, Germany). A metal halide lamp (X-Cite, Exfo, Quebec, Canada) served as light source. A digital CCD camera (sensicam qe, PCO, Kehlheim, Germany) controlled by OpenBox (version 1.77, Informationssysteme Schilling, Munich, Germany) recorded the images. The size of

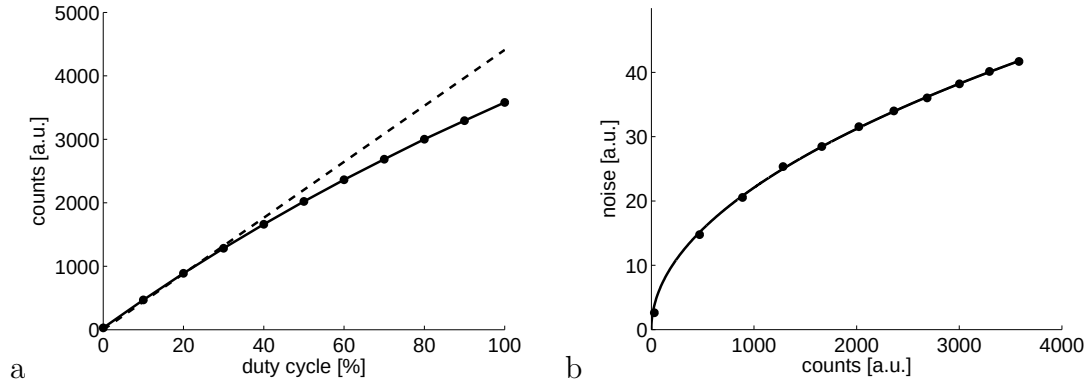

Figure 2.10: a) Linearity profile of the camera. Dots: data, full line: Guideline for the eye, dotted line: Ideal linear profile. b) Shot noise dependence on the signals' intensity. The data can be well fitted applying equation 2.1. dots: data, full line: fit.

the square pixels was determined by means of a standard micrometer scale (Carl Zeiss, Göttingen, Germany) for the microscope set-up equipped with two objectives: 63x EC Plan-Neofluar Antiflex 1.25 oil and 20x LD Achroplan 0.4 air (results see Table 2.1).

Since the intensity was used to extract quantitative information, the linearity of the camera was checked. For this purpose, a function generator (DS 345, Stanford Research Systems, Sunnyvale, CA) was used to trigger a red diffused light emitting diode (HLMP-4700, Hewlett Packard, Palo Alto, CA), and the resulting intensity signal was recorded through a 20x air objective. Duty cycles of 0%, 10%, ..., 100% were used to illuminate at a frequency much faster than image acquisition. Camera settings typical for our experiments were chosen. The camera showed distinct deviations from a linear profile at intensities higher than 2000 counts. The deviation increases from 10% at 2000 counts to 30% at the maximum number of counts 4096 (see Figure 2.10 a). Since high intensities were reached in some of the measurements, all data were corrected for camera nonlinearities prior to any image processing.

The data series for the camera calibration was also used to estimate the noise σ for all intensity values.

First, the temporal and spatial mean intensity $\bar{I}$ of each image stack was calculated. Second, the mean picture of each stack was subtracted from every picture in the stack. The resulting pixel values were squared, the squared difference pictures were temporally and spatially averaged and than the root was extracted. This mean de-

viation $\bar{\Delta}$ was plotted against $\bar{I}$. The resulting curve was fitted using the following fit function (see Figure 2.10 b):

$$\sigma = \bar{\Delta}(\bar{I}) = k * \sqrt{\bar{I}} \tag{2.1}$$

Since the detected intensity is quantized in photons a fluctuation of the signal proportional to the square root of the signal is expected according to Poisson statistics [93]. Knowing k the corresponding random fluctuation due to shot noise for a single intensity data point could be calculated. k was 0.698 for the camera in the described set-up. This result was later on applied to determine the reduced χ^2 values that serve as a measure for the quality of fits (see Section 3.2.4). Since the measured signal could have been fitted well with Eq. 2.1, readout noise (4 - 5 e^- per pixel) and dark current (0.025 e^- per pixel) could be neglected.

2.3.2 Standard Light Microscopy Techniques

Since the typical size of the vesicles was in the μm range, light microscopy was a suitable tool to observe them. The properties of light (wavelength, amplitude, phase) can be exploited in several ways to image objects. Depending on the parameter to be determined - size, mobility or height - the appropriate tool was used.

2.3.2.1 Phase Contrast Microscopy

In order to label free image GUVs, phase contrast microscopy was used. Simple bright field microscopy did not yield satisfactory contrast because thin membranes do not absorb enough light. On the other hand GUVs act on the phase of light. This feature is exploited by phase contrast microscopy that converts phase shifts to detectable intensity differences. To achieve this, a 'minimal microscope' consisting of a light source, a condensor for illumination, an objective, and a tubus lens plus camera for observation has to be supplemented with two additional components (see Figure 2.11). An annular aperture is placed in the back focal plane of the condensor so that the object is illuminated only by a hollow cone of light. Those rays interacting with the object are diffracted and the corresponding phase Φ is shifted by $\Delta\Phi$ due to the differences in refractive indices of object and surrounding medium. However,

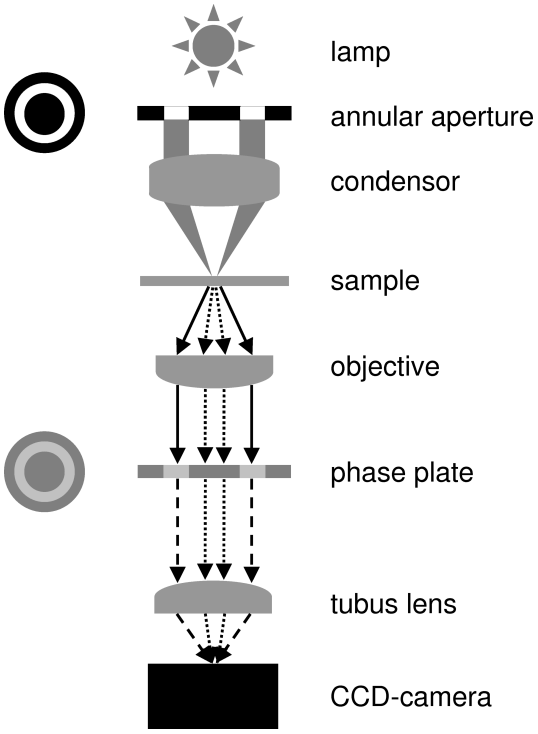

Figure 2.11: Light path in a phase contrast microscope. Full line: non-diffracted light, dotted line: diffracted light with small phase shift ($\Delta\Phi$), dashed line: non-diffracted light with phase shift ($\pi/4$). Modified sketch courtesy of C. Monzel, IBN4, FZJ.

the major part of the light cone passes the dilute sample without interaction and thus without phase shift. The second component, an annular phase plate, is put in the back focal plane of the objective. The non-diffracted light passes this phase plate in a defined annular region, while the diffracted light covers the whole surface of the plate. The plate is constructed in such a way that the differences in optical path length for the diffracted and non-diffracted light cause a $\pi/4$ phase shift as well as reduce the amplitude of the non-diffracted light. As a consequence the total phase difference between diffracted and non-diffracted light sums up to $\Phi_{total} = \Delta\Phi + \pi/4$. Because the amplitudes of diffracted and non-diffracted light are now comparable constructive or destructive interference occurs depending on Φ_{total}. Therefore, the detectable amplitude contrast can be positive or negative.

In this thesis phase contrast microscopy was applied to determine the diameter of the GUVs and to perform certain bead assays.

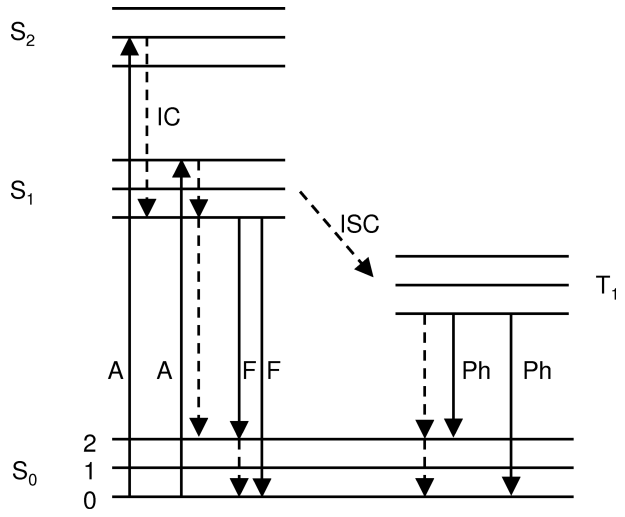

Figure 2.12: Jablonski diagram. Full line: Transitions with creation or absorption of a photon. Dashed line: Non-radiative process. S_i: electronic singulet states, T_1: electronic triplet state, A: Absorption, IC: Internal conversion, F:Fluorescence, ISC: Intersystem crossing, Ph: Phosphorescence

2.3.2.2 Fluorescence Microscopy

Fluorescence is a process by which a system of electrons undergoes transition from an excited to the ground state S_0 by emission of radiation. A photoactive molecule, e.g. a dye in the ground state, can absorb a suitable quantum of light and change to a higher vibrational level of the electronic state S_1 or S_2 (see Figure 2.12). Within a few picoseconds this state relaxes to the lowest vibrational state of S_1. This process is called internal conversion (IC). Depending on the lifetime of the excited state one of the dye molecules statistically emits a fluorescence photon with energy E. E corresponds to the difference of the lowest vibrational state of S_1 and one of the vibrational states of S_0. In case the final state is not the lowest, the system relaxes again without emitting radiation. These radiation less transitions are the source of a phenomenon called Stokes shift. It describes the fact that the emitted fluorescence light is red-shifted with respect to the absorption. Its wavelength is typically 20-50 nm longer because a part of the absorbed energy is lost in the system due to competitive processes. In addition to IC there is another relaxation process called intersystem crossing (ISC, see Figure 2.12). In this process the system can also undergo transition to the first triplet state T_1. Since this transition requires a spin flip

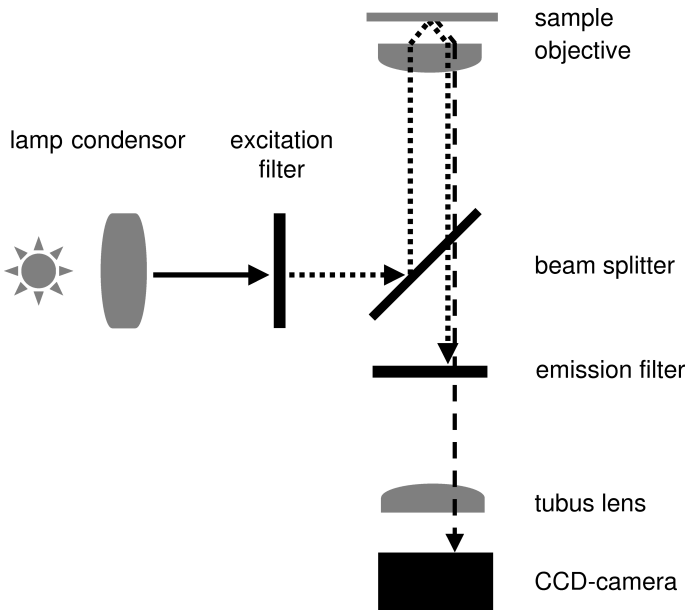

Figure 2.13: Light path in a fluorescence microscope. Dotted line: Short wavelength excitation light, dashed line: Stokes shifted emission light. Modified sketch courtesy of C. Monzel, IBN4, FZJ.

it occurs rarely [2]. Besides relaxing to the ground state phosphorescence (Ph) occurs with low probability. This transition again requires spin flip. That is the reason why the lifetime of the T_1 state is much longer than for example of the S_1 state. Hence, fluorescence and phosphorescence can be distinguished on the timescale. In principle, there are two variants of fluorescence: primary and secondary fluorescence. Primary fluorescence occurs in animals (e.g. *Aquorea victoria* - GFP) and plants (e.g. green leaves - chloroplasts) exhibiting fluorescence naturally. All other structures have to be labeled with a suitable fluorescent dye, so that they can show secondary fluorescence.

In order to image fluorescently labeled objects a 'minimal microscope' has to be equipped with a filter cube consisting of an excitation filter, a beam splitter and an emission filter (see Figure 2.13). The excitation filter selects the correct wavelength to excite the fluorophore from the spectrum of the mercury lamp used for illumination. This wavelength is reflected by the beam splitter and focused onto the sample by the objective. The emitted red-shifted fluorescence light is collected by the same objective. Due to the shift in wavelength it can pass the beam splitter and

[2]The probability for this transition depends on the explicit conditions. O_2 and heavy elements catalyze intersystem crossing.

the emission filter. If the intense illumination light is blocked by suitable filters the relatively weak fluorescence signal can generate a high contrast image.
A standard fluorescence microscope was used to check the quality of the SLBs and to measure diffusion constants of lipids and proteins applying the continuous photobleaching technique (see Chapter 2.3.4.1).

2.3.2.3 Confocal Laser Scanning Microscopy (CLSM)

A CLSM is an improved version of a fluorescence microscope. A laser is used for illumination enabeling simultaneous application of several fluorescent dyes with minimized cross talk. Moreover, a combination of two pinholes - one in the illuminating and one in the detection light path - allows for point like illumination and detection (see Figure 2.14). The pinholes are placed in the back focal plane of two identical lenses - the objective and the collector lens[3]. The incoming light passes through the first pinhole and is focused by the objective onto the sample. The same objective creates an intermediate image of the sample that is at the same time sharp in the back focal plane of the objective and in the focal plane of the collector lens (confocal). Thus, the second pinhole allows only light from the focal plane to pass and blocks background fluorescence from adjacent layers (see Figure 2.14). As a consequence, it decreases the depth of focus. The third advantage is a scanning unit that guides the focus laterally and axially through the sample creating a three dimensional image with high optical resolution ($\sim$ 200 nm laterally, $\sim$ 500 nm axially).
The first confocal scanning microscope was developed by Minsky in 1961 [94] and combined with laser illumination by Brakenhoff in 1979 [95]. Further improvements in computer and laser technology contributed to the development of user friendly high resolution confocal laser scanning fluorescence microscopy [96,97]. Today, CLSM is widespread used in biological and medical research [98] also.
In this work, a confocal microscope was used to perform fluorescence recovery after photobleaching measurements (see Section 2.3.4.1 and 2.3.4.2).

[3]In a real CLSM only one objective is employed for illumination and detection.

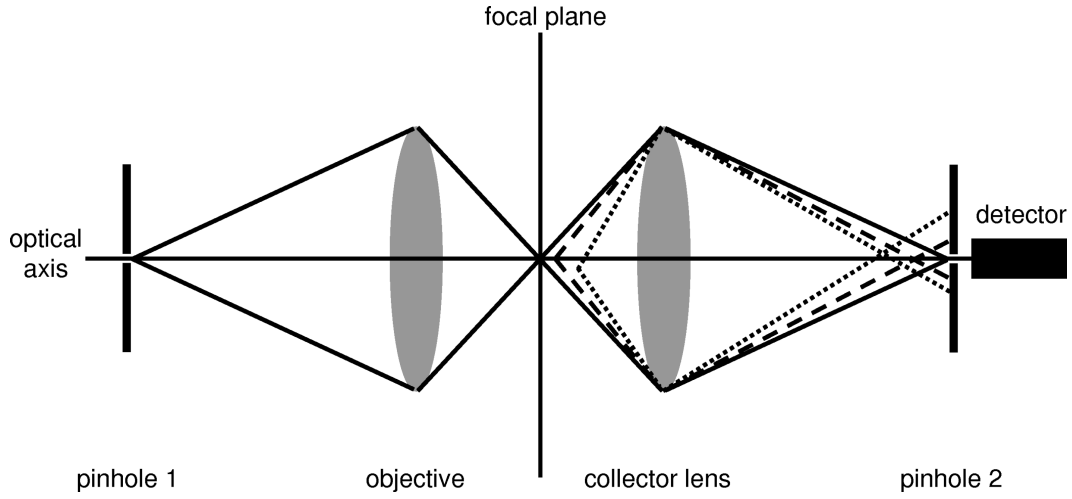

Figure 2.14: Confocal principle. Only light from the focal plane and the optical axis can be detected. Dashed line: light from out of focus, dashed line: light from out of focus and of the optical axis.

2.3.3 Microinterferometry

2.3.3.1 Introduction

Reflection interference contrast microscopy (RICM) is a optical technique used to reconstruct height profiles of objects near the substrate from the interference pattern of light being reflected at the objects' surface [99]. RICM was initially introduced to analyze optics of thin films [100]. In 1964 Curtis applied RICM for the first time to study cell adhesion on a glass substrate [101]. Since then, RICM has been serving as a versatile tool to observe and quantify characteristics of adhering cells and model cells (GUVs). It yielded information on static and dynamic features connected with height and shape: adhesion energies, elastic properties, fluctuations, ... [76,81,102–104]. The antiflex technique [105] improved the applicability of RICM substantially. The achieved contrast enhancement allowed to study also objects with low reflectivities. Another improvement was the introduction of dual wavelength RICM [106]. It extended the absolute height to be unequivocally measured by RICM to $\sim$ 800 nm.

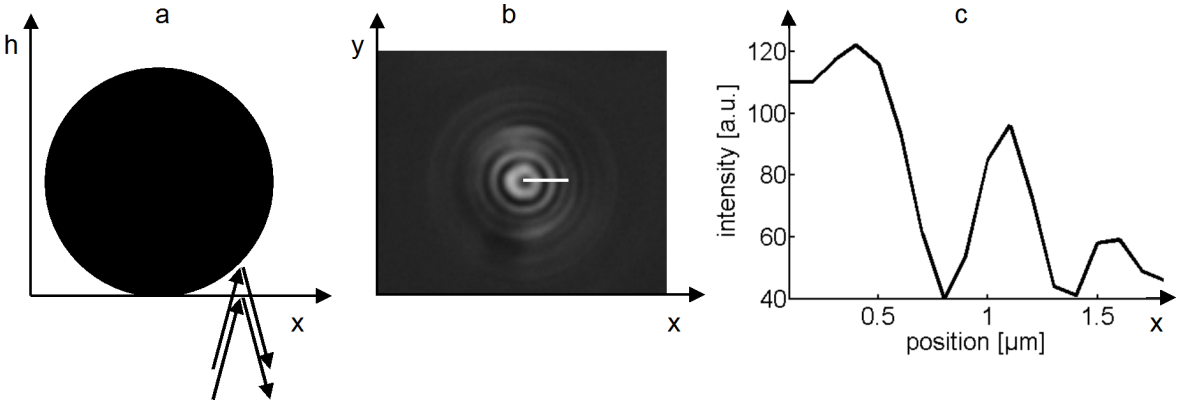

Figure 2.15: Bead with Newton fringes. a: Side view of the bead, b: RICM micrograph of the bead, c: Intensity profile along the white line in b.

2.3.3.2 Image Formation

Generally, incoming light is refracted and partially reflected at optical interfaces within a specimen composed of layers with different refractive indices. The reflected parts interfere with each other in a constructive or destructive manner depending on the difference Δ of their optical path length. Thus, height differences in the sample are observed as intensity variations. Dark rings correspond to minimal and bright rings to maximal intensity (Newton rings, see Figure 2.15). The exact description of the image formation given follows Wiegand *et al.* [99]. The intensity $I(x, y)$ observed in the image plane is formed by the time average of the squared electric field $\mathbf{E}(\mathbf{r}, t)$ of the light wave:

$$I(x, y) = \langle \mathbf{E}^2 \rangle_t, \tag{2.2}$$

$$\mathbf{E}(\mathbf{r}, t) = E(\mathbf{r}) \exp\left[i(\Phi(\mathbf{r}) + \omega t)\right], \tag{2.3}$$

where $\Phi(\mathbf{r})$ is the phase. A prerequisite for interference is the coherence of the light source. Usually a high pressure mercury lamp is used for illumination. Due to its finite size, this source is only partially coherent and thus treated like a composition of several point sources. Only light waves originating from one source are able to interfere. The resulting electric field vector $\mathbf{E}_r$ of the reflected light in the image plane can be described as the sum of all electric field vectors being reflected at the different layers i within the sample (see Figure 2.16):

$$\mathbf{E}_r = \sum_i \mathbf{E}_{r,i}, \tag{2.4}$$

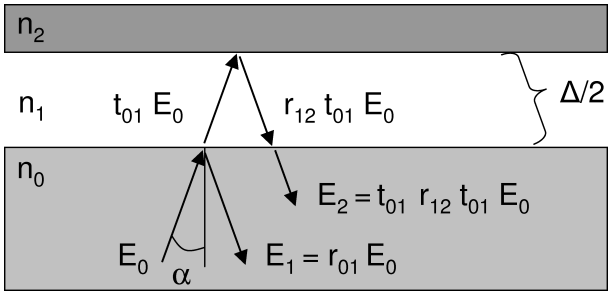

Figure 2.16: RICM image formation in the case of reflection at two interfaces (m = 1).

The amount of light reflected at an interface depends on the refractive indices of the adjacent layers n_i and n_j and the angle of incidence α. These information are summarized in the reflection coefficient r_{ij} defined by Fresnel as follows:

$$r_{ij}^{s}(\alpha) = \frac{n_i \cos\alpha_i - n_j \cos\alpha_j}{n_i \cos\alpha_i + n_j \cos\alpha_j}, \tag{2.5}$$

$$r_{ij}^{p}(\alpha) = \frac{n_j \cos\alpha_i - n_i \cos\alpha_j}{n_j \cos\alpha_i + n_i \cos\alpha_j}, \tag{2.6}$$

where s and p denote the polarization direction of the reflected wave. The remaining part of the incident light is transmitted. The transmission coefficient t_{ij} is consequently defined as $t_{ij} = \sqrt{(1 - r_{ij}^2)}$. The transmitted light E_j transverses the adjacent layer with refractive index n_j and thickness d_j and can be reflected at a second interface before it interferes with the part of incident light E_i that is reflected at the first interface. Assuming perpendicular incidence of light, it travels $\Delta_j = 2n_j d_j$ further than its interference partner (see Figure 2.16). As the velocity of light changes with the refractive index of the surrounding medium, the extra Δ_j in the optical path length also acts on the phase of the wave shifting it by $k\Delta_j$, where $k = 2\pi/\lambda$ is the wave number and λ the wavelength of light. The reflection coefficients and the phase shifts of all the interfering rays $\mathbf{E}_{r,i}$ can be combined to yield an effective reflection coefficient R describing the reflectivity of the whole system:

$$\mathbf{E}_r = RE_0, \tag{2.7}$$

where E_0 is the electric field vector of the incident light. Assuming perpendicular incidence of light Eq. 2.5 simplifies and R is expressed as:

$$R = r_{01} + \sum_{i=1}^{m} \left[\prod_{s=1}^{i} (1 - r_{s-1,s}^2) \exp(-ik\Delta_s) \right] r_{i,i+1}, \tag{2.8}$$

$$I(x,y) = R^* R E_0^2 = R^* R I_0, \tag{2.9}$$

where m is the number of layers between the substrate 0 and the adjacent layer m+1. For a more accurate analysis of RICM micrographs the finite aperture of illumination [107, 108] and multireflections [109] have to be taken into account. In case of non-planar interfaces additional corrections are necessary [99]. In the present work Eq. 2.8 is used. The condition of perpendicular incidence of light is approximately achieved by closing the aperture thus blocking non-paraxial light.

2.3.3.3 Three-Interface Reflection Interference Contrast Microscopy (RICM)

Traditionally, RICM measurements on GUVs were evaluated taking into account three layers and thus two reflections (as depicted in Figure 2.16, see [104] and references within). Due to oil immersion of the objective the first reflection takes place at the glass-buffer interface. The second reflective interface is formed by the buffer and the vesicle membrane. Thus, the height profile can be calculated from the measured intensity distribution according to Eq. 2.8 with $m = 1$ as follows:

$$I(h) \quad = \quad I_1 + I_2 + 2\sqrt{I_1 I_2}\,\cos\left(\frac{4\pi n}{\lambda}h\right), \tag{2.10}$$

where I is the measured intensity, I_1 and I_2 the intensities of the reflected light, k the wave number, n_1 the refractive index of the layer with the height h and λ the wavelength.

However, a recent study demonstrated that absolute height measurements require a more detailed view of the system to be imaged [104]. Usually, the GUV is filled with a sucrose solution to enable its sedimentation in a aqueous environment due to gravity. The refractive indices of the vesicle membrane and inner solution differ substantially. As a result a third reflection takes place at this interface. Taking into consideration the third reflection and the exact heights and refractive indices of the layers involved, it was shown that the traditional analysis underestimates the real height by h_0. h_0 is characteristic for each system and depends on the refractive indices of inner and outer buffer. To demonstrate the meaning of h_0 it is necessary to study at the exact procedure to convert measured intensities to heights. As I_0 in Eq. 2.8 is usually not known, the theoretically expected intensity for m = 2 has to be normalized with respect to the first reflection.

$$I_{norm}(h) \quad = \quad \frac{I - I_1}{I_1} \quad \text{with} \quad I_1 = r_{01}^2 I_0. \tag{2.11}$$

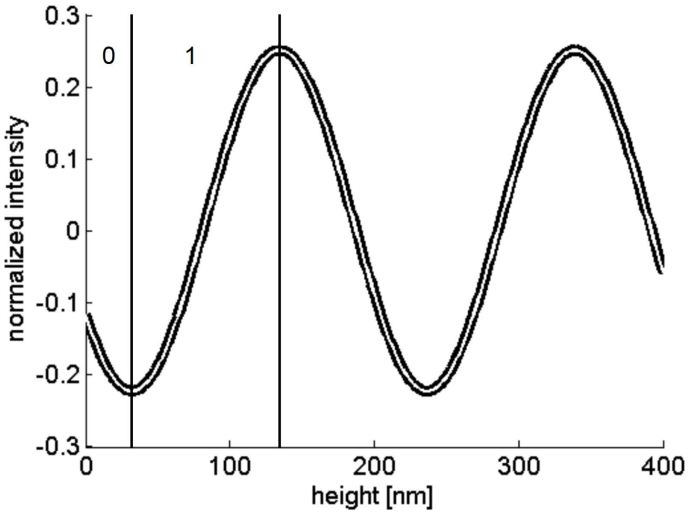

Figure 2.17: Normalized intensity. Black line: Calculated values according to Equation 2.11 (m = 2). White line: Fit according to Equation 2.12. 0 and 1 denote the zeroth and first branch of the calibration curve.

Hereby, I is the measured intensity in every pixel of the image and I_1 is the measured intensity in the background. The resulting I_{norm} can be described by a simple function:

$$I_{norm}(h) \quad = \quad y_0 - A\cos\left(\frac{4\pi n_{out}}{\lambda}(h - h_0)\right), \tag{2.12}$$

where y_0, A and h_0 are constants, determined numerically by fitting of Eq. 2.12 to Eq. 2.11 (see Figure 2.17). Inversion of Eq. 2.12 yields a relation between intensity and height for a specific stratified system with a given set of refractive indices and thicknesses. The following values were used: $n_0 = n_{glass} = 1.525, n_1 = n_3 = n_{lipid} = 1.486$ [108], $n_2 = n_{out}$ and $n_4 = n_{in}$. The refractive indices n_{out} and n_{in} for the outer and inner buffer were measured after each experiment; typical values were $n_{out} = 1.335$ and $n_{in} = 1.344$. Comparison of Eq. 2.10 and 2.12 yields the consequences of considering a third reflection. The periodicity of the cosine stays unchanged, but the intensity minimum is shifted to h_0. Thus the minimum of intensity is observed at a finite height h_0, whereas zero height yields a higher intensity. As a consequence in the first branch a continuous decrease of height corresponds to an intensity profile that is falling in the beginning, but turns and increases again till zero height is reached. The effect is illustrated in Figure 2.18. h_0 depends solely on the refractive indices of inner and outer buffer. Typical values of n_{in} and n_{out} yield $h_0 = 34$ nm. In case of an adhering vesicle with a circular adhesion

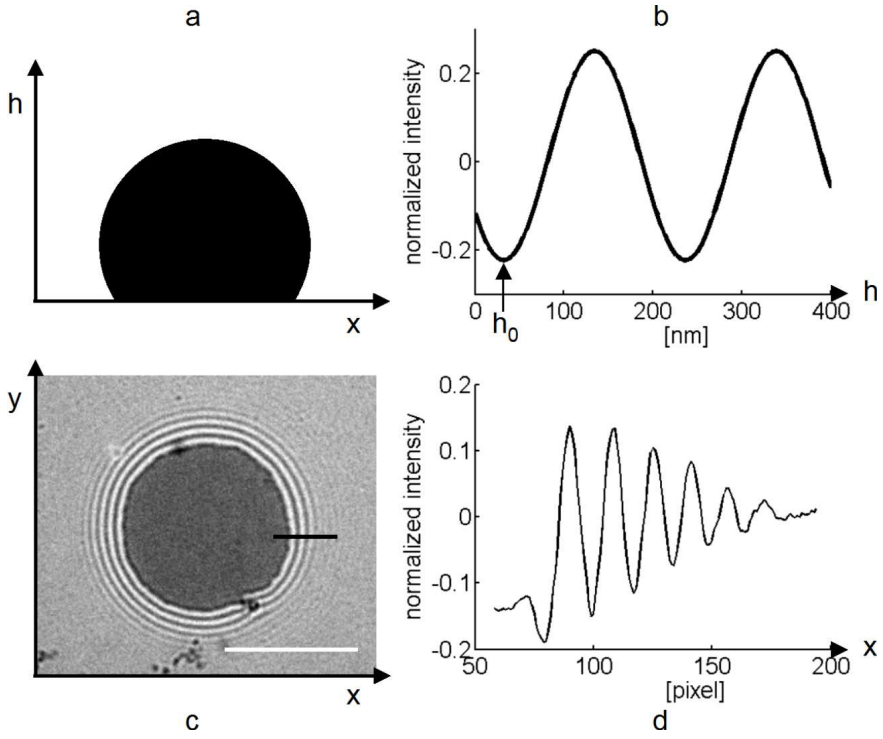

Figure 2.18: Formation of the black rim. a: Sketch of an adhering vesicle (side view), b: Calibration curve, c: RICM image of an adhering vesicle exhibiting a black rim, d: Intensity along the black line in c. Scale bar: 10 μm.

zone isohypses (regions with identical heights) at $h = h_0$ appear as a black rim. This black rim enables unequivocal intensity to height conversion because it leaves a mark indicating which branch of the periodical calibration curve (Equation 2.12) has to be used. All heights inside the black rim are calculated with the zeroth branch whereas all intensities between the black rim and the first maximum are calculated with the first branch. For the definition of the branch numbering see Figure 2.17. The validity of such a scheme was established in [104] from experiments where the inner vesicle buffer was varied.

2.3.3.4 Antiflex Technique

The antiflex technique [105] (see Figure 2.19) is a method that increases image contrast by eliminating stray light. Applying antiflex to RICM enables to image systems with tiny refractive index variation appropriately (e.g. a model membrane in aqueous solution reflects only 0.1% of the incident light). Use of a pair of crossed polarizers in combination with a $\lambda/4$-plate enables for optimum elimination of stray

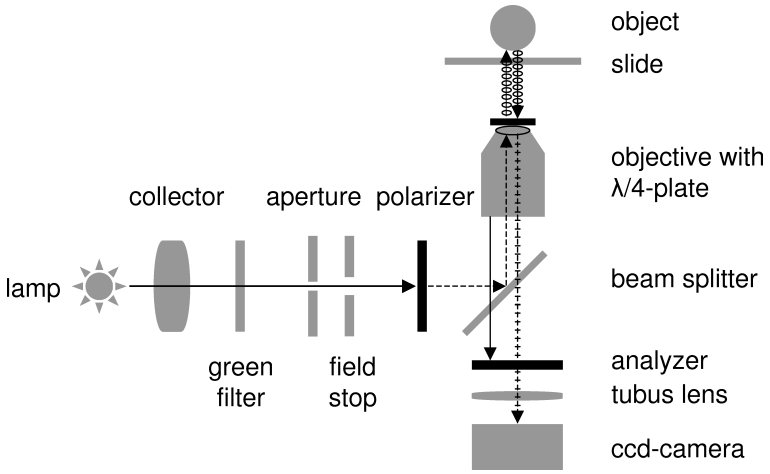

Figure 2.19: Light path in a reflection interference contrast microscope with implemented antiflex technique. - linear polarized light, + vertical to - linear polarized light, o circular polarized light.

light. In this method the incident light is linearly polarized by a polarizer and afterwards deflected onto the specimen by a beam splitter. The antiflex objective has an in-built $\lambda/4$-plate causing a change from linear to circular polarized light. Due to reflections at different interfaces within the specimen the polarization direction is inverted. When passing the $\lambda/4$-plate a second time, the polarization state of the reflected light is changed back to linear polarized, but this time perpendicular to the initial polarization. A second polarization filter, called analyzer, is placed before the detector and oriented perpendicular to the polarizer. Hence, all light reflected by the object has the correct polarization to pass this analyzer. On the other hand, almost all scattered stray light from within the optics is blocked. Consequently, this technique enhances the contrast of the RICM image substantially. While the lateral resolution of a reflection interference contrast microscope corresponds to that of a usual light microscope (Rayleigh criterion: $d_{lateral} = 0.61\ \lambda/NA = 266$ nm, $d_{axial} = 2\ n\ \lambda/NA^2 = 1006$ nm, $\lambda = 546$ nm, NA = 1.25, n = 1.44), the resolution in axial direction is increased up to 4 nm [104] due to the use of microinterferometry.
In this work, RICM is used to identify the adhesion state of a GUV (see Chapter 7 and 4), measure the height of the bound state of the membrane (see Chapter 4) and analyze membrane fluctuations (see Chapter 6). Moreover, knowledge of the overall vesicle profile allows for the calculation of adhesion energy densities (see Chapter 4).

2.3.3.5 Image Acquisition

RICM images were acquired using the inverted microscope and camera system described before (see Chapter 2.3.1). The green line of the metal halide lamp (X-Cite, Exfo, Quebec, Canada) was selected using an appropriate interference filter (546 ± 12 nm). To achieve maximum contrast the antiflex technique was applied [105]. The microscope was equipped with a 63x Antiflex Plan-Neofluar oil objective with a numerical aperture of 1.25 and built in $\lambda/4$-plate (Carl Zeiss, Göttingen, Germany) and a filter cube with crossed polarizers (Carl Zeiss). The numerical aperture of illumination was set to approximately 0.5. Image sequences of static vesicles in RICM consisted of 50 frames while adhesion processes required recording of some 1000 frames with an individual exposure time of 100 ms each. To observe vesicle adhesion processes the vesicles were observed in phase contrast while sedimenting and RICM movies were started as soon as the vesicle had touched the substrate.

2.3.4 Diffusion Measurements

There is large interest to better understand the interplay between membrane processes and cellular function. That is why tools were developed to investigate the fluidity of membranes and the mobility of their constituents.

One idea is to study a tracer molecule as a *pars pro toto* of the whole membrane. The underlying assumption is that the tracer does not disturb the matrix and reflects its mobility. All the techniques described in this section are based on a phenomenon called photobleaching. Thus, this process is explained first. When an ensemble of immobile fluorescent molecules is continuously illuminated the intensity of the emitted light decreases till zero is reached. One reason for the decrease is photodestruction. If a very powerful illumination source is utilized it can directly impact on the structure of the fluorescent molecules that in turn loose their photoactivity. Moreover, prolonged illumination drives the fluorescent molecules through many cycles: ground state, excited state, ground state, ... During each cycle there is a probability to enter the triplet state T_1 after excitation. With increasing number of cycles more and more molecules reach the long-living T_1 state. Since the transition from T_1 to the ground state requires a forbidden spin-flip non-radiative

processes dominate and the ensemble emits less fluorescence light. Moreover, fluorescent molecules in the T_1 state are easily oxidized in the presence of oxygen [110]. The extent of photobleaching depends mainly on the individual dye, the intensity of the illuminating light but also on secondary environmental factors like temperature, oxygen content and mobility.

2.3.4.1 Continuous Photobleaching

To measure the diffusion constant of lipids in a SLB with the continuous photobleaching (CP) technique [92] the sample is constantly illuminated and thus irreversibly bleached in a defined area. Throughout this process the fluorescence intensity is recorded. Since the fluorescent molecules are able to diffuse within the plane of the bilayer, the fluorescence intensity does not drop to zero homogeneously all over the illuminated area. Instead bleached fluorophores can be replaced by fresh ones at the edges of the illumination field. After prolonged exposure the illuminated area is bleached but a bright rim is visible just inside its edges (see Figure 3.10b). The width of the rim is a measure for lipid diffusivity. Thus, the quantity that has to be observed is the concentration of the fluorescent lipids in time and (two dimensional) space $c(r,t)$. $c(r,\ t)$ is the solution of the diffusion equation (see also Section 7.2) extended by an additional term to account for photobleaching:

$$\frac{\partial c(r,t)}{\partial t} \quad = \quad D\nabla^2 c(r,t) - B(r)c(r,t)\,, \tag{2.13}$$

where D is the diffusion constant and $B(r)$ the first-order rate constant of photobleaching. $B(r)$ is constant within the illuminated area and zero outside. The transition from the illuminated to the dark region is assumed to be infinitely sharp. Eq. 2.13 was solved for an illuminated half-plane at long times [92] with the boundary conditions of initially constant concentration and vanishing flow at infinity:

$$c(\xi,\tau) \;=\; c_\infty(\xi \;=\; 0,\tau)e^{-\xi} + e^{-\tau}\,, \tag{2.14}$$

where ξ and τ are dimensionless variables:

$$\xi \;=\; \frac{x}{\sqrt{D/B}} \quad \tau \;=\; tB. \tag{2.15}$$

Equation 2.14 is valid only for $\tau > 4$. B can be determined individually because on time scales well below R^2/D, where R denotes the radius of the illumination area, intensity changes at the center are entirely due to photobleaching. Despite the fact that the prefactor $c_\infty(\xi = 0, \tau)$ in Eq. 2.14 is not stationary, D can be determined unequivocally. The shape of the spatial profile is always monoexponetially decreasing with a decay length of $\sqrt{D/B}$.

The main advantage of CP is that it can be applied with minimal technical expense. The required equipment is a standard fluorescence microscope with an HBO or metal halide lamp and a field stop to define the bleaching area. Moreover, it is possible to observe the same site within a sample also with RICM.

In this thesis CP was applied to measure the lateral diffusion constant of tracer lipids in a SLB. Their mobility reflected the fluidity of the bilayer and allowed to analyze the influence of different factors (protein binding, membrane adhesion). Moreover, the mobility of receptor proteins was studied as a function of concentration and membrane adhesion.

2.3.4.2 Fluorescence Recovery After Photobleaching

While CP monitors the bleaching of tracer molecules, fluorescence recovery after photobleaching (FRAP) [111, 112] exploits the recovery of the fluorescent signal after bleaching to determine the diffusion constant. In order to separate the effects of diffusion and bleaching, a short intense laser pulse is used to irreversibly bleach the sample locally (ideally no diffusion taking place while bleaching) and an attenuated laser beam is used to monitor the influx of unbleached tracers from outside the bleaching region (ideally no bleaching taking place while monitoring). The experimentally observed quantity is the relative fluorescence intensity:

$$f(t) \quad = \quad \frac{F(t) - F(0)}{F(\infty) - F(0)}\,, \tag{2.16}$$

where $F(\mathrm{t})$ is the actual fluorescence intensity, $F(0)$ the intensity directly after bleaching and $F(\infty)$ the fully recovered fluorescence signal. If the ideal condition of no bleaching during monitoring and 100% mobile fraction are fulfilled, $F(\infty)$ equals the intensity before bleaching $F_{initial}$. Only partial recovery is observed if not all

tracer lipids are mobile . Eq. 2.16 then yields the mobile fraction if $F(\infty)$ is replaced by $F_{initial}$ and $F(t)$ by the final intensity. Soumpasis solved the corresponding problem of efflux of bleached molecules after bleaching with a uniform circular disk profile beam [113]. If the underlying transport process is pure normal diffusion the relative fluorescence intensity can be described as follows:

$$f(t) \quad = \quad e^{-\frac{r^2}{2Dt}} \left(K_0 \left(\frac{r^2}{2Dt} \right) + K_1 \left(\frac{r^2}{2Dt} \right) \right) , \tag{2.17}$$

where K_0 and K_1 are modified Bessel functions of second kind and zeroth or first order, respectively. r denotes the radius of the bleached spot and D the diffusion constant.

In this work FRAP was used to determine the mobile fraction of tracer lipids in the bilayers studied. This quantity was not accessible with CP.

Chapter 3

Technical Developments

This chapter describes the experimental techniques that were newly developed during this thesis. First, a new microscope set-up is described that enables simultaneous application of two already established techniques: RICM and fluorescence microscopy. Then, bead assays are explained that were introduced to check the functionality of the model protein Ecad. Finally, several analysis tools including the five-reflection interference contrast microscopy developed for this thesis, were implemented. They are explained in detail in the last section of this chapter.

3.1 Instrumentation and Assays

3.1.1 Simultaneous Application of RICM and Fluorescence Microscopy

In order to thoroughly investigate the physical processes contributing to cell-cell adhesion it is necessary to study the interplay between membrane adhesion and receptor clustering. Therefore, it is essential to observe the vesicle's membrane height and receptor distribution on the SLB beneath the same vesicle during the adhesion process. Two solutions to this task were implemented: simultaneous recording of one vesicle in both microscopy modes and sequential recording of the vesicle in RICM and fluorescence.

The simultaneous approach required changes in the microscope set-up described in

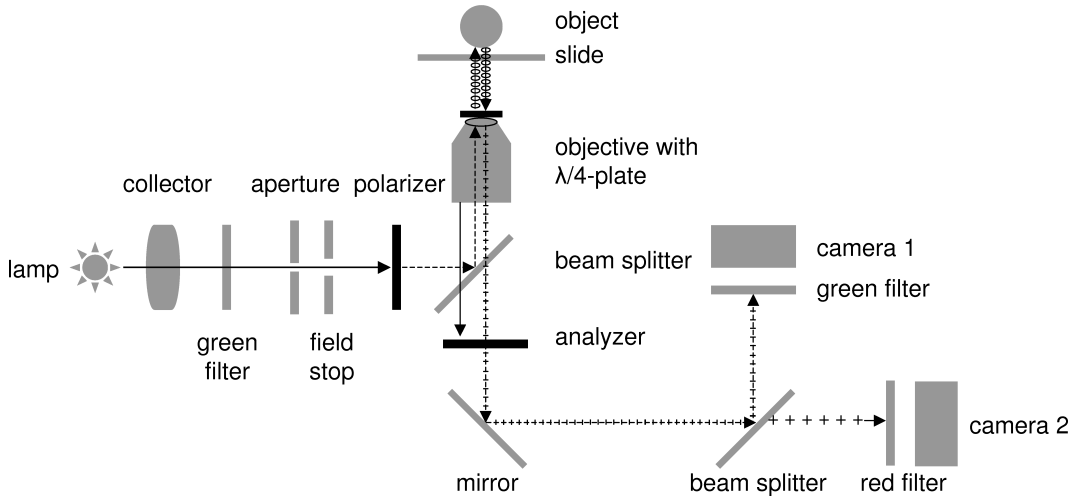

Figure 3.1: Microscope set-up for simultaneous application of RICM and fluorescence microscopy. - - - linear ploarized light, + + + vertical to - - - linear polarized light, o o o circular ploarized light, + + + lines with wider spacing represent the shifted fluorescence light. Camera 1 detects the RICM image and camera 2 the fluorescence image of the object.

Section 2.3.1. The new light path is depicted in Figure 3.1. The bright green line of the lamp's spectrum was chosen for illumination as for pure RICM (see Figure 2.19). Thus, receptors with a suitable fluorescent label were applied: neutravidin-TMR. In principle the standard RICM/ Antiflex set-up (see Section 2.3.3.4) was used and new components were added behind the analyzer. During observation of a fluorescently labelled sample, one part of the illuminating light was reflected within the sample while another part excited the fluorescent labeled receptors. As a result a mixture of phase shifted reflected and wavelength shifted fluorescent light entered the objective. This light was reflected to the side port of the microscope by a built-in mirror. Outside the microscope a double video adapter was attached that guided the light to a dichroic mirror(BS FT 580, Carl Zeiss, Göttingen, Germany). There the green RICM light was separated from the fluorescence contribution. The beam splitter reflected the green RICM light that afterwards passed a green filter identical to the one behind the light source to ensure a pure RICM signal. The red shifted fluorescence light was transmitted and passed an emission filter (FF01-593/40-25, Semrock, Rochester, NY) to single out the emitted fluorescence signal. Two identical CCD-cameras (sensicam qe, PCO, Kehlheim, Germany) were used for detection at the end of each light path. To ensure simultaneous acquisition camera 1 triggered camera 2.

Prior to any image analysis the two images had to be overlayed. To do so, the field stop was used as a calibration object. The corresponding algorithm was written in Matlab (R2008b, The MathWorks, Natick, MA) by N. Kirchgessner, IBN4, Research Center Jülich. A dodecagon was fitted to the field stops in both images. A built-in function used this information to overlay the field stops in the two images. Translation, rotation and scaling were allowed in this algorithm. The resulting transformation matrix was applied to the full images.

The described set-up enabled us to follow vesicle adhesion and observe the vesicles' membrane shape at the same time as the receptors on the SLB. The main drawback was that the fluorescence light had to pass through the analyzer and the exciting light was attenuated by the polarizer. Therefore, only a very weak fluorescence signal was detected with a closed aperture. If the aperture was opened to increase the fluorescence signal, the assumption of vertical incidence of light required for the RICM analysis was no longer valid (see Section 2.3.3.2). In order to make a compromise between both requirements, the field stop was opened to a medium extent and the integration time of the camera recording the fluorescence signal was increased (3.5 s). Consequently, fast receptor events could not be resolved. Due to the described issues a second approach was used as well.

The second idea was to image the same object sequentially in RICM and fluorescence mode. After the RICM acquisition was complete, the green filter was removed from the light path, the field stop was opened completely and the filter wheel was turned to replace the RICM filter set by the required fluorescence filter set. Then the fluorescence image was recorded. Special care had to be taken not to move the sample while turning the filter wheel. This approach yielded fluorescence images with a good signal to noise ratio, but it did not allow to observe fast vesicle dynamics at high receptor concentrations.

In future, a configuration where the analyzer is placed directly in front of camera 1 may improve the contrast also in the simultaneous approach.

3.1.2 Bead Assays

Bead assays were designed for the purpose of checking the calcium dependent function of Ecad. 4.5 μm polystyrene beads (Polybead Microspheres 2.5% solids, slightly negatively charged due to sulfate ester groups on the surface, Polysciences Inc., Warrington, PA) were diluted 1:50 in ultrapure water and vortexed. They were mixed with 5 mM NaH_2PO_4 in a volume ratio of 1:10 and unspecifically coated with Ecad (6 μg/ml, 3 h). To this end Ecad was transferred from Tris buffer to phosphate buffer by dilution. The bead solution was centrifugated for five minutes at 9300 g to wash the beads by exchanging the supernatant against fresh phosphate buffer. This step was repeated five times. In a next step the beads were blocked with 5 mg/ml BSA (98% purity, Sigma, Saint Louis, MO) in 5 mM NaH_2PO_4 for 30 min. Before usage the beads were washed again three times. The calcium dependent function of Ecad was checked in all other buffers used (PBS, HEPES, PIPES).

3.1.2.1 Bead-Bead Assay

For the bead-bead assay 100 μl of the resulting bead solution was incubated with 750 μM $CaCl_2$ for 1 h in 400 μl 5 mM NaH_2PO_4 in an observation chamber. Bright-field images were collected in 25 randomly chosen places with the inverted microscope described before (see Chapter 2.3.1). To do this it was equipped with a 20x LD Achroplan air objective with a numerical aperture of 0.4 (Carl Zeiss, Göttingen, Germany). After incubation with 5 mM EGTA (ethylene-bis(oxyethylenenitrilo)tetraacetic acid, Sigma, Saint Louis, MO) for 3h the sample was scanned again. The bright-field images were analyzed using a self written routine in Matlab (R2007a, The MathWorks, Natick, MA) which separately counted single beads, and bead clusters having two or more beads. Beads were identified via thresholding. The bright field images displayed beads as black circles (for exemplary experimental data see Figure 3.2 a). The whole image processing procedure is illustrated in Figure 3.3 with synthetic data [1]. To eliminate small dirt particles and defocused out of plane beads the bright background (A) was dilated in a first step (B). Then all pixels were identified which

[1] Detailed information on the used image processing functions can be found in [114]

a

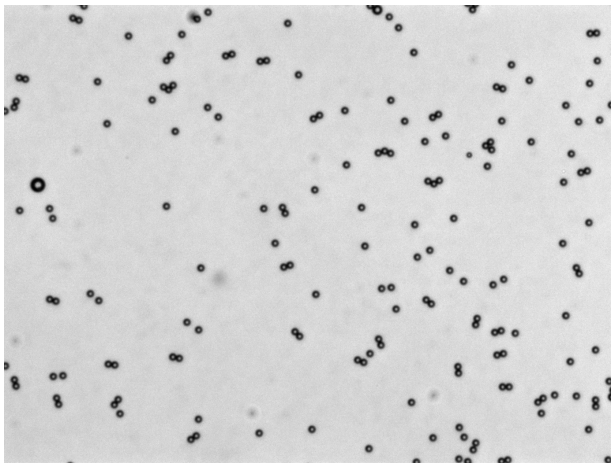

b

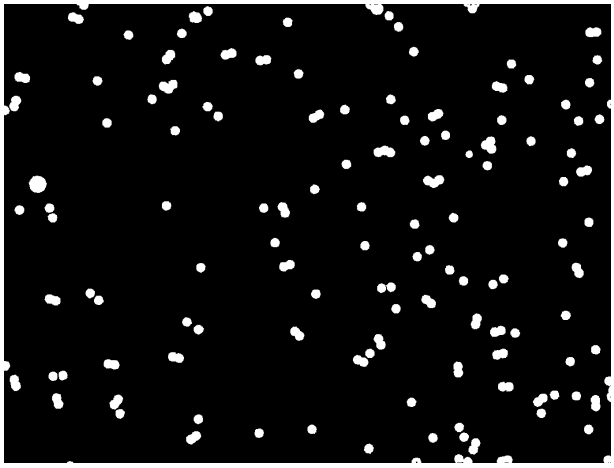

c

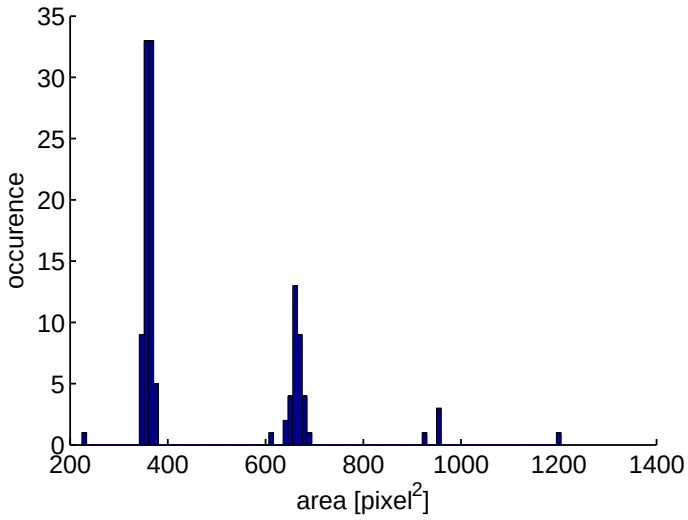

Figure 3.2: Exemplary bead-bead assay data to illustrate the evaluation scheme. a: Original bright field image, b: Identified objects, c: Histogram of the detected areas. The field of view is 300x400 μm

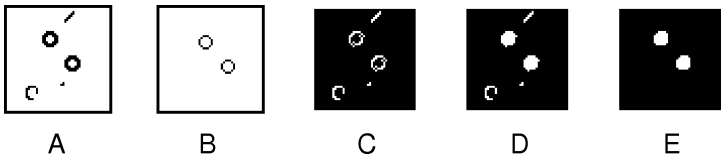

Figure 3.3: Synthetic data illustrating the image processing procedure to find the size of a bead starting from a bright field image (A). B: Background dilation, C: Thresholding, D: Filling, E: Opening.

now had an intensity value that was larger than 110% of the initial value. Thereby all sites of dilation were found (C). They were filled only if they exhibited a closed ring structure (D). All other structures were eliminated by opening the image (E). The area of all persisting objects was determined and a histogram was displayed (Figure 3.2 c shows the histogram corresponding to Figure 3.2 a). The areas found were $\sim$350 pixels^2 and multiples of $\sim$350 pixels^2. Thus, $\sim$350 pixels^2 was identified as the size of one bead. A threshold of 400 pixels^2 (1 pixel = 311 nm see 2.3.1) was used to separate single beads and clusters. This threshold corresponded to a circular object of approximately 7 μm diameter. Thus no single bead (d = 4.5 μm) was mistaken as a doublet. Clustering was used as a signature of bead-bead binding (see also 4.2.2.1).

3.1.2.2 Bead-Surface Assay

For the bead surface assay a cleaned coverslip (for details on the cleaning procedure see Section 2.1.4) was coated with 20 μg/ml Ecad in 5 mM NaH_2PO_4 for 3 h and washed. BSA served as a blocking agent (5 mg/ml BSA in 5 mM NaH_2PO_4, 30 min) to eliminate unspecific adhesion due to generic forces. After incubation with BSA the beads were washed again. The prepared surface was exposed to a dispersion of coated beads (50 μl, $5 \cdot 10^{-3}$% solids) in a buffer volume of 500 μl (750 μM $CaCl_2$ in 5 mM NaH_2PO_4 or 5 mM Hepes, Sigma, Saint Louis, MO) for 5 min. Reflection interference contrast microscopy (RICM) image sequences were recorded using a 63x Antiflex Plan-Neofluar 1.25 oil objective with a numerical aperture of 1.25 (Carl Zeiss, Göttingen, Germany) and the appropriate filter set. After incubation with 5 mM EGTA for 2.5 h the recording was repeated. The position of the center of the beads was determined using an algorithm implemented in OpenBox (version

1.77, Informationssysteme Schilling, Munich, Germany) which detects radially symmetrical objects [106]. The displacement of the beads between two time frames was calculated for 50 time frames at a recording rate of 100 ms. A reduction in the mean displacement indicated bead-surface binding (see also Section 4.2.2.1).

3.2 Analysis Tools

3.2.1 Quantitative Five-Interface Reflection Interference Contrast Microscopy

As already explained in Section 2.3.3.3 absolute height measurements with RICM require detailed knowledge of the samples' structure. All dielectric layers have to be considered to derive an exact relation between measured intensity and height. The model system used in this thesis required two more layers to be taken into account: the SLB and a thin water layer beyond the SLB [61]. The SLB thickness and refractive index corresponded to that of the vesicle membrane ($h_{bilayer} = 4$ nm, $n_{lipid} = 1.486$). The thickness of the water layer depended on the cleaning procedure of the SLB glass substrate. Here, a medium value of $h_{water} = 1$ nm was assumed [61]. Consequently, reflections from five interfaces generate the interference pattern in the image plane (m = 4 in Eq. 2.8, see Figure 3.4):

$$I(x,y) = R^* R E_0^2 = R^* R I_0, \quad \text{with} \tag{3.1}$$

$$R = r_{01} + \sum_{i=1}^{4} \left[\prod_{s=1}^{i} (1 - r_{s-1,s}^2) \exp(-ik\Delta_s) \right] r_{i,i+1}. \tag{3.2}$$

The normalization is carried out with respect to the reflection at the interface SLB/outer buffer because the interesting height is that of the vesicle membrane over the SLB:

$$I_{norm}(h) = \frac{I - I_3}{I_3}, \tag{3.3}$$

I_3 has to be calculated according to Equation 2.8. Here again, I is the measured intensity in every pixel of the image and I_3 is the measured intensity in the background. The explicit expression for I_{norm} is quite complicated, but it can still be

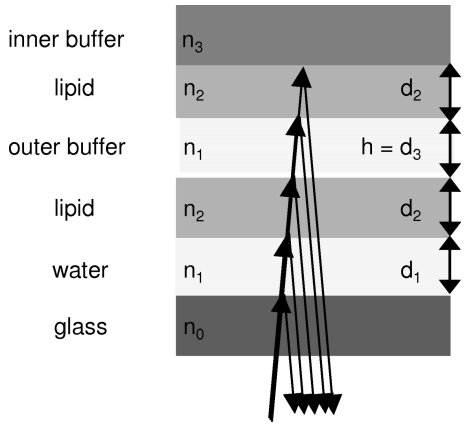

Figure 3.4: Dielectric layers to be taken into account for five-interference RICM analysis.

fitted properly with Equation 2.12. The black rim appears in this case at $h_0 = 32$ nm.

Height Reconstruction

The first step in image analysis aiming at correct height reconstruction was background subtraction. To eliminate influence of inhomogeneities in the illumination each image of the stack was background corrected. This part was done with a routine written by C. Monzel, IBN4, FZJ [76] in Matlab (R2008a, The MathWorks, Natick, MA). The resulting image was normalized with the mean background intensity according to Equation 3.3. Next, characteristic regions had to be defined: the contact zone and the black rim zone. If a vesicle exhibited fringes, the contact zone was defined as the area within the first bright rim (see Figure 3.5 a and b). The black rim zone was the area within the black rim (see Figure 3.5 b and c). Extremely tightly bound vesicles did not show any fringes but only a black rim (see Figure 3.5 c). In these cases the contact zone was considered identically to the black rim zone. The circumferences of the zones were found as follows:

1. Vesicles with fringes: The mean image of the stack was displayed and support points were picked manually along the bright rim. A spline through these points was used to initialize a curve. The intensity values of the mean image were mapped along perpendicular lines with length L [pixels] centered around the initialized curve. The intensity profiles along each line were searched for the first appearing maximum starting at pixel index ((L-1)/2 -2) slightly left of the center, in outwards direction. The corresponding coordinates (x_{max}, y_{max}) were used to create a mask for the

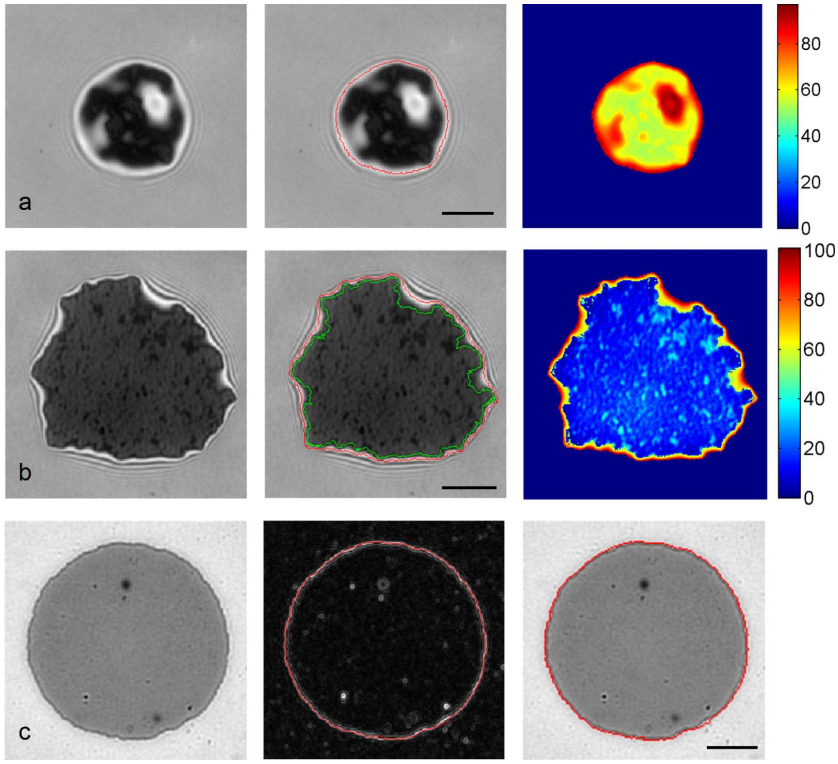

Figure 3.5: Definition of the contact zone (red line) and black rim zone (green line) for free vesicles with fringes (a), bound vesicles with fringes (b) and bound vesicles without fringes (c). In presence of fringes the bright rim (black rim) was found in the mean image, without fringes the gradient image was used. For details see text. The reconstructed height [nm] is shown for case a and b. Scale bar: 5 μm.

contact zone. Analogous for finding the black rim, the lines were searched for a minimum starting at pixel (x_{max} - 2, y_{max} - 2) in inwards direction. A second mask was defined by the coordinates of the black rim (x_{br}, y_{br}).

2. Vesicles without fringes: The gradient image of the mean image was used to detect the edge of the adhesion zone. Again support points were picked manually along a bright rim which now matched pixels with high gradient. The lines perpendicular to the initialized curve were searched for the exact position of the maximum. A mask was created analogous to the case of a vesicle with fringes.

The intensity values in the different zones were converted to height values by application of the respective branch of the calibration curve. Inside the black rim the zeroth branch was used whereas outside the first branch was applied.

$$h_{inside}(I) \quad = \quad -\arccos\left(\frac{y_0 - I}{A}\right)\frac{\lambda}{4\pi n_{out}} + h_0, \tag{3.4}$$

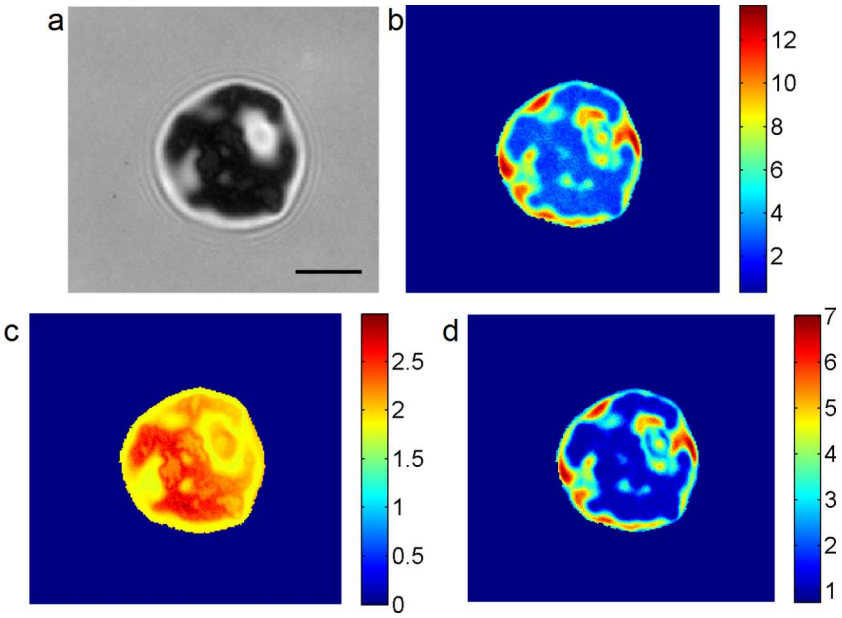

Figure 3.6: a: Mean intensity image, b: Mean fluctuation image [nm], c: Mean shot noise image [nm], d: Fluctuation map in units noise. Scalebar: 5 μm.

$$h_{outside}(I) \quad = \quad \arccos\left(\frac{y_0 - I}{A}\right)\frac{\lambda}{4\pi n_{out}} + h_0, \tag{3.5}$$

A few pixels inside the black rim ($\sim 5\%$) exhibited intensity values outside the definition range of the arccos function due to experimental noise. These values were replaced by the mean values of the adjacent pixels. Two more scenarios caused difficulties. Some vesicles exhibited a broken black rim or had 'bubbles' inside the black rim. In these cases not all pixels inside the black rim mask could be treated equally. All pixels that had been assigned negative heights because their intensity value was outside the range of the zeroth branch could be identified and corrected by evaluating in the first branch. These difficulties emerged only at very low receptor-ligand concentrations. For these cases, the reconstructed height was not determined as an absolute value, but only used to construct fluctuation maps to judge the adhesion state (see the following section). The final result (percentage of adhered area) was not sensitive to the selection of the arccos branch.

3.2.2 Fluctuation Analysis

RICM movies of typically 50 frames were recorded to analyze fluctuations of the vesicle membrane. The measured intensities in each pixel of each frame were converted to heights as described above. Additionally, the temporal mean and standard deviation of the heights were calculated for each pixel. The standard deviation image showed the measured fluctuations of the membrane. This representation was still distorted by the shot noise of the intensity signal (see Figure 3.6 b). In order to identify real height fluctuations caused by membrane fluctuations in the noisy image the standard deviation image was normalized with respect to the noise and displayed in units noise (fluctuation map, see Figure 3.6 d). The required noise map was constructed with the help of the calibration measurement described in Section 2.3.1. This experiment allowed the quantification of the shot noise signal connected with a single intensity measurement: I_{shot} =0.698$\cdot\sqrt{I}$. In order to calculate the height change (h_{shot}) corresponding to this intensity change two synthetic versions of the initial intensity image I were constructed: $I_{max} = I + I_{shot}$ and $I_{min} = I - I_{shot}$. Both intensity images were converted to height images h_{max} and h_{min}, and h_{shot} was calculated for each pixel:

$$h_{shot} = \frac{1}{2}(h_{max} - h_{min}), \tag{3.6}$$

for all first branch pixels and

$$h_{shot} = \frac{1}{2}(h_{min} - h_{max}), \tag{3.7}$$

for all zeroth branch pixels.

Figure 3.6 shows one exemplary data set. Please note that because of the varying slope of the calibration curve a given I_{shot} can result in different h_{shot} depending on the absolute I_{norm} value. Figure 3.7 illustrates two examples ($I_{norm,1} = 0.05$, $h_{shot,1} = 3$ nm; $I_{norm,2} = 0.2$, $h_{shot,2} = 4.5$ nm). The fluctuation map was used to create a mask separating the adhered membrane patches from the free sites. For details see results in Chapter 6.

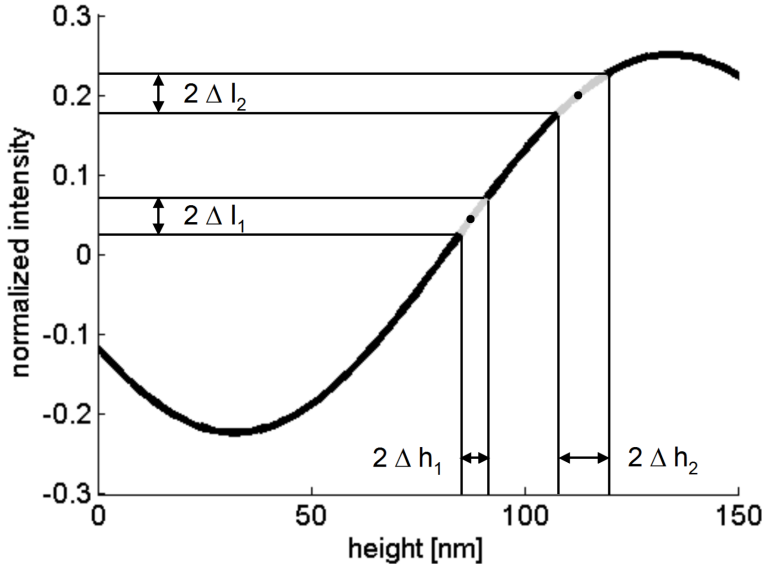

Figure 3.7: Non-linear relation between the noise connected with a measured intensity value (ΔI) and the reconstructed height (Δh). The same ΔI results in different Δh depending on the absolute intensity value.

3.2.3 Fluorescence Maps

In order to analyze the correlation of membrane adhesion and receptor clustering the identical area used for analysis of the RICM data was also investigated in fluorescence. The image was background subtracted as explained earlier. A typical image showed homogeneous intensity on the SLB far from the vesicle (background) and higher intensity at the sites of vesicle adhesion where the receptors were accumulated. All background pixels were averaged to calculate a mean intensity that served as a measuring unit for the extent of accumulation. Figure 3.8 represents a characteristic example of an adhering vesicle with a low initial concentration of receptors on the SLB. The representation of the fluorescence signal in units background is henceforward termed fluorescence map. These maps served as a basis to create masks for the accumulated regions in the adhesion zone, henceforward called accumulation mask. For details see results in Chapter 6.

3.2.4 Diffusion Analysis

In this work a combination of both techniques to measure diffusion constants described in Section 2.3.4 was applied to analyze SLBs with respect to their fluidity.

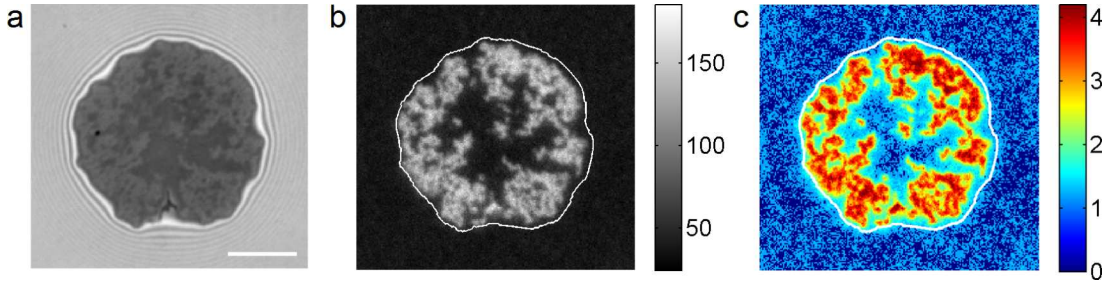

Figure 3.8: a: Intensity image in RICM mode, b: Intensity image in fluorescence mode, c: Fluorescence intensity in units background. The white line depicts the circumference of the contact zone determined from the RICM image. The scale bar is valid for all images: 5 μm.

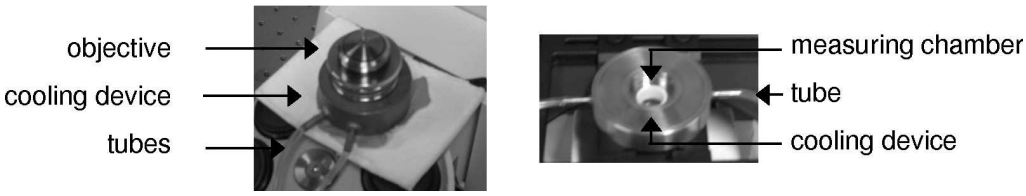

Figure 3.9: Cooling system.

Diffusion constants were determined with CP while mobile fractions were measured with FRAP.

For CP, the microscope set-up (see Section 2.3.1) was equipped with the filter set appropriate for OregonGreen and NBD. The opening of the field stop (50 μm in a field of view of 100 μm) defined the bleaching area. In case of vesicle adhesion this area was chosen such that the adhesion disk was bisected by one edge of the field stop (see Figure 3.10). To prevent pre-bleaching during focussing, I first focussed on the sample surface with green light in RICM mode and then switched to fluorescence mode (excitation filter: 450-490 nm). During NBD bleaching, movies of approximately 400 frames were recorded at a rate of 100 ms. Since Oregon Green is more stable, 1000 frames were required for bleaching of neutravidin-OG. One sample was typically scanned at 20 widely separated positions. The temperature was held constant at 21°C by means of a water cooling system. It consisted of two hollow brass rings connected to a water bath and circulator (Julabo, Seelbach, Germany). One ring enclosed the objective and the other ring was put on top of the measuring chamber (see figure 3.9 and for technical details, see Appendix A). The pump was turned on one hour before to the experiment to pre-cool the rings and cool down

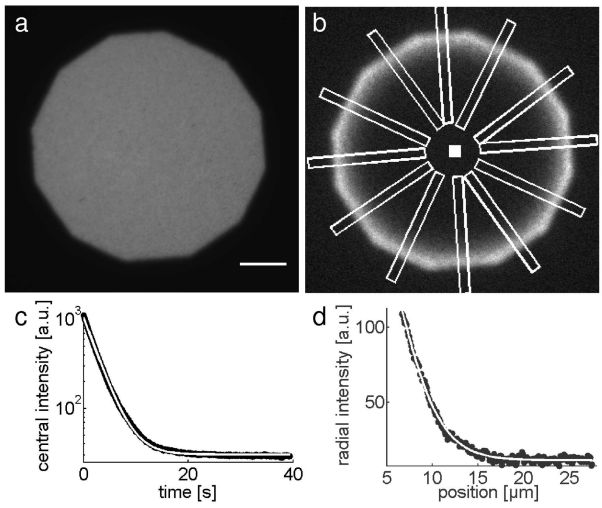

Figure 3.10: Continuous Photobleaching. a: SLB before bleaching. Scale bar: 10 μm (valid also for b) b: SLB after 40 s of bleaching. The central square and the rectangles radiating from the center mark the regions of interest (ROIs) for the temporal and spatial fit respectively. c: mean intensity measured in the central ROI (white square in b) over time. Line: Fit according to Eq. 3.8, B = 0.4 s^{-1}. d: mean intensity measured along one of the radial ROIs after bleaching. Line: Fit according to Eq. 3.10, D = 2.3 $\mu m^2/s$.

the objective. Due to the small volume of the sample some minutes were sufficient to stabilize the system. Thus, a stability of ± 0.1 °C was achieved. Temperature measurements were carried out using a Pt 100 sensor (Heraeus, Hanau, Germany). Diffusion measurements were started approximately 15 minutes after addition of the vesicles to ensure complete adhesion. The observation chamber was filled completely with PBS and covered with a glass slide to avoid drift and osmolarity changes due to evaporation.

The analysis of bleaching movies was automated by self-written routines in Matlab (R2008a, The MathWorks, Natick, MA). First, the bleaching constant B was determined from the time course of the intensity at the center of the field stop. The average intensity in a square area (width 1.5 μm) was calculated in each frame and linearized. For this the information of the camera calibration measurement was used to calculate a correction function from the difference of the measured calibration curve (see also Section 2.3.1) and the theoretically expected linear curve. The resulting corrected intensity curve $I(t)$ was fitted with the following model function

in accordance with the theoretical description (see Eq. 2.14):

$$I(t) \quad = \quad I_0 e^{-B\,t} + I_{Bg}\,, \tag{3.8}$$

where I_0, B and I_{Bg} were fitting parameters. Consequently, this model can be applied only if the bleaching behavior of the fluorescent label can be described by a single exponential. This condition is equivalent to the theoretical assumption that bleaching can be described by a single first-order rate constant. Fitting was done in a least squares sense with the Levenberg Marquardt algorithm. In order to weigh the individual data points appropriately their standard deviations were equated to the shot noise of the camera and calculated according to Equation 2.1. To check the quality of the fit residuals were plotted and χ^2 values were calculated:

$$\chi^2 \quad = \quad \frac{1}{\nu - 1} \sum_i \frac{(f(\vec{a}_i, t) - I_i)^2}{\sigma_i^2} \tag{3.9}$$

where ν was the number of degrees of freedom, f the fitting function, $\vec{a} = (I_0,\ B,\ I_{Bg})$ a vector containing all fitting parameters, and I_i the measured intensity value at time t_i. Fits were accepted for χ^2 values up to ten. It was ensured that the time course of the intensity at the center of the field stop was independent of diffusion effects because in lipid diffusion measurements R^2/D was typically > 300 s and thus, one order of magnitude larger than the observation time of 40 s (see also Section 2.3.4). Knowing B, the diffusion constant D could be extracted from the spatial intensity distribution at the edge of the field stop. To do this, a mean intensity curve was calculated from the intensity distribution averaged over a 2 μm wide line drawn perpendicular to the edge of the field-stop (see Figure 3.10). After linearization *I(x)* was fitted with an exponential function:

$$I(x) \quad = \quad I_0 e^{-x\sqrt{B/D}} + I_{Bg}\,. \tag{3.10}$$

I_0, I_{BG} and $\sqrt{B/D}$ were the free parameters. Fitting was done as described above. The fitting range was determined as follows. The position of the edge was detected as the highest intensity value along the line. A safety margin of typically five pixels to the inside was kept in front of the first pixel belonging to the fitting range. The fit range was chosen to ensure complete levelling of the curve. From each bleached area 12 diffusion constants were measured along radial lines separated by 30° and

one mean value was calculated. A typical example of the raw data and fitted curves are presented in Figure 3.10.

To measure the mobile fraction the sample and the cooling system were transferred to a laser scanning confocal microscope (LSM-510, Carl Zeiss, Göttingen, Germany) where FRAP measurements were carried out. The microscope was equipped with a 1.40 NA 63x Plan Apochromat objective and blue laser excitation (488 nm). 100% laser intensity (30 mW) was used to bleach a circular spot of 5 μm diameter for 0.28 s. Before and after bleaching the same spot was monitored with 1% laser intensity every 0.5 s. A typical measurement curve can be seen in Figure 3.11. Additionally, four more spots of 5 μm diameter were recorded in the background, but not bleached. Their intensity served as an internal control for bleaching during monitoring. The 'meanROI' function implemented in the LSM software (LSM 510 META, Carl Zeiss, Göttingen, Germany) was used to calculate the spatial mean intensity for each spot. This information was exported to a text file and further processed. One mean curve $I_{Bg}(t)$ was calculated from the four spots in the background. The bleached profile $I_b(t)$ was corrected by division and rescaling:

$$I_{b,corr}(t) \quad = \quad \frac{I_b(t)}{I_{Bg}(t)} I_{Bg}(0)\,. \tag{3.11}$$

The mobile fraction mf was calculated from this profile as follows:

$$mf \quad = \quad \frac{I_f - I_{min}}{I_i - I_{min}}\,, \tag{3.12}$$

where I_f is the final recovered intensity, I_{min} the minimum intensity directly after bleaching and I_i the initial intensity before bleaching. I_i and I_f are calculated as the mean of the 10 first (last) recorded intensity values.

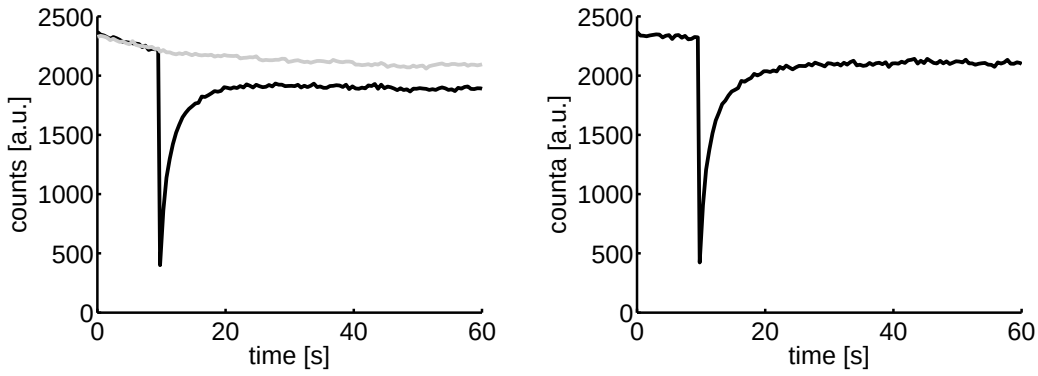

Figure 3.11: Left side: Raw measurement (black line) and intensity of the background (grey line). Right side: Corrected bleaching curve. Recovery was determined to be 88% for this data set ($I_i = 2341$, $I_f = 2103$ and $I_{min} = 423$).

Chapter 4

Vesicle Adhesion: Limit of High Receptor Concentrations (Statics)

This chapter first presents the principle theoretical concepts of vesicle adhesion. One popular approach to estimate the free energy of adhesion - the Bruinsma model - is explained in detail. The results section comprises the experiments carried out to characterize the different model systems with respect to their specificity, binding configuration, binding height of the vesicle over the substrate and free energy of adhesion.

4.1 Introduction and Theory

4.1.1 Interaction Potential

In order to correctly interpret observations/outcomes of adhesion experiments with the specified model system, it is necessary to identify all parameters contributing to the vesicle-surface interaction potential. Besides the specific interaction mediated by receptor-ligand pairs, there is a variety of unspecific interactions to be considered [a]. In a typical experiment, a vesicle is filled with a sucrose solution that has a higher density than the surrounding buffer to allow for sedimentation towards the substrate due to gravity. Whenever two surfaces approach, there are different forces

[a] A detailed explanation of the interactions briefly introduced in this section can be found in [59].

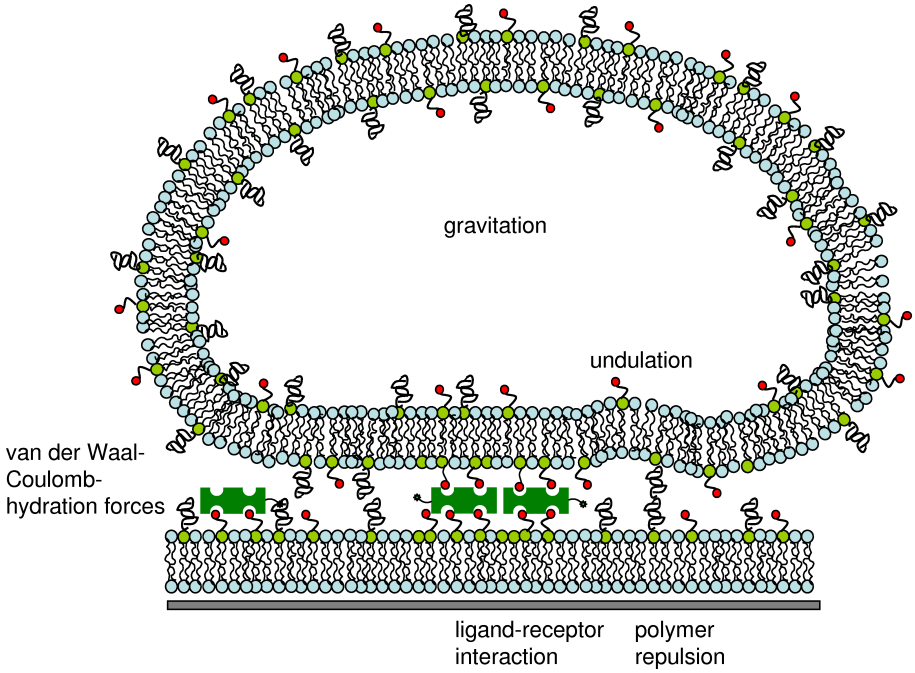

Figure 4.1: Illustration of the physical forces contributing to the interaction potential of an adhering vesicle.

controlling their interaction. Here, van der Waals interactions between permanent and induced dipoles as well as Coulomb interactions between charges are restricted to very short ranges. The high ionic strength of the buffer employed (physiological conditions: 150 mM NaCl) screens the electric potentials efficiently with a Debye length of less than one nanometer. However, the aqueous environment introduces an additional effect: the hydration force. Due to the large dipole moment of water molecules, hydrophilic surfaces are preferentially wetted while hydrophobic surfaces are expelled from water. As a consequence, hydrophilic surfaces like lipid bilayers repel each other if they are brought in close contact because the water molecules at the interface are forced to reorient. The effective range of this interaction is about three to five nanometers [59]. Another repulsive contribution to the interaction potential arises from thermally induced fluctuations of the vesicle membrane. The amplitude of the fluctuation depends on the bending elasticity (κ) and tension (σ) of the specific membrane [115, 116]. These membrane fluctuations were first described by Helfrich in 1978 and are therefore termed Helfrich undulations [117]. He showed that the effective steric potential of a fluctuating membrane close to a wall (mean height h) decays as $T^2/\kappa h^2$, where T is the temperature. Depending

on the temperature and bending stiffness the range of this interaction can be up to several hundreds of nanometers. Helfrich undulations counteract adhesion because the necessary freezing of the fluctuations is entropically unfavorable. Figure 4.1 illustrates the physical forces contributing to vesicle adhesion.

In order to isolate the specific contributions to adhesion from the unspecific contributions a strategy of real cells was transferred to model systems. Unspecific cell adhesion is prevented by the so-called glycocalix. This hydrated mesh of negatively charged polysaccharides induces steric repulsion. To mimic this effect polymer coupled lipids are frequently used in model systems (see for example [103]). Another strategy to minimize unspecific interactions is passivation of surfaces with bovine serum albumin. This protein adsorbs on hydrophilic as well as on hydrophobic surfaces and forms a thin film on top of the substrate [118].

Bruinsma *et al.* applied a superposition approximation to calculate the effective unspecific potential resulting from gravitation and other generic interactions [81]. They found a double well potential with one sharp minimum close to the surface (h ≈ 5-10 nm, van der Waals dominated) and a broad minimum further away (h ≈ 100 nm, gravitation dominated). The effective shape of the potential depends moreover on the extend of membrane fluctuations and the steric repulsion and chemical potential of the polymer lipids. For example, the presence of polymer lipids in the model membranes can screen the undesirable first minimum. If, in addition, specific receptor-ligand interactions are turned on, the specific interaction potential is superimposed. A harmonic approximation can be used in case of moderate interaction potentials [119, 120]:

$$V_{specific}(h) = V_0 + \frac{V''}{2}(h - h_{eq})^2, \tag{4.1}$$

where h_{eq} is the equilibrium binding distance. It depends on the length of the receptor-ligand pair and its deformability [121, 122] as well as on the elastic properties of the membranes to which the binders are linked [81]. The transition of the vesicle from the gravitation minimum to the specific minimum resembles a first order wetting transition characterized by a nucleation and growth process [81].

4.1.2 Spherical Cap

Seifert and Lipowski [123] calculated the possible shapes of adhering vesicles by minimizing the free energy functional F:

$$F = F_\kappa + F_W + F_P + F_\Sigma \tag{4.2}$$

$$= (\kappa/2) \oint dA(C_1 + C_2 - C_0)^2 - WA + P \int dV + \Sigma \oint dA. \tag{4.3}$$

Herein, F_κ is the curvature energy. It depends on the two principal curvatures C_1 and C_2, on the spontaneous curvature C_0, which is an intrinsic property on the membrane, and on the membrane's bending rigidity κ. F_W is the adhesion free energy of a membrane in a contact potential[b] W at contact area A. In order to account for the constraints of constant vesicle volume and constant vesicle surface the Lagrange multipliers P and Σ are introduced. They correspond to the osmotic pressure and the tension in the membrane. The authors find, that the contact potential W and the bending rigidity κ determine the curvature C_1 of the vesicle at the contact point[c]:

$$C_1 = \left(\frac{2W}{\kappa}\right)^{1/2} \tag{4.4}$$

In the case of adhesion of an object with finite elasticity the contact angle itself is restricted to π. Since any sharp edge costs an infinite amount of bending energy the contour of the object approaches the substrate tangentially. For an object without defined elasticity, like a water droplet on a solid, the contact angle is given by the balance of interfacial tensions ($\Sigma_{VS} = \Sigma_{LS} + \Sigma_{LV}\ \cos\theta_Y$, where L = liquid, S = solid, V = vapor). In this case, the famous Young-Dupré equation yields the adhesion energy density directly as a function of the contact angle[d] θ_Y:

$$W = \Sigma_{LV}(1 + \cos\theta_Y) \tag{4.5}$$

[b] The replacement of the numerous discrete bonds by a contact potential explains experimental observations astonishingly well. The contact potential is also called adhesion energy density in the following.

[c] The confinement due to the substrate on one side implied, that the membrane was curved only in one direction and $C_2 = 0$ along the line of contact.

[d] According to Young the contact angle is defined as the angle between the water droplet and the normal to the substrate.

In case of a vesicle membrane with small bending rigidity (e.g. SOPC membrane: $\kappa = 20$ k_BT [124] and references within) and/or large adhesion energy density an effective contact angle $\theta_{Y,eff}$ can be defined. Then, the curvature at the contact point is large and the corresponding radius of curvature r_c is small. Under these conditions, the shape of the vesicle is that of a spherical cap where r_c is small in comparison to the vesicle size. The effective contact angle of a spherical cap obeys the Young-Durpé equation:

$$W = \Sigma(1 + \cos\theta_{Y,eff}) \tag{4.6}$$

4.1.3 Bruinsma Model

In case of strong vesicle adhesion the whole contact zone is adhered and the spreading pressure exerts tension on the edge of the adhesion disc. In these cases the vesicles adopt a shape close to the described spherical cap configuration and an effective adhesion energy density can be determined with the help of the Bruinsma model [125]. This model describes adhesion of a sphere-like vesicle at constant volume. In order to establish an adhesion zone (radius u) the vesicle has to increase its radius and surface area. Another assumption of the model is that the profile of the membrane $h(s)$ is linear ($h(s) = -\theta_{B,eff}s$) far away from the contact point at $s = 0$ (see Figure 4.2) while inside the adhesion disc $h(s) = 0$. The width of the rim region in between the two linear regimes is termed s_0. For short-range forces the adhesion free energy contributes solely within the contact region ($s > s_0$). Minimizing the free energy in the harmonic approximation

$$\Delta F \approx 2\pi u \left[\int_{-\infty}^{s_o} ds \left\{\frac{1}{2}\kappa\left(d^2h/ds^2\right)^2 + \frac{1}{2}\Sigma\left(dh/ds\right)^2\right\} - \int_{s_0}^{\infty} W ds\right] \tag{4.7}$$

yields the profile of the membrane:

$$\begin{aligned} h(s) &= -\theta_{eff}s + \theta_{eff}\lambda\exp\frac{s-\lambda}{\lambda} && s < \lambda \\ h(s) &= 0 && s > \lambda, \end{aligned} \tag{4.8}$$

where $\lambda = \sqrt{\kappa/\Sigma}$ is the so-called characteristic length scale. From Eq. 4.8 follows the identity $\lambda = s_0$. As a consequence, the membrane profile $h(s)$ is bending dominated for $s < s_0$ and tension dominated for $s > s_0$. This result of the Bruinsma model in

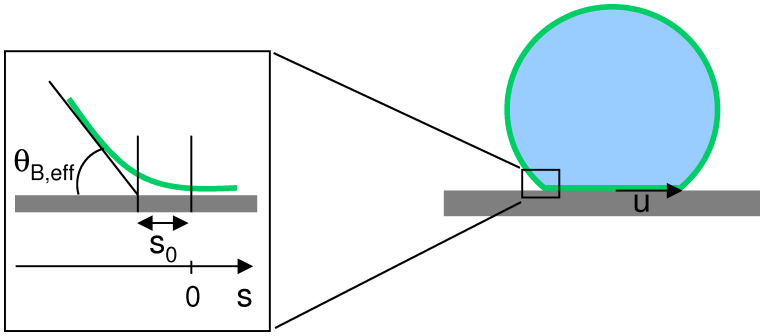

Figure 4.2: Bruinsma model of vesicle adhesion. The geometrical parameters $\theta_{B,eff}$ and s_0 allow for an estimation of the effective adhesion energy density.

combination with Eq. 4.6 allows to estimate the effective adhesion energy density of an adhering vesicle from the geometrical parameters s_0 and $\theta_{B,eff}$.

$$W = \frac{\kappa}{s_0^2}(1 - \cos\theta_{B,eff})^{\mathrm{e}} \tag{4.9}$$

s_0 and θ_{eff} can be determined from the reconstructed vesicle profile measured with RICM (see Sections 2.3.3 and 3.2.1).

4.1.4 Smith-Seifert Model

Besides the Bruinsma model, several theoretical approaches have been introduced to take into account different aspects of vesicle adhesion [126–132]. The recently developed Smith-Seifert model merges the global view of the vesicle with the discrete nature of receptor ligand bonds [133, 134]. The authors provide a thermodynamical framework wherein the equilibrium adhesion state is principally governed by the gain in binding enthalpy accompanied by a loss in mixing entropy and the elastic deformation of the entire vesicle. The included parameters are namely: (i) the interaction enthalpy of active molecules such as ligands, and repelling molecules specifically binding to receptors or locally interacting with the substrate, (ii) the mobility of the active molecules through a contribution of the mixing entropy, (iii) the bending energy of the vesicle, (iv) the finite number of ligands and repelling

[e]Please note, that the different sign of the cosine in comparison to 4.6 results from the different definition of the contact angle. In 4.6 θ_Y is defined as the angle between the water drop and the surface >90° while Bruinsma defined $\theta_{B,eff}$ as the angle between the membrane and the horizontal <90°. Thus θ_Y = 180° - $\theta_{B,eff}$.

molecules in the vesicle, (v) the density of mobile or immobile receptors on the substrate, and (vi) the constraints of the total reduced area and volume of the vesicle [134]. The model has been successfully applied to explain experimental observations like the antagonist induced unbinding or unbinding under force [134–136]. In the near future, this model will be extended to account also for the scenario studied in this thesis.

4.2 Results and Discussion

4.2.1 Biotin-Neutravidin: Limit of Strong Binding

4.2.1.1 Setting-up the System

The specificity of the binding of the avidin analogue neutravidin to the biotinylated lipids in a SLB was checked with a fluorescently labelled version of the protein: neutravidin-OG. Without passivation with BSA, there was significant amount of unspecific binding as judged from experiments with SLBs free of biotinylated lipids. In this case, the fluorescence did not recover after bleaching indicating that the neutravidin-OG was bound directly to the rigid glass substrate presumably to small defects in the bilayer. On the scale accessible to fluorescence microscopy no structures were detectable. Figure 4.3 shows a fluorescence micrograph of a NBD labelled SLB that is perfectly homogeneous. Passivation with 5 mg/ml BSA suppressed unspecific binding almost completely. The ratio of intensity after protein binding for unspecific and specific case was 1:1000 at identical settings.

4.2.1.2 Heights and Adhesion Energy Densities

Giant unilamellar vesicles doped with biotinylated lipids were allowed to sediment onto SLBs which were already decorated with neutravidin. Following the classical pattern, the floppy vesicles fluctuated typically few minutes and than spread within a few minutes to form an adhesion disc visible in RICM as a dark circle surrounded by circular fringes. Two control experiments were carried out to ensure specific vesicle adhesion. In the first experiment vesicles without biotinylated lipids in the

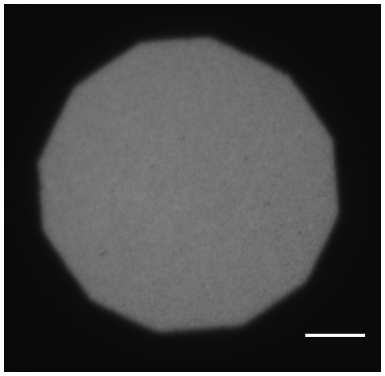

Figure 4.3: Fluorescence micrograph of a supported lipid bilayer bounded by the microscopes' field stop. The bilayer contained 1% fluorescently labelled NBD lipids. Scale bar: 10 μm.

membrane were employed to check the interaction between the unfunctionalized vesicle membrane and the functionalized supported lipid bilayer without additional passivation with BSA. Vesicles were exposed to the bilayer and recorded for more than one hour. On the typical timescale for specific binding no vesicle adhered. Even after more than one hour only 10 % of the vesicles adhered completely. In the second control experiment with biotinylated lipids in the vesicle, but without neutravidin on the bilayer, the bilayer was additionally passivated with BSA before and after incubation with neutravidin. Under these conditions not a single vesicle adhered after more than one hour. Consequently, specificity of vesicle binding could be ensured with and without BSA passivation on time scales of more than one hour. Figure 4.4 shows the RICM image of a typical vesicle after adhesion. The height topography of the membrane in the adhesion disc was mapped for each vesicle with respect to the SLB. Analyzing 10 exemplary vesicles for each case yields $h_{1\%} = (8 \pm 1)$ nm and $h_{5\%} = (7 \pm 1)$ nm. The size of avidin as determined by crystallography is $h_{cry} = 4$ nm [48]. The length of the linker (cap, see 2.2.2) connecting the biotin and the lipid, as measured by X-ray reflectivity, was 8 $\mathring{A}$ [137]. Since the linker had to be counted twice, this gave a theoretical total height of 5.6 nm. Within the expected resolution of RICM ($\Delta h = 4$ nm [104]) the measured and calculated values agreed very well.

In each case five of these 10 vesicles exhibited enough fringes to reconstruct the height profile far away from the adhesion disc. Thus, the effective adhesion energy density could be determined according to Bruinsma [125]. The geometrical parame-

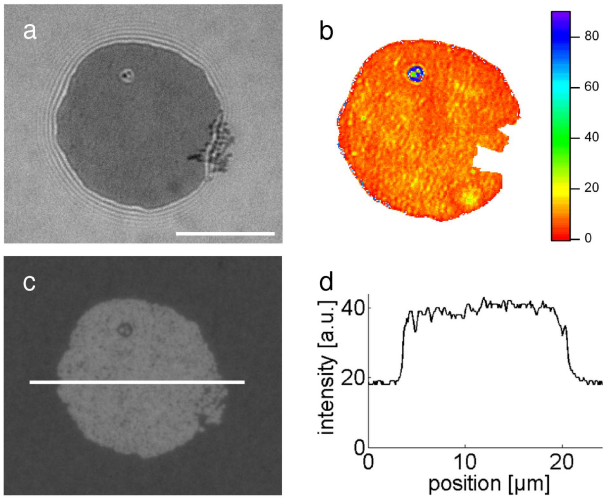

Figure 4.4: a: RICM micrograph of an adhering vesicle. b: Reconstructed height [nm] in the adhesion disc. c: Fluorescence micrograph of accumulated neutravidin in the adhesion disc. The initial biotin concentration on the SLB is 2%. d: Intensity profile along the white line in c. The scale bar in a is valid for a - c: 10 μm.

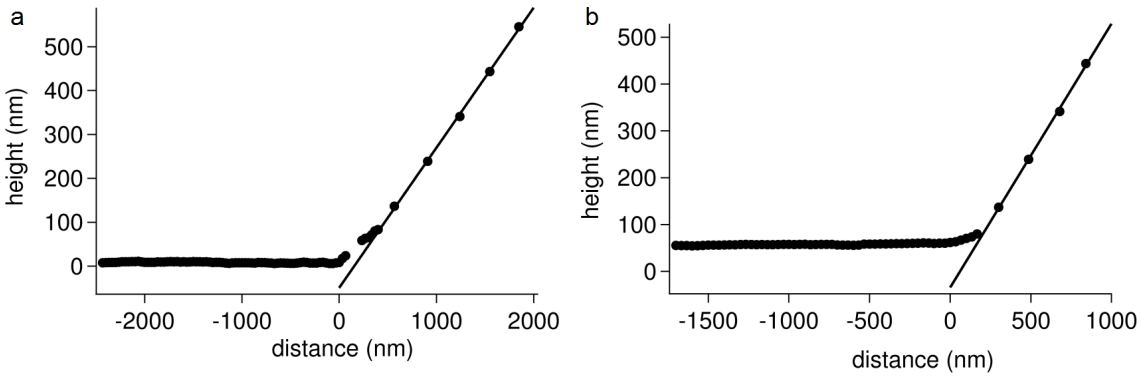

Figure 4.5: Reconstructed vesicle profile. Black dots: data, black line: Linear fit to determine s_0 and $\theta_{B,eff}$ a: Biotin-neutravidin binding case. In this example: $s_0 = 53$ nm and $\theta_{B,eff} = 20°$ and thus $W = 2 \circ 10^{-6}$ J/m^2, b: Ecad-Ecad binding case. In this example: $s_0 = 143$ nm and $\theta_{B,eff} = 23°$ and thus $W = 3 \circ 10^{-7}$ J/m^2

ters $\theta_{B,eff}$ and s_0 were extracted from RICM images with a routine already existing in the lab [104] (see Figure 4.5). The adhesion energy density was calculated with Eq. 4.9 using $\kappa_{SOPC} = 20$ k_BT (see [138] and references within). For both cases a range from $W_{NAV} = (0.2 - 2)\cdot 10^{-6}$ J/m^2 was obtained. As s_0 was measured and κ_{SOPC} was known, the membrane tension Σ could be calculated as well: $\Sigma_{1\%} = (0.2 - 4.1)\cdot 10^{-5}$ J/m^2 and $\Sigma_{5\%} = (0.1 - 1.9)\cdot 10^{-5}$ J/m^2 (see also Table 4.2). It has to be noted, that these values represent only the lower limit of the adhesion energy density and tension because the adhesion state with fringes was not the equilibrium state of the vesicles. Most of the vesicles lost their fringes at later times (t>30 minutes, see also Figure 4.6). This fact indicated that the tension in the membrane was still rising and thus the adhesion energy was eventually considerably higher.

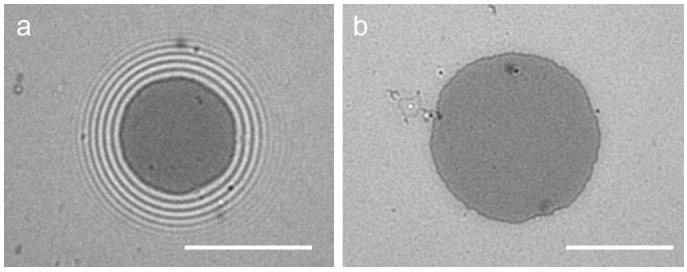

Figure 4.6: 1% GUV on 1% SLB. [f] a: Vesicle with fringes 20 minutes after addition of the vesicles to the sample. b: Different vesicle without fringes at t = 35 minutes. Scale bar 10 μm.

To infer the protein distribution beneath the vesicle, we used fluorescently labelled neutravidin (neutravidin-OG) and monitored the fluorescence intensity of the area under the vesicle before and after vesicle binding. After completion of the adhesion process, a distinct enrichment of the protein in the adhesion disc of an adhering vesicle was seen (Figure 4.4c). To determine the steady-state concentration of neutravidin in the adhesion disc, a series of vesicle binding experiments on SLBs with six different biotin concentrations (0.4%, 1%, 2%, 3%, 5% and 7%) was carried

[f]This abbreviated notation is used to describe the ligand and receptor concentrations in the respective membranes. 1% GUV means that 1% biotinylated lipids were present in the vesicles' membrane. 1% SLB also means that the solid supported bilayer contained 1% biotinylated lipids, but it has to be noted that one neutravidin molecule on the bilayer binds two biotinylated lipids and consequently the neutravidin concentration is only half of the given concentration.

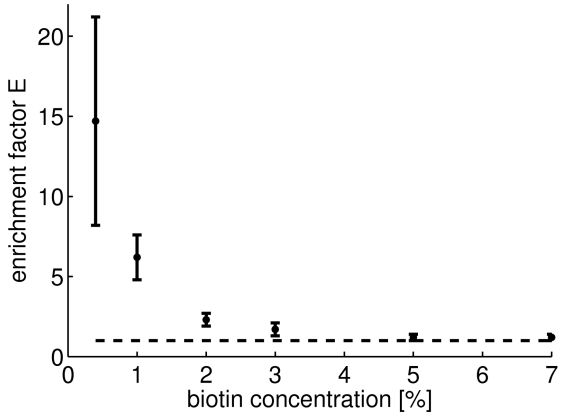

Figure 4.7: Neutravidin-OG enrichment. Points: the ratio of the fluoresence intensity measured in the adhesion disc and on the bilayer. Dotted line: ratio = 1. The error bars represent single standard deviations.

out. After complete adhesion the intensity within the adhesion disc $I_{vesicle}$ was compared to the intensity of the neutravidin coated SLB $I_{bilayer}$ close by (see Figure 4.4c). As Figure 4.7 shows, the ratio $I_{vesicle}/I_{bilayer}$ decreased with increasing biotin concentration on the SLB and reached saturation close to 5%. The background intensity was less than 10% of the specific signal and hence neglected. The mobility of the neutravidin led to the situation that the concentration in the adhesion disc was close to 5% for all cases studied. This fact explained why the adhesion energy densities for initial concentrations of 1% and 5% biotinylated lipids were the same.

4.2.1.3 Determination of Binding Stoichiometry

The exact binding stoichiometry of biotin and neutravidin could be clarified from the same series of measurements. Neutravidin exhibits four biotin binding sites [48]. If the ligands are presented in a planar geometry, as in this case on a SLB, in principle, two binding sites should be accessible. In order to determine whether each neutravidin is bound by one or two biotinylated lipids, the following assumptions were made:

1. The number density of neutravidin ρ_{NAV} is controlled by the density of biotinylated lipids ρ_L:

$$\rho_{NAV} \quad = \quad \rho_L/\alpha\,, \tag{4.10}$$

where the stoichiometric parameter α is the number of biotinylated lipids per neutravidin molecule.

2. The maximum density of neutravidin ρ^*_{NAV} is restricted by the geometry of neutravidin:

$$\rho^*_{NAV} = \frac{1}{A_{NAV}}, \tag{4.11}$$

where A_{NAV} denotes the area of one neutravidin molecule ($A_{NAV} = 28$ nm^2. [48])

3. The maximum neutravidin concentration is established in the adhesion disc of a specifically bound vesicle. Thus, the enrichment factor E, describing the increase in neutravidin concentration after vesicle binding, can be measured experimentally.

$$E = \frac{\rho^*_{NAV}}{\rho_{NAV}} = \frac{I_{vesicle}}{I_{bilayer}} = \frac{\alpha}{\rho_L\, A_{NAV}}. \tag{4.12}$$

Plotting E against $(\rho_L\, A_{NAV})^{-1}$ yielded a straight line with the slope $\alpha = 2.0$ supporting the hypothesis of 2:1 binding. This information was used to estimate the maximum neutravidin density expected from geometrical considerations. Since one neutravidin covers an area of 28 nm^2, approximately 40 lipids (area per lipid molecule at 20 mN/m [139]: 0.69 nm^2) can be placed beneath one protein. If two biotins bind to one neutravidin, every 20th lipid (=5% of the lipids) has to be biotinylated. Thus, the 5% saturation limit observed experimentally corresponds to the theoretical limit of coverage.

4.2.2 E-cadherin-E-cadherin: Limit of Weak Binding

4.2.2.1 Setting-up the System

The Ca^{2+} dependent functionality of the Ecad construct used in experiments was checked each time after reconstitution from the lyophilized state by measuring its ability to cluster (bead-bead assay) or immobilize (bead-surface assay) beads in presence and absence of Ca^{2+}. It should be noted that Ecad was bound unspecifically to the beads and hence the protein immobilization was independent of nickel chelation. Bead assays were carried out with all buffers used together with Ecad. In case of a bead-bead assay the percentage of single beads in calcium free buffer served as a negative control. It was repeatedly determined to be 98%. The function

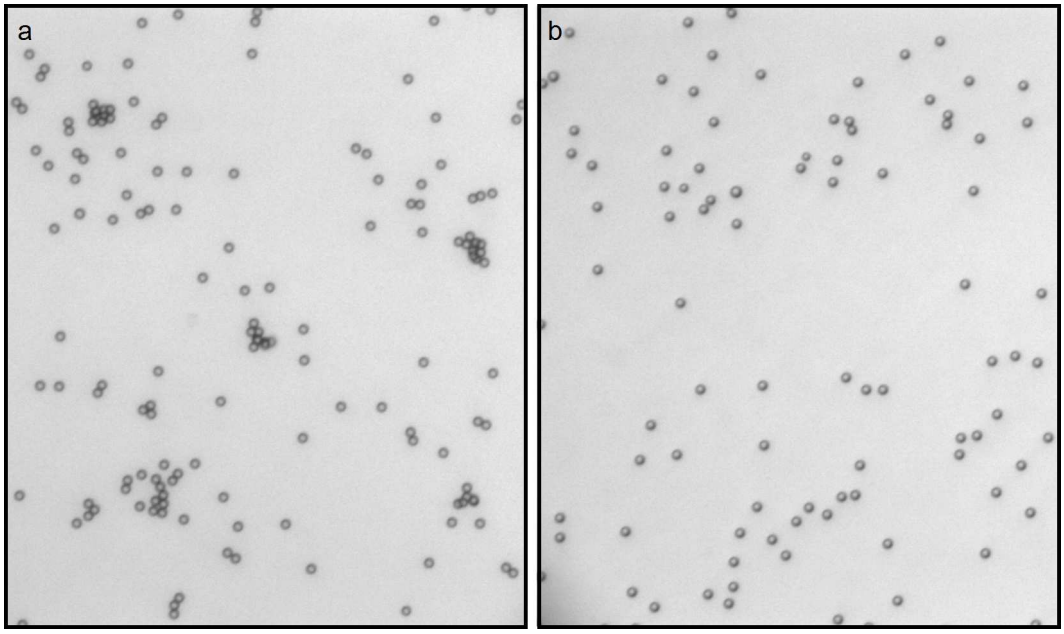

Figure 4.8: Exemplary data for the bead-bead assay to check the Ca^{2+} dependent functionality of E-cadherin. a: Cadherin coated beads in a buffer containing 750 μM $CaCl_2$, b: Cadherin coated beads after addition of 5 mM EGTA. The field of view is (270x320) μm each time.

of Ecad clearly depended on the presence of Ca^{2+}. Upon Ca^{2+} trapping by EGTA the amount of beads bound to each other dropped (+Ca^{2+}: 30% of all objects are clusters, -Ca^{2+}: 11% of all objects are clusters) and the absolute value of objects rose considerably by a factor of 2.3 indicating that mostly dimers were formed and dissolved (see Figure 4.8). As a control BSA coated beads were observed in presence of Ca^{2+} and after addition of EGTA. EGTA had either no effect or increased the amount of monomers slightly by 2%. Therefore, clustering was caused by Ecad-Ecad binding and not by bridging via Ca^{2+}.

In the bead-surface assay the reduced mobility of Ecad coated beads placed on an Ecad-coated glass surface indicated successful binding. A negative control showed that the beads lacking Ecad, execute random walks typical of thermal fluctuations if placed on a BSA coated surface. A second negative control with Ecad on both beads and surface, but in a buffer depleted of Ca^{2+}, proved the Ca^{2+} dependence of the binding. Comparing the Ecad/Ecad interaction in presence of Ca^{2+} with the negative control showed a reduction of the mean trajectory length covered by a bead per unit time by a factor 4. Complete immobilization occurred for 55% of the beads. Even if all the fully immobilized beads were neglected, the mean distance covered by

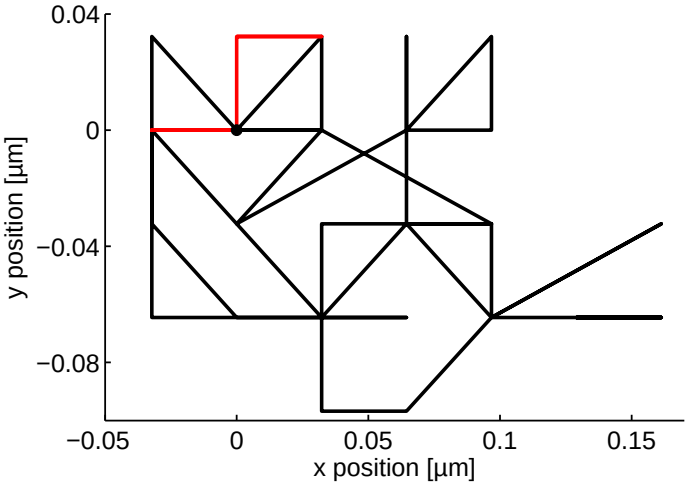

Figure 4.9: Exemplary data for the bead surface assay to check the Ca^{2+} dependent functionality of E-cadherin. Red trajectory: Cadherin coated bead in a buffer containing 750 μM $CaCl_2$. Black trajectory: Cadherin coated bead in a buffer containing 5 mM EGTA. The black dot marks the starting position for both beads. The total distances travelled in the given example were 6 and 16 μm respectively.

Table 4.1: Exemplary bead-surface assay. d_{xy0} is the mean of all distances including completely immobilized beads , while d_{xy} is the mean of all distances without completely immobilized beads. N denotes the number of beads analyzed and N_{stuck} those with zero movement.

	Ca^{2+}	d_{xy0} [μm]	d_{xy} [μm]	N_{stuck}	N
control	+	15.6	15.6	0	36
	-	7.2	9.6	5	40
Ecad	+	2.2	4.9	17	31
	-	9.2	9.8	5	92

the still fluctuating beads was minor (factor 2). Figure 4.9 compares the trajectories of two beads for the aforementioned case. Addition of EGTA and thus depletion of Ca^{2+} initiated unbinding of immobilized beads (see also Table 4.1). Incidentally, our experimental conditions of low receptor concentration and long binding times ensure that the his_6-NTA bond is stable throughout the experiment [140].

The specificity of Ecad binding was probed by immunofluoresence. The immunolabel was chosen to be TRITC labelled protein A which binds to the Fc region of the Ecad construct and could therefore be used to label and localize Ecad binding to the

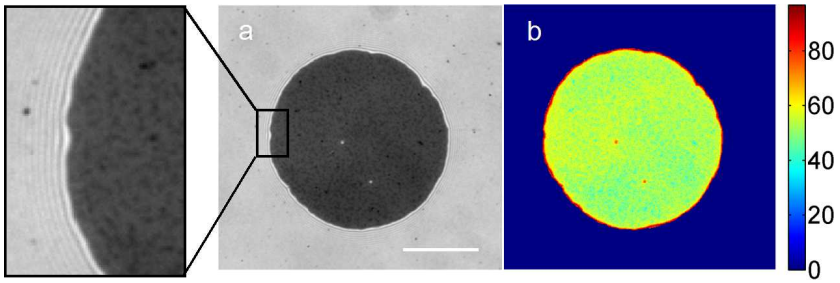

Figure 4.10: a: RICM micrograph of an adhering vesicle. b: Reconstructed height [nm] in the adhesion disc. The scale bar is valid for both images: 10 μm.

SLB. Two SLBs exhibiting either 5% NTA lipids or no NTA lipids were passivated with BSA and incubated with Ecad. The sample was washed with PBS and again passivated with BSA before incubation with fluorescent protein A. Comparison of the measured fluorescence intensities for the SLB with and without NTA with identical microscope and camera settings showed that 90% of the signal originated from specific binding. Thus, unspecific interaction of the Ecad construct with the SLB was negligible.

4.2.2.2 Heights and Adhesion Energy Densities

As discussed before, the Ecad receptor was used in the form of a dimeric chimera with all five E-cadherin ectodomains genetically fused to an immunglobulin Fc-fragment exhibiting a hexahistidin tag (his_6). The his_6-tags were used to bind the construct to the SLB and GUV via nickle chelating lipids (NTA). Due to the weakness of the Ecad-Ecad bond it was necessary to work at high NTA concentrations in both the SLB and the vesicle to enable stable vesicle binding. We used 5% NTA in each. GUVs doped with NTA-lipids and coated with Ecad were allowed to sediment onto SLBs which were already decorated with Ecad. The floppy vesicles fluctuated for a while and adhered within a few minutes to form an adhesion disc visible in RICM as a dark circle (Figure 4.10a). Control vesicles without NTA lipids did not adhere even after 90 minutes. Unlike in the strong binding case, many of the bound vesicles did not exhibit a dark rim or had only a broken dark rim. Therefore the height was calculated in the first ($h > h_0$) branch of the cosine function (Eq. 2.12). As in the strong binding case, the topography of the entire adhesion zone was mapped (Fig-

Table 4.2: Vesicle heights h, membrane tensions Σ and adhesion energy densities W for the binding scenario biotin-neutravidin and Ecad-Ecad. N denotes the number of measurements. STD represents the single standard deviation.

	$h \pm$ STD [nm]	N_h	Σ [10^{-5} N/m^2] [g]	W [10^{-6} J/m^2]	N_W
1% biotin	8 ± 1	10	> (0.2 - 4.1)	>(0.2 - 2)	5
5% biotin	7 ± 1	10	> (0.1 - 1.9)	>(0.2 - 2)	5
5% NTA	54 ± 9	30	0.3 - 0.7	0.3 - 0.9	5

ure 4.10b) and the average inter-membrane distance was calculated to be h_{RICM} = 54 ± 9 nm. Close inspection of the calculated heights show that for some pixels, (roughly 5% in each vesicle), ambiguity remains about whether the height should be calculated in the first or the zeroth branch. Thus 54 nm represents an upper-limit - the real inter-membrane distance may be slightly lower (∼2 nm).

For the case of Ecad mediated binding the adhesion energy density could be measured in the equilibrium state because the vesicles retained their fringes over the whole observation period. Five exemplary vesicles were analyzed and exhibited adhesion energy densities of W_{Ecad} = (0.3 - 0.9)· 10^{-6} J/m^2 and tensions of Σ_{Ecad} = (0.3 - 0.7) ·10^{-5} N/m^2. Comparison with the energy densities and tensions achieved in the biotin/neutravidin model system (up to 2· 10^{-6} J/m^2 and 4 ·10^{-5} N/m^2 as a lower limit) confirmed that Ecad mediated vesicle adhesion was effectively weaker (see also Table 4.2).

4.2.2.3 Binding Configuration

As already described in Section 2.2.2 it is not yet clear which binding geometry E-cadherins adopt. Mainly three scenarios are under discussion: overlap of the outmost domains only, overlap of the three outmost domains and complete overlap. In the present case, the size of the Ecad receptors can be estimated since the size of Fc-fragment and Ecad ectodomains are known from their crystal structure to be 7 nm [141] and 19 nm [29] respectively and the size of the his_6 was determined from

[g] The large spread in tension for the biotin/neutravidin model system originated from the pooling of data from different days. It is very difficult to produce GUVs with identical tension in different experiments as the tension is extremely sensitive to changes in the osmotic conditions.

its chemical structure to be 2 nm. From these considerations, the expected inter-membrane distance for the proposed binding scenarios can be calculated to be: h_{11} = 52 nm, h_{33} = 45 nm or h_{55} = 37 nm. Our result of 54 ± 9 nm (upper-limit) for the inter-membrane distance argues for a predominance of the (EC01 EC01) and the (EC01-EC03 EC01-EC03) states.

4.3 Conclusion

In this chapter the equilibrium states of adhering vesicles were investigated for the limiting cases of strong and weak adhesion. For neutravidin/biotin mediated adhesion, it was shown that the lateral mobility of receptors in the plane of the SLB led to an accumulation of receptors in the adhesion disc. The final adhesion energy densities of vesicles with initially different concentrations of binding partners on the SLB were the same. Adhesion energy densities and tensions were found to be extremely high (>$10^{-}6\mathrm{J/m^2}$ and >$10^{-}5\mathrm{N/m^2}$) and resulted in complete loss of Newton fringes in the RICM micrographs. E-cadherin mediated adhesion on the other hand was characterized by a lot of Newton fringes and considerably lower adhesion energy densities and tensions ($10^{-}7\mathrm{J/m^2}$ and $10^{-}6\mathrm{N/m^2}$).

The measured membrane distance of biotinylated vesicles adhered by neutravidin was found to be in very good agreement with the expected height calculated from the molecular size of neutravidin plus the lengths of the biotin linkers. The corresponding measurement on the E-cadherin bound vesicle supports the hypothesis that E-cadherin binds mainly with its first domain.

Chapter 5

Vesicle Adhesion: Limit of High Receptor Concentrations (Dynamics)

This chapter first gives a summary on the actual consensus on the dynamics of vesicle adhesion. Second, the results achieved in this work are presented. It is the first time that the dynamics of vesicle adhesion is thoroughly studied in a scenario with both mobile receptors and ligands. The influence of the receptor and ligand concentration as well as the reduced volume of the vesicle are discussed in detail.

5.1 Introduction and Theory

Adhesion of cells to each other and to external substrates is a complex process essential for the existence of multicellular organisms. A large variety of specific adhesion molecules is mediating cell adhesion. It is strictly regulated by many signal cascades. There is large interest in elucidating the underlying processes both from the biological and the physical side. Especially in the early states of adhesion (up to $\sim$ 1 min) physical laws are expected to dominate because the cell needs some time to initiate an active response. To study the underlying physical principles, simplified biomimetic systems were introduced that allow for quantitative analysis. Thereby, the cell is usually mimicked by a giant unilamellar vesicle.

Adhesion of vesicles to solid substrates is generally believed to be a first order wetting transition characterized by a nucleation and growth process [81]. First, a vesicle filled with a solution of higher density than the surrounding, sediments towards the substrate and is then weakly bound in the minimum of the unspecific interaction potential (see also Section 4.1.1). Subsequently, cooperative binding of several ligands establishes the first contact (nucleation) and drives the system towards the lower specific energy minimum. Depending on the detailed conditions of the experiment (relative receptor-ligand concentrations, binding rates, reduced volume, accessability of binding partners, unspecific contributions, ...) several scaling laws for the growth process were theoretically proposed and experimentally observed [130–132,142–145]. Finally, spreading is stalled when the gain in free enthalpy (Gibbs free energy) due to receptor-ligand binding is balanced by bending and stretching of the membrane [123]. In this work, the scenario of specific vesicle binding mediated by mobile receptor ligand pairs was realized by two receptor-ligand pairs. In order to mimic high-affinity binding, biotinylated vesicles were used in combination with neutravidin functionalized bilayers. Weak binding was established by homophilic E-cadherin bonds. Both systems were studied with vesicles exhibiting a large excess area. So far, a theoretical model including the mobility of both ligands and receptors is still missing. There is only one experimental approach already described: Puech *et al.* studied a biotin-streptavidin model system [144]. When the vesicles were deflated, they produced multiple adhesion patches, which fused at later times. The authors propose that in early stages of adhesion the adhered area A_{adh} evolves almost linearly in time: $A_{adh} \sim t^{\alpha}$ with $\alpha = 1.26$. They observe linear growth. Nevertheless, their theoretical approach did not account for the mobility of both binding partners and the authors admit difficulties in reproducibility of the data.

As the vesicles in the present study have a large excess area, it is interesting compare with a recently published study where the influence of membrane shape fluctuations on the adhesion process was elucidated [145]. In that work, the concept of an effective binding affinity was introduced to describe the adhesion process in the limit of weak binding and reaction limited dynamics. The effective binding affinity accounts for the confinement of receptors and ligands to surfaces. This confinement leads effectively to a distance dependency of the affinity because the molecules are anchored

to opposing membranes whose distance will in general not match the molecular sizes. This distance is controlled by the membrane's bending elasticity and fluctuations. Comparison of simulations and experiments with the sialyl-LewisX/E-selectin binding pair revealed the importance of fluctuations that induce the first contact by driving one membrane patch from the unspecific energy minimum to the lower specific minimum. Moreover, the interplay between weak binding and membrane fluctuation led to the appearance of several nucleation centers and disturbance of the radial growth of the adhesion patches. The adhesion dynamic was found to depend on the receptor density: at high densities the growth was best described by a linear function of time while with decreasing density exponential saturation provided a proper characterization.

So far there are only a few studies on vesicle adhesion with mobile receptor-ligand pairs. They elucidated the influence of mobile receptors on the adhesion energy density and force-induced adhesion-strengthening [136, 146–148]. Mobile receptors were found to increase the adhesion strength as well as the resistance to de-adhesion by externally applied point forces. Here, the first thorough investigation of vesicle adhesion dynamics mediated by mobile receptor-ligand pairs is presented.

5.2 Experimental Realization and Analysis Details

5.2.1 Experimental Realization

In order to observe adhesion processes of vesicles to solid supported bilayers, GUVs and SLBs were prepared and functionalized according to the protocols in Section 2.2.1 and 2.2.2. Depending on the density of GUVs, 10 to 50μl of the swelling solution were added to the observation chamber with the SLB in $\sim$ 800 μl PBS for the biotin-neutravidin binding pair and PBS with 750 μM $CaCl_2$ (PBS-Ca) for the Ecad-Ecad interaction. PIPES or HEPES were alternatively used in the Ecad case. The chamber was filled completely with PBS (PBS-, PIPES-, HEPES-Ca) and covered with a glass slide. GUVs were located with the phase contrast mode

of the microscope and observed during sedimentation. When the vesicles were close to the supported bilayer the mode was switched to RICM and the adhesion process was recorded at an image rate of 10 Hz. After the adhesion process was stalled, the vesicles were also recorded in phase contrast in order to measure their diameters. For biotin-neutravidin the late states of adhesion were additionally characterized with fluorescence microscopy.

5.2.2 Analysis Details

First, the onset of adhesion was analyzed with the help of fluctuation maps (see Section 3.2.2). Second, in order to study the dynamics of the adhesion process area vs. time growth curves were constructed from the RICM movies as follows. The adhered area was identified as the low intensity pixels via thresholding. First, all frames of the movie were background subtracted and the intensities were normalized as described earlier (see Section 3.2.1). The threshold was determined from the last image of the movie showing the adhered vesicle in its final steady state. A histogram of all intensity values in the image was displayed. It exhibited two peaks corresponding to the background and the adhered pixel. This distribution was fitted with two Gaussians. The intersection of the two curves defined the threshold. This threshold was applied to the first frame of the adhesion movie. In order to exclude the dark interference fringes and isolated dark pixels caused by noise two constraints were added. A curve was initialized that enclosed the interior of the contact zone. Only those dark pixels were considered that were located within this zone. The remaining dark objects were labeled and measured. Only those with an area of at least five pixels were kept. Then the dark objects in all other frames were identified and included if they covered pixels that were already found in the previous frame, i.e. if they overlapped with the already found adhesion area. This way, the contact zone had not to be determined in every frame to exclude the fringes, but the algorithm was constrained to one nucleation center. In cases with more than one nucleation center the program was rerun for each and the time points of appearance of new nucleation centers (NC) and merging of two adhesion zones were identified. The

corresponding total areas were calculated individually and summed up to get the total area. Depending on the total time of the adhesion process either every tenth or every twentieth frame was evaluated.

5.3 Results and Discussion

5.3.1 Biotin-Neutravidin: Limit of Strong Binding

Various combinations of receptor and ligand concentrations on the SLB and GUV were investigated experimentally. The cases with 1% on the SLB and 1% on the GUV, 5% on the SLB and 1% on the GUV and 5% on the SLB and 2% on the GUV were analyzed quantitatively to study the effect of increased receptor and ligand concentration, respectively.

5.3.1.1 Fluctuation Analysis

Typically five to seven fluctuation maps were constructed to trace the establishment of nucleation centers. Thereby, it became evident that within each combination of concentrations the vesicles split into two groups of different behavior. The two groups exhibited different levels of fluctuations in the free state. The vesicles of the first group (I) showed a smaller mean (1.9 ± 0.1 noise[a]) and maximum (4.1 ± 0.5) fluctuation amplitude (A_{mean}, A_{max}) than the vesicles of the second group (II) (A_{mean} = 2.5 ± 0.2 noise, A_{max} = 4.8 ± 0.5). For single values see column 3 in Table 5.2. For each case there was a larger fraction of type II vesicles (1% SLB 1% GUV: two (I) and four (II), 5% SLB, 1% GUV: two (I) and three (II), 5% SLB, 2% GUV: four (I) and six (II)).

The heavily fluctuating vesicles (II) established a larger contact zone (CZ) with a diameter d_{CZ} that was more than half the diameter of the vesicle d_{PC} ($\frac{d_{CZ}}{d_{PC}}$ = 0.62 ± 0.17) and very frequently more than one nucleation center (NC) appeared (see column 6 in Table 5.1). The less fluctuating vesicles (I) had a smaller CZ with a diameter that was less than half the diameter of the vesicle ($\frac{d_{CZ}}{d_{PC}}$ = 0.30 ± 0.13)

[a]For the usage of noise as an unit see Section 3.2.2

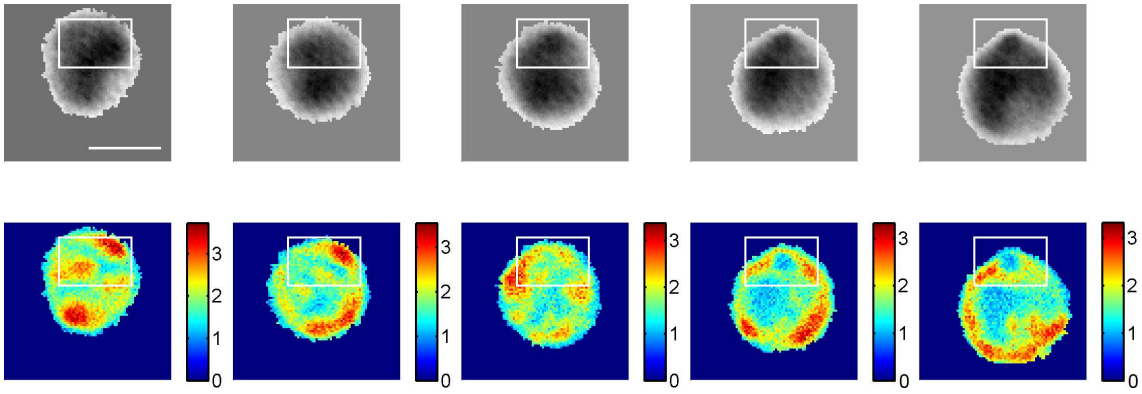

Figure 5.1: Development of a nucleation center for a vesicle with low fluctuation amplitude. Upper row: Mean RICM micrograph, lower row: Fluctuation map in units noise. Each frame represents an average over two seconds. Subsequent successive time steps are shown. Scale bar: 10 μm.

Table 5.1: Dependence of the number of nucleation centers on the fluctuation amplitude. Σ gives the total number of vesicles evaluated in the groups with low and high fluctuation amplitude.

	1	2	3	4	5	6	$\sum$
low	6	2	0	0	0	0	8
high	2	2	4	2	2	1	13

and predominately only one nucleation NC (see Table 5.1) emerged. While this nucleation center appeared in the mean RICM image the corresponding fluctuation maps showed a continuous decrease in fluctuation amplitude at the same site (see Figure 5.1). Because of the relatively small fluctuation amplitude and roughness of the membrane the overall height of the vesicle in the CZ was fairly homogeneous. Thus, the contact of the vesicle's membrane with the SLB could happen only when the entire vesicle approached closely.

On the other hand, the more fluctuating vesicles behaved differently. A hotspot of fluctuation marked the transition from a free to a bound membrane patch. Since the vesicle's membrane fluctuated a lot it could locally approach the SLB even when the vesicle's mean height was large. This way the hotspot appeared. If the bonds persisted the corresponding area showed suppressed fluctuations in the next fluctuation map (see Figure 5.2). In the region where the nucleation center evolved either medium (case A, see Figure 5.2) or suppressed (case B, see Figure 5.3) membrane

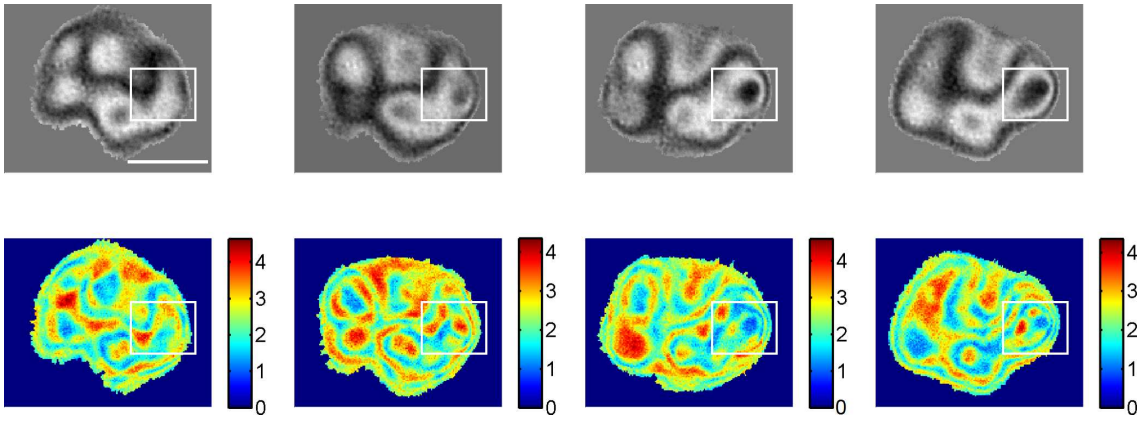

Figure 5.2: Development of a nucleation center for a vesicle with high fluctuation amplitude (case A). Upper row: Mean RICM micrograph, lower row: Fluctuation map in units noise. Each frame covers two seconds. Scale bar: 10 μm.

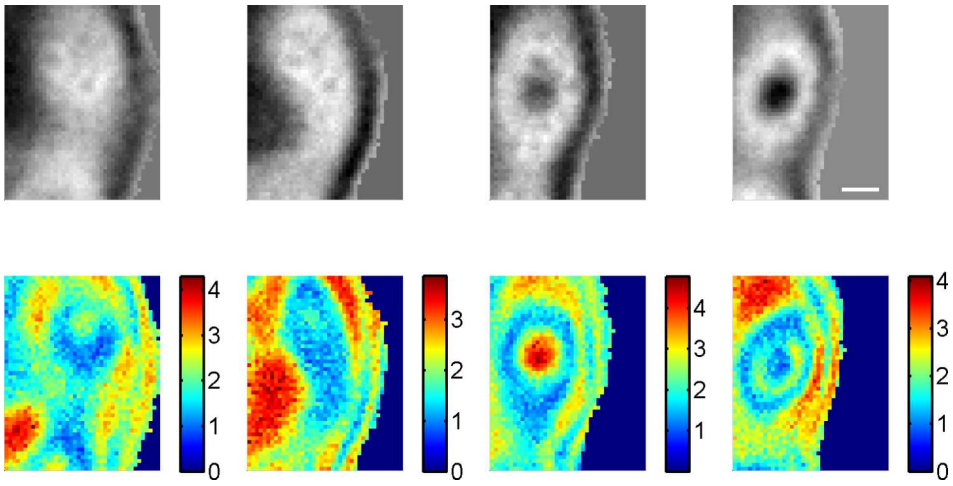

Figure 5.3: Development of a nucleation center for a vesicle with high fluctuation amplitude (case B). Upper row: Mean RICM micrograph, lower row: Fluctuation map in units noise. Each frame covers two seconds. Scale bar: 1 μm.

fluctuations were observed prior to the hotspot. One approach to explain the suppressed fluctuations could be the following: In the given model system with a soft membrane (bending $\sim$ stiffness 20 k_BT) and strong bonds ($\Delta G_0 = 35\ k_BT$) very few bonds allow for deformation of the membrane and binding. Thus, it is possible that a few bonds pinned the membrane already before the hotspot appeared. Such pinning centers could not be seen directly in RICM because they are below the optical resolution. These adhesion clusters then facilitated binding of more ligands in the adjacent area. Finally, a larger membrane area was bound and was now also visible in RICM. The observation of suppressed fluctuation before establishment of a nucleation center was already reported by Smith et al. [136]. In their experiments with RGD-integrin mediated vesicle adhesion the freezing of the membrane was directly followed by adhesion. Why, in the present study, afterwards a hotspot emerged is not yet fully understood.

The appearance of several nucleation centers is atypical for high affinity binding. Up to now all publications on vesicle adhesion agreed that one NC forms and the adhesion spreads very fast radially so that no competing NCs could be formed [143]. This study shows that the nucleation characteristic depends on an additional parameter: the fluctuation amplitude. Heavily fluctuating vesicles easily established a large CZ where the probability to bind was increased due to the large fluctuation amplitude. Because of the strength of the bond the initial contacts persisted very often.

5.3.1.2 Area vs. Time

In this section the growth of the adhered area with time is investigated. Each adhesion process was characterized by a nucleation, a growth and a saturation phase. If the whole process was recorded each phase could be characterized with a parameter. For this, the nucleation region was fitted with an exponential $A(t) = a \exp[k_1 t] + b$, the growth region with a power law $A(t) = a + t^{\alpha}$ and the saturation region also with an exponential $A(t) = (a - b \exp[-k_2 t]) + c$. Figure 5.4 displays an exemplary area vs. time curve with the corresponding fits. Since the exponent of the power law was always close to one, linear growth was assumed and the growth region was fitted

Table 5.2: Summary of the parameters characterizing the adhesion dynamics: Mean fluctuation amplitude directly before adhesion A_{mean}, slope of the area vs. time growth curve in the linear regime, time till the adhered area saturated t_{sat}, number of nucleation centers NC ratio of the diameter of the contact zone and the diameter of the vesicle $\frac{d_{CZ}}{d_{PC}}$ and ratio of the diameter of the adhered area and the diameter of the vesicle $d_{ADH}d_{PC}$ as a measure for the reduced volume. * This vesicle was extremely large (54 μm), ** this versicle was extremely small (12 μm), - fitting failed.

case SLB	case GUV	vesicle No.	A_{mean} [noise]	slope [$\mu m^2/s$]	t_{sat} [min]	NC	$\frac{d_{CZ}}{d_{PC}}$	$\frac{d_{ADH}}{d_{PC}}$
1%	1%	1	1.8	1.8	3	1	0.2	0.4
		2	1.8	1.6	3	1	0.5	0.3
5%	1%	3	2.1	2.5	4	2	0.5	0.7
		4	1.9	1.8	4	2	0.3	0.6
5%	2%	5	1.8	1.7	4	1	0.2	0.6
		6	2.0	3.2	2	1	0.3	0.6
		7**	1.9	0.9	2	1	0.2	0.7
		8	2.0	2.7	2	1	0.2	0.7
1%	1%	9	2.6	3.2	3	4	0.8	0.7
		10	2.4	2.4	1	4	0.4	0.8
		11	2.2	-	3	2	0.5	0.5
		12	2.5	7.9	5	5	0.9	1.0
5%	1%	13	2.6	7.6	3	5	0.7	0.9
		14*	2.5	-	6	6	0.6	0.6
		15	3.0	4.5	4	3	0.5	0.6
5%	2%	16	2.5	5.0	4	2	0.6	0.8
		17	2.3	5.3	2	3	0.8	1.0
		18	2.5	4.1	2	1	0.6	0.8
		19	2.4	1.9	3	1	0.3	0.5
		20	2.3	3.9	3	3	0.6	0.8
		21	2.6	8.1	4	3	0.8	1.0

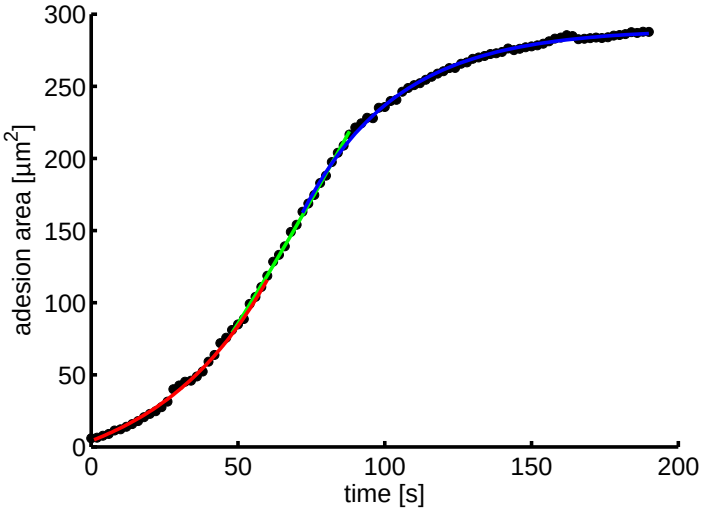

Figure 5.4: Exemplary area vs. time curve with fits. Black dots: Data points, red line: Fit for nucleation ($\tau_1 = 26\ s^{-1}$), green line: Fit for growth ($\alpha = 1.2$), blue line: Fit for saturation ($\tau_2 = 31\ s^{-1}$).

again to determine the slope m: A(t) = a+mt. In particular, the values for nucleation and saturation were difficult to determine because nucleation was sometimes very fast and thus not covered if only every tenth frame was taken into account and saturation was not always reached. That is why only the coefficients for the slope are explicitly given (see column 4 Table 5.2). The influence of the nucleation and saturation process was determined from the comparison of the total time needed to reach saturation (or as close as possible to saturation, see column 5 in Table 5.2). To do so, it is necessary to choose vesicles of comparable sizes (20 to 30 μm diameter). All vesicles of extreme sizes are marked with an asterisk in the overview Table 5.2. Due to the complexity of the experiment and the large variety of vesicle characteristics (fluctuation amplitude, number of nucleation sites, bubbles) it was difficult to collect large numbers of directly comparable data. As a consequence, in this thesis I do not emphasize absolute values but rather aim to establish trends.

Figures 5.5 to 5.20 give an overview of the observed adhesion processes and the corresponding area vs. time curves. Within all cases the type II vesicles with large fluctuations had a distinctly steeper slope (see column 4 in Table 5.2). As it was already shown that vesicles with higher fluctuation amplitude created multiple nucleation centers, it was reasonable that these vesicles spread faster. On the other hand, heavily fluctuating vesicles were less successful in finishing the adhesion pro-

cess. For this observation, there are two explanations. First, in these cases the most fluctuations had to be suppressed and, second, the large number of NCs increased the probability for bubbles. Bubbles appeared when buffer was trapped beneath the adhering vesicle. Sometimes the vesicles succeeded in squeezing out the buffer (for example vesicle No. 12, see Figure 5.16). But this process took a very long time.

Type I and type II vesicles did not only differ with respect to the onset of adhesion (number of NC) and growth velocity but also in the final adhered state. In order to quantify the extend of spreading, the ratio of the diameter of the adhered area (d_{ADH}) and the diameter of the vesicle, as determined by phase contrast microscopy (d_{PC}), was calculated. Vesicles with a lower fluctuation amplitude spread till their adhesion zone had a diameter of $(0.55 \pm 0.13)d_{PC}$, while the vesicles with a higher fluctuation amplitude reached $(0.78 \pm 0.17)\ d_{PC}$. $\frac{d_{ADH}}{d_{PC}}$ is a measure for the reduced volume. This parameter quantifies the excess area of a vesicle available for spreading. It is defined as the ratio of the vesicles' volume and the volume of a perfect sphere with the same surface area. It is logically consistent that vesicles with a smaller reduced volume and thus lager excess area exhibit more fluctuations. Lorz *et al.* [103] already discussed the influence of the reduced volume on the adhesion energy density. They found increasing apparent energy values with increasing reduced volumes as a result of changes in membrane tension. Here, it was shown that the reduced volume also highly influenced the dynamics of the adhesion process.

Comparison of the 1% SLB 1% GUV with the 5% SLB 1% GUV cases revealed an increase in the slope but also an increase in the total time needed to complete adhesion. A higher receptor density on the SLB improved the *ad hoc* availability of binding partners, but with increasing time, diffusion of receptors into the adhesion disc became more and more important. In Chapter 7 it is shown that the receptor mobility dropped rapidly with increasing concentration. At 5% the receptors were practically immobile. As a consequence they could not effectively facilitate saturation. Comparison of the 5% SLB 1% GUV with the 5% SLB 2% GUV cases yielded accelerated growth and saturation. The increase in ligand concentration improved the availability of binding partners without disadvantages as the diffusion constant of the ligand was almost independent of the ligand concentration (see Chapter 7). Moreover, in the case of vesicles with large fluctuation amplitude, the number of

nucleation centers was halved. With increasing growth velocity of a single adhesion domain, there was less time to establish more than one nucleation center before the adhesion process was completed. The reduced number of nucleation centers also lead to a reduced chance of fluid trapping and bubble formation. Thus, the saturation process was facilitated.

To summarize, increasing the receptor concentration could accelerate the adhesion process but only to a limited extent. If the concentration was too high the advantages were canceled by the decreased mobility of the receptors. Thus, the fastest spreading should be reached when the both the receptor concentration and mobility is maximized. In contrast, an increase of the ligand concentration in the membrane of the GUV should always accelerate the adhesion process.

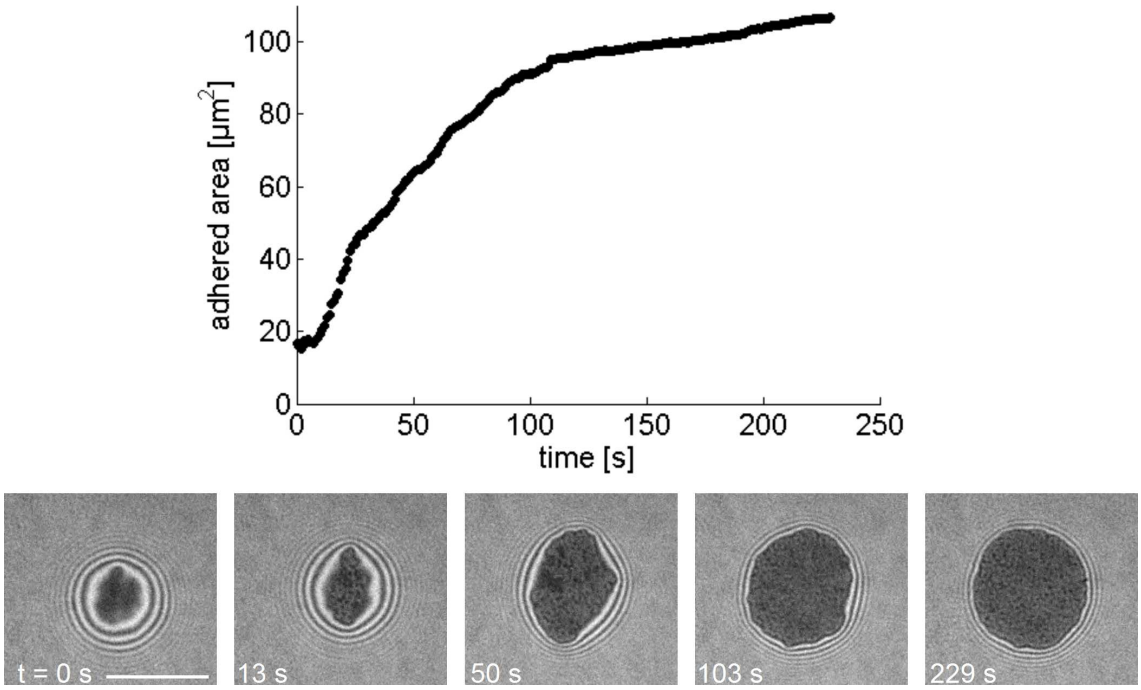

Figure 5.5: Adhesion process of vesicle No. 1 (1% GUV and 1% SLB) with low fluctuation amplitude. The RICM images represent characteristic states and the plot shows the corresponding area vs. time curve. Scale bar: 10 μm.

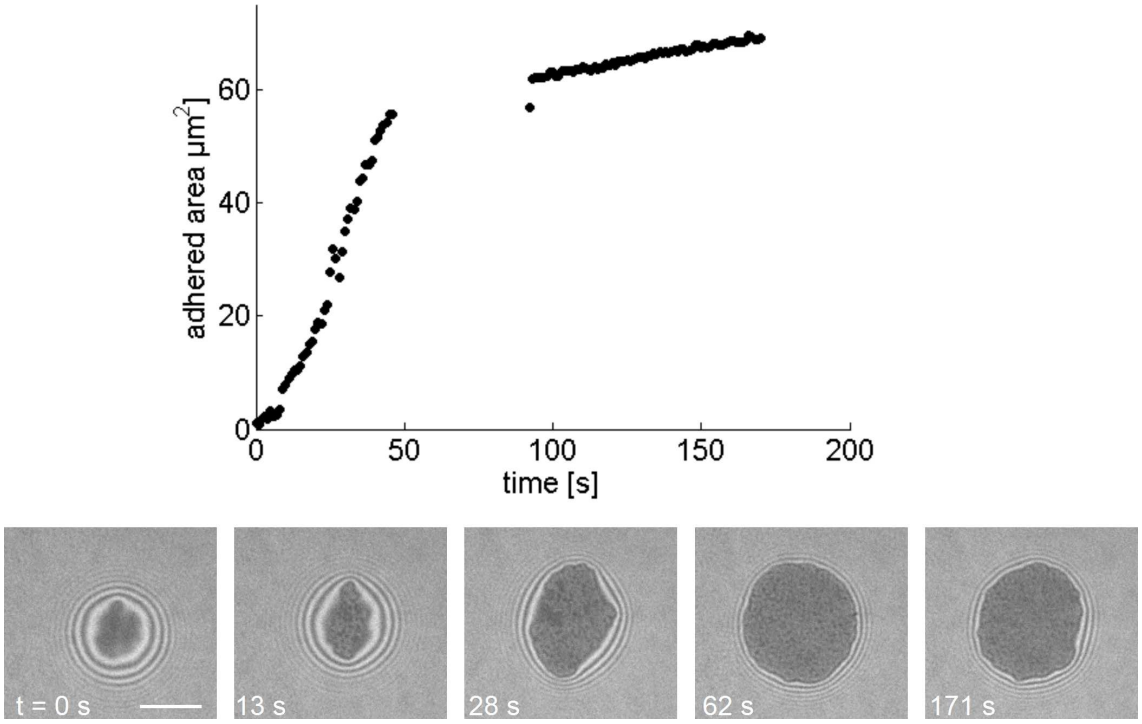

Figure 5.6: Adhesion process of vesicle No. 2 (1% GUV and 1% SLB) with low fluctuation amplitude. The RICM images represent characteristic states and the plot shows the corresponding area vs. time curve. Scale bar: 10 μm.

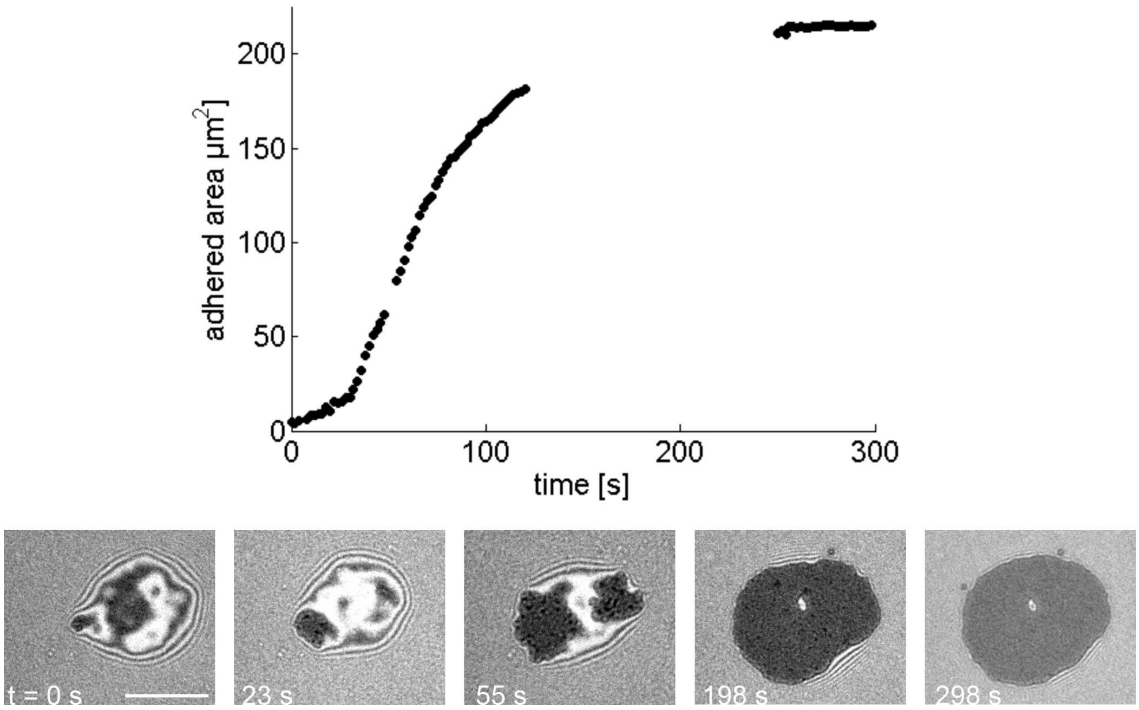

Figure 5.7: Adhesion process of vesicle No. 3 (1% GUV and 5% SLB) with low fluctuation amplitude. The RICM images represent characteristic states and the plot shows the corresponding area vs. time curve. Scale bar: 10 μm.

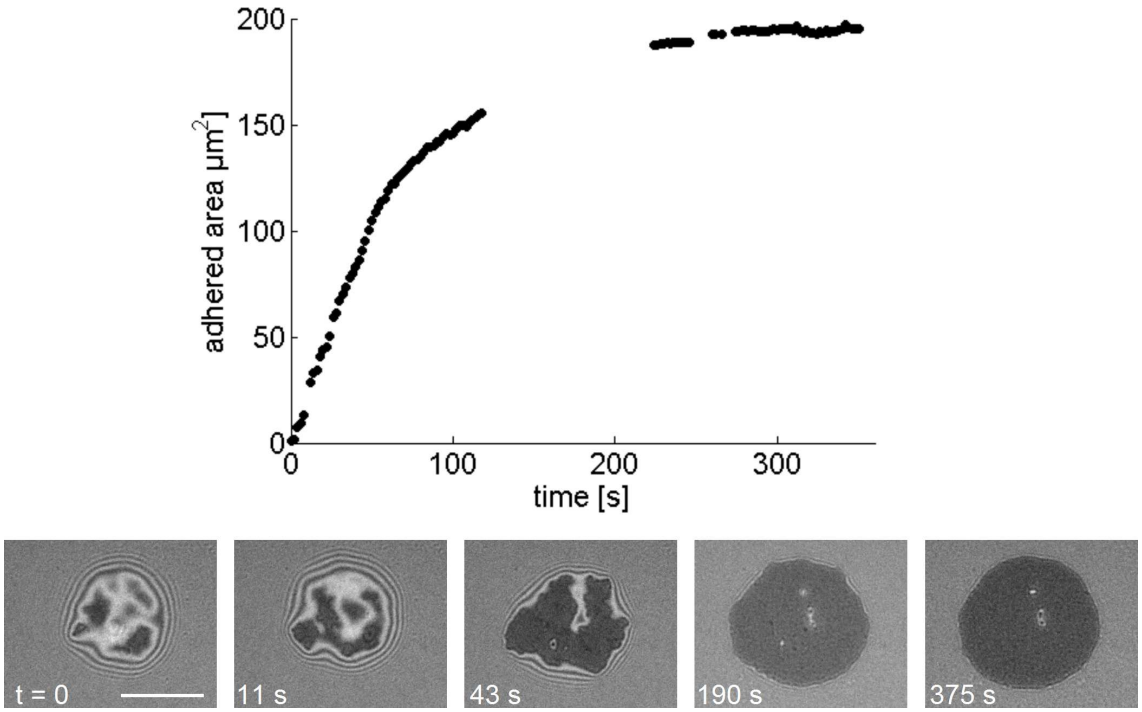

Figure 5.8: Adhesion process of vesicle No. 4 (1% GUV and 5% SLB) with low fluctuation amplitude. The RICM images represent characteristic states and the plot shows the corresponding area vs. time curve. Scale bar: 10 μm.

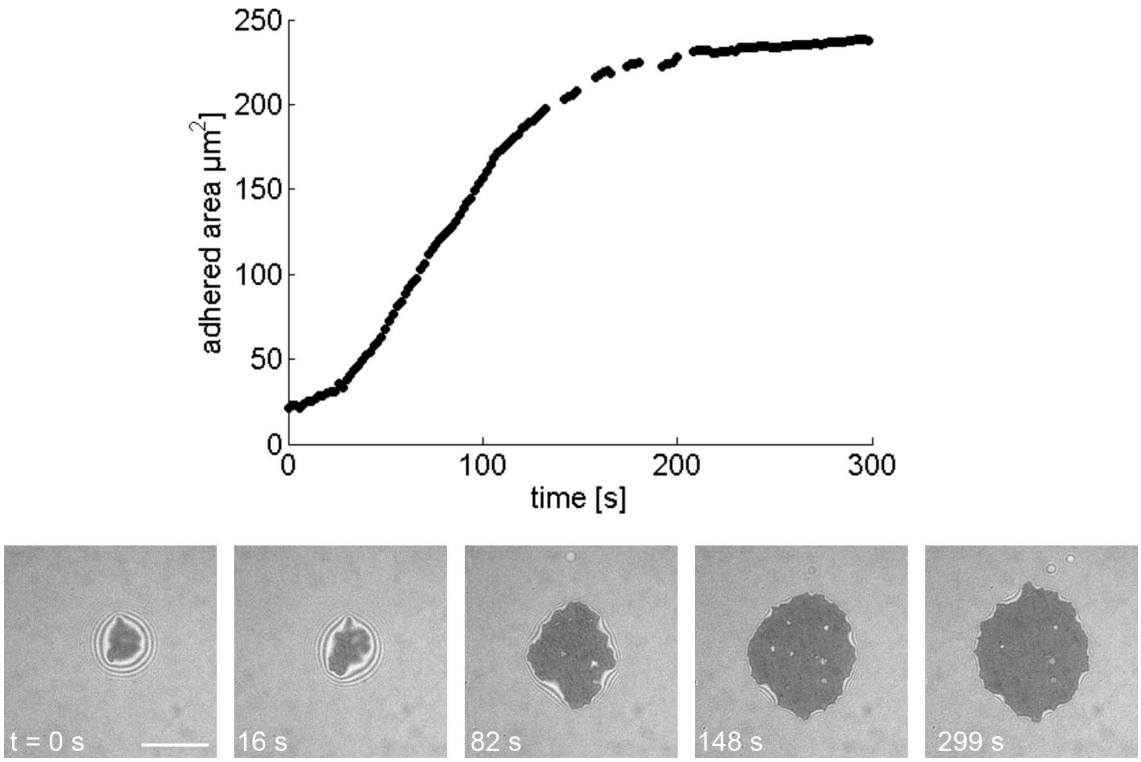

Figure 5.9: Adhesion process of vesicle No. 5 (2% GUV and 5% SLB) with low fluctuation amplitude. The RICM images represent characteristic states and the plot shows the corresponding area vs. time curve. Scale bar: 10 μm.

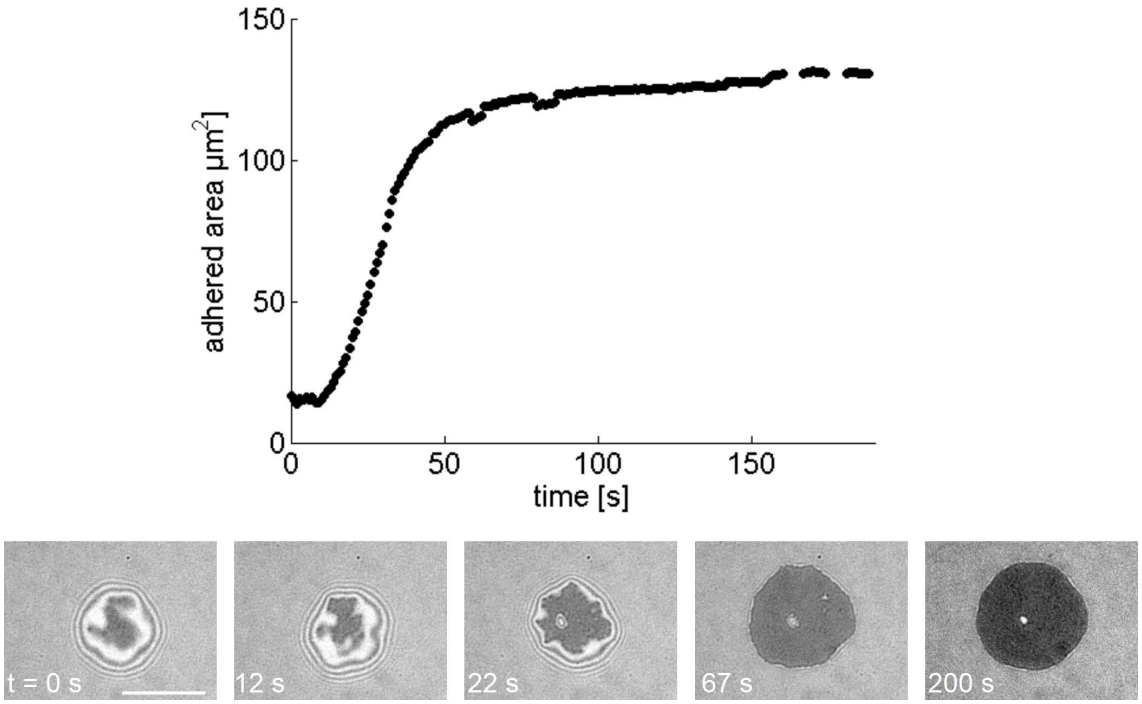

Figure 5.10: Adhesion process of vesicle No. 6 (2% GUV and 5% SLB) with low fluctuation amplitude. The RICM images represent characteristic states and the plot shows the corresponding area vs. time curve. Scale bar: 10 μm.

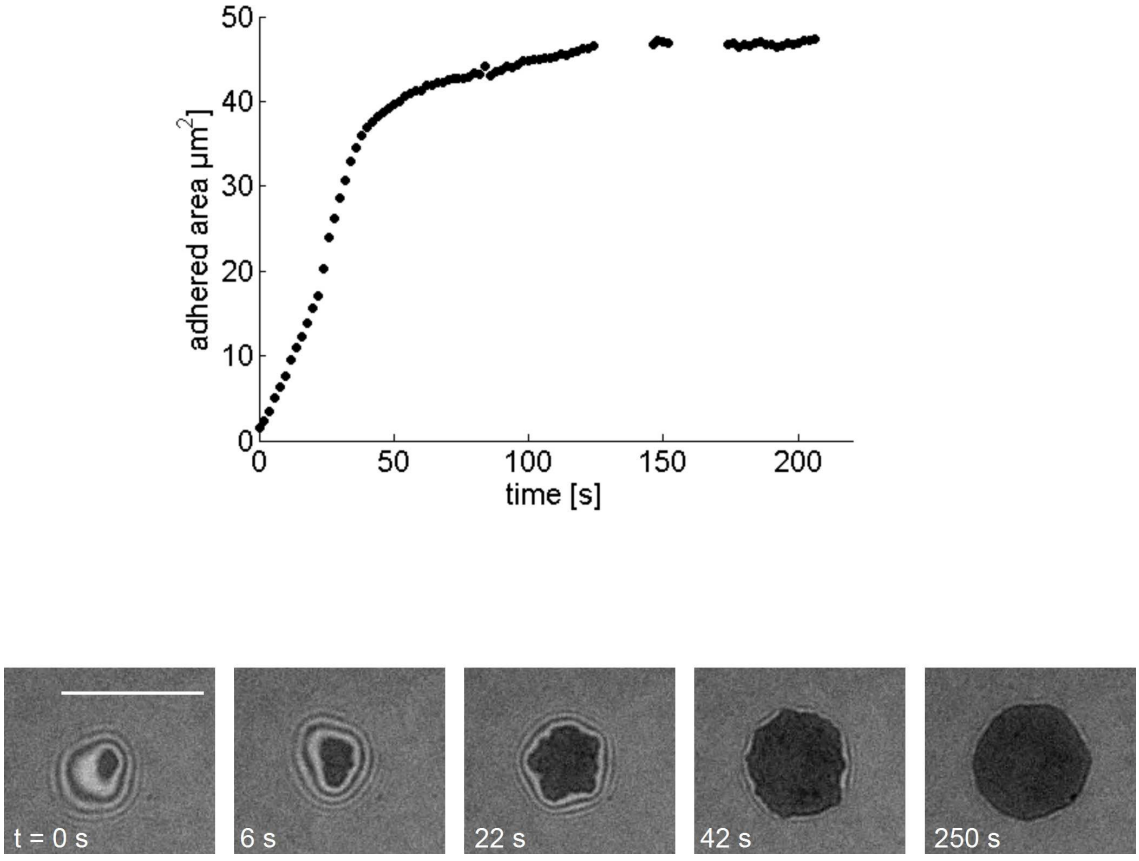

Figure 5.11: Adhesion process of vesicle No. 7 (2% GUV and 5% SLB) with low fluctuation amplitude. The RICM images represent characteristic states and the plot shows the corresponding area vs. time curve. Scale bar: 10 μm.

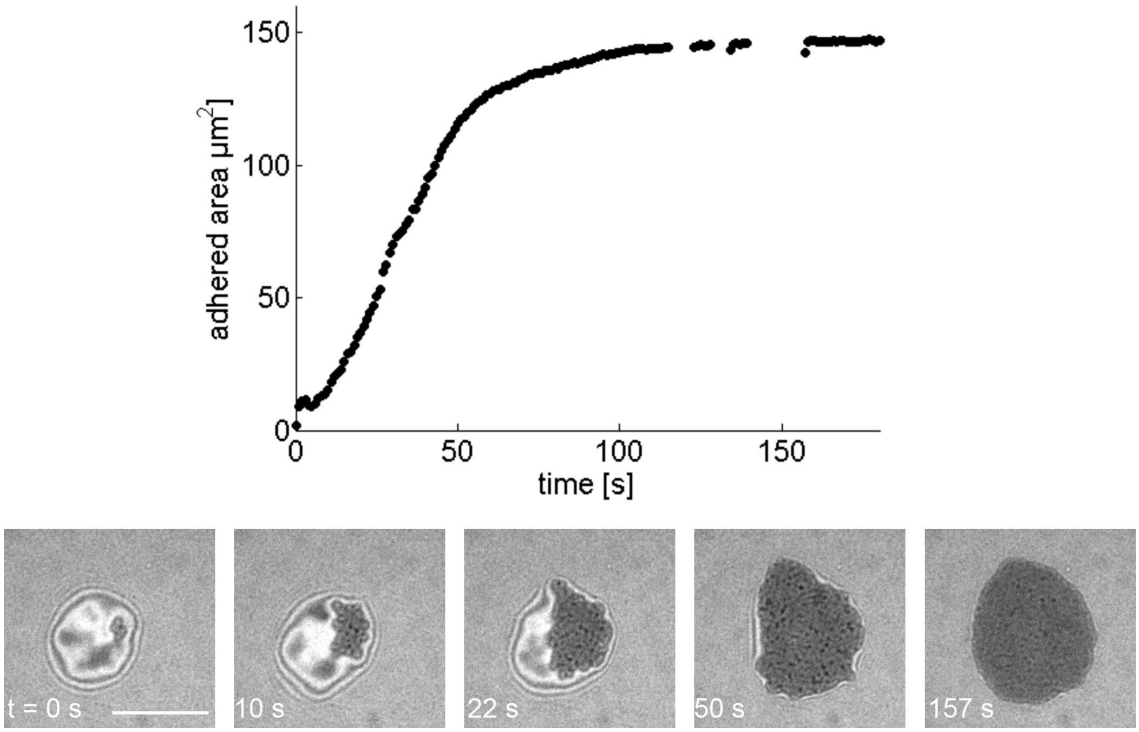

Figure 5.12: Adhesion process of vesicle No. 8 (2% GUV and 5% SLB) with low fluctuation amplitude. The RICM images represent characteristic states and the plot shows the corresponding area vs. time curve. Scale bar: 10 μm.

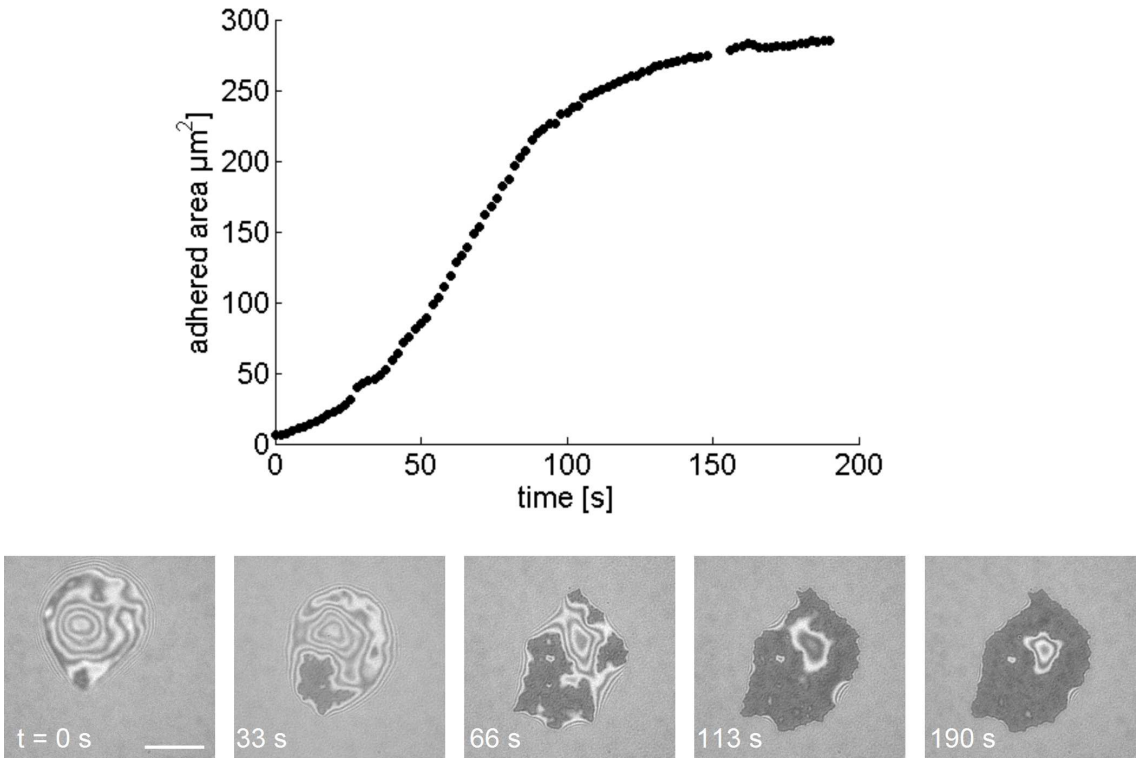

Figure 5.13: Adhesion process of vesicle No. 9 (1% GUV and 1% SLB) with high fluctuation amplitude. The RICM images represent characteristic states and the plot shows the corresponding area vs. time curve. Scale bar: 10 μm.

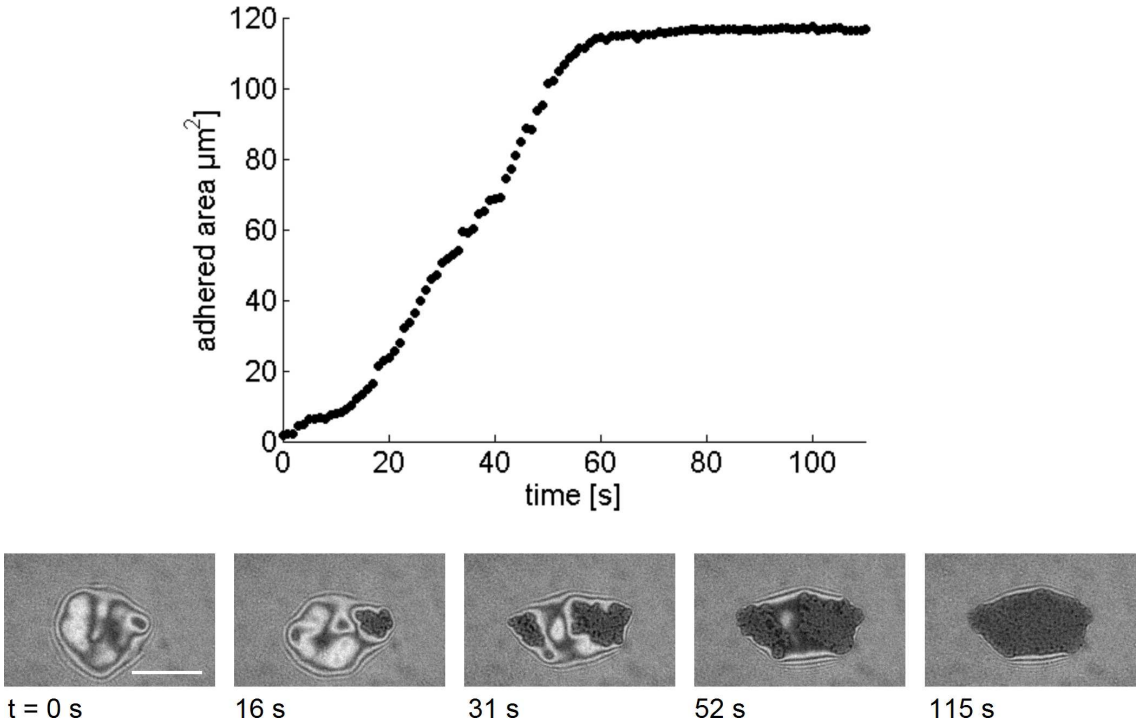

Figure 5.14: Adhesion process of vesicle No. 10 (1% GUV and 1% SLB) with high fluctuation amplitude. The RICM images represent characteristic states and the plot shows the corresponding area vs. time curve. Scale bar: 10 μm.

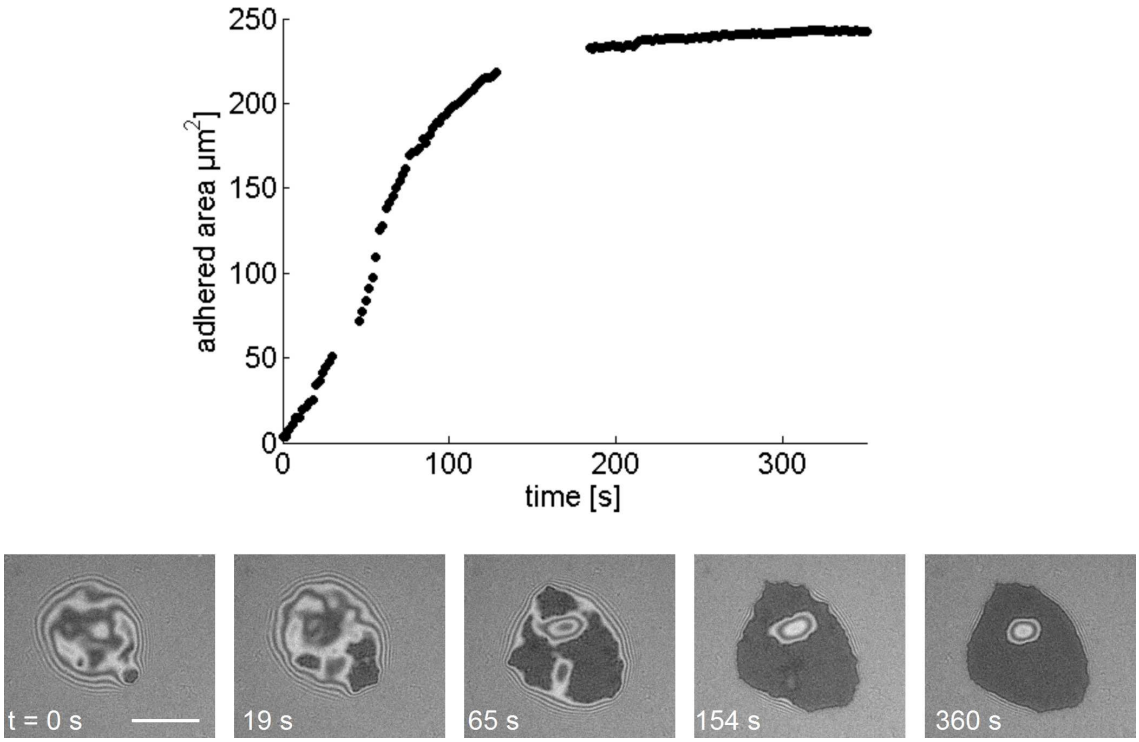

Figure 5.15: Adhesion process of vesicle No. 11 (1% GUV and 1% SLB) with high fluctuation amplitude. The RICM images represent characteristic states and the plot shows the corresponding area vs. time curve. Scale bar: 10 μm.

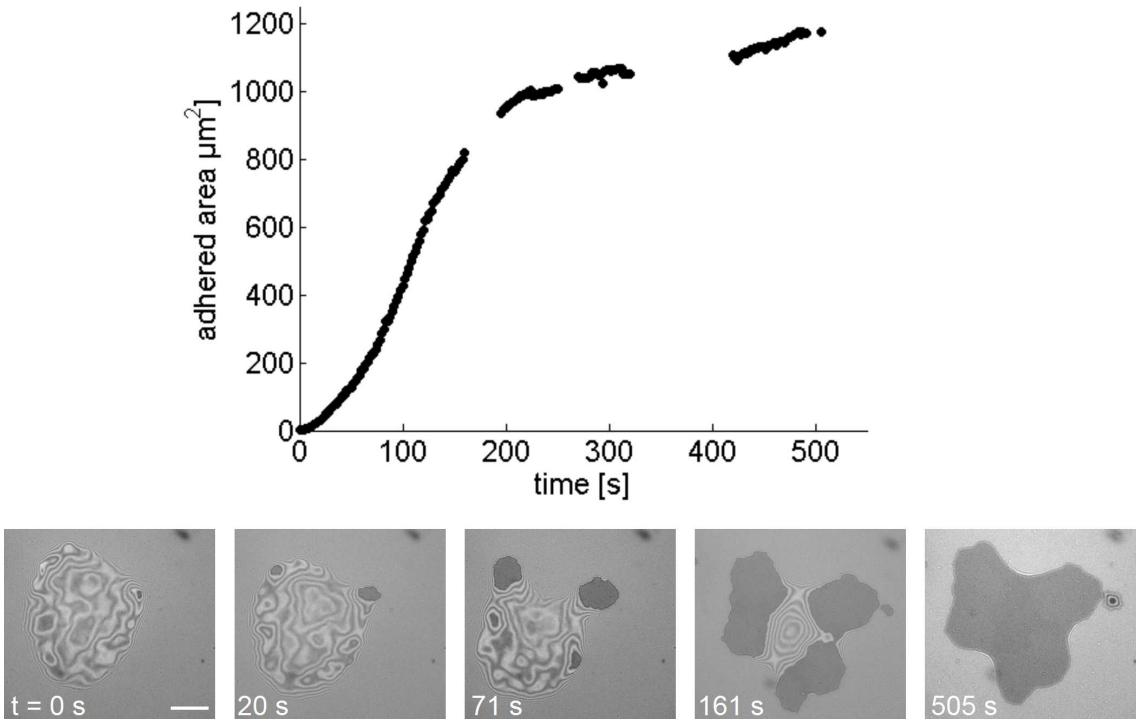

Figure 5.16: Adhesion process of vesicle No. 12 (1% GUV and 1% SLB) with high fluctuation amplitude. The RICM images represent characteristic states and the plot shows the corresponding area vs. time curve. Scale bar: 10 μm.

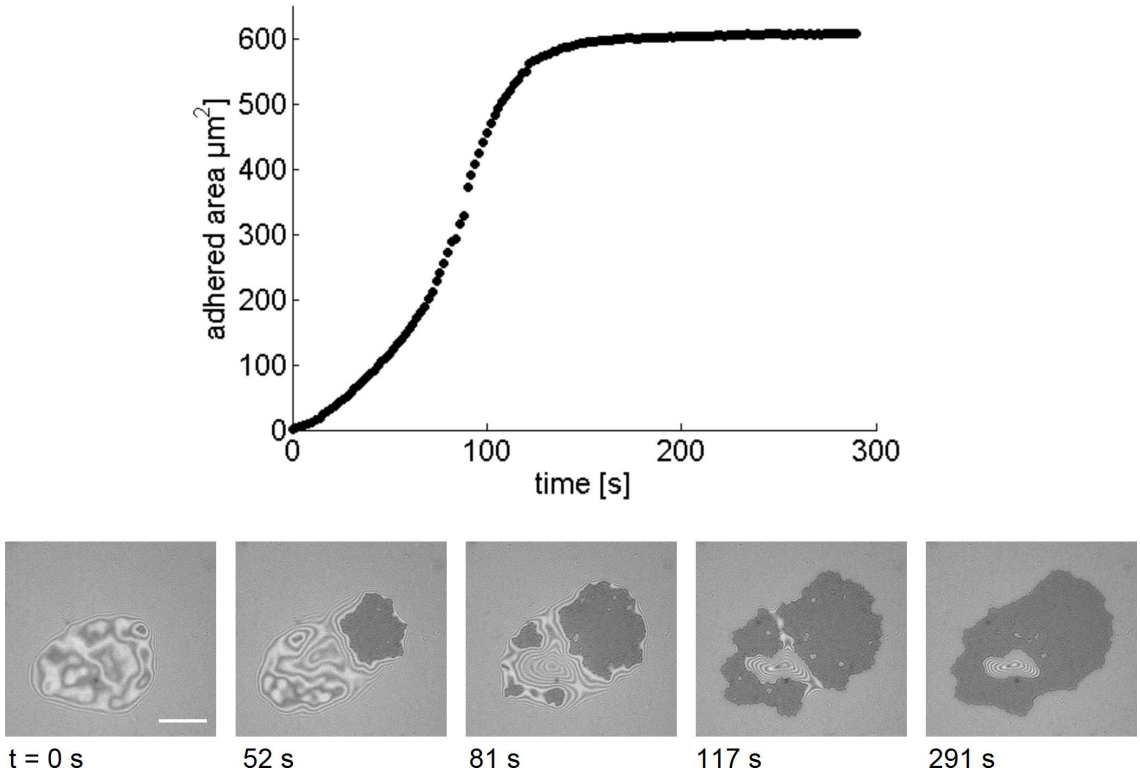

Figure 5.17: Adhesion process of vesicle No. 13 (1% GUV and 5% SLB) with high fluctuation amplitude. The RICM images represent characteristic states and the plot shows the corresponding area vs. time curve. Scale bar: 10 μm.

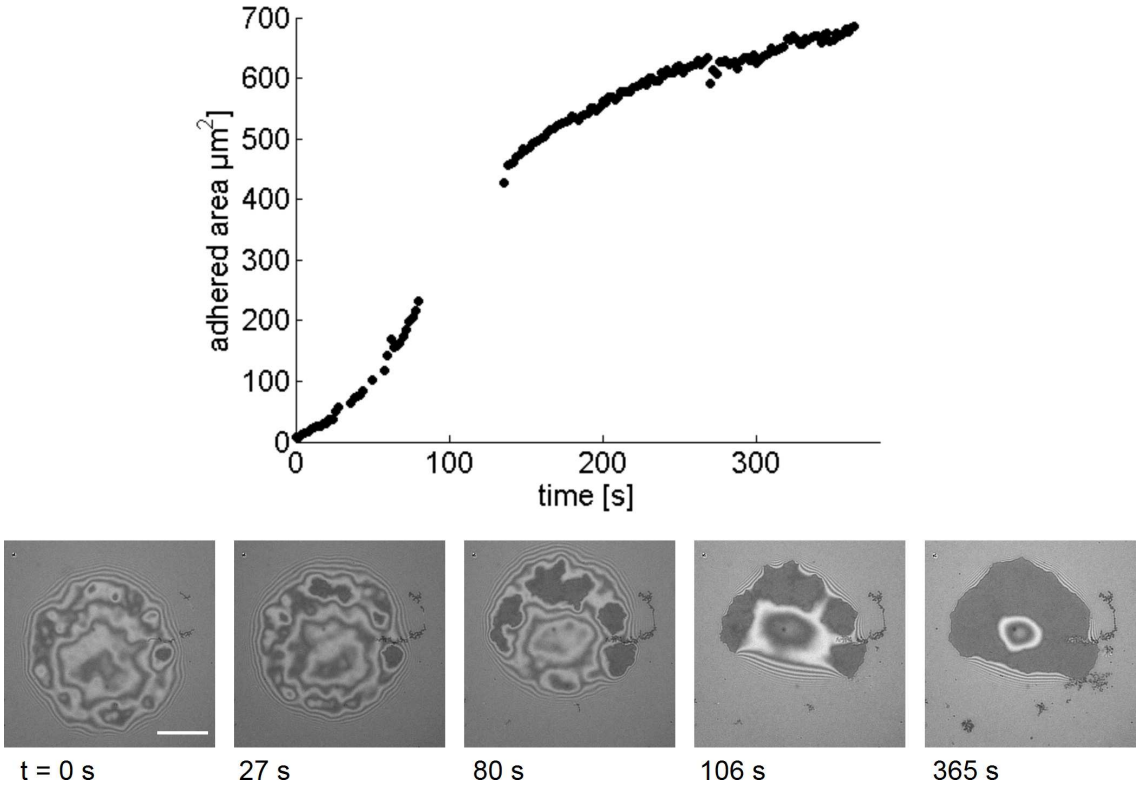

Figure 5.18: Adhesion process of vesicle No. 14 (1% GUV and 5% SLB) with high fluctuation amplitude. The RICM images represent characteristic states and the plot shows the corresponding area vs. time curve. Scale bar: 10 μm.

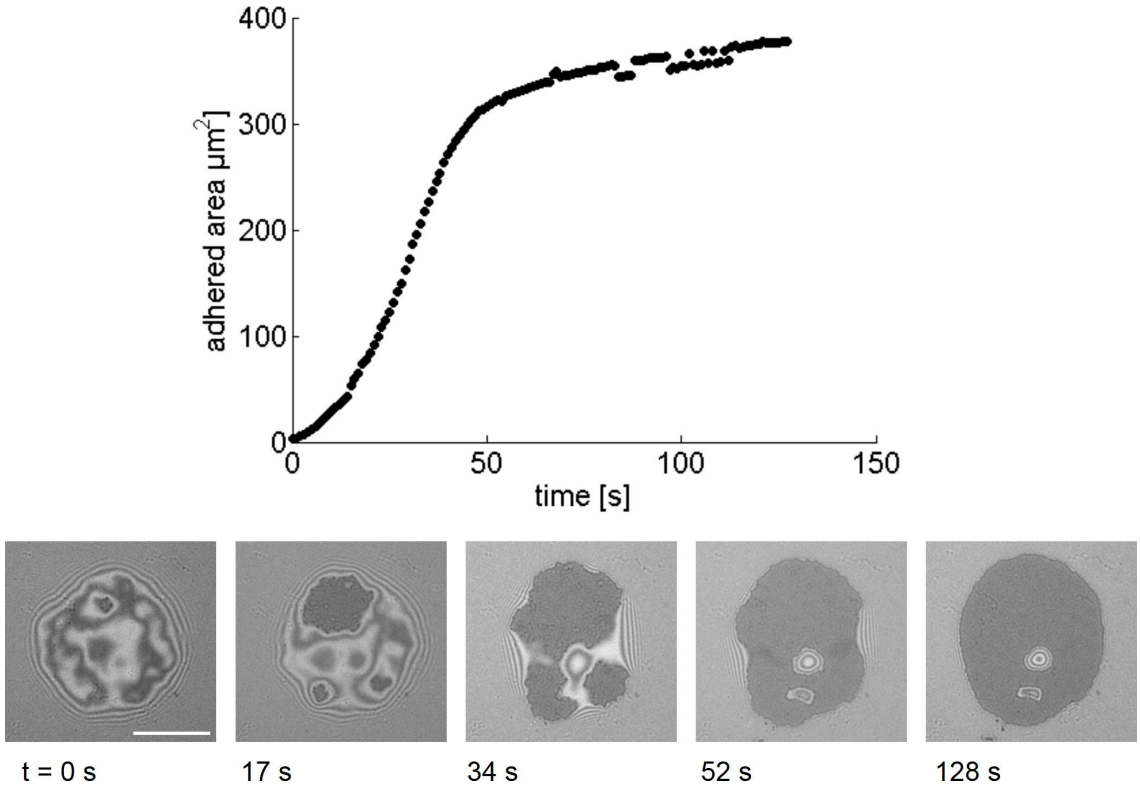

Figure 5.19: Adhesion process of vesicle No. 15 (1% GUV and 5% SLB) with high fluctuation amplitude. The RICM images represent characteristic states and the plot shows the corresponding area vs. time curve. Scale bar: 10 μm.

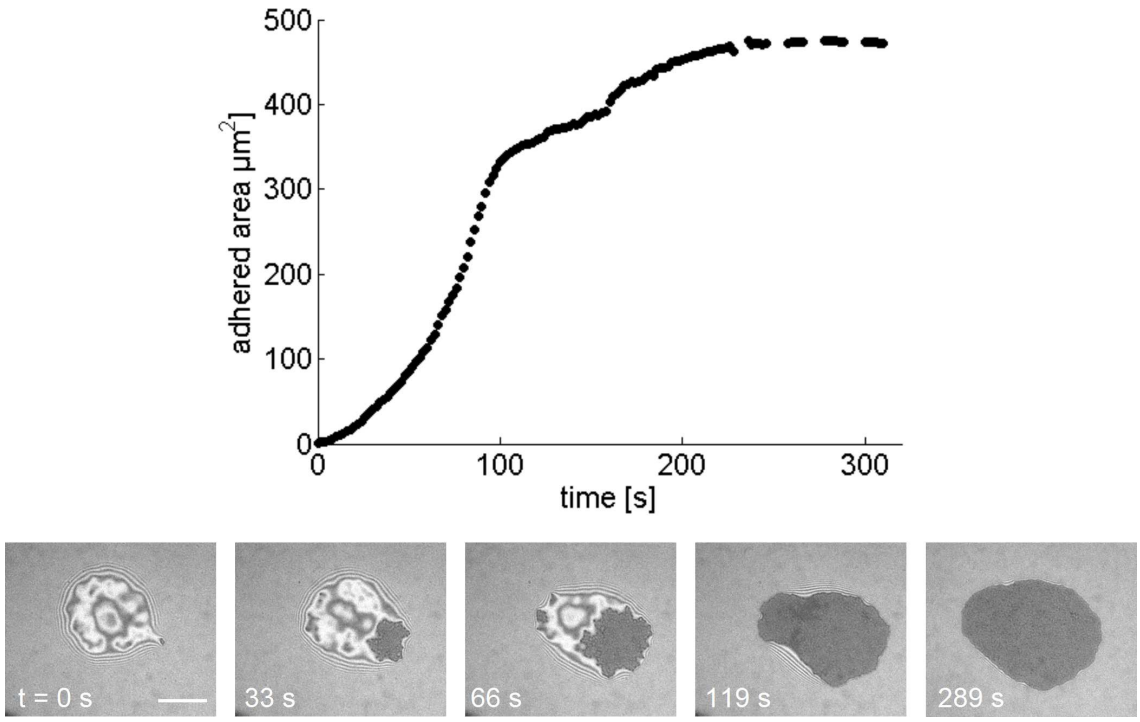

Figure 5.20: Adhesion process of vesicle No. 16 (2% GUV and 5% SLB) with high fluctuation amplitude. The RICM images represent characteristic states and the plot shows the corresponding area vs. time curve. Scale bar: 10 μm.

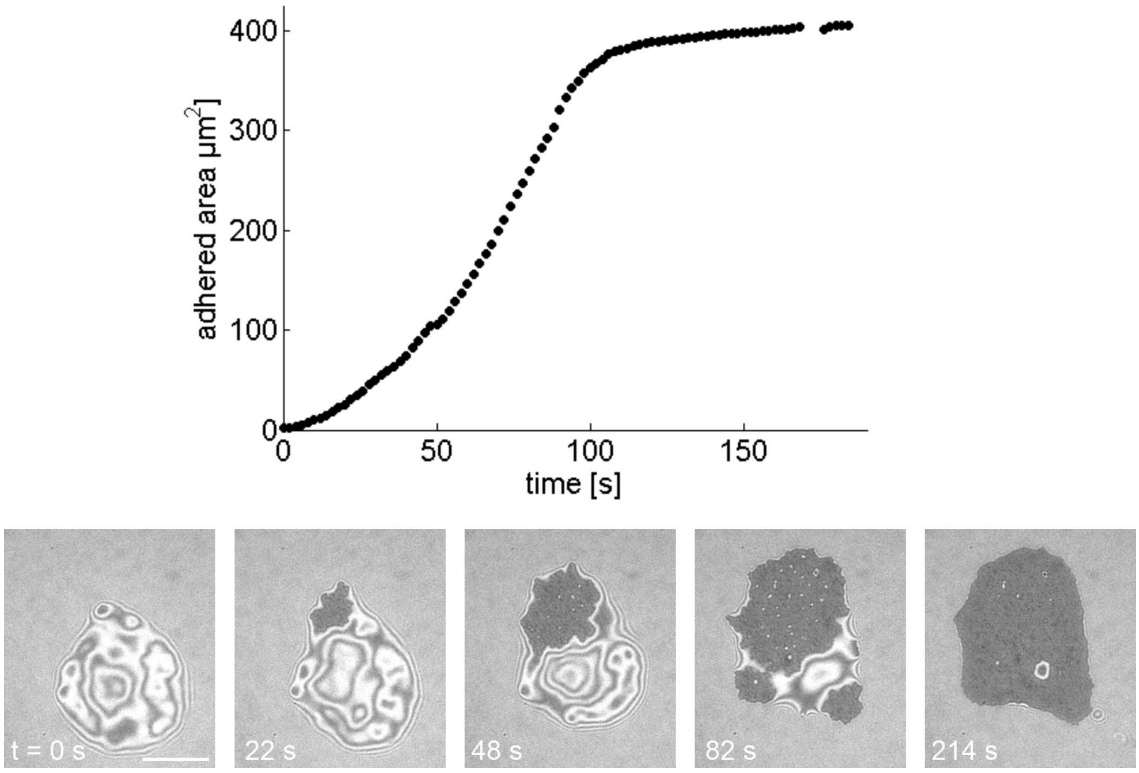

Figure 5.21: Adhesion process of vesicle No. 17 (2% GUV and 5% SLB) with high fluctuation amplitude. The RICM images represent characteristic states and the plot shows the corresponding area vs. time curve. Scale bar: 10 μm.

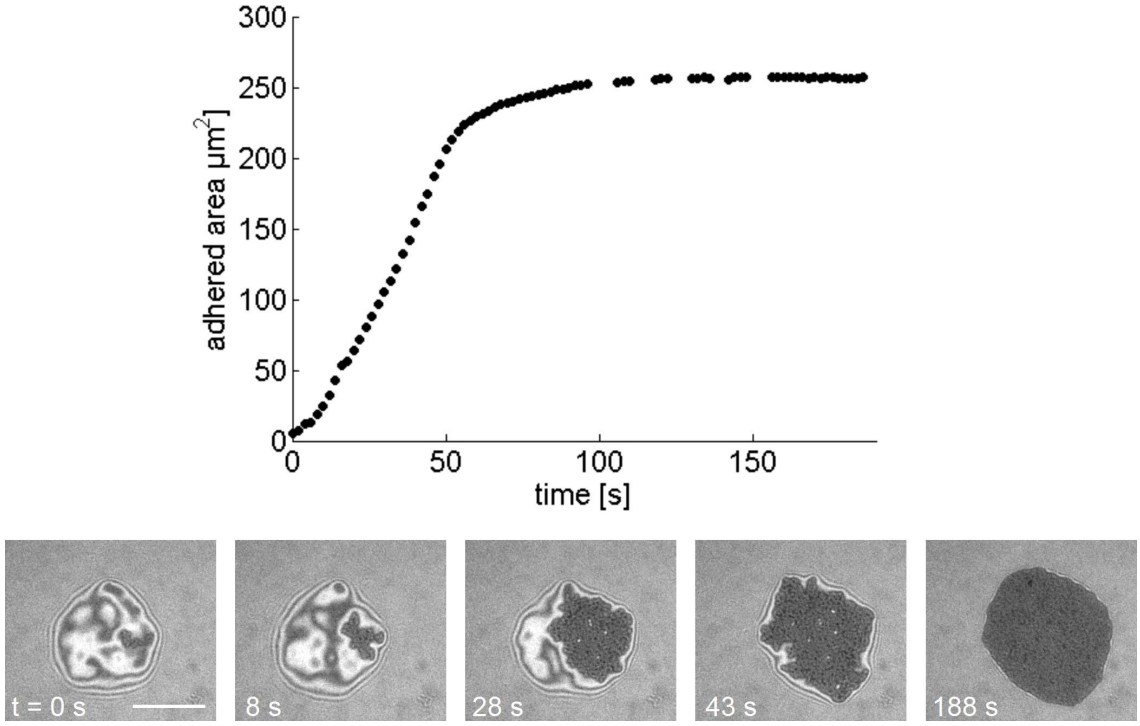

Figure 5.22: Adhesion process of vesicle No. 18 (2% GUV and 5% SLB) with high fluctuation amplitude. The RICM images represent characteristic states and the plot shows the corresponding area vs. time curve. Scale bar: 10 μm.

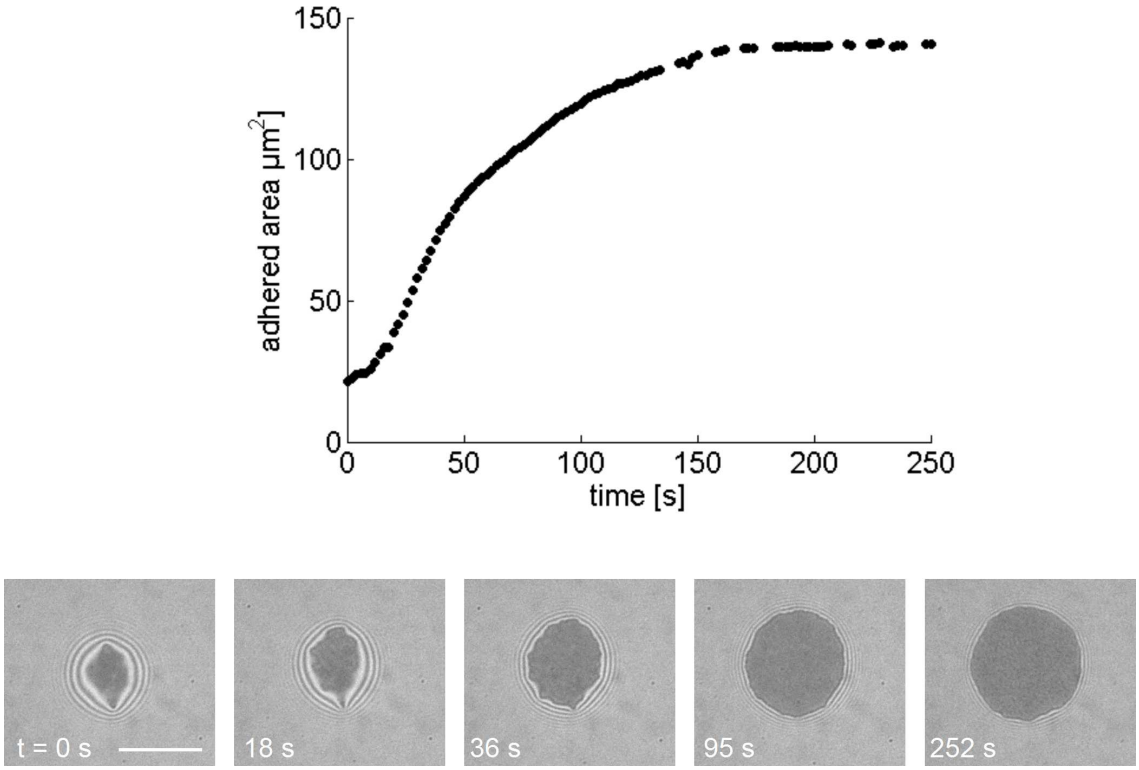

Figure 5.23: Adhesion process of vesicle No. 19 (2% GUV and 5% SLB) with high fluctuation amplitude. The RICM images represent characteristic states and the plot shows the corresponding area vs. time curve. Scale bar: 10 μm.

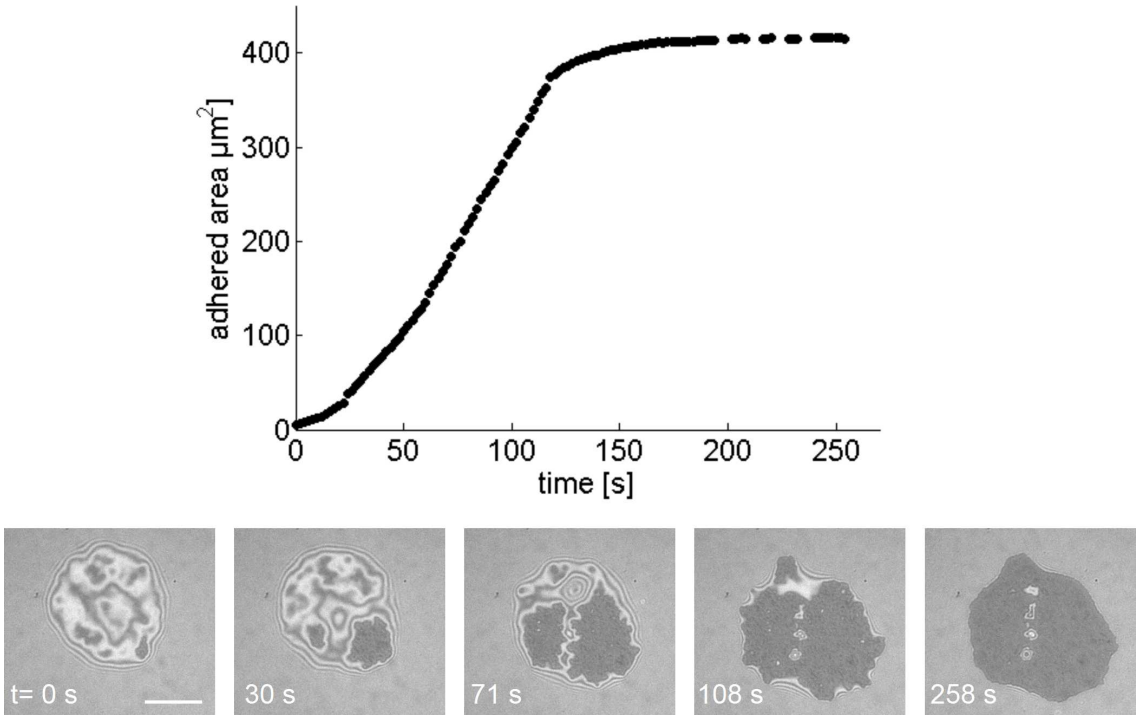

Figure 5.24: Adhesion process of vesicle No. 20 (2% GUV and 5% SLB) with high fluctuation amplitude. The RICM images represent characteristic states and the plot shows the corresponding area vs. time curve. Scale bar: 10 μm.

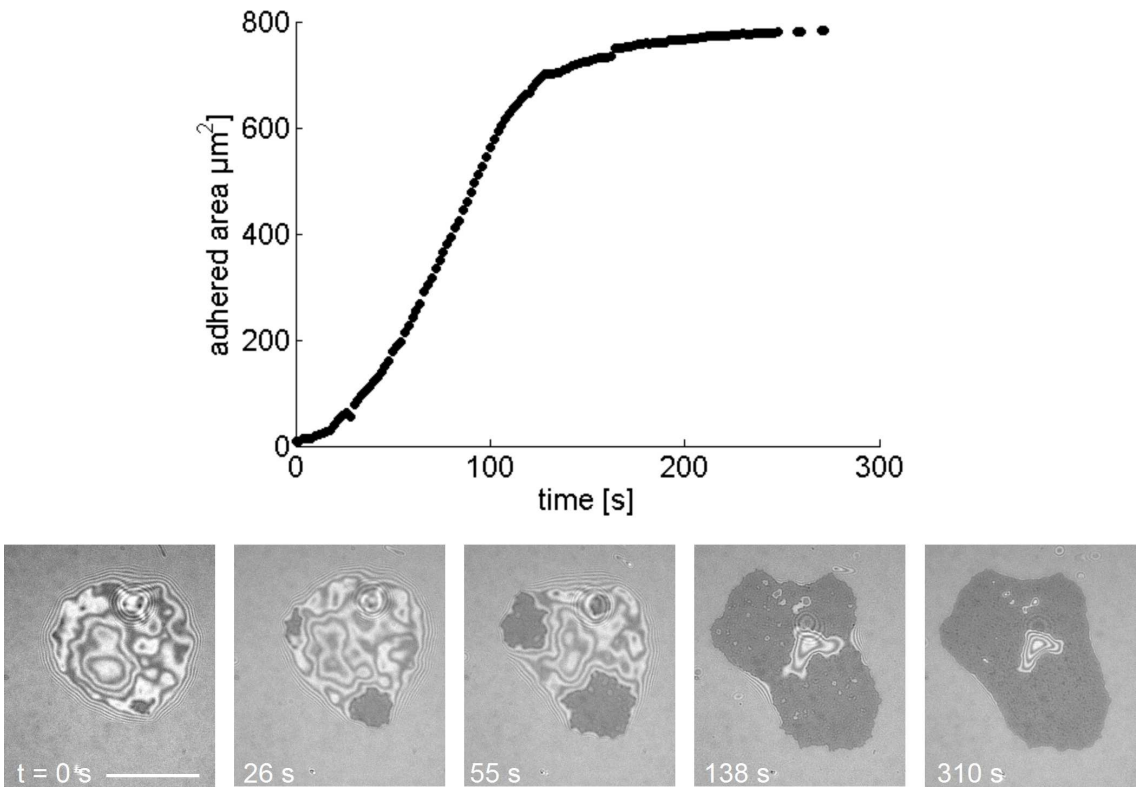

Figure 5.25: Adhesion process of vesicle No. 21 (2% GUV and 5% SLB) with high fluctuation amplitude. The RICM images represent characteristic states and the plot shows the corresponding area vs. time curve. Scale bar: 10 μm.

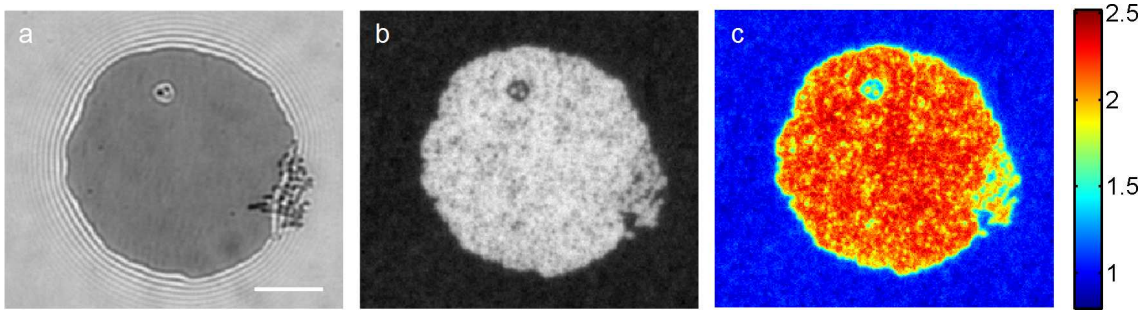

Figure 5.26: Neutravidin distribution in the adhered state. a: RICM image, b: Fluorescence image, c: Fluorescence map in units background. Scale bar: 5 μm.

5.3.1.3 Fluorescence Analysis

After the vesicles completed the adhesion process the distribution of the neutravidin-OG receptor in the adhesion disc was studied. Figure 5.26 shows one exemplary vesicle (2% GUV on 2% SLB). The fluorescent signal perfectly overlayed with the adhesion disc as seen in the RICM image. The receptors were distributed everywhere in the adhesion disc. Comparison of the intensity in the background far away from the vesicle with the intensity beneath the adhering vesicle revealed full accumulation till 5% (see also Section 4.2.1.2). Neither the degree of accumulation nor the size of the accumulated area increased further after the adhesion process stopped. Thus, in the limit of high receptor-ligand concentrations, the membrane adhesion and receptor accumulation proceeded simultaneously.

5.3.2 E-cadherin-E-cadherin: Limit of Weak Binding

Nine adhesion processes were recorded with the model system where specific binding was mediated by Ecad on the vesicle and the bilayer. All experiments except for one were carried out with GUVs containing 1% NTA lipids on SLBs containing 1% NTA lipids. In the single experiment the GUV as well as the SLB contained 5% NTA lipids. Again, the GUVs did not exhibit uniform behavior but three types of adhesion processes were observed. Figures 5.27-5.30 show the RICM micrographs of characteristic stages for each vesicle.

I. Most of the vesicles (five out of nine, including the 5% GUV 5% SLB case) adhered in a nucleation and growth manner with few nucleation centers (2, 2, 2, 3, 7).

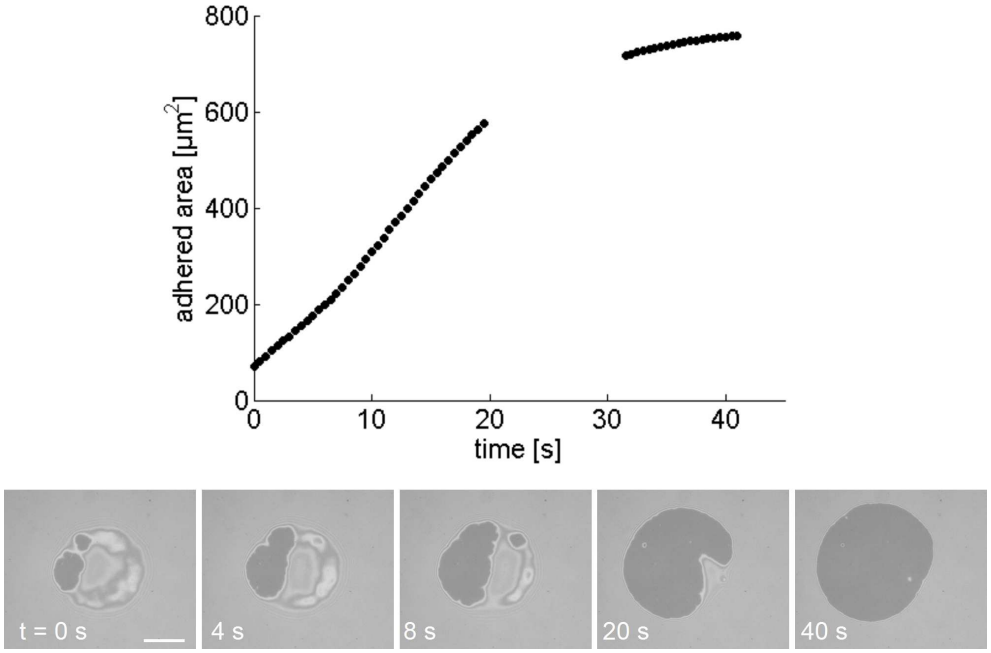

Figure 5.27: Ecad mediated adhesion process of a type I vesicle (1% GUV and 1% SLB). The RICM images represent characteristic states and the plot shows the corresponding area vs. time curve. Scale bar: 10 μm.

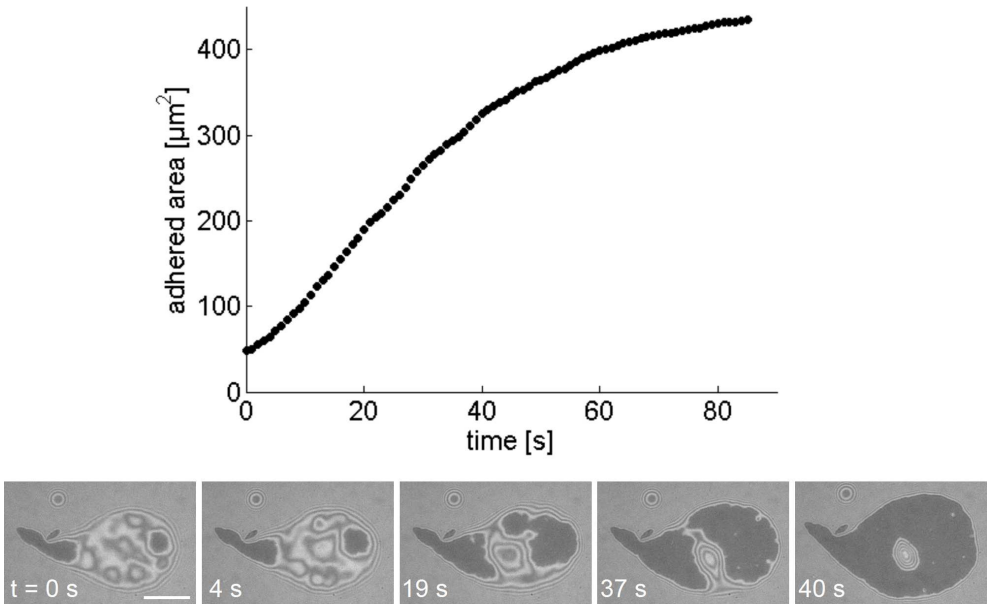

Figure 5.28: Ecad mediated adhesion process of a type I vesicle (1% GUV and 1% SLB). The RICM images represent characteristic states and the plot shows the corresponding area vs. time curve. Scale bar: 10 μm.

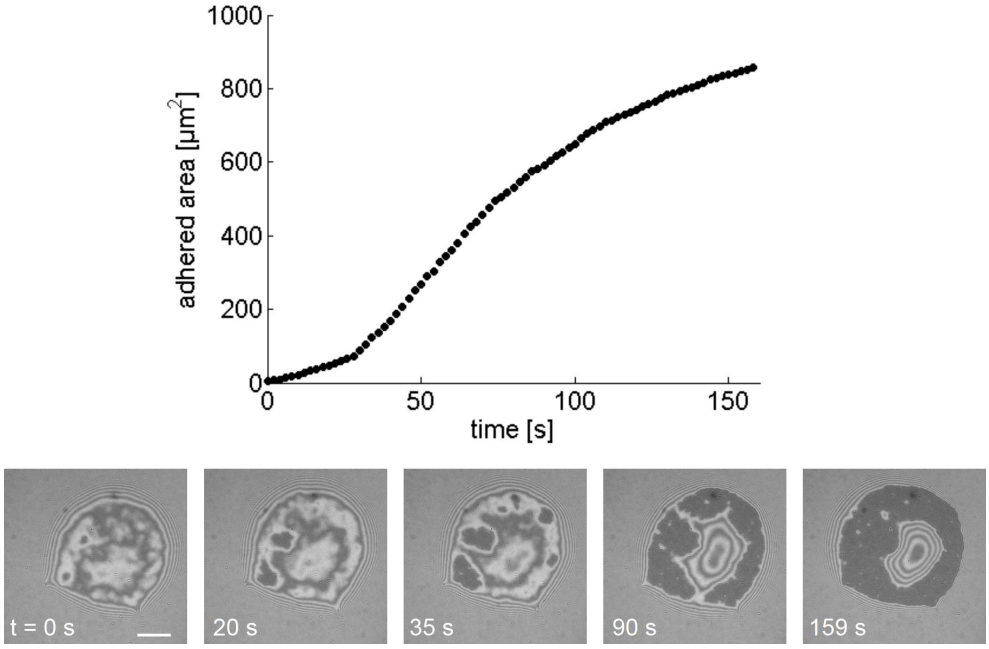

Figure 5.29: Ecad mediated adhesion process of a type I vesicle (1% GUV and 1% SLB). The RICM images represent characteristic states and the plot shows the corresponding area vs. time curve. Scale bar: 10 μm.

For these cases area vs. time curves have been constructed when the process was mapped appropriately. They are displayed in Figures 5.27-5.29 together with the RICM images. If this was not possible only the RICM images are shown (see Figure 5.30 a+b). Fluctuation analysis of the nucleation center building process revealed a hotspot as already described for floppy vesicles in the strong binding scenario.

II. Two vesicles adhered without formation of pronounced nucleation centers (Figure 5.30 e+f). Initially the GUV was pinned at one (or more) site(s). Then the whole membrane within the contact zone came down simultaneously and the pinning centers were retracted. The corresponding area vs. time curve showed a fast increase, a maximum and finally an on-going decrease. Thus, no stable adhesion was established in these cases. Comparison of RICM images and fluctuation maps in early stages yielded coincidence of grey patches in RICM and suppressed fluctuations. Figure 5.31 shows an example where one smeared out grey area in RICM corresponded to two small bond clusters visible in the fluctuation map representation (marked with white arrow). The clusters merged and formed one stable adhesion patch close to the pinning center. This patch still looked grey in RICM. Most probably an ensemble of dilute bonds pins the membrane at several sites while the main part was

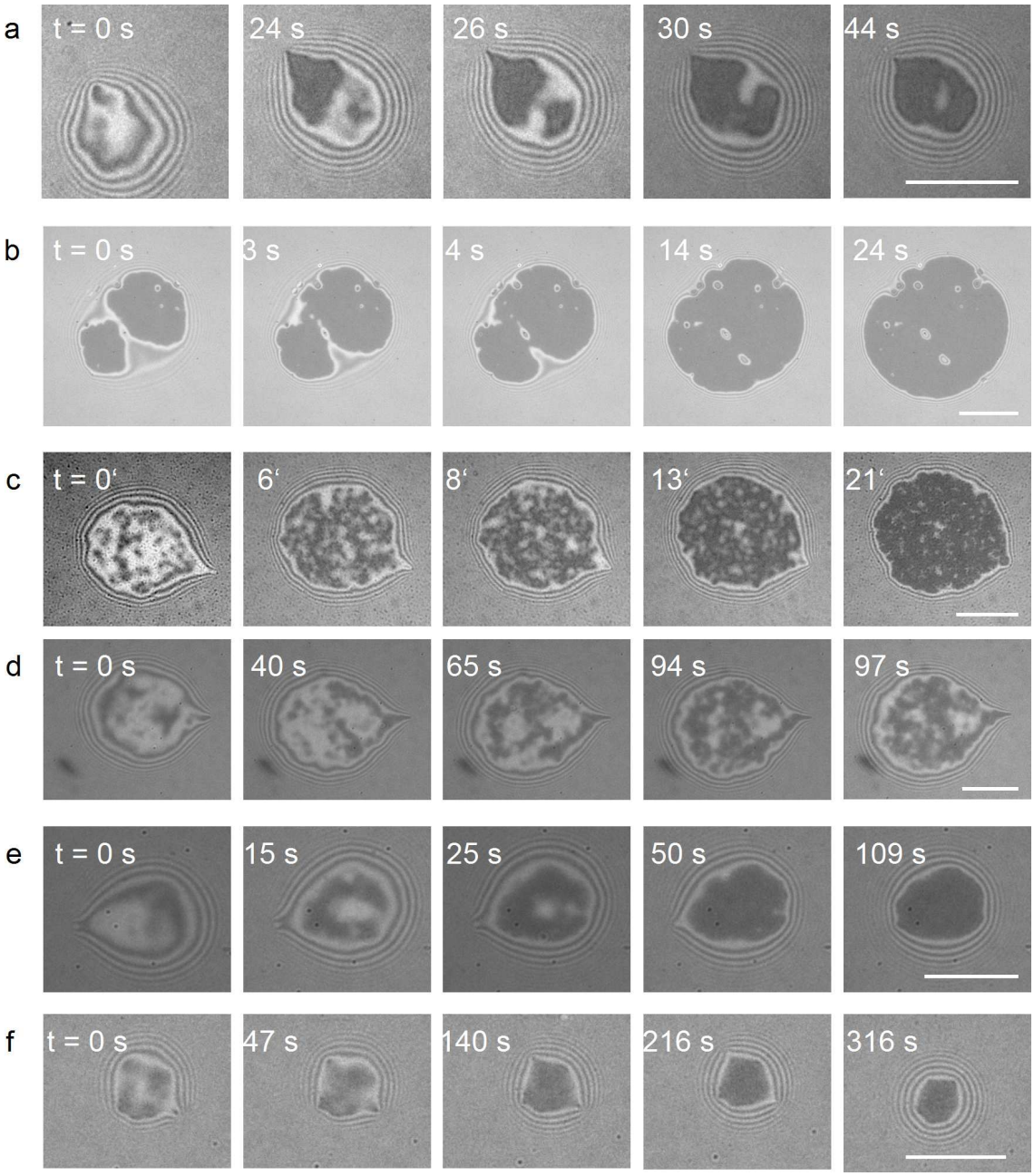

Figure 5.30: Ecad mediated adhesion process: a+b type I vesicle, c+d type III vesicle and e+f type II vesicle. All vesicles except a belong to the 1% GUV and 1% SLB group, a: 5% GUV and 5% SLB. Scale bar: 10 μm.

still further away from the substrate. Throughout the contact zone several frozen patches appeared but not all of them were stable over time.

III. The third type of adhesion process was characterized by an abundance of small nucleation centers (see Figure 5.30 c+d). Here, the fluctuation map was similar to the type two vesicles, but this time full adhesion was successfully established. All three types of vesicles were observed within one sample. Analysis of the mean fluctuation amplitude ($A_{mean} = 1.9$), size of the contact zone ($\frac{d_{CZ}}{d_{PC}} = 0.3$), and extent of spreading ($\frac{d_{ADH}}{d_{PC}} = 0.4$) did not reveal obvious differences.

In summary, the model system with weak binders showed a broad spectrum of adhesion behavior. Due to the weakness of the bonds (2 k_BT) the system was very sensitive to small changes in physical or chemical parameters (e.g. of the reduced volume). The competition between membrane adhesion and fluctuation was almost balanced. As a result, at concentrations of 1% NTA in the GUV and SLB, stable adhesion was not always achieved. The 5% GUV 5% SLB case showed undisturbed nucleation and growth. Most of the other vesicles did not reach full saturation within the observation period, two even started to deadhere. This behavior was also observed with the strong binding model system at very low receptor-ligand concentrations (see Chapter 6).

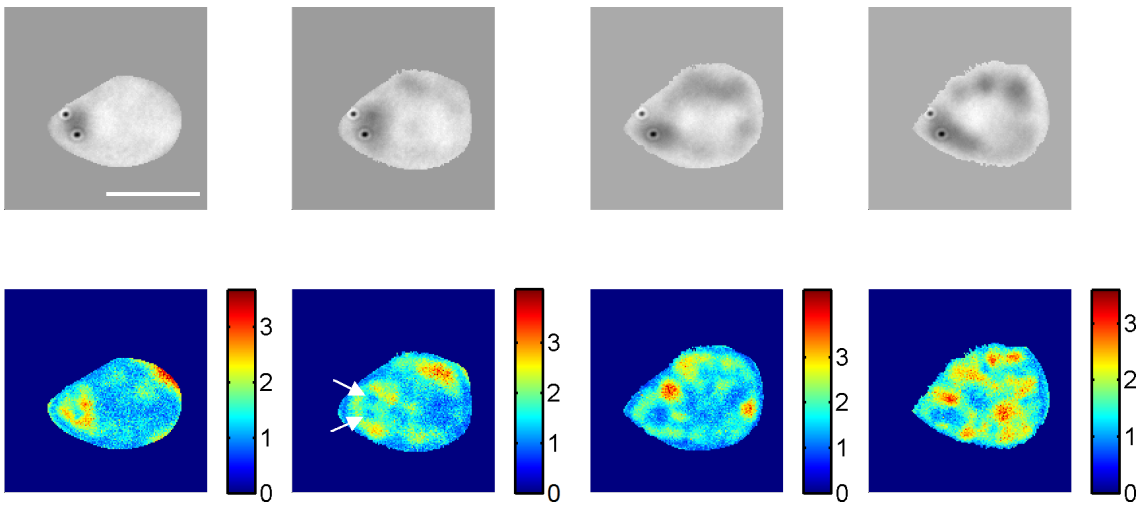

Figure 5.31: Fluctuation analysis of early states of a weakly adhering vesicle. Upper row: Mean RICM micrograph, lower row: Fluctuation map in units noise. Arrows point at the bond clusters. Each frame represents an average over two seconds. Subsequent successive time steps are shown. Scale bar: 10 μm. The prominent black dots in the RICM images are dirt particles on the camera.

5.4 Conclusion

In this Chapter the dynamics of vesicle adhesion mediated by mobile-receptor ligand pairs were studied for weak and strong binding pairs. In the case of strong binding the adhesion process followed the classical pattern of nucleation, linear growth and saturation. It was shown that the reduced volume of the vesicle and the resulting fluctuation amplitude of the vesicle membrane influenced the adhesion process in all three stages. Vesicles exhibiting large fluctuations were found to establish multiple nucleation centers and consequently their area vs. time curves were characterized by a steeper slope. While the high number of NCs accelerated the growth regime, saturation was retarded by the competing NCs and the resulting high probability for trapped bubbles.

Variation of the receptor and ligand concentrations revealed the influence of mobile receptor-ligand pairs on the adhesion dynamics. Increasing the receptor concentration on the bilayer resulted in accelerated growth but also in retarded saturation because at high concentrations the receptors were immobilized by jamming. Due to the small size of the ligands, increasing the ligand concentration in the vesicle membrane was not accompanied by reduced mobility, and therefore the overall adhesion process was accelerated.

In the case of weak binding, the adhesion process was predominantly classical as described above, but in addition two different types of adhesion dynamics, characterized by either only dilute bonds or an abundance of small NCs, respectively, were observed. This was interpreted as a sign for the sensitivity of the system to small environmental changes.

Chapter 6

Vesicle Adhesion: Limit of Low Receptor/Ligand Concentrations

This section presents the results obtained for vesicle adhesion at low concentrations of receptors and ligands in the model system biotin/avidin. Low concentrations span the region from 0.1% to 1% biotinylated lipids in both the vesicle and the bilayer. Due to the weakness of the Ecad bond this region no adhesion is observed.

6.1 Experimental Realization and Analysis Details

6.1.1 Experimental Realization

An overview of the dynamics of the adhesion process was obtained by scanning the whole sample in randomly chosen places. To map the complete adhesion process image acquisition started directly after vesicle addition and ended when the vesicles completed adhesion or latest after three hours. Thus, the whole vesicle ensemble contributed to one area vs. time curve that was representative for the given concentration and was based on good statistics. Table 6.1 gives an overview of the different biotin concentration combinations of bilayer and vesicle studied.

Surprisingly, at these low biotin concentrations the observation process usually

Table 6.1: Concentration of biotinylated lipids in SLB and GUV. Crosses mark the combinations studied.

SLB \ GUV	0.1%	0.5%	1%
0.1%	x		x
0.25%			x
0.5%		x	
1%	x	x	x

interfered with the adhesion process. Therefore, different different experimental techniques were required in comparison to high concentrations . It was not possible to observe and record one vesicle during the whole adhesion process. Attempts to do so failed. The observed vesicle did not adhere but if the sample was scanned in several positions it turned out that (depending on the observation time) all other vesicles started to adhere or adhered in the meantime. Reasons for this behavior could be either local heating or photochemical destruction. If the focused illumination light locally heated the sample, the temperature difference with the remaining parts of the sample created a flux that retarded membrane adhesion in the case of diluted bonds. On the other hand, the illumination light could also directly interact with the components of the model system. Due to the relatively low radiation pressure of the source (for example in comparison to laser illumination) it is not very likely that the protein will be denaturated and destroyed. But the ester bonds connecting the phosphate group of the lipid head and the carboxyl group of the lipid chains within the SLB are easily hydrolyzed. Thus, the head and chain of the lipid are separated and negatively charged. They remain within the membrane and act like detergents. As a consequence, the membrane is softened and fluctuates with a larger amplitude. These enhanced undulations prevent adhesion at low receptor concentrations. The effect is probably negligible when the concentration is high and therefore the interaction is strong.

6.1.2 Analysis Details

Determination of the adhesion state of each vesicle was done based on the fluctuation analysis described in Section 3.2.2. A fluctuation map in units noise was created and all pixels with a fluctuation amplitude of less than 1.5·noise were treated as adhered. Their position was used to build an adhesion mask indicating the adhered regions. All pixels inside the mask were summed up and compared with the size of the contact zone (for the definition of contact zone see Section 3.2). The portion of adhered area was calculated relative to the size of the contact zone and is termed relative adhesion area (RA) in the following. If the vesicles adhered with 95% of the contact zone their state was termed completely adhered. Micrographs of neutravidin-TMR were evaluated by means of accumulation maps with respect to the background intensity of the SLB. Depending on the acquisition mode (simultaneous or sequential, see also Section 3.1.1) the signal-to-noise ratio varied quite a bit. Thus, no global threshold was set, but the threshold was adjusted to the quality of the image. To elucidate the role of the vesicle size in the adhesion process the vesicles were grouped in three categories: I. small vesicles with a diameter of maximum 25 μm, II. normal vesicles with a diameter between 25 and 35 μm and III. large vesicles with a diameter of more than 35 μm.

Figure 6.1 illustrates the usefulness of fluctuation maps as an additional source of information on the adhesion state of vesicles. The RICM micrograph (a) shows an adhering vesicle with a bubble in the adhesion disc. Comparison of the fluctuation (b) and the fluorescence map (c) distinctly shows that the areas where neutravidin is accumulated adhere tightest and show least fluctuations. Moreover, there are regions with intermediate fluctuation amplitude that appear adhered in RICM and free regions exhibiting the highest fluctuation amplitudes. Thus, fluctuation analysis yields a more detailed view of the membrane adhesive states. In addition, it allows to deduce information on the receptor distribution that could not be inferred from the RICM image solely.

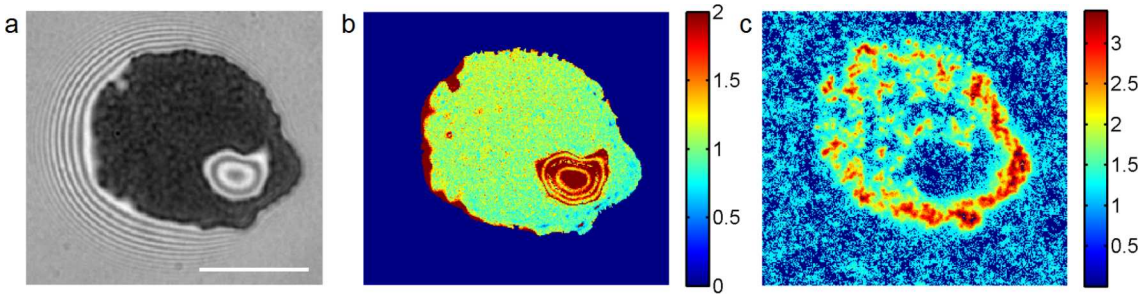

Figure 6.1: Fluctuation Analysis. a: RICM micrograph of an adhering vesicle, b: Fluctuation map in units noise, c: Fluorescence map in units background. Scale bar: 10 μm.

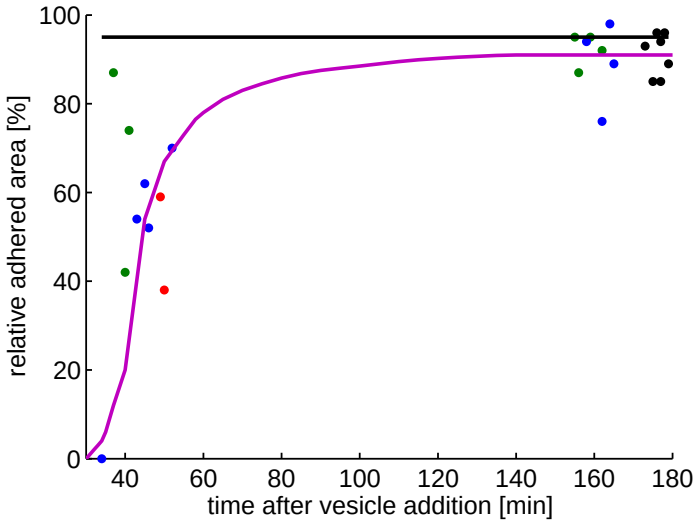

Figure 6.2: Growth curve of the adhered area relative to the contact zone. The concentration of biotinylated lipids was 0.1% in the GUV as well as in the SLB. green (blue, red) dots: Vesicles from category I (II, III), black line: Limit 95%, purple line: Guideline for the eye.

6.2 Results and Discussion

6.2.1 Adhesion Behavior: 0.1% vesicle - 0.1% bilayer

The combination with the lowest concentration of receptor (neutravidin) on the SLB and ligand (biotin) in the GUV corresponded to 0.1% biotinylated lipids in both membranes (Please note that two biotins bind one neutravidin, see Section 4.2.1.3). In this experiment one vesicle was observed for $\sim$ 30 minutes and did not adhere. Scanning the sample for 20 more minutes revealed vesicles in different adhesion states with RA ranging from 40% to 90% (see Figure 6.2). Small vesicles adhered earlier than large vesicles but none of the vesicles adhered completely after

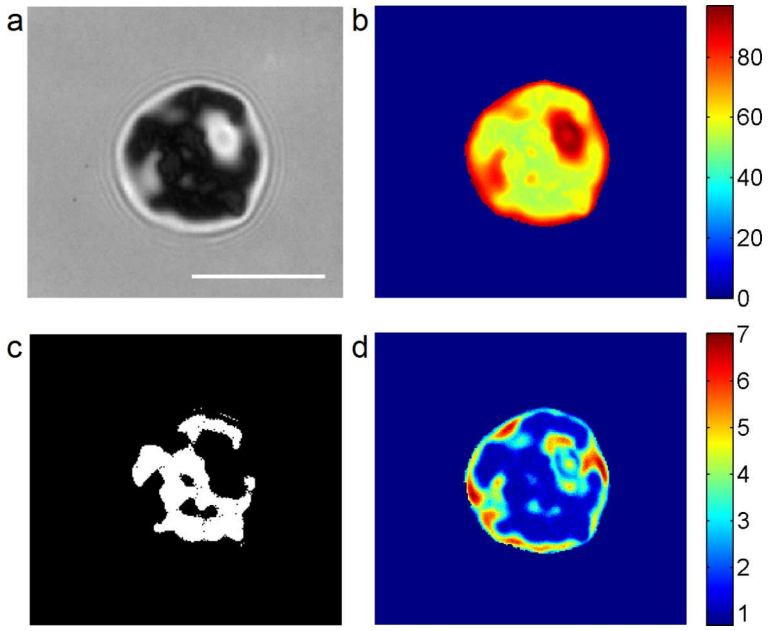

Figure 6.3: 0.1% GUV on 0.1% SLB (early). a: RICM micrograph, b: Height in nm, c: Adhesion mask, d: Fluctuation map in units noise. The scale bar is valid for all images: 10 μm.

50 minutes. The vesicles resided at mean heights of 60-70 nm and exhibited fringes as well as fluctuations (Figure 6.3 shows an exemplary vesicle). Three hours after the addition of vesicles the sample was scanned again. Independent of their size the vesicles showed a broad range of adhesion states: 74% - 98% RA. Only 6 out of 16 vesicles adhered completely even at this late time. All vesicles retained their fringes and a fluctuating rim, but all except one now exhibited a black rim and resided at distinctly lower heights (∼10 nm) in the adhesion zone (see Figure 6.4). In this experiment the nucleation process was not mapped and it was not clear when saturation began. But it could be concluded that at long times the vesicles reached a final state that was in most cases not complete adhesion: ∼90% of the contact zone was adhered.

In the second observation period seven vesicles were studied not only with RICM but also with fluorescence microscopy. The fluorescence micrographs mapped the receptor distribution in the adhesion zone. They showed neutravidin accumulation in a ring along the outer edge of the adhesion zone while the center remained clear (see Figure 6.4 e). Thus, the bond density in the center was similar to the receptor density on the SLB adjacent to the adhesion zone. These dilute bonds did not fix the vesicle membrane as efficiently as the accumulated bonds. As a result the membrane

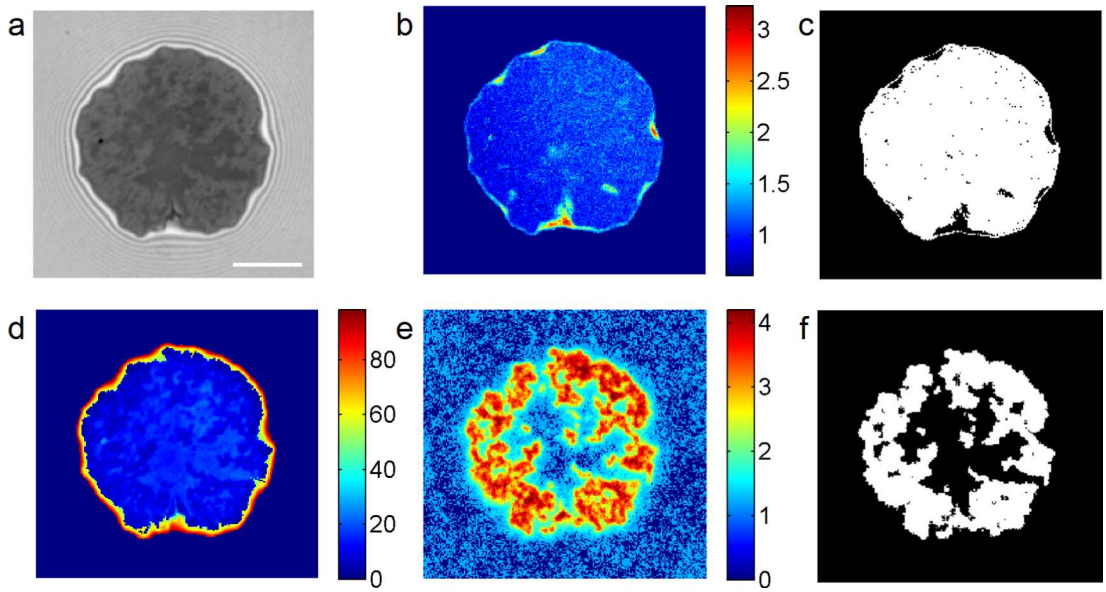

Figure 6.4: 0.1% GUV on 0.1% SLB (late). a: RICM micrograph, b: Fluctuation map in units noise, c: Adhesion mask (threshold 1.5), d: Height in nm, e: Fluorescence map in units background, f: Accumulation mask (threshold 2.7). The scale bar is valid for all images: 5 μm.

goes up in between the bonds and exhibits a slightly higher distance from the SLB as can be slightly seen in the corresponding height map (see Figure 6.4 d). The area with accumulated fluorescence was calculated relative to the adhered area. It did not increase with time and scattered around values of 60%. From the accumulation experiments done to infer the neutravidin concentration on the SLB in the adhesion disc (see Section 4.2.1.2), a final concentration of 5% was expected. For those experiment GUVs with a biotin concentration of 1% were employed. Here, with only 0.1% the achieved maximum concentration after 3 hours was 0.5% corresponding to a 5-fold increase with respect to the initial concentration on the SLB.

6.2.2 Adhesion Behavior: 1% vesicle - 0.1% bilayer

For the next scenario studied the concentration in the SLB was kept at 0.1%, but the concentration in the GUV was increased to 1%. Two data sets were recorded. In the first experiment (A) two vesicles were constantly observed for 40 minutes and did not adhere at all. Sampling of the whole preparation showed 1/3 of all vesicles already completely adhered after 50 minutes (see Figure 6.5). At t = 3

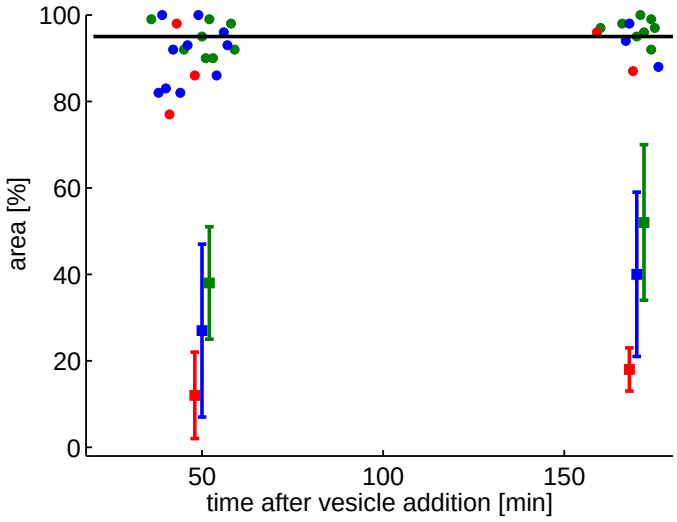

Figure 6.5: 1% GUV on 0.1% SLB. Comparison of the adhered area in RICM (dots) and the accumulated area in fluorescence (squares). Black line: Limit 95%. Green (blue, red): Vesicles from category I (II, III).

hours 1/3 of the vesicles were still not completely adhered. All vesicles were also recorded in the fluorescence mode. The percentage of the area with accumulated fluorescence with respect to the contact zone scattered quite a bit even within one vesicle category (see Figure 6.5). The mean values for each category at t = 50 minutes were 38% (I), 27% (II), 12% (III). Exemplary vesicles for each case are displayed in Figure 6.6. The larger the area that was needed to be filled, the longer it took. The underlying process was of course identical in each case: diffusion of the receptor. The different values origin from the normalization with respect to the contact zone. The absolute areas covered after comparable times were of the same order. The exemplary vesicles in Figure 6.6 accumulated 140 (I), 160 (II) and 150 (III) μm^2. With increasing time the relative accumulated area also expanded. At t = 3 hours the following values were achieved: 52% (I), 40% (II), 18% (III) The spatial distribution of the fluorescent molecules was again predominately ring like (see previous section). Despite the expected final concentration of neutravidin (5%), only 0.9% were detected. Direct comparison of the RICM and fluorescence data clearly showed a time lag in the growth of the relative adhered and accumulated area with time (see Figure 6.5). The first vesicles adhered completely at t = 50 minutes. However, the accumulation was not yet complete even at t = 3 hours.

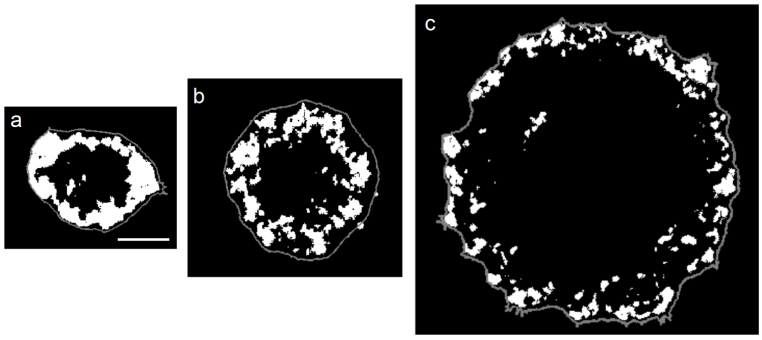

Figure 6.6: 1% GUV on 0.1% SLB. Neutravidin accumulation in the contact zone after 50 minutes. a: Small vesicle (category I, d = 20 μm, 45% accumulated), b: Medium vesicle (category II, d = 27 μm, 28% accumulated), c: Large vesicle (category III, d = 42 μm, 11% accumulated). The scale bar is valid for all images: 5 μm. The grey line depicts the edge of the contact zone.

Figure 6.7: 1% GUV on 0.1% SLB. Long term study of receptor accumulation. The fluorescence mask is given. Starting two hours after vesicle addition the vesicle was recorded once every hour. Please note, that the contact zone was still increasing. Scale bar: 5 μm.

Thus, the time lag was at least two hours.

In order to find out whether full accumulation is finally reached, one vesicle was observed over several hours. The sample was kept dark and imaged once every hour. On the timescale of two to seven hours after vesicle addition the vesicle still increased its contact area (from 40 μm^2 to 68 μm^2) and relative adhesion area (from 82% to 85%). The absolute accumulated area also rose (from 19 μm^2 to 23 μm^2, see Figure 6.7) but less than the contact zone or adhesion area. Hence, the relative accumulated area with respect to the contact zone (adhesion area) decreased from 48% to 34% (58% to 40%). The extent of accumulation did not further increase and the concentration stayed at 0.9%. Review of the sample after seven hours showed that only very small vesicles with diameters of less than 20 μm succeeded in filling the entire adhesion zone with fluorescent receptors.

Repetition of the experiment (B) and scanning from the very beginning allowed for

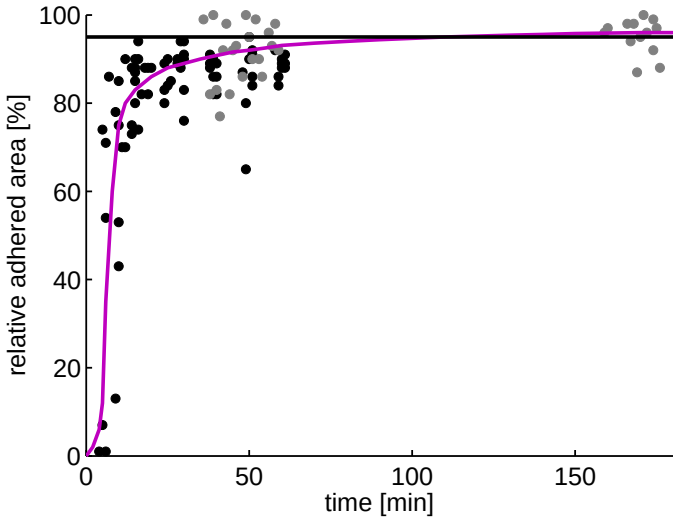

Figure 6.8: 1% GUV on 0.1% SLB. Overlay of both data sets. Gray dots: Experiment A, black dots: Repetition experiment B, black line: Limit 95%, purple line: Guideline for the eye.

good mapping of the nucleation and growth processes. Vesicles started to adhere 10 minutes after addition and increased their adhesion zone rapidly (see black dots in Figure 6.8). After 20 minutes the relative adhered area did not rise any more but the RA was scattered between 80% and 95% with completely adhered states occurring only rarely till t = 1 hour. Overlay of both data sets showed good overlap. It should be noted that the vesicles in the repetition experiment all belonged to the first category of small vesicles and consequently adhered readily. If the saturation time was judged from the overlay curve representing all categories it was determined to be ∼50 minutes. Nevertheless, 90% of the vesicles exhibited fringes till the end.

6.2.3 Adhesion Behavior: 0.1% vesicle - 1% bilayer

The next scenario with 0.1% lipids in the vesicle and 1% biotinylated lipids in the bilayer was also investigated in two experiments. The first experiment (A) failed to cover nucleation and growth appropriately (see grey dots in Figure 6.11). But for the first time the saturation time could be determined as no observed vesicle adhered with less than 95% of its contact zone after 45 minutes. The vesicles predominately adhered in a pinned mode. Initially, they had had a pinned shape that rounded off with increasing time (for examples see Figure 6.9). Exemplary fluorescence data of

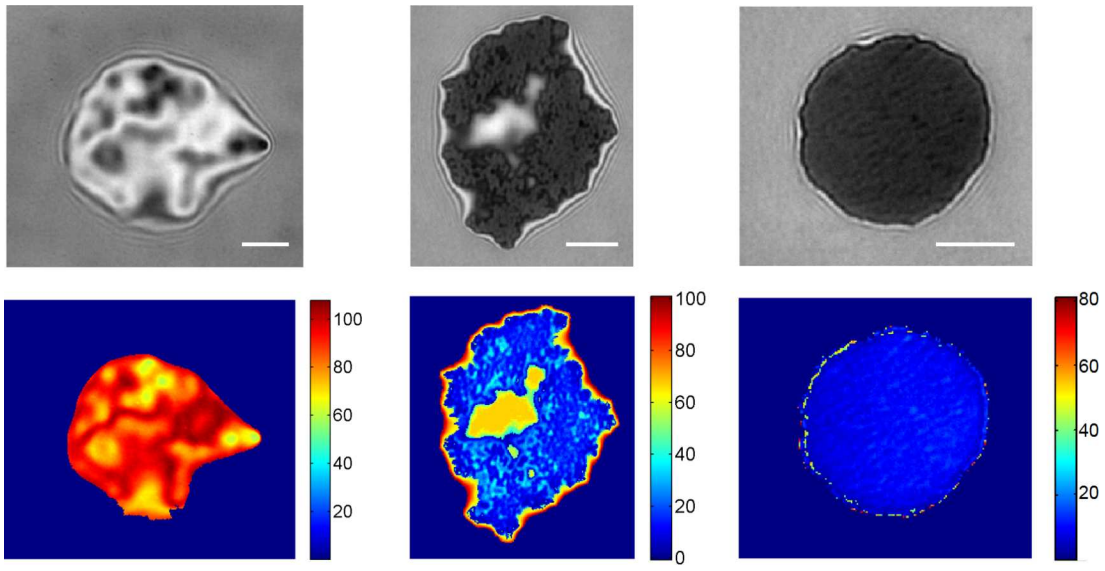

Figure 6.9: 0.1% GUV on 1% SLB with increasing time (from left to right: t = 32, 52, 55 min). Different vesicles are shown. Upper row: RICM images, lower row: Corresponding height maps, scale bar: 5 μm.

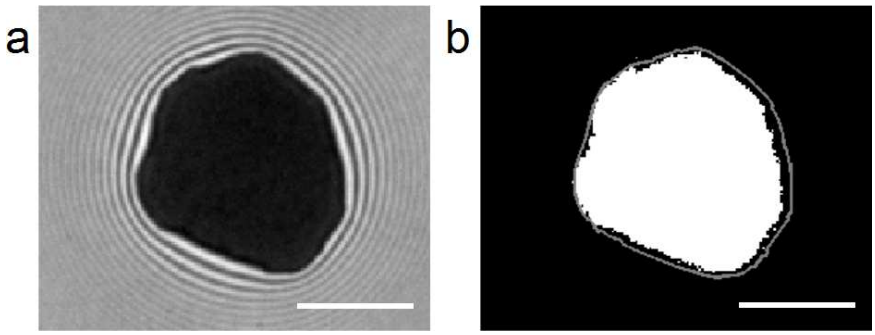

Figure 6.10: 0.1% GUV on 1% SLB. a: a: Round vesicle at late times (t = 70 min), b: Corresponding receptor accumulation in the contact zone (gray line), scale bar: 5 μm.

the final state (t = 70 minutes) showed that the receptors explored also the center of the adhesion zone (see Figure 6.10). The calculated value for the relative accumulated area beneath this vesicle was 90%. The deviation from 100% was caused by the bright rim. There, the vesicle membrane was immobilized (no fluctuations) but not bound to the SLB. Thus, no receptors were accumulated. Everywhere else the receptor density increased till 2.5%.

While repeating the experiment (B) special care was taken to cover the whole adhesion process. Despite some very small or very large vesicles, nucleation started after 30 minutes. The adhesion zone grew till t = 60 minutes and saturated above 95%

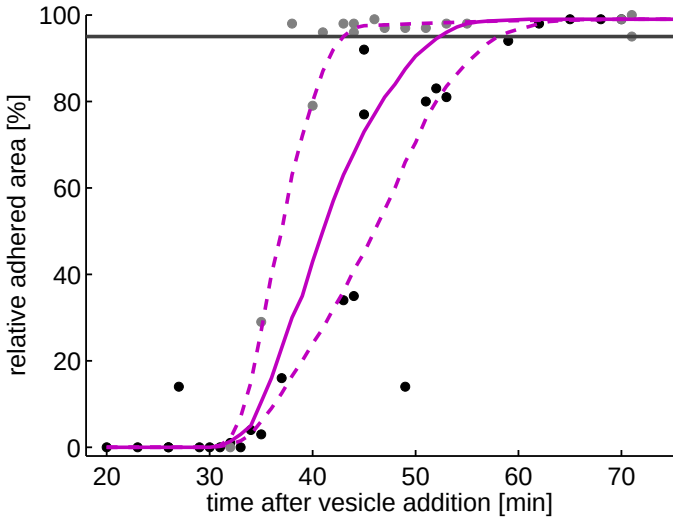

Figure 6.11: 0.1% GUV on 1% SLB. Experiment A (gray dots) and B (black dots) with guidelines (dotted). The mean adhesive behavior is described by the full line. All purple lines are mere guidelines for the eye. Black line: Limit 95%.

(see black dots in Figure 6.11). The phenotype of the adhesion state changed with time: starting at high heights without black rim but with fringes the vesicles came down and developed a black rim. Since they retained their fringes they exhibited areas in close contact with the substrate within the black rim, and at larger heights outside the black rim. While entering the state of complete adhesion some of the vesicles also lost their fringes. Thus, the membrane was bound at the same height all over the adhesion zone that is now identical with the contact zone. Exemplary vesicles for each state are given in Figure 6.9 together with the corresponding height maps.

All vesicles were simultaneously observed in fluorescence. The growth of the accumulated fluorescent signal (relative to the contact zone) over time is given in Figure 6.12. As expected small vesicles (with a smaller contact zone) accumulated receptors faster than larger vesicles. The overall onset of increase in area takes place around t = 40 minutes. In contrast to the adhered area no saturation is reached until t = 70 minutes. Plotting the relative fluorescent area against the relative adhered area revealed that low percentages of adhered area supported accumulation to a smaller extent than high percentages. The relative amount of fluorescent area rose first very slowly and later very fast (see Figure 6.13). Direct comparison of the

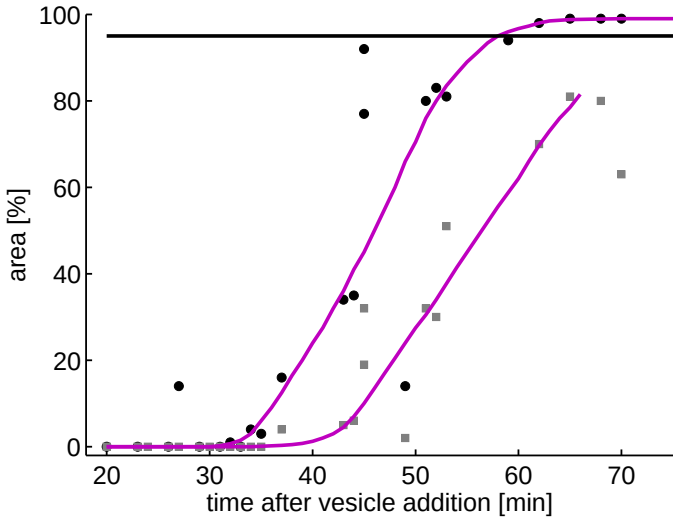

Figure 6.12: 0.1% GUV on 1% SLB. Comparison of the increase in adhered (black dots) and accumulated (gray squares) area for experiment B. Purple lines: Guidelines for the eye, black line: Limit 95%.

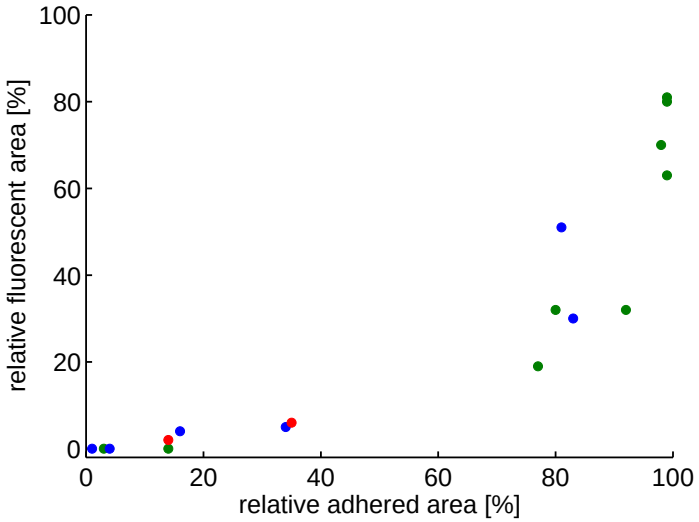

Figure 6.13: 0.1% GUV on 1% SLB. Interrelationship of the fluorescent area covered by accumulated receptors and the area of membrane adhesion. Green (blue, red): Vesicles from category I (II, III).

adhesion and accumulation growth curve indicated that adhesion forwent accumulation (see Figure 6.12). The time lag between the two processes was ∼10 minutes at the onset of growth and larger at the saturation. To predict the time point of saturation for the fluorescence accumulation, comparison with other data set was necessary. There, the time lag between full adhesion and accumulation saturation was 25 minutes. The comparison also pointed out that the adhesion process in the repetition experiment was remarkably slower. There was only one experimental difference. In the initial experiment 10 μl of vesicles were added while in the second experiment 100 μl were put because the vesicle density after swelling was quite low. As a consequence the concentration of sucrose in the outer buffer of the second experiment was higher. This circumstance led to increased water flow out of the vesicles (osmotic effect) and hence to a larger excess area together with augmented fluctuations. These membrane undulations may have retard adhesion at low ligand concentrations.

6.2.4 Adhesion Behavior: 1% vesicle - 1% bilayer

This case is already described in detail in Section 5.3.1.2. In this chapter, it is important because it represents the transition from low to high receptor-ligand concentrations. The interesting parameters for the comparison with the cases of lower concentrations are: dwell time (3 minutes), adhesion saturation (7 minutes), time lag between adhesion and accumulation ($\rightarrow 0$) and final neutravidin concentration (5%). One exemplary adhesion process and the corresponding area vs. time curve is shown in Figure 6.14. Please note, that the zero time point indicated in the graph marks the onset of adhesion and not the addition of the vesicles as before. Now the four cases corresponding to the corners of Table 6.1 are described. The results of the intermediate combinations are summarized in the following section.

6.2.5 Adhesion Behavior: Intermediate states

1% vesicle - 0.25% bilayer: The vesicles started to adhere readily and the relative adhered area saturated after $\sim$ 30 minutes at 90%. Thus, like for the cases

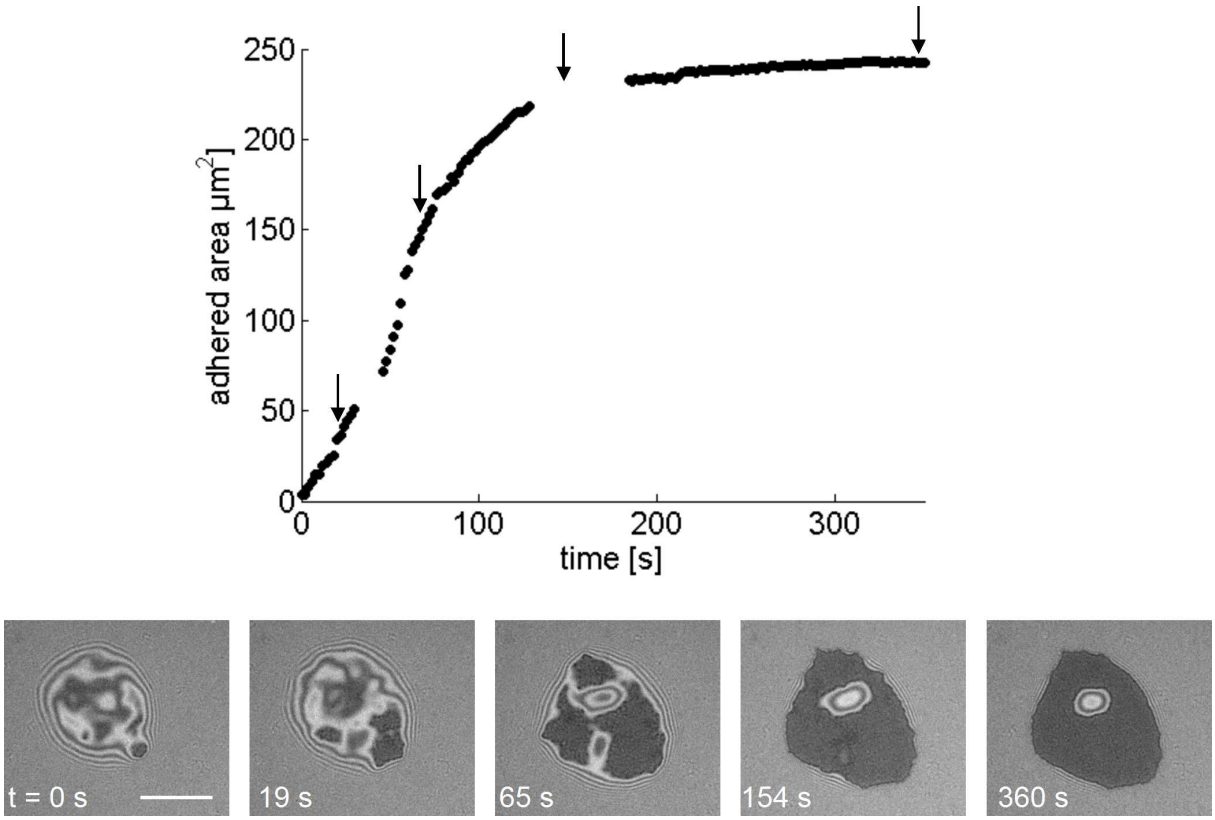

Figure 6.14: Adhesion process of a typical vesicle from the 1% SLB and 1% GUV group. The arrows mark the points on the curve corresponding to the RICM image shown. These images depict characteristic states of the adhesion process. The scale bar is valid for all images: 10 μm.

0.1% vesicle - 0.1% bilayer and 0.1% bilayer - 1% vesicle no complete adhesion was established till 60 minutes. The time lag between onset of growth of the relative adhered and the relative accumulated area was $\sim$ 30 minutes. Like for the other cases with depleted ligand in the SLB the accumulated receptors did not fill the central region of the adhesion zone but only the rim. 60 minutes after addition of the vesicles 46% (54%) of the contact zone (adhesion zone) were filled. Thereby, the accumulated receptors established a concentration of 1%.

0.5% vesicle - 0.5% bilayer and 0.5% vesicle - 1% bilayer: In both cases the adhesion process was completed within at least 20 minutes. The dynamical development was not mapped. Membrane adhesion and receptor accumulation occurred almost instantaneous. The time lag was less than 5 minutes. Fluorescence was accumulated everywhere within the adhesion zone and filled at least 90% of the contact zone. The latest recorded receptor concentration was 2.4% for 0.5% initial concentration on the SLB and 3.8% for 1% initial concentration.

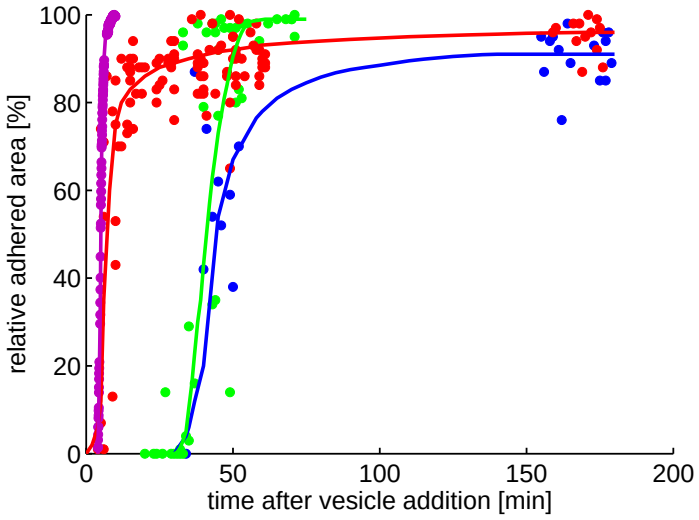

Figure 6.15: Relative adhered area vs. time plots for the boundary cases. purple: 1% SLB and 1% GUV, red: 0.1% SLB and 1% GUV, green: 1% SLB and 0.1% GUV, blue: 0.1% SLB and 0.1% GUV

6.2.6 Adhesion Behavior: Discussion

Comparison of the different scenarios studied allowed to deduce some general rules. First, the development of the adhered area with time was scrutinized (see Figure 6.15). One eye-catching feature was the splitting of the data in two groups with respect to nucleation: the adhesion area of the vesicles in the first group started to grow almost immediately while the vesicles in the second group needed ~ 30 minutes to initiate adhesion. The concentration of ligands in the vesicle set this time point. The vesicles in the first group had 1% biotinylated lipids while the vesicles in the second group had only 0.1%. Thus, at 0.1% of biotin a stable adhesion patch acting as a nucleation center was not easily formed. One idea could be that single bonds formed and broke repeatedly, but only cooperative binding of several biotin-avidin pairs enabled stable binding. For this purpose, several ligands had to be accumulated via diffusion. The probability to find another ligand in time increased with increasing concentration and/or increasing diffusivity of the ligands in the vesicle. The adhesion process in the ligand-depleted state was therefore diffusion limited. Most probable diffusion also determined the adhesion process of the vesicles in the first group as the overall shape of the growth curves was similar. But, due to the higher concentration of ligands and thus smaller diffusion distances, the onset of

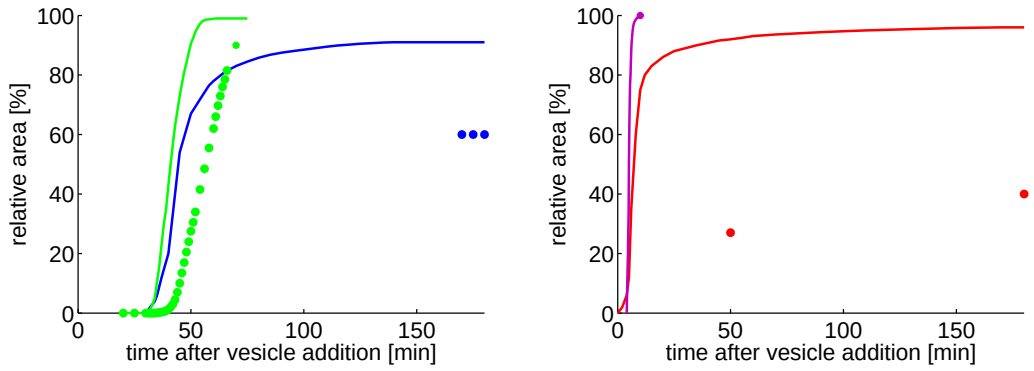

Figure 6.16: Fixed concentration of ligand on the GUV. Left: 0.1%, green: 1% on the SLB and blue: 0.1% on the SLB. Right: 1%, purple: 1% on the SLB and red: 0.1% on the SLB. Full lines represent the adhered area and dots the accumulated area.

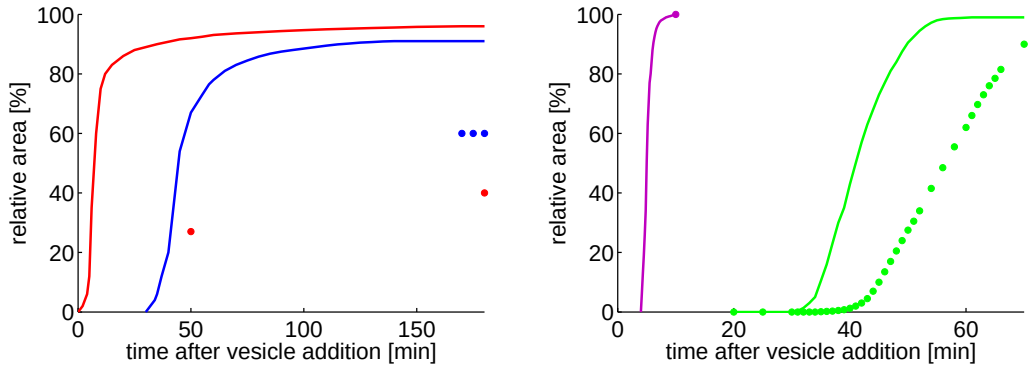

Figure 6.17: Fixed concentration of receptor on the SLB. Left: 0.1%, red: 1% on the GUV and blue: 0.1% on the GUV. Right: 1%, purple: 1% on the GUV and green: 0.1% on the GUV. Full lines represent the adhered area and dots the accumulated area.

adhesion was not dramatically delayed. Since the 0.5% vesicles adhered completely after 20 minutes, they belonged to the first group. Hence, the transition of the delayed to the *ad hoc* nucleation occurred between concentrations of 0.1% and 0.5% biotinylated lipids in the vesicle's membrane.

While the ligand concentration in the GUV influenced the onset of adhesion the concentration of receptors on the SLB effected mainly the final adhered state. Only in those scenarios with at least 0.5% neutravidin all GUVs of one ensemble adhered completely on a finite time scale. In all other cases the GUVs exhibited fringes and a fluctuating rim till the end. In order to explain this result the fluorescence data had to be considered. Figure 6.16 and 6.17 show the adhered area together with the accumulated area as a function of time at fixed concentrations in the vesicle

and bilayer, respectively. The completely adhered vesicles were identical to those that accumulated receptors everywhere in the adhesion zone at a high final concentration. In these cases the process of adhesion and accumulation occurred almost simultaneously. With decreasing initial concentration of neutravidin on the SLB the time lag between adhered and accumulated area increased up to 2 hours. The rate of accumulation was set by the diffusion process. The distance between the receptors increased linearly with decreasing concentration, but, as the distance travelled by a diffusing particle scales with the root of time, the effect on the rate of accumulation was much larger. Independent of the receptor-ligand concentrations small vesicles always adhered and accumulated faster (with respect to their contact zone) than large vesicles.

From the accumulated area vs. adhered area plots we learned that the accumulated area grew only slightly at low percentages of adhered area but accumulation accelerated at high percentages. This result can be explained with the help of the information acquired from diffusion experiments (see Chapter 7). There, we observed a decrease in receptor mobility in response of increased friction imposed by the adhering membrane. As a consequence, the slowed down receptors experienced a higher binding probability in the adhesion zone. Due to the different time scales of adhesion and accumulation most of the receptors were confronted with an already adhered membrane and had to enter the adhesion disc from outside. Underneath the vesicle they frequently met ligands from the opposing vesicle membrane. Since the binding affinity of biotin and avidin is very high, the receptors were bound and immobilized early and acted as obstacles for still diffusing receptors (see results in Chapter 7). Hereby, they jammed the edge of the adhesion disc while the center stayed at the initial concentration. Moreover, the level of accumulation depended critically on the initial concentrations of receptor and ligand. Table 6.2 gives an overview for all cases studied. In presence of excess binding partner, depletion of ligand reduced the final receptor concentration by a factor $\sim$2, but depletion of receptor reduced the final concentration by a factor $\sim$5. Comparison of the fluorescence maps and the fluctuation maps revealed that the ring of accumulated receptors together with the dilute bonds in the center was strong enough to freeze the membrane fluctuations in the center but not at the edge. This observation can

Table 6.2: Final maximum concentration of receptor [%] in the adhesion disc for given initial concentrations of biotinylated lipids in SLB and GUV after $\sim$ 1 hour.

SLB/GUV	0.1%	0.5%	1%
0.1%	0.5		0.9
0.25%			1
0.5%		2.4	
1%	2.5	3.8	5

be explained in view of reference [149]. The authors studied the surface extension of a vesicle under tension with a micropipette set-up. They found a fast area increase at low tension followed by a very slow increase at high tension and explain the result as follows. The first increase arises due to flattening of thermally induced membrane undulations which requires only small tension while the second increase corresponds to costly stretching of the membrane. In the present system, the GUV uses its excess area to build up a contact zone during adhesion. If the gain in adhesion energy was large enough the vesicle bound, fluctuations were smoothed out and the vesicle was bend at the edge of the adhesion disc. Only if the spreading pressure was very large the membrane tension was increased as the vesicle was stretched to further increase the adhesion area. This could only happen if the membrane was bound with a high density of bonds throughout the whole adhesion zone. All fringes then disappeared from the RICM images. It is worthwhile to mention that such a behavior was never observed when the concentration of neutravidin on the SLB was less than 0.5%.

While nucleation and saturation were extremely sensitive to changes in the ligand and receptor concentration, the scaling in the growth region was the same for all cases. The relative adhered area increased linearly with time. This behavior was already reported as a signature of diffusion limited adhesion [130, 132, 142, 143]. Figures 6.16 and 6.17 reveal that both augmentation of the receptor and ligand concentration accelerated the adhesion process (slope in the linear growth region). Table 6.3 compares the time needed till nucleation plus growth were complete. It is obvious that the required time decreased with increasing ligand and receptor concentrations.

The results obtained are in accordance with a recent study on vesicle adhesion with

Table 6.3: Time [min] till end of linear growth for given concentrations of biotinylated lipids in SLB and GUV.

SLB/GUV	0.1%	0.5%	1%
0.1%	>60		50
0.25%			30
0.5%		<20	
1%	50	<20	7

fixed receptors and weak bonds [145]. There, an increase in receptor density accelerated the adhesion process, too. Since the receptors were fixed, the adhered area with respect to the contact zone decreased with decreasing receptor densities. Here, the same effect was observed if the receptor concentration was extremely low. Then the recruitment of receptors from the SLB took extremely long. Thus, the scenario with very dilute receptors approached the fixed case since the receptors were effectively immobilized.

6.2.7 Vesicle Unbinding by Competitive Binding of Free Biotin

In order to study the influence of antagonists on the adhesion state of a GUV free biotin was employed in large excess. Vesicles with 0.1% biotinylated lipids were allowed to adhere completely on a neutravidin functionalized bilayer with 1% biotinylated lipids. Then, 400 μl of the outer buffer (300 mOsM PBS) were carefully removed and replaced by a buffer containing 0.2 mg/ml biotin (300 mOsM PBS-biotin). The functionality of the biotin solution was checked beforehand as described in the following. SLBs were incubated with 30 μg fluorescently labeled neutravidin-TMR in either 500 μl pure PBS or PBS-biotin for 30 minutes. Afterwards the samples were washed extensively with pure PBS. The mean fluorescence intensity measured in a square region of 35 times 35 μm was compared for 15 positions in each sample. The images were acquired with the microscope set-up described in Section 2.3.1. The presence of free biotin in the solution during incubation reduced binding to $\sim$ 10% of the amount bound in pure PBS.

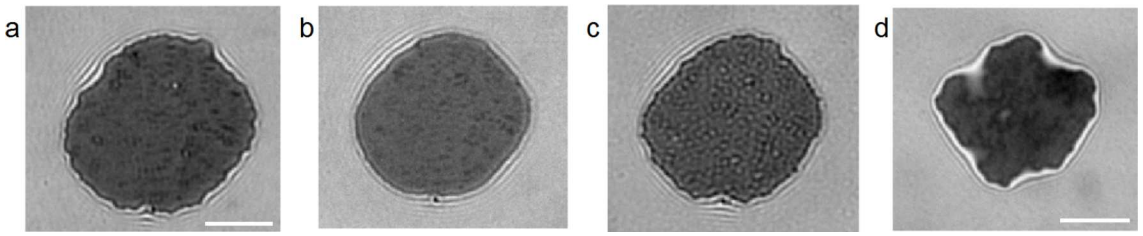

Figure 6.18: Antagonist induced deadhesion. a: Completely adhered GUV1 (98% of the contact zone is adhered). b: GUV1 directly after addition of free biotin. The contact zone retracted and smoothed. c: GUV1 one hour after biotin addition exhibiting small fluctuations (96% of the contact zone is adhered). The contact zone was partially re-established. d: GUV2 one hour after biotin addition. The edge of the contact zone is already fluctuating. Scale bar: 5 μm.

Next, the stability of the bond connecting the neutravidin to the biotinylated lipids on the SLB was tested. To this end, the SLB that was incubated with neutravidin-TMR in PBS was used. The PBS buffer was exchanged against PBS-biotin. The sample was kept dark for 30 (60, 90) minutes and washed with pure PBS to interrupt the competitive binding. Then the sample was scanned again and the mean intensity was determined as described above. No effect could be found. For a long time study the sample was incubated again with PBS-biotin and was checked after 3 (15) hours. On this long timescale some unbinding could be detected. The measured mean intensity dropped from 100% to 86% (72%). As a result, neutravidin binding on biotinylated SLBs could be assumed to remain stable even in presence of free biotin till 90 minutes of incubation.

For the experiments with vesicles the adhesion state before the buffer exchange had to be determined. Some exemplary vesicles were analyzed and showed $\sim$ 99% of the contact zone adhered. This result was in accordance to the values found in the analysis of the adhesion process (see previous section). One vesicle was observed during the buffer exchange. It was disturbed by the hydrodynamic flow but stayed in contact with the SLB (see Figure 6.18 b) with a reduced contact zone (150 μm^2 $\rightarrow$ 130 μm^2). One hour later the sample was scanned again and 10-15 exemplary vesicles were recorded. The contact zone had increased again (140 μm^2), but did not reach the original value. Large vesicles (diameter $>$ 30 μm) exhibited fluctuations and small bubbles in the adhesion zone (see Figure 6.18 c). They adhered with $\sim$ 95% while smaller vesicles (diameter $<$ 25 μm) detached at the edges of the contact

zone and adhered only with $\sim 89\%$ (see Figure 6.18 d).

To separate the hydrodynamic effect from the competitive binding another control experiment was done. In this experiment the same amount of buffer was removed but this time it was replaced by PBS instead of PBS-biotin. Ten exemplary vesicles were recorded before and one hour after buffer exchange. They exhibited unchanged adhesion states. 90% of the contact zone was adhered. For this experiments vesicles were employed that were already older than the usual 24 hours. Thus, the uneffective binding (90% instead of 99%) could be attributed to this fact. As the main purpose of this control experiment was to study the variation after hydrodynamic disturbance rather than the absolute extend of binding, the conditions of the control experiment were not optimal but can be accepted.

Antagonist-induced de-adhesion of specifically adhered vesicles was already studied in a model system with weak binding partners and fixed receptors [135]. The provided theoretical model explained the unbinding as a two step process. A first step, marked by the retraction of the contact zone, is established by the equilibrium between the vesicle's spreading pressure and the antagonist induced lateral pressure. In a second step, antagonists enter the contact zone. If a bond opens the antagonist can replace the ligands resulting in partial de-adhesion of the vesicle. Astonishingly, the same effects were also observed with the present model system and strong interaction.

To sum up, it was shown that the extreme high stability of the avidin-biotin interaction cannot be directly transferred to related models. Here, biotinylated lipids were used instead of free biotin molecules. Thus, it was not clear from the beginning whether the binding was entirely identical for the two cases (For details on the avidin-biotin binding see Section 1). Especially, the lid enclosing the biotin in the avidin binding pocket may not work properly when a lipid is attached. This explains the unbinding of neutravidin from the SLB on long time scales. The vesicle unbinding was accelerated when compared to the neutravidin unbinding. Hence, another effect had to play a role. One idea could be that thermically induced fluctuations of the membrane additionally weaken the bond.

The results presented in this section are not yet final, but they indicate that the biotin-avidin bond exhibits unbinding kinetics.

6.3 Conclusion

In this Chapter vesicle adhesion was investigated at very low concentrations of ligands and receptors in the limit of strong binding. It was shown that low ligand concentrations ($c_{ligand} < 0.5\%$) in the vesicle hampered the establishment of the initial nucleation center while low concentrations of receptors on the bilayer mainly influenced the final adhered state. Complete adhesion and full receptor accumulation was reached only for $c_{receptor}>0.5\%$. Simultaneous observation of the adhered area in RICM and the corresponding receptor distribution in fluorescence revealed that adhesion and accumulation go hand in hand at $c_{receptor}>0.5\%$ but at lower concentrations a large time lag between the two processes was found. Receptors were accumulated only at the edges of the adhesion zone where they were immobilized and acted as obstacles for newly arriving receptors.

Finally, experiments on vesicle unbinding by competitive binding of free biotin molecules were performed. As expected, the bond between neutravidin and a biotinylated lipid from the bilayer was found to be extremely stable. However, the situation was different in the case of neutravidin mediated vesicle adhesion. Addition of free biotin to a completely adhered vesicle led to retraction of the contact zone and partial unbinding of the vesicle membrane. Weakening of the bond due to thermally induced membrane fluctuations was proposed as an explanation for this surprising observation.

Chapter 7

Diffusivity of Lipids and Receptor Proteins

This chapter first explains the phenomenon of diffusion in general. Second, the theoretical concepts of diffusion in a membrane are introduced that were applied to analyze lipid and protein diffusion on the supported lipid bilayer. The aim was to elucidate the influence of membrane binding on the mobility of lipids and receptors mediating the binding.

7.1 Introduction

In recent years, structure and dynamics of the essentially fluid cell membrane and its nanoscale inhomogeneities have attracted much interest [14–16]. Diffusion of lipids and proteins in the plane of the membrane impacts directly on the local dynamic structure of the membrane. Diffusion thus plays a vital role in many membrane related functions including adhesion, recognition and transport. Intriguingly, the diffusion of proteins in a cell membrane was measured to be a couple of orders of magnitude slower than the diffusion in artificial membranes of similar lipid composition [150]. This was attributed to the combined effect of molecular crowding on the cell surface, hydrodynamic drag, clustering and attachment to the cytoskeleton. Biological and biophysical studies have probed each of these effects in cells [151–154] - however, in cellular studies, it is difficult to quantify and separate

these effects. Supported lipid bilayers (SLB [155–157]) and giant unilamellar vesicles (GUVs [134, 158–160]) have therefore been extensively used as well defined cell membrane models.

7.2 Theory of Diffusion

7.2.1 Diffusion in General

Diffusion terms the process of thermally driven equilibration of concentrations. The individual particles perform a random walk (Brownian motion). A common model conception describes Brownian motion as follows. Each particle moves statistically in one direction till it hits another particle and changes direction. Starting from an initially inhomogeneous distribution of particles in a box (dense half, dilute half) homogeneity is reached because the probability that a particle from the dense half enters the dilute half is much higher than for the transition in the opposite direction. As the probability for displacement is the same for each particle the half with the higher number of particles is more prone to displacement. The net flux of particles from the dense to the dilute half goes on till the concentration gradient vanishes and the flux in both directions is equal. This way the system reaches a state of maximum entropy. Building on T. Grahams work [161–163], A. Fick described the process of diffusion in two famous laws [164]: Fick's first law states that the net flux j is proportional to the concentration gradient $\partial c/\partial x$:

$$j = -D\frac{\partial c}{\partial x}, \tag{7.1}$$

with the proportionality constant D, called diffusion constant. Fick's second law utilizes conservation of mass (equation of continuity):

$$\frac{\partial c}{\partial t} = -\frac{\partial j}{\partial x}, \tag{7.2}$$

to yield an expression for the temporal change of the concentration c:

$$\frac{\partial c}{\partial t} = \frac{\partial}{\partial x}(D\frac{\partial c}{\partial x}) = \nabla(D\nabla c). \tag{7.3}$$

Assuming a stationary situation ($\partial c/\partial t = 0$) and an isotropic diffusion constant, the diffusion equation 7.3 simplifies to a Laplace equation:

$$\Delta c = 0, \tag{7.4}$$

with $\Delta = \nabla^2$. This elliptic partial differential equation has to be solved for a given set of boundary conditions to get the concentration at a given point in time and space.

In case the particles are situated in an external field $U(x)$ the particles are driven by a force F

$$F = -\frac{\partial U(x)}{\partial x} = \frac{v}{\mu}, \tag{7.5}$$

where v is the particle velocity and μ its mobility. As a result there is an additional contribution to the flux:

$$j_F = cv = -c\mu\frac{\partial U(x)}{\partial x}. \tag{7.6}$$

Hence, the total flux is $j_t = j + j_F$. In thermal equilibrium the particles are Bolzmann distributed:

$$c_{eq} \sim \exp(-\frac{U(x)}{k_B T}), \tag{7.7}$$

and the net flux vanishes

$$j_{t,eq} = 0. \tag{7.8}$$

Solving Eq. 7.8 yields the famous Einstein relation, that A. Einstein found in 1905 on a thermodynamical basis [165]. Herein, he combined the microscopic movement of single particles with the macroscopic occurrence of diffusion to get a relation for the diffusion constant D:

$$D = \mu k_B T. \tag{7.9}$$

This relation was independently derived by M. Smoluchowski [166].

7.2.2 Diffusion in a Free Membrane

The theoretical description of diffusion of lipids in a free bilayer was given by Saffman and Delbrück (SD) [167] and verified by Axelrod [112]. In this description, the

membrane is treated as a two dimensional fluid into which cylindrical objects are embedded. These inclusions diffuse due to thermal motion. The diffusion constant of such an object embedded in a pure lipid bilayer floating freely in a low viscosity fluid depends only logarithmically on the size of the hydrophobic moiety of the object. The drag on the hydrophilic moiety protruding from the bilayer can be neglected. Therefore, binding of a monomeric protein to a lipid head group is not expected to influence diffusion. Multivalent ligands, on the other hand, cluster receptors on the cell surface, thus creating diffusive structures that are much larger in size and hence diffuse more slowly [155]. An extreme example is the binding of polymers adsorbed to a membrane where the polymer "footprint" creates lipid domains that diffuse as a single unit [168].

7.2.3 Friction in a SLB

If the membrane is close to a solid surface, as is the case in supported bilayers, the hydrodynamic drag on an embedded diffusing object is increased. It now depends much more strongly on size since momentum transfer to the solid support via a thin film of fluid enhances and alters hydrodynamic resistance. The theoretical description of diffusion of such an embedded object, which may be a lipid or a trans-membrane protein, was given by Evans and Sackmann (ES) [169] and verified experimentally by Merkel et al. [62] and others [170,171]. In this approach, the inertialess equations of motion for membrane flow in SLBs in a fluid state were written assuming proportionality between interfacial shear stress and membrane velocity. In such a model the friction coefficient for particle motion is the key parameter. For low friction the SD result is recovered whereas for high friction the diffusion coefficient depends strongly on the size of the diffusing particle, as expected from ES theory. Like SD, the ES description ignores the discrete nature of the bilayer which is composed of lipids and proteins. Introduction of discrete obstacles (for example non-diffusing proteins) may, however, hinder the diffusion of lipids in the membrane.

The frictional drag on the lipid was calculated from the measured diffusion constant following the approach of Evans and Sackmann [62, 169–171] which gives the

following expression for D:

$$D = \frac{k_B T}{4\pi\eta_m}\left(\frac{1}{4}\epsilon^2 + \epsilon\frac{K_1(\epsilon)}{K_0(\epsilon)}\right)^{-1}, \tag{7.10}$$

where k_B is the Boltzmann constant, T the temperature and K_1 and K_0 modified Bessel functions of second kind and first or zeroth order, respectively. η_m is the membrane surface viscosity (i.e. bulk viscosity times membrane thickness) and ϵ the dimensionless particle radius given by:

$$\epsilon = R\sqrt{\frac{b}{\eta_m}}. \tag{7.11}$$

where R is the radius of the diffusing particle and b the friction coefficient.

7.2.4 Obstacles in Membranes/SLBs

Obstacles may be introduced due to binding of multivalent soluble proteins or ligand-receptor mediated specific adhesion of the membrane to another surface. Specific adhesion of membranes to a solid surface, for example cell adhesion to the extracellular matrix, inevitably leads to an immobilization of the bound receptors. Membrane to membrane adhesion, modeled by adhesion of a GUV to a supported bilayer (analogous to cell-cell adhesion) leads to a different scenario: prior to binding, the binding partners are both free to diffuse in their respective membrane-planes but after binding, they slow down due to increased friction. Thus, adhesion may introduce mobile or immobile obstacles into the membrane around which lipids have to diffuse. A continuum description is no longer valid.

To deal with the discreet nature of the bilayer, theories of diffusion of tracers around immobilized or mobile obstacles have been developed [172,173]. Small tracer molecules, in our case the labeled lipids, diffusing in a sea of slow moving (or stationary) obstacles exhibit reduced diffusion due to tracer-obstacle excluded volume interactions. The theoretical expression for the relation between the fraction c of the obstacles and the relative diffusion constant $D^*(c)$ was derived by Tahir-Kheli [174] and van Beijeren and Kutner [175]. $D^*(c)$ is defined as the ratio of the diffusion constant of the tracer at a given c and at $c = 0$: $D^*(c) = \frac{D(c)}{D(0)}$. Diffusion in metallic alloys or of particles in hard-core lattice gases served as model systems for the

theoretical considerations. Saxton adapted this approach to describe the diffusion in a SLB in presence of mobile obstacles [172]. Lipids were assumed to reside on a lattice with lattice constant a and move in a continuous time random walk, the two-dimensional diffusion constant was therefore written as $D(0) = a^2\ \Gamma_T/4$. Here, Γ_T is the jump rate of the tracer. If both the tracer and the obstacle are mobile, the relative diffusion constant could be expressed as a function of the relative jump rate γ of tracers and obstacles ($\gamma = \Gamma_T/\Gamma_O$) and the fraction of obstacles c [172]:

$$\begin{aligned} D^*(c,\gamma) &= \frac{1-c}{2\gamma(1-c)f_0}\left[(1-\gamma)(1-c)f_0+c]^2+4\gamma(1-c)f_0^{2^{1/2}}\right] \\ &\quad -\frac{1-c}{2\gamma(1-c)f_0}\left[(1-\gamma)(1-c)f_0+c\right], \end{aligned} \tag{7.12}$$

with

$$f_0 = \frac{[1-\alpha]}{[1+(2\gamma-1)\alpha]}. \tag{7.13}$$

α is a constant which depends on the lattice that was chosen. However, Saxton showed in his Monte-Carlo simulations that the final results were not sensitive to the choice of the lattice. For our calculations, we chose $\alpha = 1\text{-}2/\pi \sim 0.363$, corresponding to a square lattice.

In the case of stationary obstacles the exact diffusion coefficient for a random walk on a square lattice with randomly excluded sites (=obstacles) in the limit of low obstacle density was given by Nieuwenhuizen *et al.* [176]. It can also be obtained by putting appropriate limits in equation 7.12.

$$\frac{D(c)}{D(0)} = 1-(\pi-1)c-0.85571c^2. \tag{7.14}$$

The slowing down of tracer lipid diffusion due to binding of a protein has been demonstrated experimentally [137, 155]. It was shown that this retardation can be attributed to the introduction of stationary or slowly diffusing obstacles rather than to direct protein-membrane interaction [137]. Even though there has been considerable progress in understanding the effect of binding of proteins on the diffusivity of background lipids, much less is known on the effect of binding to another membrane. A series of ground breaking publications from the laboratory of Dustin [138,177,178] on cells binding to a SLB, report a slowing down of the adhesion proteins in the cell-SLB contact area after cell adhesion. However, since it is nearly impossible to

control the composition of a cell membrane, the causes of this slowing down could not be unambiguously traced. Analogous experiments on diffusion of tracer lipids have not been reported.

7.3 Results and Discussion

7.3.1 Biotin-Neutravidin: Limit of Strong Binding

7.3.1.1 Lipid Diffusion

Effects of Protein Binding

In these experiments, three different concentrations (0%, 1% and 5%) of biotinylated lipids were employed in the SLB. The resulting diffusion constants of chain-labeled fluorescently tracer lipids (NBD-PC) were measured with continuous photobleaching (see Section 2.3.4.1). They were found to decrease with increasing biotin concentration: $D_{0\%} = (2.5 \pm 0.2)\,\mu\text{m}^2/\text{s}$ (N = 22), $D_{1\%} = (2.3 \pm 0.2)\,\mu\text{m}^2/\text{s}$ (N = 103) and $D_{5\%} = (2.2 \pm 0.2)\,\mu\text{m}^2/\text{s}$ (N = 123). The presented error bars refer to single standard deviations. These values agree very well with the D measured by Horton *et al.* [137] for diffusion in a SOPC SLB: $D = 2.3\ \mu\text{m}^2/\text{s}$. The mean diffusivities for the threes cases were found to be statistically different (Student's t-test α=1%). Therefore, for further evaluation, each case was considered separately.

The presented error bars reflect contributions from mainly two sources, inhomogeneity of the illumination intensity for bleaching and inherent inhomogeneity of the sample. The contribution from inhomogeneity of the illumination was 6%, as determined from the diffusion constants evaluated by considering for each position the intensity profile along twelve radial lines separated by 30° (see Figure 3.10). The contribution of the sample was calculated as the standard deviation of diffusion constants measured at different positions. Usually 20 positions were scanned for each case resulting in an error of typically 3% for one sample. While averaging over 5 samples this contribution rose to 7% indicating that the SLBs are not absolutely identical. Since the two errors are independent, they add up quadratically to a total error of 9%.

Table 7.1: Diffusion constants of the tracer lipid in the SLB before and after binding of protein or vesicle for various concentrations of biotin-lipids in the SLB. The number of measurements for each case is given in brackets. Error bars represent single standard deviations.

biotin	bare [μm^2/s]	+NAV [μm^2/s]	+NAV +vesicle [μm^2/s]
1%	2.3 ± 0.2 (103)	2.1 ± 0.2 (56)	1.8 ± 0.2 (91)
5%	2.2 ± 0.2 (123)	1.7 ± 0.2 (71)	1.5 ± 0.2 (99)

The mobile fraction of tracer lipids in the bilayer was measured with FRAP. The mobile fraction was between 87% and 93% for all the concentrations of biotin lipids studied. Thus, ∼10% of the lipids acted as stationary obstacles. Eq. 7.14 was used to calculate the expected diffusion constant in the absence of obstacles: $D_{0\%} = (3.2 \pm 0.2)\,\mu$m^2/s, $D_{1\%} = (3.0 \pm 0.2)\,\mu$m^2/s and $D_{5\%} = (2.8 \pm 0.2)\,\mu$m^2/s. Applying Eq. 7.10 and Eq. 7.11 the diffusion constants of NBD-lipids ($R = 4.8$ Å) [139] in the upper leaflet of the bilayer ($\eta_m = 0.16 \cdot 10^{-9}$ Pa s m) [179] for the three cases were converted to friction coefficients b of $5 \cdot 10^7$ Pa s/m, $6 \cdot 10^7$ Pa s/m and $7 \cdot 10^7$ Pa s/m. These values were consistent with the coefficient Merkel *et al.* [62] obtained for the friction between two fluid monolayers ($b = 10^7 - 10^8$ Pa s/m) applying FRAP. This result was also confirmed by independent measurements with different techniques [180–182]. Purrucker *et al.* [171] recently measured an one order of magnitude larger frictional coefficient for lipids diffusing in a monolayer supported by a layer of hydrophobic polymer applying CP.

To probe the effect of binding a protein to functionalized lipids on the mobility of tracer lipids, SLBs with two different biotin concentrations (1% and 5%) were used. The tetravalent avidin analogue neutravidin was used as model protein. It was already shown in Section 4.2.1.3 that the geometry of neutravidin allows to bind at most two biotin groups if these are arranged on a plane as is in the present case. Table 7.1 shows the comparison of the diffusion constants measured in free SLBs and in SLBs with bound neutravidin (see column 2 and 3). After incubation with neutravidin the mobile fraction remained unchanged, but the membrane fluidity decreased significantly for both biotin concentrations ($D_{1\%} = (2.1 \pm 0.2)$ μm^2/s, $D_{5\%} = (1.7 \pm 0.2)$ μm^2/s). Two different effects may have contributed to this reduction. First, protein binding to ligand-carrying lipids may have slowed

them down (or pinned them) thus, inducing them to act as mobile (or fixed) obstacles and second, the bound proteins may have formed a dissipative layer of high viscosity just adjacent to the membrane thus increasing the hydrodynamic drag on the diffusing tracers.

The effect of the obstacles could be estimated with the help of data from protein diffusion experiments (see Section 7.3.1.2) as follows: the obstacles were formed by biotinylated lipids pairwise connected to the same neutravidin molecule. This formed one large object which either diffused slower than single lipids or was completely pinned. In Eq. 7.12 the relative jump rate γ is defined as the ratio of the diffusion constants of the single tracer lipid D_{lipid} in absence of obstacles, and the lipid-protein complex $D_{complex}$. In the 1% case, the complex was found to be mobile. $D_{lipid} \sim 2.3\ \mu m^2/s$ and $D_{complex} \sim 0.3\ \mu m^2/s$ (D/B was measured from protein diffusion to be 2.8 μm^2 (see Section 7.3.1.2). $B_{OregonGreen}$ could not be measured exactly since the bleaching curve was not purely mono-exponential. However, forcing the fit allowed to estimate $B_{OregonGreen} \sim 0.1\ s^{-1}$. Comparison with the value obtained for NBD by a regular fit ($B_{NBD} = 0.4\ s^{-1}$) confirmed the estimation.). Thus, γ was ~ 10. By application of Eq. 7.12 and 7.13 the theoretical diffusion constant in the presence of 1% mobile obstacles was calculated: $D_{1\%th} = 2.2\ \mu m^2/s$. In the 5% case, the complex was found to be immobile and, hence, Eq. 7.14 was applied: $D_{5\%th} = 2.0\ \mu m^2/s$. Comparison of theoretical and experimental results ($D_{1\%th} = 2.2\ \mu m^2/s$ and $D_{1\%exp} = 2.1\ \mu m^2/s$, $D_{5\%th} = 2.0\ \mu m^2/s$ and $D_{5\%exp} = 1.7\ \mu m^2/s$ shows that consideration of mobile (fixed) obstacles does not fully account for the depression of diffusion of tracers after protein binding.

The additional retardation of lipid diffusion can be attributed to a direct increase in friction. After binding of the receptors, the distal surface of the SLB was no longer bounded by the low viscosity buffer but a dilute (1%) or densely packed (5%) protein layer. The effective friction coefficient introduced by the protein layer, was calculated using Eq. 7.10 and Eq. 7.11 as: $b_{NAV,1\%} = 2 \cdot 10^7$ Pa s/m and $b_{NAV,5\%} = 1 \cdot 10^8$ Pa s/m. Since the friction coefficient b due to a viscous layer is given in the most simple approximation by the product of layer viscosity and thickness, the fivefold increase in b from 1% to 5% implied that the viscosity of the protein layer formed with 5% biotinylated lipids was five times more viscous than the less dense

protein layer formed on a SLB with 1% biotinylated lipids.

Comparison of the scatter of the data in the free bilayer case with the protein coated case showed that the random error due to inhomogeneous illumination expectedly stayed the same at 6%. In contrast, the variation caused by the sample itself rose from 3% to 6% for one sample and from 7% to 9% for all three samples considered for each case. Thus, the total scatter increased slightly from 9% to 11%. This small increment implied that the protein was bound fairly homogeneously to the SLB.

To ensure specific binding of neutravidin, in certain experiments the SLB was incubated with BSA before adding avidin. In the 1% case, the diffusion constant dropped from 2.3 μm^2/s to (2.1$\pm$ 0.2) μm^2/s (N = 149) after incubation with BSA but did not drop further after incubation with neutravidin. In the 5% case, the diffusion constant dropped from 2.2 μm^2/s to (1.9$\pm$ 0.2) μm^2/s (N = 149) but dropped further to (1.7$\pm$ 0.2) μm^2/s (N = 71) upon incubation with neutravidin. A Comparison of the diffusion constants measured after neutravidin binding with passivation plus neutravidin binding yielded: $D_{NAV1\%}$ = (2.06 $\pm$ 0.22) μm^2/s, $D_{BSANAV1\%}$ = (2.03 $\pm$ 0.27) μm^2/s, $D_{NAV5\%}$ = (1.65 $\pm$ 0.21) μm^2/s, $D_{BSANAV5\%}$ = (1.67 $\pm$ 0.21) μm^2/s. It is noteworthy, that the final diffusion constant after neutravidin binding was independent of the additional BSA incubation step. Using fluorescently labeled BSA and light microscopy we found that BSA binds to the SLB homogeneously (data not shown). A second passivation step after neutravidin incubation had no effect on SLB fluidity. For 1% and 5% biotin the diffusivities measured before and after the second passivation step differed only by 0.04%. Statistical analysis applying the Student t-test showed that these differences were not significant (α = 1%).

Effects of Vesicle Binding

The diffusion constant of the tracer lipids below a bound vesicle was measured. The mobility of the tracer lipids in the SLB dropped from $D_{1\%}$= 2.1 μm^2/s ($D_{5\%}$ = 1.7 μm^2/s) to 1.8 μm^2/s (1.5 μm^2/s) as a result of vesicle binding (see column 4 inTable 7.1). The mobile fraction was not significantly altered and remained at $\sim$ 90%. As pointed out in Section 4.2.1.2 neutravidin flows into the adhesion disc following vesicle binding, and accumulates to a final concentration of 5%. Therefore, for the case of 5% biotin-lipids in the SLBs, the amount of neutravidin which corresponded to the amount of mobile obstacles was not expected to increase after vesicle binding.

Thus, the drop in diffusion should be caused solely by enhanced friction due to the presence of the vesicle membrane. Applying Eq. 7.11 the friction coefficient was calculated to be $b_m = 1 \cdot 10^8$ Pa s/m.

In the case of 1% initial biotin concentration a decrease in diffusivity similar to the case of 5% was expected because the amount of mobile obstacles was increased to 5% by vesicle binding. Moreover, the friction with the vesicle membrane should be the same because the vesicles are bound at similar heights in both cases. The fact, that the decrease was smaller, pointed at an additional effect to be taken into consideration. At 5% neutravidin concentration only a very small free volume was left. With decreasing free volume the protein layer approached a glass transition. There, the viscosity of the layer and hence the friction with the lipids depended very strongly on the protein density [183]. Therefore, even small differences in density that were not visible in fluorescence caused measurable differences in lipid diffusivities. It is very well possible that the protein layer formed by accumulated neutravidin (initially 1%) was not quite as dense as the 5% layer, because the proteins had to diffuse in a more and more viscous matrix in a self- inhibiting process.

Besides, it is necessary to discuss effects arising from neutravidin possible bound unspecifically to the glass because vesicles will also interact with those molecules. We know that these molecules were immobile and made up 25% of the specific signal for 1% biotinylated lipids (see 4.2.1.1). If 1% (5%) biotinylated lipids corresponded to 75% (95%) of the signal, 25% (5%) indicated 0.33% (0.33%) immobile obstacles. The influence of immobile obstacles could be calculated according to Eq. 7.14. The result for D(0.33%)/D(0%) is greater than 0.99. Therefore, the effect of unspecifically bound immobile obstacles could be neglected.

7.3.1.2 Protein Diffusion

Consequences of Increasing Protein Concentration

Clearly, it would be interesting to directly probe the retardation in diffusion of the receptors (in this case neutravidin) due to membrane adhesion. To this end continuous bleaching experiments were performed analogous to those described above but now neutravidin was replaced by neutravidin-OG leaving out the fluorescent

lipids from the SLB. However, in this case, the bleaching of the fluorophore was not described by a single exponential decay. Therefore, Eq. 3.8 does not hold. An alternative experimental approach using FRAP failed because the fluorescent signal did not recover on time scales of the experiment indicating that the protein (neutravidin) was in a kind of gel phase as already reported for avidin [137,184]. This result is in accord with our hypothesis of an approach to a transition to a glassy state. To circumvent this drawback, continuous photobleaching was used and D is reported not directly but as a function of B because we can only fit for D/B in Eq. 3.10. Assuming that B does not change after vesicle binding D/B reflects changes in D. This assumption seems reasonable as we saw no change in B for lipid data where Eq. 3.8 could be applied. Comparison of D/B for three different SLB compositions, namely 1%, 2% and 5% biotinylated lipids clearly showed the decrease in diffusivity due to crowding even in absence of an adhering membrane. D/B dropped from 2.8 μm^2 for 1% to 1.6 μm^2 for 2% to 0.4 μm^2 for 5% (see Table 7.2). This accelerating decrease supported the thesis of a close glass transition (see 7.3.1.1).

Effects of Vesicle Binding

Vesicle adhesion slowed down protein mobility due to binding to the vesicle membrane followed by accumulation of the protein for all cases. This decrease was very pronounced in those cases where the protein was sparse in the beginning (1% and 2%). D/B dropped from 2.8 μm^2 to 0.3 μm^2 for 1% and from 1.6 μm^2 to 0.2 μm^2 for 2%. In the case of 5% biotin-lipids, there was no extra protein accumulation in the adhesion disc. Thus, the diffusion constant indeed decreased not only due to protein accumulation as demonstrated before but also as a direct consequence of membrane binding. The additional friction from the membrane reduced D/B from 0.4 μm^2 to 0.2 μm^2. All D/B results are summarized in Table 7.2.

Figure 7.1 illustrates the different decay lengths for 1% and 5% biotin-lipids as measured on the bilayer and beneath the adhering vesicle. The fluorescence micrograph of the bleached state shows a distinct shift of the bright rim under the vesicle when compared to the outside. This effect indicates quasi immobile neutravidin because if immobilized BSA-FITC was bleached a similar thin bright rim evolved that moved outwards with increasing time. It was caused by the illumination profile of the field stop. It is technically impossible to create a truly step-like transition from bright to

Table 7.2: Decay length of the intensity profile after prolonged bleaching D/B, for the protein neutravidin in the SLB before and after vesicle binding for various concentrations of biotin-lipids in the SLB. The drop points at extremely low mobility. The number of measurements for each case is given in brackets. Error bars represent single standard deviations.

biotin	SLB [μm^2]	SLB+vesicle [μm^2]
1%	2.8 ± 0.6 (8)	0.3 ± 0.1 (8)
2%	1.6 ± 0.3 (8)	0.2 ± 0.1 (8)
5%	0.4 ± 0.2 (18)	0.2 ± 0.1 (18)

dark. The measured profile perpendicular to the field stop could be described with a Fermi function: $F(x) = (1 + \exp(-x))^{-1}$ with a width of about 500 nm. As a consequence, the fluorophores were bleached with rates corresponding to the illumination distribution, meaning that the outmost proteins bleached slower. Simulation of bleaching with a Fermi function like illumination profile proved the existence of an intensity maximum moving outwards. Therefore, we could not determine whether the proteins beneath the vesicle are diffusing extremely slowly or are entirely immobile. As we are operating at the resolution limit of the technique we cannot quantify the membrane effect on the proteins like we did for the lipids. But, as shift at 5% was still visible, it could be qualitatively deduced that again the proteins outside were moving faster than the proteins in contact with the membrane. In light of this discussion, the absolute values of D/B given above for high protein concentrations should be treated with caution and indicate only upper limits for diffusivities.

7.3.2 E-cadherin-E-cadherin: Limit of Weak Binding

The fluidity of the bilayer was probed with head-labeled tracer lipids (NBD-PE) following receptor binding (in this case: Ecad) and vesicle adhesion. Retarding effect upon Ecad binding could not be resolved: $D_{bare} = (4.2 \pm 0.2)$ μm^2/s (N = 25) and $D_{5\%} = (4.4 \pm 0.3)$ μm^2/s (N = 25) or vesicle binding: $D_{5\%} = (3.5 \pm 0.6)$ μm^2/s (N = 6) $D_{ves} = (3.4 \pm 0.4)$ μm^2/s (N = 6). Note, that the differences for $D_{5\%}$ resulted from the measuring conditions. The temperatures were T = 25° and T = 21°, respectively.

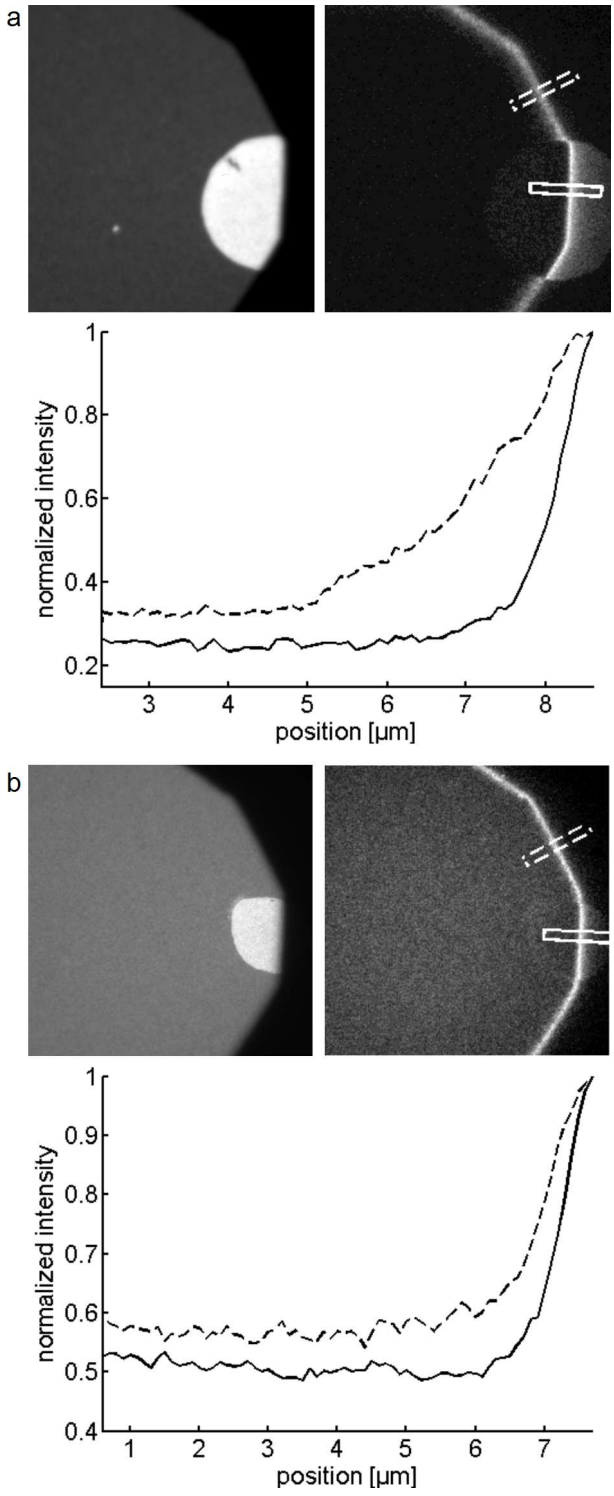

Figure 7.1: Fluorescence micrographs illustrating the bleaching experiment to analyze neutravidin mobility. a: neutravidin concentration 1%. b: neutravidin concentration 5%. Left: beginning of bleaching. Right: bleached state. Below: intensity distribution along the regions of interests defined in the right picture displaying different decay lengths according to differences in mobility. Full line: intensity distribution under the vesicle, dotted line: intensity distribution on the SLB.

7.3.2.1 Effects of Protein Binding

At the first glance, the lack of retardation after receptor binding was surprising since the Ecad construct was a dimer and its binding should therefore have introduced, as in the strong-binding case, mobile obstacles in the form of coupled NTA lipids. However, this lack could be understood when the structure of the Fc fragment was considered. The his_6 tags were bound to the C-terminals which were only 14 Å apart. Thus the effective radius of the protein-lipid complex (7 $\mathring{A}$) was too small to have a measurable impact on the tracer lipid diffusivity.
A competing hypothesis could have been that the lack of retardation resulted from the weakness of the bond. According to this hypothesis, rapid binding and release of Ecad bonds on the time-scale of tracer diffusion would have ensured that effectively only one lipid at a time was bound to the receptor. Unlike the permanent lipid dimers formed by neutravidin binding, such ephemeral lipid dimers in the Ecad case would then not have acted as mobile obstacles. The typical life-time of an Ecad bond is $\sim$ 2 sec [185]. In the present system, this time was sufficient for a lipid to travel about 8 μm^2 - many times its own size. Thus, the bond life-time was too large to explain the lack of retardation after receptor binding.

7.3.2.2 Effects of Vesicle Binding

The lack of retardation after vesicle binding on the other hand could be explained in the view of the height measurements. In contrast to the close biotin-neutravidin interaction, in the case of Ecad the vesicle membrane and main protein volume were far away from the bilayer since his_6 and Fc-fragment provided a long linker. As a consequence, no intense interaction between tracer lipids and protein layer as well as the vesicle membrane took place. Therefore, no substantial dissipative friction retarding the tracers was introduced. It should be noted that since the Ecad construct was more bulky than neutravidin, and neutravidin was saturated at 5%, Ecad should have been also saturated at 5%. Thus, we are operating at the saturation limit from the beginning and neither additional receptor accumulation nor a resulting slowing down of tracers was expected.

7.4 Conclusion

A well defined model system with tightly controlled composition and physical properties was used to probe the influence of specific ligand-receptor mediated intermembrane adhesion on lipid and receptor diffusion. It was shown that the slowing down of non-participating background lipids in a supported lipid bilayer by specific binding of a receptor or by receptor mediated adhesion of a GUV depended strongly on the choice of receptors. Retardation was expected for divalent receptors that bound two lipids and thus introduced slower moving obstacles into the bilayer. However, the effect was significant enough to be measured only if the binding pockets were widely spaced (neutravidin-biotin). In the case where a retardation in diffusion of tracer lipids took place, it was shown that consideration of the introduction of slow moving obstacles did not yet fully account for the retardation. Therefore, it was concluded that the protein formed a dissipative layer on the surface of the lipid thus adding another source of retardation. The viscosity of this layer was found to scale with the concentration of the protein. Importantly, the dissipative protein layer influenced diffusion of lipids in the membrane only if the interaction was intimate. If the ligand was linked to the lipid by a relatively long anchor, the tracer-lipids were far from the dissipative layer and retardation was not observed. This result has implication for the idea of exploiting this retardation for devising binding assays [155]: clearly, lipid-diffusion is not a reliable indicator of protein binding unless the conditions discussed above are fulfilled.

In addition, retardation of in-plane diffusion of the receptors themselves was observed as a function of membrane binding. In case of the strongly interacting neutravidin receptors, this retardation was significant and arose from a combined effect of the receptor accumulation and increased friction with the membrane. In the case of the weaker E-cad mediated adhesion, direct observation of protein diffusion was not possible due to technical reasons related to the difficulty of labelling E-cadherin while retaining its biological activity. However, the absence of any retardation of tracer lipids strongly indicated that in this system, the receptors retain their mobility both at saturation and after vesicle binding.

The result on retardation of diffusivity of proteins due to membrane adhesion sheds

light on observation of similar retardation in the adhesion zone between a SLB and immune cells [138, 177, 186]. As far back as 1991 it was demonstrated [186] that adhesion proteins accumulate into the contact area between a cell and a liposome - this was usually explained based on the idea of active, cytoskeleton driven accumulation (see references in Dustin *et al.* [177]). The present experiments with a cell free system proved unambiguously that passive processes contribute at least partially to the accumulation. Such a passive accumulation can be understood theoretically from a balance of adhesion energy, elastic energy of vesicle deformation and entropy of free ligands and receptors [134]. Further, in cells a reduction of 50-75% in the diffusion coefficient of binding proteins was observed. In comparison, here either total immobilization in case of strong binding or no retardation at all for the case of weak binding was observed. At 35 k_BT, our strong binding limit was much stronger than most biological bonds and at 2 k_BT, the weak binding limit was much weaker than the integrin bonds ($\sim$ 10 k_BT) that have been typically probed in cell experiments. Based on these considerations as well as theoretical understanding [134], it can be speculated that the extent of protein accumulation as well as the extent of retardation of receptor diffusion is governed by the strength and geometry of the ligand/receptor bonds.

Appendix A

Technical Drawings

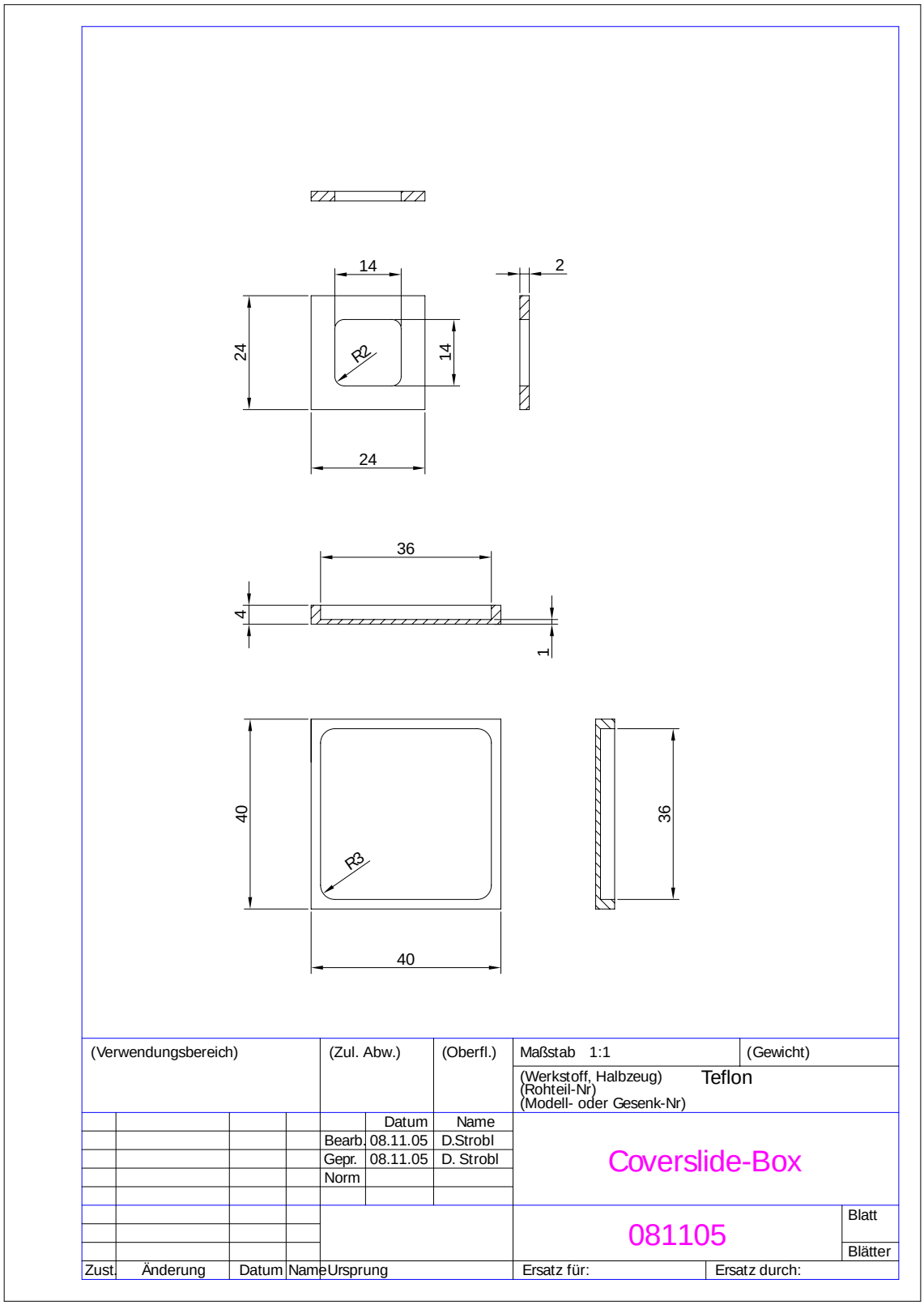

Figure A.1: Teflon box to transport the solid supported lipid bilayer under water.

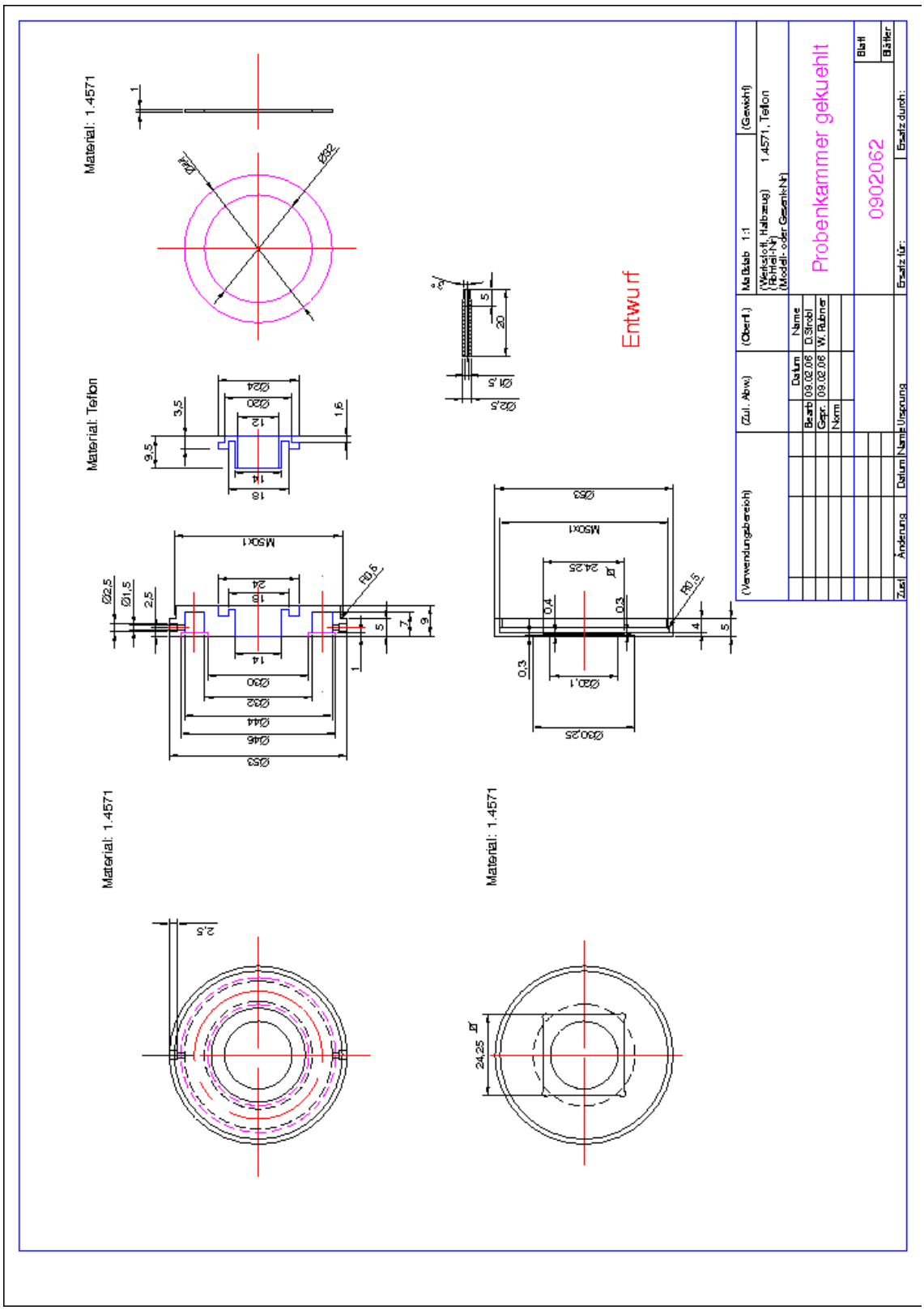

Figure A.2: Measuring chamber with cooling device.

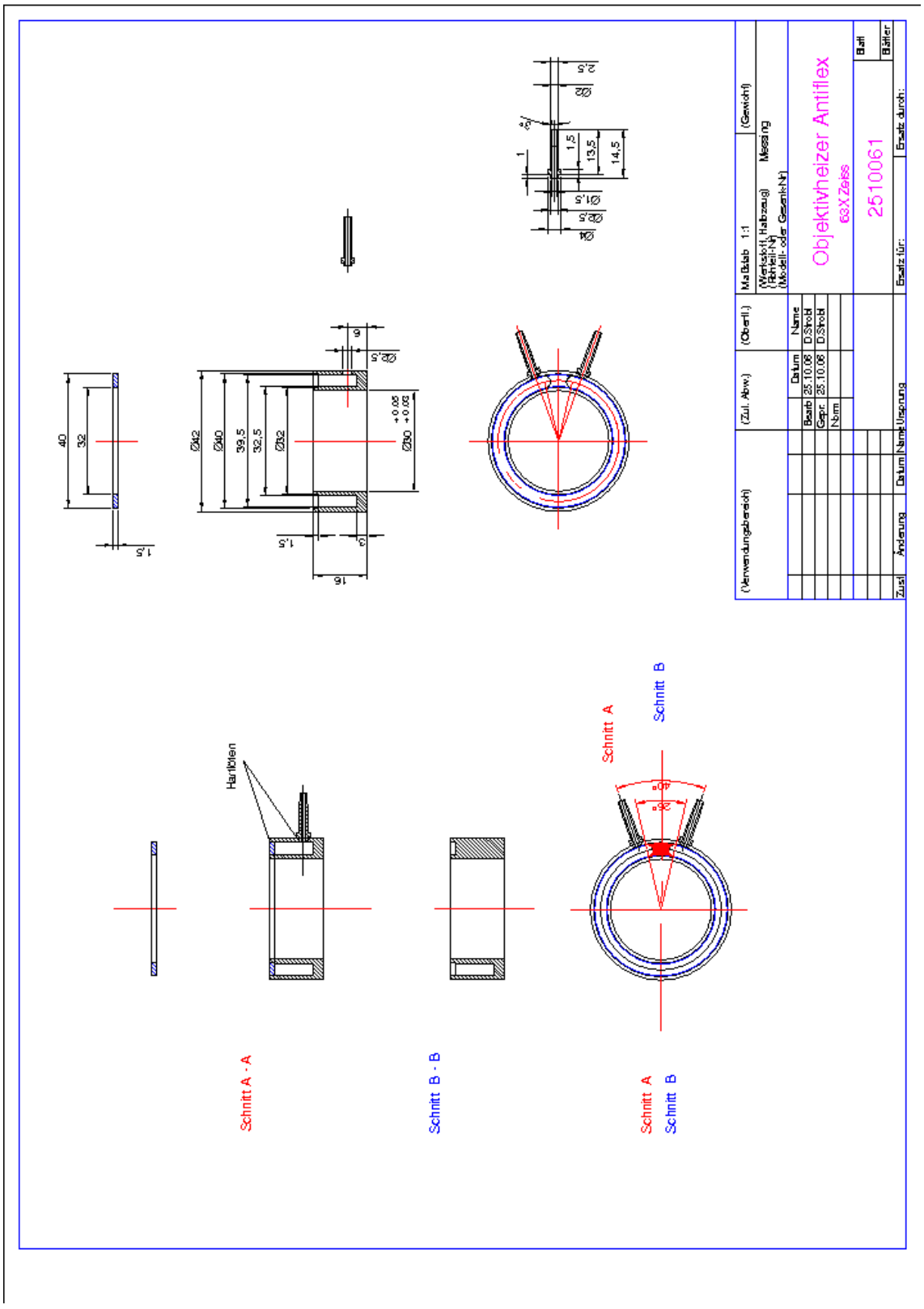

Figure A.3: Cooling device for the Antiflex objective.

Appendix B

List of Abbreviations

A	Absorption
B	Bleaching constant
BSA	Bovine Serum Albumin
CAM	Cell Adhesion Molecule
CCD	Charge-Coupled Device
CLSM	Confocal Laser Scanning Microscopy
CP	Continuous Photobleaching
CZ	Contact Zone
D	Diffusion constant
DOGS-NTA	1,2-dioleoyl-sn-glycero-3-[(N-(5-amino-1-carboxypentyl) iminodiacetic acid)succinyl]
DOPE-cap-biotin	1,2-dioleoyl-sn-glycero-3-phosphoethanolamine-N-(cap biotinyl)
DOPE-PEG 2000	1,2-dioleoyl-sn-glycero-3-phosphoethanolamine-N- (methoxy(polyethylene-glycol)-2000)
E	Enrichment factor

Ecad	homophilic cell adhesion molecule E-cadherin
ECM	Extracellular Matrix
EGTA	ethylene-bis(oxyethylenenitrilo)tetraacetic acid
F	Fluorescence
FM	Fluorescence Microscopy
FRAP	Fluorescence Recovery After Photobleaching
GFP	Green Fluorescent Protein
GUV	Giant Unilamellar Vesicle
HEPES	4-(2-hydroxyethyl)piperazine-1-ethanesulfonic acid)
IC	Internal Conversion
ISC	Intersystem Crossing
ITO	Indium Tin Oxide
NA	Numerical Aperture
NBD	6-(N-(7-Nitrobenz-2-oxa-1,3-diazol-4-yl)aminohexanoic acid))
NBD-PC	1-oleoyl-2-[12-[(7-nitro-2-1,3-benzoxadiazol-4-yl)amino]dodecanoyl]-sn-glycero-3-phosphocholine
NBD-PE	1,2-dioleoyl-sn-glycero-3-phosphoethanolamine-N-(7-nitro-2-1,3-benzoxadiazol-4-yl) ammonium salt
NC	Nucleation Center
OG	Oregon Green (fluorescent label)
PEG	polyethylene glycol
Ph	Phosphorescence
Pipes	piperazine-N,N'-bis(ethanesulfonic acid)

RA	Relative Adhesion Area
RICM	Reflection Interference Contrast Microscopy
S_0	Singulet ground sate
S_1	first excited Singulet state
SLB	Solid Supported Lipid Bilayer
SOPC	(1-stearoyl-2-oleoyl-sn-glycero-3-phosphocholine)
STD	single standard deviation
T_1	first excited Triplet state
TMR	Tetra-Methyl-Rhodamine (fluorescent label)
W	adhesion energy density

Appendix C

Curriculum Vitae and List of Publications

Personal details:

Name	Susanne Franziska Fenz
Date of birth	21.11.1979
Place of birth	Frankfurt am Main, Germany

Education:

Since Nov. 2005	PhD student at the Institute of Bio- and Nanosystems (IBN-4), Research Center Jülich, Germany and Rheinische Friedrich-Wilhelms-University of Bonn, Germany
Aug. 2004 - Aug. 2005	Completion of diploma thesis at the Kirchhoff Institute for Physics Department: Applied Optics and Information Processing, Ruprecht-Karls Univertity of Heidelberg, Germany
Oct. 2002 - July 2005	Studies at the Faculty of Physics and Astronomy, Ruprecht-Karls Univertity of Heidelberg, Germany
Oct. 2000 - Sept. 2002	Studies at the Faculty of Physics and Astronomy, Juluis-Maximilians University of Würzburg, Germany
Sept. 1990 - June 2000	Secondary School, Karl-Theodor- von Dalberg-Gymansium, Aschaffenburg, Germany

List of Publications:

S. Fenz, H. Mathèe , G. Kreth , D. Baddeley , Y. Weiland , J. Schwarz-Finstlerle, C. G. Cremer and U. J. Birk. Two-color intranuclear distance measurements of gene regions in human lymphocytes. Proc. of SPIE-OSA Biomedical Optics. SPIE Vol. 6630, 663002-1, 2007

S. F. Fenz, R. Merkel and K. Sengupta. Diffusion and Inter-Membrane Distance: Case Study of Avidin and E-cadherin Mediated Adhesion. Langmuir, *in press*

Bibliography

[1] B. Alberts, A. Johnson, J. Lewis, M. Raff, K. Roberts, and P. Walter. *Molecular biology of the cell*. Garland Science, New York, 2002.

[2] P Verkade and K. Simons. Robert feulgen lecture 1997. Lipid microdomains and membrane trafficking in mammalian cells. *Histochem Cell Biol.*, 108:211 – 220, 1997.

[3] T. Kurzchalia and R. Parton. Membrane microdomains and caveolae. *Curr. opin. Cell Biol.*, 11:424 – 431, 1999.

[4] C. Fielding. Caveolae and signaling. *Curr. Opin. Lipidol.*, 12:281 – 287, 2001.

[5] J. B. Helms and C. Zurzolo. Lipids as targeting signals: lipid rafts and intracellular trafficking. *Traffic*, 5:247 – 254, 2004.

[6] http://cellbiology.med.unsw.edu.au/units/science/lecture0803.htm. University of New South Wales, Sydney, Australia. webpage, December 08.

[7] S. J. Singer and G. L. Nicolson. The fluid mosaic model of the structure of cell membranes. *Science*, 175:720 – 731, 1972.

[8] K. Simons and E. Ikonen. Functional rafts in cell membranes. *Nature*, 387:569 – 572, 1997.

[9] K. Simons and G. van Meer. Lipid sorting in epithelial cells. *Biochemistry*, 27:6197 – 6202, 1998.

[10] D. Brown and E. London. Structure and function of sphingolipid- and cholesterol-rich membrane rafts. *J. Biol Chem*, 275:17221 – 17224, 2000.

[11] C. Dietrich, Z. Volovyk, M. Levi, N. Thompson, and K. Jacobson. Partitioning of thy-1, gm1, and cross-linked phospholipid analogs into lipid rafts reconstituted in supported model membrane monolayers. *Proc. Natl. Acad. Sci. USA*, 98:10642 – 10647, 2001.

[12] C. Dietrich, L. Bagatolli, Z. Volovyk, N. Thompson, M. Levi, K. Jacobson, and E. Gratton. Lipid rafts reconstituted in model membranes. *Biophys. J.*, 80:1417 – 1428, 2001.

[13] J. Korlach, P. Schwille, W. Webb, and G. Feigenson. Characterization of lipid bilayer phases by confocal microscopy and fluorescence correlation spectroscopy. *Proc. Natl. Acad. Sci.*, 96:8461 – 8466, 1999.

[14] K. Jacobson, O. G. Mouritsen, and R. G. W. Anderson. Lipid rafts: at a crossroad between cell biology and physics. *Nat. Cell Biol.*, 9:7 – 14, 2007.

[15] D. M. Engelman. Membranes are more mosaic than fluid. *Nature*, 438:578 – 580, 2005.

[16] A. Kusumi and K. Suzuki. Toward understanding the dynamics of membrane-raft-based molecular interactions. *Biochim. Biophys. Acta*, 1746:234 – 251, 2005.

[17] G. M. Edelman. Cell adhesion and morphogenesis: the regulator hypothesis. *Proc. Natl. Acad. Sci.*, 81:1460 – 1464, 1984.

[18] M. Takeichi. Morphogenetic roles of classic cadherins. *Curr. Opin. Cell Biol.*, 7:619 – 627, 1995.

[19] P. S. Frenette and D. D. Wanger. Adhesion molecules - Part 1. *N. Engl. J. Med.*, 334:1526 – 1529, 1996.

[20] B. M. Gumbiner. Regulation of cadherin-mediated adhesion in morphogenesis. *Nat. Rev. Mol. Cell Biol.*, 6:622 – 634, 2005.

[21] J. M. Gooding, K. L. Yap, and M. Ikura. The cadherin-catenin complex as a focal point of cell adhesion and signalling: new insights from three-dimensional structures. *BioEssays*, 26:497 – 511, 2004.

[22] E. Zamir and B. Geiger. Components of cell-matrix adhesions. *J. Cell Sci.*, 114:3577 – 3579, 2001.

[23] D. Leckband and A. Prakasam. Mechanism and dynamics of cadherin adhesion. *Annu. Rev. Biomed. Eng.*, 8:259 – 287, 2006.

[24] A. S. Yap, W. M Brieher, and B. M. Gumbiner. Molecular and functional analysis of cadherin-based adherens junctions. *Annu. Rev. Cell Dev. Biol.*, 13:119 – 46, 1997.

[25] A. Tomschy, F. Charlotte, R. Landwehr, and J. Engel. Homophilic adhesion of E-cadherin occurs by a cooperative two-step interaction of N-terminal domains. *EMBO J.*, 15:3507 – 3514, 1996.

[26] A. W. Koch, S. Pokutta, A. Lustig, and J. Engel. Calcium binding and homoassociation of E-cadherin domains. *Biochemistry*, 36:7697 – 7705, 1997.

[27] O. Pertz, A. Bozic, C. Fauser, A. Brancaccio, and J. Engel. A new crystal structure, Ca^{2+} dependence and mutational analysis reveal molecular details of E-cadherin homoassociation. *EMBO J.*, 18:173847, 1999.

[28] B. Nagar, M. Overduin, I. Mitsuhiko, and J. M. Rini. Structural basis of calcium induced E-cadherin rigidification and dimerization. *Nature*, 380:360 – 364, 1995.

[29] T. J. Boggon, J. Murray, S. Chappuis-Flament, E. Wong, B. M. Gumbiner, and L. Shapiro. C-cadherin ectodomain structure and implications for cell adhesion mechanisms. *Science*, 296:1308 – 1313, 2002.

[30] A. Nose, K. Tsuij, and M. Takeichi. Localization of specificity determining sites in cadherin cell adhesion molecules. *Cell*, 61:147 – 155, 1990.

[31] L. Shapiro, A. M. Fannon, P. D-Kwong, A. Thomson, M. S. Lehmann, G. Grubel, J. F. Legrand, J. Als-Nielsen, D. R. Colman, and W. A. Hendrickson. Structural basis of cell-cell adhesion by cadherins. *Nature*, 374:327 – 337, 1995.

[32] S. Sivasankar, W. Brieher, N. Lavrik, B. Gumbiner, and D. Leckband. Direct molecular force measurements of multiple adhesive interactions between cadherin ectodomains. *Proc. Natl. Acad. Sci.*, 96:11820 – 11824, 1999.

[33] B. Zhu, S. Chappuis-Flament, E. Wong, I. E. Jensen, B. M. Gumbiner, and D. Leckband. Functional analysis of the structural basis of homophilic cadherin adhesion. *Biophys. J.*, 84:4033 – 4042, 2003.

[34] A. K. Prakasam, V. Maruthamuthu, and D. E. Leckband. Similarities between heterophilic and homophilic cadherin adhesion. *Proc. Natl. Acad. Sci.*, 103:15434 – 15439, 2006.

[35] F. Steinitz. Über das Verhalten phosphorhaltiger Eiweisskörper im Stoffwechsel. *Arch. Ges. Physiol.*, 72:75 – 104, 1898.

[36] V. du Vigneaud. The structure of biotin. *Science*, 96:455 – 461, 1942.

[37] S. A. Harris, D. E. Wolf, R. Mozingo, and K. Folkers. Synthetic biotin. *Science*, 97:447 – 448, 1943.

[38] W. Traub. Crystal structure of biotin. *Nature*, 178:649 – 650, 1956.

[39] W. Friedrich. *Vitamins*. Walter de Gruyter, 1988.

[40] W. Kuri-Harcuch, L. S. Wise, and H. Green. Interruption of the adipose conversion of 3T3 cells by biotin deficiency: differencation without triglyceride accumulation. *Cell*, 14, 1978.

[41] J. T. Kung, C. G. Mackenzie, and D. W. Telmage. The requirement for biotin and fatty acids in the cytotoxic T-cell response. *Cellul. Immunulogy*, 48, 1979.

[42] N. M. Green. *Methods in Enzymology 184*, chapter Avidin and Streptavidin, pages 51–67. Academic Press, London, 1990.

[43] R. E. Eakin, E. E. Snell, and R. J. Williams. A constituent of raw egg white capable of inactivating biotin in vitro. *J. Biol. Chem.*, 136:801 – 802, 1940.

[44] P. Gyorgy. *The Vitamins*. Academic Press, New York, 1954.

[45] R. E. Eakin, E. E. Snell, and R. J. Wiliams. The concentration and assay of avidin, the injury-producing protein in raw egg white. *J. Biol. Chem.*, 140:535 – 543, 1941.

[46] J. K. Korpela, M. S. Kulomaa, H. A. Elo, and P. J. Tuohimaa. Biotin-binding proteins in eggs of oviparous vertebrates. *Experientia*, 37, 1981.

[47] N. M. Green. Avidin. *Adv. Prot. Chem.*, 29:85 – 133, 1975.

[48] L. Pugliese, A. Coda, M. Malcovati, and M. Bolognesi. Three-dimensional structure of the tetragonal crystal form egg-white avidin in its functional complex with biotin at 2.7 Å resolution. *J. Mol. Biol.*, 231:1535 – 1555, 1993.

[49] C. A. Helm, W. Knoll, and J. N. Israelachvili. Measurement of ligand-receptor interactions. *Proc. Natl. Acad. Sci.*, 88:8169 – 8173, 1991.

[50] P. C. Weber, D. H. Ohlendorf, J. J. Wendolowski, and F. R. Salemme. Structural origins of high-affinity biotin binding to streptavidin. *Science*, 243:85 – 88, 1989.

[51] O. Livnah, E. A. Bayer, M. Wilchek, and J. L. Sussman. Three-dimensional structures of avidin and the avidin-biotin complex. *PNAS*, 90:5076 – 5080, 1993.

[52] M. Gonzalez, L. A. Bagatolli, I. Echabe, J. L. R.Arrondo, C. E. Argarana, C. R. Cantor, and G. D. Fidelio. Interaction of biotin with streptavidin. Thermostability and conformational changes upon binding. *J. Biol. Chem.*, 25:11288 – 11294, 1997.

[53] D. H. Williams, E. Stephens, and M. Zhou. Ligand binding energy and catalytic efficiency from improved packing within receptors and enzymes. *J. Mol. Biol.*, 329:389 – 399, 2003.

[54] M. Wilchek, E. A. Bayer, and O. Livnah. Essentials of biorecognition: The (strept)avidin-biotin system as a model for protein-protein and protein-ligand interaction. *Immunology Letters*, 103:27 – 32, 2006.

[55] N. Voiculetz, I. Motoc, and Z. Simon, editors. *Specific interactions and biological recognition processes*. CRC Press, Boca Raton, FL, 1993.

[56] M. Gonzales, C. E. Argarana, and G. D. Fidelio. Extremely high thermal stability of streptavidin and avidin upon biotin binding. *Biomol. Eng.*, 16:67 – 72, 1999.

[57] S. E. Ross, S. D. Carson, and L. M. Fink. Effects of detergents on avidin-biotin interaction. *BioTechniques*, 4:350 – 354, 1986.

[58] O. H. Laitinen, V. P. Hytönen, H. R. Nordlund, and M. S. Kulomaa. Genetically engineered avidins and streptavidins. *Cell. Mol. Life Sci.*, 63:2992 – 3017, 2006.

[59] J. N. Israelachvili. *Intermolecular and Surface Forces*. Academic Press, 1992.

[60] E. Sackmann. *Handbook of Biological Physics*, chapter 5. Elsevier Science B.V., 1995.

[61] J. Kim, G. Kim, and P. S. Cremer. Investigations of water structure at the solid/liquid interface in the presence of supported lipid bilayers by vibrational sum frequency spectroscopy. *Langmuir*, 17:7255 – 7260, 2001.

[62] R. Merkel, E. Sackmann, and E. Evans. Molecular friction and epitactic coupling between monolayers in supported lipid bilayers. *J. Phys. France*, 50:698 – 710, 1989.

[63] S. J. Johnson, T. M. Bayerl, D. C. McDermott, G. W. Adam, A. R. Rennie, R. K. Thomas, and E. Sackmann. Structure of an adsorbed dimyristoylphosphatidylcholin bilayer measured with specular reflection of neutrons. *Biophys. J.*, 59:289 – 294, 1991.

[64] E. Kalb, S. Frey, and L. K. Tamm. Formation of supported planar bilayers by fusion of vesicles to supported phospholipid monolayers. *Biochim Biophys Acta*, 1103:307 – 316, 1992.

[65] C. A. Keller, K. Glasmästar, V. P. Zhdanov, and B. Kasemo. Formation of supported membranes from vesicles. *Phys. Rev. Lett.*, 84:5443 – 5446, 2000.

[66] H. M. McConnell, T. H. Watts, R. M. Weis, and A. A. Brian. Supported planar membranes in studies of cell-cell recognition in the immune system. *Biochim. Biophys. Acta*, 864:95 – 106, 1986.

[67] L. K. Tamm and H. M. McConnell. Supported phospholipid bilayers. *Biophys. J.*, 47:105 – 113, 1985.

[68] A. W. Adamson and A. P. Gast. *Physical cehemistry of surfaces*. Wiley, New York, 1997.

[69] J. P. Reeves and R. M. Dowben. Formation and properties of thin-walled phospholipid vesicles. *J. Cell Physiol.*, 73:49 – 60, 1969.

[70] F. Olson, C. A. Hunt, F. C. Szoka, W. J. Vail, and D. Papahadjopoulos. Preparation of liposomes of defined size distribution by extrusion through polycarbonate membranes. *Biochim. Biophys. Acta*, 557:9 – 23, 1979.

[71] M. I. Angelova and D. S. Dimitrov. Liposome electroformation. *Faraday Discuss.*, 81:303 – 311, 1986.

[72] M. Karlsson, K. Nolkrantz, M. J. Davidson, A. Strömberg, F. Ryttsén, B. Akerman, and O. Orwar. Electroinjection of colloid particles and biopolymers into single unilamellar liposomes and cells for bioanalytical applications. *Anal. Chem.*, 72:5857 – 5862, 2000.

[73] F. Szoka and D. Papahadjopoulos. Procedure for preparation of liposomes with large internal aqueous space and high capture by reverse-phase evaporation. *Proc. Natl. Acad. Sci.*, 75:4194 – 4198, 1978.

[74] J. C. Stachowiak, D. L. Richmond, T. H. Li, A. P. Liu, S. H. Parekh, and D. A. Fletcher. Unilamellar vesicle formation and encapsulation by microfluidic jetting. *Proc. Natl. Acad. Sci.*, 105:4697 – 4702, 2008.

[75] G. Cevc. *Phospholipids Handbook*. Marcel Dekker Inc., New York, NY, 1993.

[76] C. Monzel. Thermische Fluktuationen zweidimensionaler, flexibler Objekte - eine Interferometrische Untersuchung an strukturiert adhärierten Lipidmem-

branen. Diplomarbeit, Rheinische Friedrich - Wilhelms - Universität, Bonn, 2008.

[77] T. Browicz. Further observation of motion phenomena on red blood cells in pathological states. *Zbl. med. Wissen*, 28:625 – 627, 1890.

[78] A. K. Parpart and J. F. Hoffman. Flicker in erythrocytes; vibratory movements in the cytoplasm. *J. Cell. Physiol.*, 47:295 – 303, 1956.

[79] F. Brochard and J. F. Lennon. Frequency spectrum of the flicker phenomenon in erythrocytes. *Journal de Physique*, 36:1035–1047, 1975.

[80] B. Lorz, R. Simson, J. Nardi, and E. Sackmann. Weakly adhering vesicles in shear flow: Tanktreading and anomalous lift force. *Europhys. Lett.*, 51:486 – 474, 2000.

[81] R. Bruinsma, A. Behrisch, and E. Sackmann. Adhesive switching of membranes: experiment and theory. *Phys. Rev. E*, 61:4253 – 4267, 2000.

[82] F. Tausig and F. J. Wolf. Streptavidin - a substance with avidin-like properties produced by micro-organisms. *Biochem. Biophys. Commun.*, 14:205 – 209, 1964.

[83] Molecular Probes. *The Handbook: A Guide to Fluorescent Probes and Labeling Technologies*, chapter 7. 2007.

[84] S. A. Darst, M. Ahlers, P. H. Meller, E. W. Kubalek, R. Blankenburg, H. O. Ribi, H. Ringsdorf, and D. R. Kornberg. Two-dimensional crystals of streptavidin on biotnylated lipid layers and their interactions with biotinylated macromolecules. *Biophys. J.*, 59:387 – 396, 1991.

[85] S. W. Wang, C. L. Poglitsch, M. T. Yatcilla, C. R. Robertson, and A. P. Gast. Solid phase coexistance in chiral domains of two-dimensional streptavidin crystals. *Langmuir*, 13:5794 – 5798, 1997.

[86] S. W. Wang, C. R. Robertson, and A. P. Gast. Molecular arrangement in two-dimensional streptavidin crystals. *Langmuir*, 15:1541 – 1548, 1999.

[87] P. Ratanabanangkoon, M. Gropper, R. Merkel, E. Sackmann, and A. P. Gast. Two-dimensional streptavidin crystals on giant lipid bilayer vesicles. *Langmuir*, 18:4270 – 4276, 2002.

[88] L. Schmitt, C. Dietrich, and R. Tampé. Synthesis and characterization of chelator-lipids for reversible immobilization of engineered proteins at self-assembled lipid interfaces. *J. Am. Chem. Soc.*, 116:8485 – 8491, 1994.

[89] Avanti Polar Lipids, Inc. *Catalogue*, April 2008. Pages 528, 867, 965, 987, 1114 and 1175.

[90] P. de Gennes. Conformations of polymers attached to an interface. *Macromolecules*, 13:1069 – 1075, 1980.

[91] J. Majewski T. L. Kuhl, M. C. Gerstenberg, J. N. Israelachvili, and G. S. J. Smith. Structure of phospholipid monolayers containing poly(ethylene glycol) lipids at the air - water interface. *Phys. Chem B*, 101:3122 – 3129, 1997.

[92] C. Dietrich, R. Merkel, and R. Tampé. Diffusion measurement of fluorescence-labeled amphiphilic molecules with a standard fluorescence microscope. *Biophys. J.*, 72:1701–1710, 1997.

[93] D. Meschede. *Physik*. Springer-Verlag, Berlin Heidelberg, 2002.

[94] M. Minsky. Microscopy apparatus. US patent, 1961.

[95] G. J. Brakenhoff, P. Blom, and P. Barends. Confocal scanning light microscopy with high aperture immersion lenses. *J. Microscopy*, 117:219 – 232, 1979.

[96] T. Wilson and C. J. R. Sheppard. *Theory and Practice of Scanning Optical Microscopy*. Academic Press London, 1984.

[97] C. Cremer and T. Cremer. Considerations on a laser scanning micrscope with high resolution and depth of field. *Microscopica Acta*, 81:31 – 44, 1978.

[98] J. B. Pawley. *Handbook of Biological Confocal Microscopy*. Plenum Press New York and London, 1990.

[99] G. Wiegand, K. R. Neumaier, and E. Sackmann. Microinterferometry: three-dimensional reconstruction of surface microtopography for thin-film and wetting studies by reflection interference contrast microscopy (RICM). *Appl. Opt.*, 37:6892 – 6905, 1998.

[100] A. Vasicek. *Optics of Thin Films*. North-Holland Publishing Company, Amsterdam, 1960.

[101] A. S. G. Curtis. The mechanism of adhesion of cells to glass: A study by interference reflection microscopy. *J. Cell Biol.*, 20:199 – 215, 1964.

[102] A. Zilker, M. Ziegler, and E. Sackmann. Spectral analysis of erythrocyte flickering in the 0.3-0.4μm-1 regime by microinterferometry combined with fast image processing. *Phys. Rev. A*, 46:7998 – 8001, 1992.

[103] B. G. Lorz, A.-S. Smith, C. Gege, and E. Sackmann. Adhesion of giant vesicles mediated by weak binding of sialyl-LewisX to E-selectin in the presence of repelling poly(ethylene glycol) molecules. *Langmuir*, 23:12293 – 12300, 2007.

[104] L. Limozin and K. Sengupta. Modulation of vesicle adhesion and spreading kinetics by hyaluronan cushions. *Biophys. J.*, 93:3300 – 3313, 2007.

[105] J. S. Ploem. *Mononuclear phagocytes in immunity, infection and pathology.* Blackwell Scientific Publications, 1975.

[106] J. Schilling, K. Sengupta, S. Goennenwein, A. R. Bausch, and E. Sackmann. Absolute interfacial distance measurements by dual-wavelength reflection interference contrast microscopy. *Phys. Rev. E*, 69:021901, 2004.

[107] D. Gingell and I. Todd. Interference reflection microscopy. a quantitative theory for image interpretation and its application to cell-substratum separation measurement. *Biophys. J.*, 26:507 – 526, 1979.

[108] J. Rädler and E. Sackmann. Imaging optical thicknesses and separation distances of phospholipid vesicles at solid surfaces. *J. Phys. France II*, 3:727 – 748, 1993.

[109] G. Wiegand, T. Jaworek, G. Wegner, and E. Sackmann. Studies of structure and local wetting properties on heterogeneous, micropatterned solid surfaces by microinterferometry. *J. Colloid. Interface Sci.*, 196:299 – 312, 1997.

[110] J. Slavik. *Fluorescent Probes in Cellular and Molecular Biology*. CRC Press, Boca Raton, FL, 1994.

[111] M. Edidin, Y. Zagyansky, and T. J. Lardner. Measurement of membrane protein lateral diffusion in single cells. *Science*, 191:466 – 468, 1976.

[112] D. Axelrod, D. E. Koppel, J. Schlessinger, E. Elson, and W. W. Webb. Mobility measurment by analysis of fluorescence photobleaching recovery kinetics. *Biophys. J.*, 16:1055 – 1069, 1976.

[113] D. M. Soumpasis. Theoretical analysis of fluorescence photobleaching recovery experiments. *Biophys. J.*, 41:95 – 97, 1983.

[114] B. Jähne. *Digitale Bildverarbeitung*. Springer Verlag Berlin Heidelberg, 2002.

[115] J. Rädler, T. Feder, H. Strey, and E. Sackmann. Fluctuation analysis of tension-controlled undulation forces between giant vesicles and solid substrates. *Phys. Rev. E*, 51:4526 – 4536, 1995.

[116] W. Häckl, U. Seifert, and E. Sackmann. Effects of fully and partially solubilized amphiphiles on bilayer bending stiffness and temperature dependence of the effective tension of giant vesicles. *Journal de Physique France II*, 7:1141 – 1157, 1997.

[117] W. Helfrich. Steric interaction of fluid membranes in multilayer systems. *Z. für Naturforschung*, 33:305 – 315, 1978.

[118] B. Smeryda-Krawiec, H. Devaraj, G. Jacob, and J. J. Hickman. A new interpretation of serum albumin surface passivation. *Langmuir*, 20:2054 – 2056, 2004.

[119] R. Lipowski and U. Seifert. Adhesion of membranes: a theoretical perspecive. *Langmuir*, 7:1867 – 1873, 1991.

[120] P. S. Swain and D. Andelmann. The influence of substrate structure on membrane adhesion. *Langmuir*, 15:8902 – 8914, 1999.

[121] M. Dembo, D. C. Torney, K. Saxman, and D. Hammer. The reaction limited kinetics of membrane-to-surface adhesion and deadhesion. *Proc. R. Soc. Lond. B Biol. Sci.*, 234:55 – 83, 1988.

[122] N. J. Burroughs and C. Wülfing. Differiantial seggregation in a cell-cell contact interface: the dynamics of the immunological synapse. *Biophys J.*, 83:1784 – 1796, 2002.

[123] U. Seifert and R. Lipowski. Adhesion of vesicles. *Phys. Rev. A*, 42:4768 – 4771, 1990.

[124] Y. Zhouy and R. M. Raphaelz. Effect of salicylate on the elasticity, bending stiffness, and strength of sopc membranes. *Biophys. J.*, 89:1789 – 1801, 2005.

[125] R. Bruinsma. Adhesion and rolling of leukocytes: a physical model. *Proc. of NATO advanced Institute on Physics of Biomaterials*, 322 of NATO ASI:61, 1995.

[126] G. I. Bell, M. Dembo, and P. Bongrand. Cell adhesion: competition between non-spedific repulsion and specific bonding. *Biophys. J.*, 45:1051 – 1064, 1984.

[127] M. Dembo and G. I. Bell. *Curr. Top. Membr. Transp.*, 29:71 – 89, 1987.

[128] D. M. Zuckerman and R. Bruinsma. Vesicle-vesicle adhesion by mobile lock-and-key molecules: Debye-Hückel theory and Monte Carlo simulation. *Phys. Rev. E*, 57:964 – 977, 1998.

[129] R. Lipowski. Flexible membranes with anchored polymers. *Colloids Surfaces A*, 128:255 – 264, 1997.

[130] F. Brochard-Wyart and P.-G. de Gennes. Adhesion induced by mobile binders: Dynamics. *PNAS*, 99:7854, 2002.

[131] P.-G. de Gennes, P.-H. Puech, and F. Brochard-Wyart. Adhesion induced by mobile stickers: a list of scenarios. *Langmuir*, 19:7112 – 7119, 2003.

[132] V. B. Shenoy and L. B. Freund. Growth and shape stability of a biological membrane adhesion complex in the diffusion-mediated regime. *PNAS*, 102:3213, 2005.

[133] A. S. Smith and U. Seifert. Effective adhesion strength of specifically bound vesicles. *Phys. Rev. E*, 71:061902, 2005.

[134] A.-S. Smith and U. Seifert. Vesicle as a model for controlled (de-)adhesion of cells: a thermodynamic approach. *Soft Matter*, 3:275 – 289, 2007.

[135] A.-S. Smith, B. G. Lorz, U. Seifert, and E. Sackmann. Antagonist-induced deadhesion of specifically adhered vesicles. *Biophys. J.*, 90:1064 – 1080, 2006.

[136] A.-S. Smith, K. Sengupta, S. Goennenwein, U. Seifert, and E. Sackmann. Force-induced growth of adhesion domains is controlled by receptor mobility. *Proc. Natl. Acad. Sci.*, 105:6906 – 6911, 2008.

[137] M. R. Horton, C. Reich, A. P. Gast, J. O. Rädler, and B. Nickel. Structure and dynamics of crystalline protein layers bound to supported lipid bilayers. *Langmuir*, 23:6263 – 6269, 2007.

[138] D.-M. Zhu, M. L. Dustin, C. W. Cairo, and D. E. Golan. Analysis of two-dimensional dissociation constant of laterally mobile cell adhesion molecules. *Biophys. J.*, 92:1022 – 1034, 2007.

[139] J. M. Smaby, J. M. Muderhwa, and H. L. Brockman. Is lateral phase separation required for fatty acid to stimulate lipases in a phosphatidylcholine interface? *Biochemistry*, 33:1915 – 1922, 1994.

[140] J. A. Nye and J. T. Groves. Kinetic control of histidine-tagged protein surface density on supported lipid bilayers. *Langmuir*, 24:4145 – 4149, 2008.

[141] P. Sondermann, R. Huber, V. Oosthuizen, and U. Jacob. The 3.2-a crystal structure of the human IgG1 Fc fragment-Fc gamma R IIIcomplex. *Nature*, 406:267 – 273, 2000.

[142] A. Boulbitch, Z. Guttenberg, and E. Sackmann. Kinetics of membrane adhesion mediated by ligand-receptor interaction studied with a biomimetic system. *Biophys. J.*, 81:2743 – 2751, 2001.

[143] D. Cuvelier and P. Nassoy. Hidden dynamics of vesicle adhesion induced by specific stickers. *Phys. Rev. Lett.*, 93:228101, 2004.

[144] P.-H. Puech, V. Askovic, P.-G. de Gennes, and F. Brochard-Wyart. Dynamics of vesicle adhesion: spreading versus dewetting coupled to binder diffusion. *Biophys. Reviews and Letters*, 1:85 – 96, 2006.

[145] E. Reister-Gottfried, K. Sengupta, B. Lorz, E. Sackmann, U. Seifert, and A.-S. Smith. Dynamics of specific vesicle-substrate adhesion: From local events to global dynamics. *Phys. Rev. Lett.*, 101:208103, 2008.

[146] D. A. Noppl-Simson and D. Needham. Avidin-biotin interactions at vesicle surfaces: adsorption and binding, cross-bridge formation, and lateral interactions. *Biophys J*, 70:1391 – 1401, 1996.

[147] C. W. Maier, A. Behrisch, A. Kloboucek, D. A. Simson, and R. Merkel. Specific biomembrane adhesion -indirect lateral interactions between bound receptor molecules. *Europhys. J. E*, 6:273 – 276, 2001.

[148] S. Goennenwein, M. Tanaka, B. Hu, L. Moroder, and E. Sackmann. Functional incorporation of integrins into solid supported membranes on ultrathin films of cellulose: impact on adhesion. *Biophys. J.*, 85:646 – 655, 2003.

[149] W. Rawicz, K. C. Olbrich, T. McIntosh, D. Needham, and E. Evans. Effect of chain length and unsaturation on elasticity of lipid bilayers. *Biophys. J.*, 79:328 – 339, 2000.

[150] M. Frick, K. Schmidt, and B. J. Nichols. Modulation of lateral diffusion in the plasma membrane by protein density. *Curr. Biol.*, 17:462 – 467, 2007.

[151] A. Kusumi, C. Nakada, K. Ritchie, K. Murase, K. Suzuki, H. Murakoshi, R. S. Kasai, J. Kondo, and T. Fujiwara. Paradigm shift of the plasma membrane concept from the two-dimensional continuum fluid to the partitioned fluid:

high-speed single-molecule tracking of membrane molecules. *Annu. Rev. Biophys. Biomol. Struct.*, 34:351 – 378, 2005.

[152] P. H. M. Lommerse, H. P. Spaink, and T. Schmidt. In vivo plasma membrane organization: results of biophysical approaches. *Biochim. Biophys. Acta*, 1664:119 – 131, 2004.

[153] E. M. Adkins, D. J. Samuvel, J. U. Fog, J. Eriksen, L. D. Jayanthi, C. Bjerggaard Vaegter, S. Ramamoorthy, and U. Gether. Membrane mobility and microdomain association of the dopamine transporter studied with fluorescence correlation spectroscopy and fluorescence recovery after photobleaching. *Biochemistry*, 46:10484 – 10497, 2007.

[154] C. Dietrich, B. Yang, T. Fujiwara, A. Kusumi, and K. Jacobson. Relationship of lipid rafts to transient confinement zones detected by single particle tracking. *Biophys. J.*, 82:274 – 284, 2002.

[155] V. Yamazaki, O. Sirenko, R. J. Schafer, and J. T. Groves. Lipid mobility and molecular binding in fluid lipid membranes. *J. Am. Chem. Soc.*, 127:2826 – 2827, 2005.

[156] K. Mossman and J. Groves. Micropatterned supported membranes as tools for quantitative studies of the immunological synapse. *Chem. Soc. Rev.*, 26:46 – 54, 2007.

[157] E. Sackmann. Supported membranes: Scientific and practical applications. *Science*, 271:43 – 48, 1996.

[158] E. Sackmann and R. F. Bruinsma. Cell adhesion as wetting transition? *Chem. Phys. Chem.*, 3:262 – 269, 2002.

[159] T. Baumgart, S. T. Hess, and W. W. Webb. Imaging coexisting fluid domains in biomembrane models coupling curvature and line tension. *Nature*, 425:821 – 824, 2003.

[160] L. Limozin and E. Sackmann. Polymorphism of cross-linked actin networks in giant vesicles. *Phys. Rev. Lett.*, 89:168103168103–1 – 168103–4, 2002.

[161] T. Graham. A short account of experimental researches on the diffusion of gases through each other, and their separation by mechanical means. *Quarterly Journal of Science, Literature and Art*, 27:74 – 83, 1829.

[162] T. Graham. On the law of the diffusion of gases. *Philosophical Magazine*, 2:175 – 190, 1833.

[163] T. Graham. The bakerian lecture - On the diffusion of liquids. *Philosophical Transactions of the Royal Society of London*, 140:1 – 46, 1850.

[164] A. Fick. Über Diffusion. *Poggendorf's Annalen der Physik und Chemie*, 94:59 – 86, 1855.

[165] A. Einstein. Über die von der molekularkinetischen Theorie der Wärme geforderte Bewegung von in ruhenden Flüssigkeiten suspensierten Teilchen. *Annalen der Physik*, 8:549 – 560, 1905.

[166] M. v. Smoluchowski. Zur kinetischen Theorie der Brownschen Molekularbewegung und der Suspensionen. *Annalen der Physik*, 21:756–780, 1906.

[167] P. G. Saffmann and M. Delbrück. Brownian motion in biological membranes. *Proc. Natl. Acad. Sci.*, 72:3111 – 3113, 1975.

[168] L. Zhang and S. Granick. Slaved diffusion in phospholipid bilayers. *Proc. Natl. Acad. Sci.*, 102:9118 – 9121, 2005.

[169] E. Evans and E. Sackmann. Translational and rotational drag coefficients for a disk moving in a liquid membrane associated with a rigid substrate. *J. Fluid. Mech.*, 194:553 – 561, 1988.

[170] M. Tanaka and E. Sackmann. Supported membranes as biofunctional interfaces and smart biosensor platforms. *Phys. Stat. Sol. A*, 203:3452 – 3462, 2006.

[171] O. Purrucker, A. Förtig, R. Jordan, E. Sackmann, and M. Tanaka. Control of frictional coupling of transmembrane cell receptors in model cell membranes with linear polymer spacers. *Phys. Rev. Lett.*, 98:078102, 2007.

[172] M. J. Saxton. Lateral diffusion in an archipelago: The effect of mobile obstacles. *Biophys. J.*, 52:989 – 997, 1987.

[173] M. J. Saxton. Anomalous diffusion due to obstacles: a Monte Carlo study. *Biophys. J.*, 66:394 – 401, 1994.

[174] R. A. Tahir-Kheli. Correlation factors for atomic diffusion in nondilute multicomponent alloys with arbitrary vacancy concentration. *Phys. Rev. B*, 28:3049 – 3056, 1983.

[175] H. Van Beijeren and R. Kutner. Mean square displacement of a tracer particle in a haed-core lattice gas. *Phys. Rev. Lett.*, 55:238 – 241, 1985.

[176] T. M. Nieuwenhuizen, P. F. J. van Velthoven, and M. H. Ernst. Diffusion and long-time tails in a two-dimensional site-percolation model. *Phys. Rev. Lett.*, 57:2477 – 2480, 1986.

[177] M. L. Dustin, L. M. Ferguson, P. Y. Chan, T. A. Springer, and D. E. Golan. Visualization of CD2 interaction with LFA-3 and determination of the two-dimensional dissociation constant for adhesion receptors in a contact area. *J. Cell. Biol.*, 132:465 – 474, 1996.

[178] T. P. Tolentino, J. Wu, V. I. Zarnitsyna, Y. Fang, M. L. Dustin, and C. Zhu. Measuring diffusion and binding kinetics by contact area FRAP. *Biophys. J.*, 95:920 – 930, 2008.

[179] M. Kühner, R. Tampé, and E. Sackmann. Lipid mono- and bilayer supported on polymer films: composite polymer-lipid films on solid substrates. *Biophys. J.*, 67:217 – 226, 1994.

[180] E. Evans and A. Yeung. Hidden dynamics in rapid changes of bilayer shape. *Chem. Phys. Lipids*, 73:39 – 56, 1994.

[181] J. Dai and M. P. Sheetz. Mechanical properties of neuronal growth cone membranes studied by tether formation with laser optical tweezers. *Biophys. J.*, 68:988 – 996, 1995.

[182] U. Seifert and S. A. Langer. Viscous modes of fluid bilayer membranes. *Europhys. Lett.*, 23:71 – 76, 1993.

[183] M. H. Cohen and D. Turnbull. Molecular transport in liquids and glasses. *J. Chem. Phys.*, 31:1164 – 1169, 1959.

[184] C. Lou, Z. Wang, and S.-W. Wang. Two-dimensional protein crystals on a solid substrate: effect of surface ligand concentration. *Langmuir*, 23:9752 – 9759, 2007.

[185] E. Perret, A.-M. Benoliel, P. Nassoy, A. Pierres, V. Delmas, J.-P. Thiery, P. Bongrand, and H. Feracci. Fast dissociation kinetics between individual E-cadherin fragments revealed by flow chamber analysis. *EMBO J.*, 21:2537 – 2546, 2002.

[186] P. Y. Chan, M. B. Lawrence, M. L. Dustin, L. M. Ferguson, D. E. Golan, and T. A. Springer. Influence of receptor lateral mobility on adhesion strengthening between membranes containing LFA-3 and CD2. *J. Cell. Biol.*, 115:245 – 255, 1991.

List of Figures

List of Tables